Superconducting Magnetic Energy Storage Haute Température Critique comme Source Impulsionnelle

Arnaud Badel

UNIVERSITE DE GRENOBLE
INSTITUT POLYTECHNIQUE DE GRENOBLE

N° attribué par la bibliothèque
|__|__|__|__|__|__|__|__|__|__|

T H E S E

pour obtenir le grade de

DOCTEUR DE L'Université de Grenoble
délivré par l'Institut polytechnique de Grenoble

Spécialité : « Génie Electrique »

préparée au laboratoire Institut Néel

et au G2ELab, Laboratoire de Génie Electrique de Grenoble

dans le cadre de **l'Ecole Doctorale**

« Electronique, Electrotechnique, Automatique & Traitement du Signal »

présentée et soutenue publiquement

par

Arnaud Badel

Le 3 Septembre 2010

Superconducting Magnetic Energy Storage using High Temperature Superconductor for Pulse Power Supply

---

DIRECTEUR DE THESE
Pascal Tixador

JURY

M.	Jean-Pascal Cambronne	, Président du Jury
M.	Michel Decroux	, Rapporteur
M.	Bernard Multon	, Rapporteur
M.	Pascal Tixador	, Directeur de thèse
M.	Michel Amiet	, Examinateur
M.	Pascale Lehmann	, Examinateur
M.	César Luongo	, Examinateur

Table of contents

General Introduction

The purpose of this work is to study the possibilities of Superconducting Magnetic Energy Storage using High Temperature Superconductor (HTS SMES) as pulse-current power source, an application for which no satisfying solution exists currently. The objective that is more specifically considered is Electro-Magnetic Launcher (EML) powering.

This work was conducted in the framework of a Délégation Générale pour l'Armement (DGA) contract in cooperation with Saint Louis Institute (ISL) where EML and pulse power sources are developed. It is based on the experience acquired at Neel Institute and Grenoble Electrical Engineering Laboratory on large scale superconductive applications. The activities on HTS magnets started in 2003, with the design and realization of a first HTS SMES demonstrator, SMES I, which was tested in 2007.

In the first chapter, the superconductivity is introduced, from an application point of view. High Temperature Superconductors, which were discovered in 1986 and whose industrial development was just beginning to emerge in 2003 when the SMES project started, are more specifically presented. The principles of Magnetic Energy Storage are also introduced, and the constraints governing SMES design, are presented. The possible applications of SMES are finally detailed, with a brief state of the art of the SMES activities around the world.

In the second chapter, the use of SMES for EML powering is investigated. After a brief introduction on EML principle, simulations of both classical capacitor-based and SMES-based EML powering are proposed, to underline the potential interest of SMES for this application. The results of this theoretical study are moderated by considerations about SMES practical realization, especially concerning the very high (tenths of kA) required operating current. In a second time, solutions are studied for SMES output current multiplication on one hand, and EML current reduction on the other. A novel concept of integrated SMES-Launcher is proposed, and the first results of such optimized configurations are presented.

The third chapter presents the studies conducted for the design of SMES II, an upgrade of SMES I. Its characteristics as demonstrator for pulse power application are first described and justified, with the expected ratings and operation modes. The design solutions are then discussed, presenting the main issues and the tools that were developed for solving them.

The fourth and last chapter describes the experimental studies that were conducted to test the design solutions, and the realization process of SMES II. The tests campaigns carried out at Grenoble and at ISL are presented, and the experimental results are compared with the expected theoretical results.

Conclusions are then drawn, presenting the promising benefits of using SMES as current pulse power source for EML powering and the foreseen mid-term perspectives of integrated SMES-EML designs.

CHAPTER 1 :
INTRODUCTION TO
SUPERCONDUCTING MAGNETIC ENERGY STORAGE

In this first chapter we introduce the superconductivity from an electrical engineering point of view, pointing up the key characteristics for application design. The presentation is focused on high temperature superconductor materials, which are used in the demonstrator presented in Chapter 3 & 4. In a second time are presented the inductive storage principle and its applications, with a brief state of the art.

1. Superconductivity: Elements for the design of applications

1.1 Description of the superconductivity phenomenon

1.1.1 Critical temperature and critical magnetic fields

The name *superconductivity* was originally chosen to describe the property of some materials to have their electrical resistivity falling to zero abruptly below a critical temperature (T_c) that varies with the material. Superconducting loops of wire have been shown to carry electrical currents for thousand years with no measurable loss which means that the resistance is null as far as it can be measured.

It was later demonstrated than superconductivity is formally a thermodynamic state. The transition between normal and superconducting state is a second-order phase transition from the thermodynamic point of view (like superfluid transition or gas-liquid transition above the critical point). It features divergent evolution of the physical parameters (electrical conductivity, magnetic susceptibility, etc.) but no latent heat as the first-order phase transitions (i.e. gas-liquid or liquid-solid transitions).

Apart from the lack of losses when circulating current in a superconducting material, other phenomena are taking place, making it impossible to consider superconductivity simply as infinite conductivity. Particularly, when the material is entering the superconducting state, its magnetic properties are modified. Three critical magnetic fields are defined, B_{c1} B_{irr} and B_{c2} :

- Below B_{c1}, the magnetic flux density is expelled from the material: it is the so-called Meissner effect. This critical value is generally very low, in the 10 mT range.
  In this state, a current circulation produces strictly no losses, but operation is very limited as the field produced by circulating current will rapidly overstep B_{c1}.
- Between B_{c1} and B_{irr} (the irreversibility magnetic flux density), magnetic flux density starts to penetrate in the material creating vortices. The material is partially superconducting and partially normal (in the vortices). B_{irr} is usually much higher than B_{c1}, up to several tenths of Tesla for some materials. The superconducting devices are classically operating in this state

- When B_{irr} is overstepped, the vortexes which were previously inert (pinned) starts moving, interacting with the circulating current. This creates losses, and an electric field appears along the conductor. However when these losses appear they are still several orders lower than the losses obtained for the same current density with the material in its normal state.

  It should be noted that B_{irr} is not an intrinsic property of the superconducting materials; it depends of many factors, especially the crystalline structure of the superconductor. For a given material it may vary up to one order of magnitude.

- Over B_{c2} the material is completely penetrated by the field and returns to the normal state, even if it stays lower than T_c.

In conclusion, the intrinsic parameters limiting the superconducting state are: T_c, critical temperature and B_{c1} - B_{c2}, critical magnetic fields, to which should be added B_{irr}. Some materials have no B_{c2}, directly going back the normal state when magnetic flux density exceeds B_{c1}. These materials (usually pure metals) are improper for applications and will not be considered any further.

1.1.2 Transition and Power Law

Transition description through power law

The interest of superconductors in electrical devices is the possibility of creating cables carrying electrical current without losses (or with drastically reduced losses). However, the maximal current density that is possible to carry with a given material in its superconducting state is not an intrinsic critical parameter, such as T_c, B_{c1} and B_{c2}. It depends of various extrinsic parameters (geometry of the conductor, oxygenation and microstructure of the material, etc.).

The so-called critical current is thus defined arbitrary as the limit below which the dissipation is considered zero. The criterion considered for this limit is the electrical field E_c, whose value is generally 0.1 μV/cm or 1 μV/cm depending on the material.

The evolution of the losses with the circulating current is sharp but continuous between zero, when the magnetic field is below B_{c1} and the normal state reached at B_{c2} and/or T_c. Close below Jc, It can be efficiently fitted with a power law, following Eq. (1-1).

$$E = E_c \left(\frac{J}{J_{c_{B,T}}} \right)^{n_{B,T}} \quad \textbf{(1-1)}$$

This equation introduces the n value describing the sharpness of the transition, and the arbitrary criterion E_c already mentioned, which defines the limit between what we consider as the non-dissipative and dissipative state.

It let us determine J_c, the *critical current density* of the material. The equation also introduces the dependency of J_c and n to the true intrinsic parameters: magnetic flux density and temperature.

Critical surface

From the designer's point of view, three parameters may therefore be considered when determining the non-dissipative operation limits of a superconducting conductor: The two intrinsic parameters, temperature and magnetic field, and the critical current density defined above.

In the (T, B, J) space, these parameters defines a critical surface (Figure 1-1). If the material operating point leaves the domain limited by this surface, it starts to dissipate until returning to the normal (resistive) state.

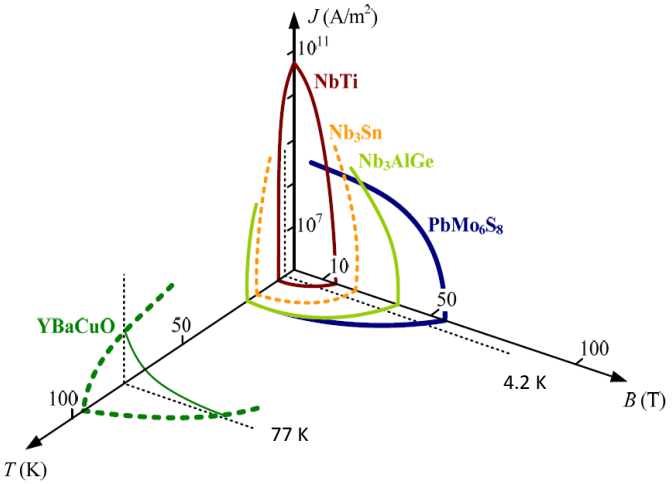

Figure 1-1: Order of magnitude of the critical surface for various superconductors

Superconducting material classification

The first discovered superconductors were metals and alloys, with critical temperatures below 30 K and operating generally around 4.2 K, the liquid helium boiling point at room pressure. They are called *Low Temperature Superconductors* (LTS). They usually have extremely sharp transitions, with *n* values higher than 100.

NbTi (Niobium titanium), with a critical temperature of 9 K is the most commonly used; most of the classical large scale applications of superconductivity up to know are using it. It is relatively easy to manufacture even in long lengths and it has good mechanical properties. The only other LTS material used in large scale applications is Nb_3Sn, harder to manufacture than NbTi but with better characteristics in terms of critical temperature (18 K) and critical magnetic flux density. It is used especially for very high field magnets, over 11T and up to 23 K.

In 1986, superconductivity at much higher temperature was discovered in a new type of material. Since then a lot of so called *High Temperature Superconductors* (HTS) were discovered. They are presented in the following section.

1.2 HTS Materials

HTS materials are usually complex ceramics, with strongly anisotropic properties. Besides their high critical temperatures, they have higher critical currents and magnetic flux densities than most LTSs. They also present smoother transitions between superconducting and resistive states with *n* values typically between 10 and 20.

The most commonly used HTS materials are BiSrCaCuO, which exists in two types depending on its crystalline structure, and YBaCuO. Their critical temperatures are:

- 86 K for BSCCO 2212 ($Bi_2Sr_2Ca_1Cu_2O_x$)
- 110 K for BSCCO 2223 ($Bi_2Sr_2Ca_2Cu_3O_x$)
- 92 K for YBCO 123 ($Y_1Ba_2Cu_3Ox$).

Since their discovery there were high expectations toward HTS materials, as their better characteristics was letting expect considerable gains for superconducting applications. Unfortunately manufacturing wires using this kind of material is much more difficult than with standard LTS and today, more than twenty years after their discovery, large scale devices using this kind of materials are just beginning to appear.

1.2.1 HTS conductors structure

HTS ceramics cannot be made into cable in their bulk form. They are too brittle and anyway the crystal growth cannot be extended to long lengths. The only way to build reasonably long wires is therefore to juxtapose small grains of HTS material. As the superconducting characteristics of the material (especially its critical current) depend of the crystal structure continuity, the different grains must be oriented identically and correctly juxtaposed. Different methods are used depending on the material.

For BSSCO, the most commonly used method is to enclose the ceramic grains in a silver or silver-alloy matrix, through a process called “Powder In Tube”. BSCCO powder is placed in silver or silver-alloy tubes. These tubes are then drawn to obtain small wires, which are stacked together and laminated to obtain a tape (Figure 1-2). The tape is then submitted to heat treatment for the BSCCO to obtain superconducting characteristics. During this process, the BSCCO cores of all the elementary tubes form continuous filaments (in black Figure 1-2) in the silver matrix (in white).

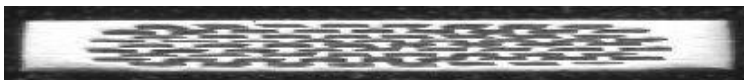

Figure 1-2 : BSSCO Powder-In-Tube tapes cross section (Nexans)

With YBCO, Coated Conductor (CC) tapes are realized. The YBCO grains are placed on a substrate through one or more buffer layers (Figure 1-3). It is the substrate and/or buffer texture that aligns the YBCO grains during their deposition. The layers deposition process is the most important issue for YBCO CC tapes developments. Different methods are used, from Pulse Laser Deposition to vapour phase deposition [Car08].

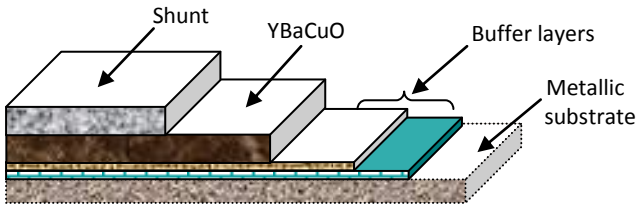

Figure 1-3: Architecture of YBCO Coated Conductor tape (not to scale)

BSCCO wires are now available in kilometric lengths; it is the base of the prototype we will present in Chapter3 and 4. YBCO wires are still under developments, but wires of hundreds of meters are already available.

1.2.2 Electrical characteristics

The critical current density J_c already introduced is a characteristic of the superconducting material. As only a small part of the HTS conductors section is actually superconducting, is not an efficient

image of the actual current transport capacity. For application design, the engineering critical current density J_e, is preferred. It is defined as the critical current I_c divided by the total conductor section, Eq. (1-2).

$$J_e = \frac{J_c \cdot S_{superconductor}}{S_{total}} = \frac{I_c}{S_{total}} \quad \textbf{(1-2)}$$

For Coated Conductor tapes, which are usually available in several tape widths, the critical current is often given in A/cm, thus for 1 centimetre width.

Temperature and magnetic field dependency

The crystalline anisotropy of HTS ceramics creates anisotropic superconducting characteristics (Figure 1-4).

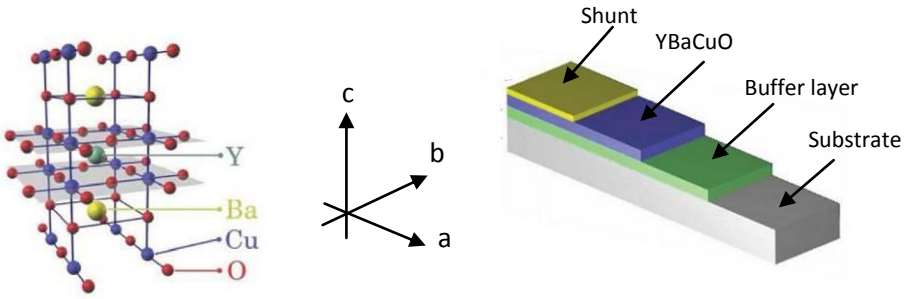

Figure 1-4 : Comparison between crystalline structure (left) and tape orientation (right) for YBCO superconductor.

Two cases have to be studied: characteristics in the *a,b* plane and characteristics along the *c* axes, respectively called *longitudinal* and *transverse*. The critical current is much lower in transverse field (Figure 1-5). This specificity must be taken into account when designing the application.

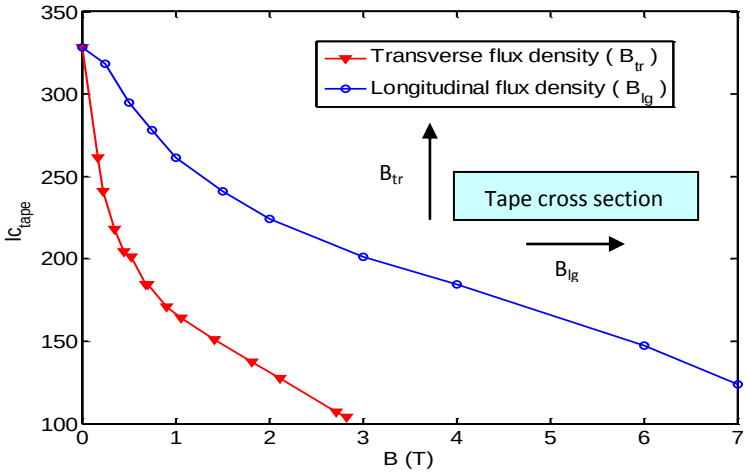

Figure 1-5: Influence of magnetic flux density orientation on BSCCO tape critical current density at 20 K [TDB+08].

The critical current densities of superconductors decrease with magnetic flux density but also with temperature. This evolution is specific to each material; in particular BSSCO have poor characteristics at high temperature when compared to YBCO, even if its T_c is higher (Figure 1-6).

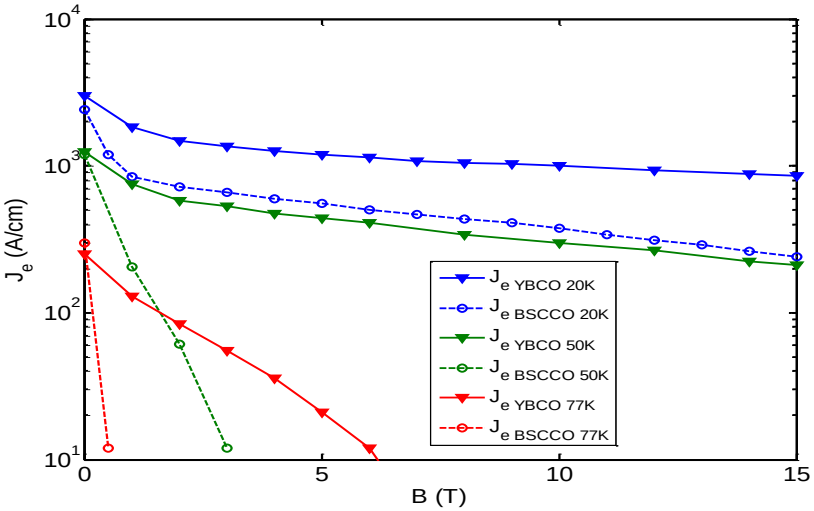

Critical current densities are presented in Amperes per centimetres width. As mentioned above, this unit makes sense for CC tapes like YBCO.

Though BSCCO is not a CC, an equivalent A/cm value was calculated for it to make comparison easier

Figure 1-6 : YBCO and BSCCO critical current density evolution under increasing magnetic flux density (longitudinal direction) for 20, 50 and 77 K

Equivalent electrical resistivity

The non-superconducting materials represent around 60 % of a BSCCO tape and reach more than 95 % of an YBCO tape.

- When the HTS material is well below its critical current and does not dissipate, the non-superconducting part of the tape is perfectly short-circuited.

  If the current is increased and the HTS material starts to dissipate, the non-superconducting part is not perfectly short circuited anymore and the wire may be seen as two resistances in parallel (Figure 1-7).

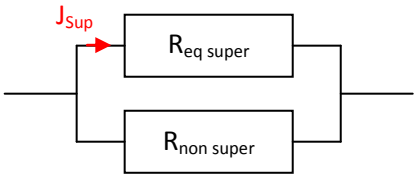

Figure 1-7: Equivalent resistance of an HTS conductor

  One represents the non-superconducting materials, whose resistance only depends on the temperature, and the other represents the HTS dissipative state. This equivalent resistance is dependent not only on the temperature but also on the current as shown by Eq. (1-3). It is easily extracted from Eq. (1-1).

$$\rho_{eq\,super} = \frac{E_c}{J_c}\left(\frac{J}{J_c}\right)^{n_{(B,T)}-1} \qquad \text{Below } T_c \qquad \textbf{(1-3)}$$

$$R_{eq\,super} = \rho_{eq\,super} \cdot \frac{l_{wire}}{S_{super}}$$

- When the temperature oversteps Tc, the equivalent resistance should be calculated taking into account the HTS material resistivity. Its value (some tens of μΩ.m) being typically 100 to 10 000 times higher than that of the non-superconducting materials (stainless steel substrate for YBCO, silver alloy matrix for BSCCO), the equivalent resistance of the tape will be in first approximation that of the non-superconducting part.

Additional dissipation phenomenon

If the conductor is submitted to a magnetic flux density that is time-dependent, either its self-field or an externally-applied field, dissipation may appear even if the current flowing through the conductor is well below its critical value. Three phenomena may take place:

- Magnetic hysteresis: The penetration of the magnetic flux density in the superconductor by means of vortexes (cf. § 1.1.1) is slightly hysteretic, which induces losses when the flux density is varying.
- Coupling losses: For conductors with superconducting filaments housed in a resistive matrix, such as BSCCO PIT tapes, a magnetic field density variation will result in the apparition of an electric field between the filaments. This electric field induces a current circulation in the matrix, and thus generates Joule losses.
- Eddy current losses: More generally, eddy current losses may take place in the resistive parts of the conductor (substrate and shunt of coated conductors, matrix of PIT tapes, thermal stabilizer, etc.).

1.2.3 Mechanical specifications

As it was already mentioned, the mechanical properties of bulk HTS ceramics are not suitable to make wires, especially for coil winding. With PIT tapes or Coated Conductors, winding is possible but special attention has to be paid to the mechanical stress to which the conductor is submitted. The deformations caused by tensile stress induce a misalignment of the crystal grains, thus a loss of the superconducting properties, before the yield point is reached. The bending radius is also limited, due to the deformation it induces.

YBCO tapes have better characteristics than BSCCO due to the nature of their metallic substrate, usually stainless steel or nickel alloy. BSCCO tapes matrix is usually made of silver whose mechanical properties are lower. Better properties may be obtained with Ag-alloy sheathing and/or by reinforcement with co-wound stainless steel tapes. Figure 1-8 present the results obtained for BSCCO tape with Ag-Mg sheathing but without stainless steel reinforcement:

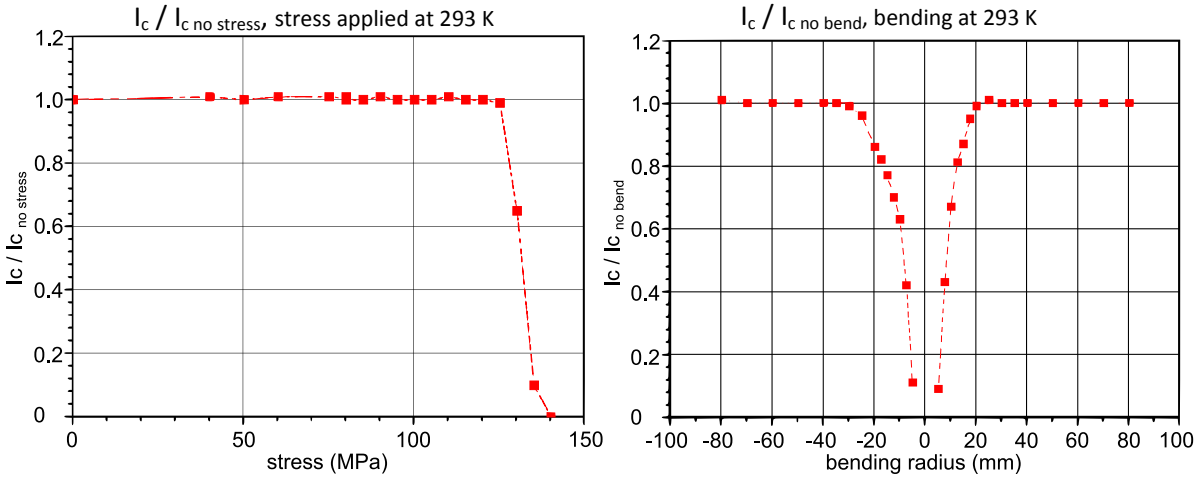

Figure 1-8: Damages induced by tensile stress (left) and bending (right) BSCCO tapes with Ag-Mg reinforcement (EHTS-Bruker)

1.3 Applications

The applications of superconductivity in large scale devices may be divided in two groups: Applications already existing with normal conductors, whose operation is improved by using superconductors, and applications specifically appearing with superconductivity.

1.3.1 Improvements to normal conductors applications

All the electric machines: transformers, motors and alternators, may be redesigned using superconductors. The main benefit is an increase in the energy per volume ratio (Figure 1-9), while the cryogenic cost is partly compensated by the reduction of the dissipation losses. However the high investments necessary to implement superconducting machines and the lack of real breakthrough brought by their use prevent large scale industrial development.

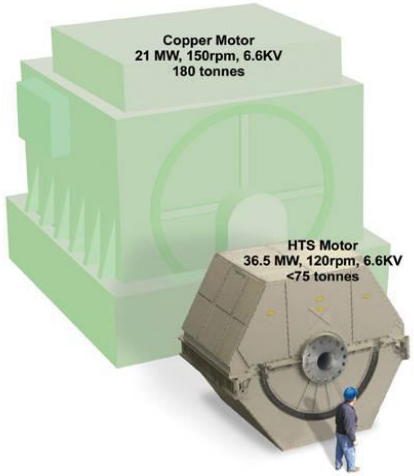

Figure 1-9: Comparison between conventional and superconducting motor (AMSC)

Figure 1-10: Lipa cables extremity (Nexans)

Energy transport cable is also an investigated application. Especially in the context of the new demand for underground and high power DC connexions. This is mainly an HTS application, as the very low magnetic field enables high temperature operation (77 K cooling bath) with HTS and therefore considerable gain in cooling power when compared to LTS. Several industrial-scale projects are already operating, including a Nexans – American Superconductor 138 kV / 574 MVA / 600 m long cable tested by LIPA (Long Island Power Authority) in the USA (Figure 1-10).

Still in the USA, a very large scale project is on-going to connect three major national grids with a triangular DC connection, the “Tres Amigas” project. It will feature American Superconductor underground 200 kV HTS cables, carrying up to 5 GW [LLC10].

Finally, Magnetic field production, either for medical or science purpose (MRI, MNR, fusion tokamaks and particle accelerators), is the only domain where superconducting applications are well developed industrially. For this purpose the energy dissipated in normal conductors is prohibitive and the gain

obtained with superconductors is major, even taking into account the cryogenic cost. For example the total power necessary to run the LHC is 40 MW, instead of 900 MW if normal conductor was used. These large magnets are usually made in LTS materials even if they require lower operation temperatures than HTS. The main reasons are that they are available in longer lengths, easier to implement, and their performances are more reproducible from one length to another. However, several programs are on-going for HTS integration in medical applications, like HTS MRI and MNR for potential operating costs reduction [Iwa06]. HTS insert are also studied for very high field magnets [WAN+09] as they are the only possibility to obtain magnetic flux densities above 23 T.

1.3.2 Specific applications of superconductivity

The two main large scale applications specific to superconductors are Superconducting Fault Current Limiters (SCFCL) and Superconducting Magnetic Energy Storage (SMES). These two applications may be designed using LTS but only few industrial applications where developed until now. The use of HTS is studied for both, HTS SCFCL for example are at the industrial level and already operating (Figure 1-11).

Fault current limitation exists without superconducting material, through active systems including power electronics devices, or simply by using fuses. However, Superconducting FCLs enable an intrinsic limitation of the current when it exceeds a pre-set value, for the resistivity of such system abruptly increases in case of transition. Compared to fuses, the SCFCL is not destroyed when used, which means that the recovery is faster. Compared to active power electronic systems, the intrinsic limitation insures a higher reliability. SCFCL are the only application where the superconducting material is used around and across transition in normal operation.

Figure 1-11: Industrial SCFCL (Nexans)

- Storing energy in a coil is only possible if the coil does not dissipate the energy. It is the application studied in this work; we will describe the SMES concept more in details in the following part.

2. Superconducting Magnetic Energy Storage

In this section we will present the concept of magnetic energy storage and why superconductors are used for this purpose. We will describe SMES characteristics as a power source and present its main applications, along with a brief state of the art.

2.1 Concept

Energy may be stored in a magnetic field, through (1-4. This magnetic field may be created by a permanent magnet, or by a circulating current in an electromagnet. In the case of a permanent magnet, the energy is trapped during the magnetization process and is not available afterwards. With an electromagnet, the energy is stored by short circuiting the coil and is easily discharged by opening the short circuit on a load (Figure 1-12a).

Storing energy this way is impossible with normal conductor, as the time constant would be too low. For example a large flat solenoid (diameter 1 m and height 0.25 m) of 16 H would have a maximum time constant of about of about 0.2 s even if wounded with pure silver. Superconducting material is therefore necessary for magnetic energy storage.

$$E_M = \frac{1}{2}\iiint \vec{B}\cdot\vec{H}dv = \frac{1}{2}\iiint \frac{B^2}{\mu_0\mu_r}dv \qquad \textbf{(1-4)}$$

Interpreting Eq. (1-4) in the framework of coil design, two observations can be done:

- As the integration is done on all the volume where the magnetic field exists. Confining the field in a restricted volume, for example in order to limit the electromagnetic pollution, reduces the storage capacity.

- The energy is stored in the areas where μ_r is minimal, in the air or vacuum. Using magnetic material does therefore not improve the storage capacities and may only be used for magnetic flux density concentration. It will reduce the storage capacity per mass, as the magnetic materials are usually heavy.

A coil may be defined by its inductance *L*. Analysing energy storage in SMES from this point of view is convenient, especially because it points out the similarity with energy storage in capacitors and the specificities of such storage, as shown in Eq. (1-5).

$$E_{self} = \tfrac{1}{2}LI^2 \quad ; \quad E_{capa} = \tfrac{1}{2}CV^2 \qquad \textbf{(1-5)}$$

SMES and capacitors are the only energy storing devices able to provide power to an electric circuit without energy conversion; this is why they are commonly said to store “electricity”. Inductances and capacities are dual, the inductance stores current in the same way as capacitors stores voltage (Figure 1-12b).

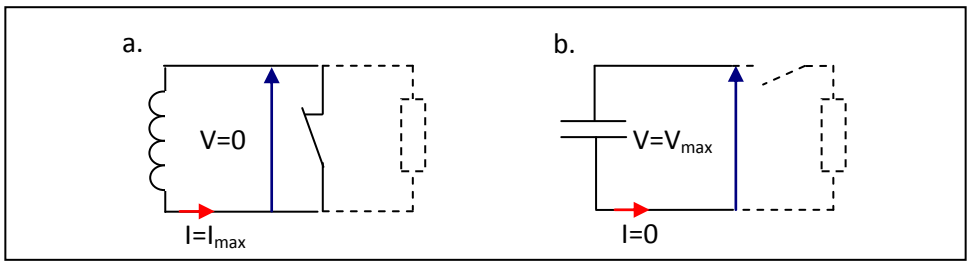

Figure 1-12 : Inductive (a) and capacitive (b) storage with discharge circuit (- -)

A perfect inductance has no resistance, while a perfect capacitor has an infinite internal resistance. A SMES may therefore be seen as a perfect current source whereas capacitors are voltage sources.

2.2 Energy density and Maximum Power

2.2.1 Position of SMES on the Ragone chart

The inductive storage energy density is limited. It is lower than using batteries, comparable with flywheel systems and in higher than capacitors (Figure 1-13). Even if a lot of parameters are to be considered for actual devices, the only theoretical limitation to this density is mechanical. The coil is submitted to Lorentz forces due to the magnetic field. The stress induced in the coil, and eventually in the mechanical reinforcement designed to maintain it, by these forces must remain lower than the materials limits. This fact is formalized by the virial theorem (cf. § 3.1.1).

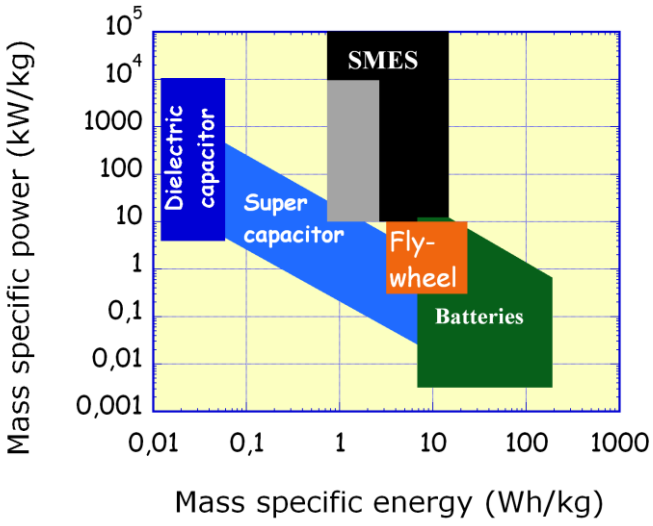

Figure 1-13 : Energy and Power densities for classical electric storage (Ragone chart)

On the contrary, there are no theoretical limitations to the power output of a SMES. The power density of SMES systems is therefore potentially one of the highest, along with that of the capacitors (Figure 1-13). In conclusion, SMES are more versatile than capacitors, their range of use being wider. Nevertheless this range is still in the domain of pulsed power applications, due to the limitations on the stored energy.

2.2.2 Discussion on SMES maximum power

Power density definition issue for SMES

Power density definition is somewhat artificial, because if energy is an extensive property, power is intensive and does not depend theoretically on the size of the device. In consequence, if the size is

reduced without changing the rated output the, a higher power density will be obtained. However, this is only true for storage systems where there is no energy conversion, like SMES and capacitors. If an energy conversion takes place, small systems cannot collect as much power as large ones. The power becomes an extensive property and the concept of power density makes sense. It is the case of batteries, for which the Ragone chart was initially proposed.

In consequence for SMES it is preferable to speak about maximum power, and positioning SMES on the Ragone chart is interesting only qualitatively for comparisons with the other storage systems.

SMES maximum power limitation

The maximum power available with a SMES is naturally the product of its maximum current by the maximum voltage it withstands.

As it was presented § 2.1, SMES coils are current sources. The maximal operating current is fixed by the coil design. It is limited by the operation conditions of the superconducting wire, and in last resort by the conductor mechanical limits as we have seen § 2.2.1.

On the contrary, the voltage is imposed by the charge impedance. For safe operation it must remain lower than the breakdown voltage of the insulation layers protecting all the conducting parts, from current leads to coil turns. However, high voltage insulation makes the cooling of the coil more difficult, and the cooling system has therefore to be more powerful. The mass of this additional cooling power has to be taken into consideration when evaluating the energy density. In consequence, a high power SMES will necessarily have a lower energy density than a low power one, especially if the device is operating at very low temperatures(below 50 K), where the ratio between the cold power produced by the cooling system and its mass is very low.

Another practical limitation to the maximal power of a SMES device results from the A.C. losses due to the fast discharges. The losses may overheat the coil and cause it to quench if they exceed the available cooling power. These losses may be reduced by proper design (cable made of transposed conductors, cooling system and cryostat optimized for eddy losses reductions, etc.) and are not usually the most critical limitation.

2.3 Applications and realisations

Historically the first considered application of SMES was daily load levelling on the electrical grid [Fer69]. The necessary energy being extremely high (in the 1 to 10 TJ range), it was foreseen as a very large scale application. The coil was expected to be a torus (in order to limit the stray field) with a diameter in the order of 1 km, to be implanted underground. The idea was to limit the amount of cold material by mechanically supporting the conductor from the outside with a “hot” structure, which could have been the ground itself (the “bedrock” concept). It has later been proven that the idea of a hot structure was unrealistic. Besides, even if the cooling cost per energy unit is lowered when the size of the system is increasing, the cooling cost for load levelling application is still prohibitive. All of the applications investigated by now are taking advantage of the high power capability of SMES to make their implementation potentially profitable.

2.3.1 SMES on the electrical grid

In order to justify the cost of the superconducting coil, with its cryogenic system and the power electronic necessary to connect it on the AC grid, high added-value applications are necessary. Two of them are commonly investigated:

Uninterruptible Power Source

SMES has been developed to guarantee power continuity for very sensible loads, for example in the microelectronic industry or military systems. The idea is still to damp variations on an electric line like for daily load levelling, but on a much smaller time scale. The targets are the sudden perturbations caused by the appearance or disappearance of a load on the line (voltage surge or sag), and the very short power failures. For this systems, a high speed response is needed which requires power output in the MW range, but the stored energy is not necessarily high, as the perturbation duration is usually very short.

1 to 10 MJ SMES-based UPS were tested since the 90's especially by the US air force. Number of prototype in the same energy range has been developed recently (Table 1-1).

Origin	Year	Conductor	Cooling	Energy / Power	Ref
Japan	2005	HTS (BSCCO)	Helium closed cycle (4.2 K)	1 MJ / 1 MW	[SMH+05]
Japan	2006	LTS	Helium bath (4.2 K)	7.3 MJ / 5 MW	[NHM+06]
Japan	2009	LTS	Conduction (4 K)	1 MJ / 1 MW	[MCK+09]
Korea	2006	LTS	Helium bath	3 MJ / 0.75 MW	[KSC+06]
Finland	2003	LTS (Nb_3Sn)	Conduction (10 K)	0.2 MJ	[MKK+03]
China	2008	HTS (BSCCO)	Helium bath 4.2 K	1 MJ/0.5 MW	[XWD+08]

Table 1-1 : Recent SMES based UPS realization

No commercial products are available for this application; the devices presented here are only demonstrators. However, some of them were tested in real conditions showing satisfying behaviours, in terms of storage efficiency and protection against voltage sags.

Flexible AC Transmission System

FACTS are usually systems composed of static elements whose role is to enhance the stability of lines under harsh working conditions (long-distance lines, unbalanced loads, etc.), by exchanging reactive power. Adding energy storage like SMES gives the possibility to accept or supply to the line active power. This kind of system requires characteristics close to that of UPS: power in the MW range and energy in the MJ range.
A commercial system was developed by General Electrics and American Superconductor and tested in the USA [Abe99]. It is implanted in a truck trailer for mobile operation (Figure 1-14).

Two versions were developed: a classical one dealing only with reactive power and a second one featuring a 3 MJ / 3 MW LTS coil adding active power exchange with the line.

The results obtained with both devices were satisfactory, but the benefit of adding active power management using SMES was not really critical in most of the cases. Most of the systems actually sold on the market were thus sold without “SMES” option.

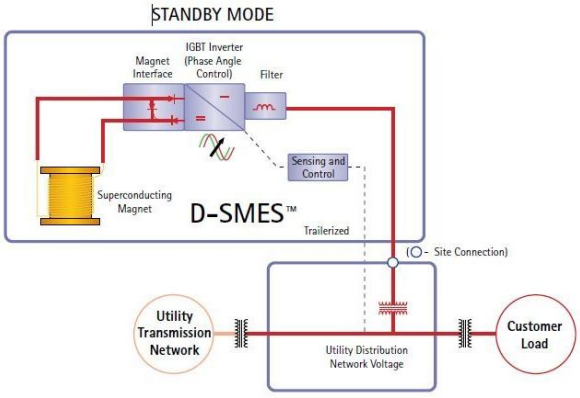

Figure 1-14 : SMES FACTS by American superconductor

2.3.2 Pulse power source

SMES are naturally adapted to pulse power application because of their high power capability (cf. § 2.2). We have seen § 2.1 that SMES is a perfect current source, contrary to capacitors which a voltage sources. SMES are therefore more specifically suitable for pulse power current source, whose applications extends from manufacturing systems such as magneto-forming to military or aerospace systems such as railguns, catapults or payload electromagnetic launchers.

The most important studies about SMES pulse power source were conducted by the USA Defense Nuclear Agency, since the 80’s [Ull95]. The design adopted for this device (SMES-ETM) was a 96 m diameter torus storing 20 MWh (72 GJ) under 200 kA. The magnet was supposed to operate in superfluid helium at 1.8 K and wound with LTS NbTi Cable in Conduit Conductor. It was foreseen as a full size test device for energetic weapon powering, as well as load leveling storage. The cable developed for this SMES was tested at the rated current (200 kA) and a small prototype was realized but the project was discontinued before its completion.

Many other small scale projects were conducted but once again they stayed at the demonstrator level and no commercialization was ever made, due to the high investment costs.

2.3.3 HTS SMES development

HTS SMES have been studied since the HTS materials discovery, but very few large scale realizations were done, due to the difficulty of producing long lengths of conductor. Apart from the Japanese and Chinese HTS UPS SMES system presented above in Table 1-1 (both cooled at 4.2 K), a pulse power SMES device was tested in Korea, storing 1 MJ in a BSCCO coil cooled at 5 K [BKK+09].

In France the DGA funded an 800 kJ pulse power SMES demonstrator, conduction-cooled at 20 K and using BSCCO cable. It was realized at Grenoble and successfully tested [TDB+08] up to 450 kJ under 250 A. The demonstrator SMES II whose design and tests will be presented in Chapter 3 & 4 is an upgrade of this device, re-using the same winding. It is one of the only large-scale realizations working at higher temperature than LTS.

3. Elements for SMES design

Practically, a SMES device consists of three elements: a magnet (with its protection), a cryostat, and a connection system to the load (with or without converter). In this part we focus on the magnet design, with its protection.

Most of the time the purpose of superconducting magnets is to produce magnetic flux density with given characteristics (uniform density, predefined gradient or flux shape, etc.) adapted to the application (MRI, MNR, dipole or quadripole for particle accelerators, etc.). In the SMES case the shape of the magnetic flux is not important, the only relevant parameter is the total energy stored. This specificity must of course be considered at the beginning of the coil design when defining the shape of the magnet, but most of the elements presented below could be applied to any type of superconducting magnet.

The mechanical constraints imposed on coil design are first introduced. The constraints induced by the use of superconductor material are described in a second time. The thermal design of such system is then presented. A presentation of the protection issues concludes this part.

3.1 Mechanical constraints and resulting SMES geometries

When current is circulating in a coil turns, the conductor has to withstand the Lorentz forces induced by the magnetic flux, following Eq. (1-6).

$$\overrightarrow{dF} = I\overrightarrow{dl} \wedge \overrightarrow{B} \tag{1-6}$$

Of course this force is null when the magnetic flux density is in the same direction than the circulating current, hence the idea of creating force-free coils that would not require mechanical structure. In fact such result cannot be obtained in a finite configuration, but an adapted geometry may optimize considerably the use of the coil material and therefore its mass and volume.

3.1.1 Virial Theorem application to coil design

It is possible to theoretically determine the minimum amount of material necessary to store a given energy, using the virial theorem. This theorem was originally presented by Clausius to describe the equilibrium of a system of particle submitted to potential and kinetic energy and was later extended to include the other existent forces, and derived in a variational form.

In our case, only mechanical and magnetic stresses are present, so the virial theorem is resumed as Eq. (1-7), where *T* is the mechanical stress tensor and *B* the magnetic flux density.

$$\int_{conduc} Tr(T)dv = \int_{space} \frac{B^2}{2\mu} dv \tag{1-7}$$

If we consider a uniform and mechanically isotropic material, submitted only to tensile and compressive stress having a constant value, Eq. (1-7) becomes:

$$\sigma \cdot (V_T - V_C) = E_{magnetic} \quad \textbf{(1-8)}$$

Where σ is the strength of the conductor, V_T is the coil volume submitted to tensile stress and V_C the volume submitted to compressive stress.

In consequence, the optimal Energy per Volume ratio, obtained considering a hypothetic geometry presenting only tensile stress, is simply Eq. (1-9):

$$E/V_{optim} = \sigma \quad \textbf{(1-9)}$$

Of course the assumptions under which this formulation is obtained are strong, but it is useful to determine the absolute limit to the stored energy in inductive storage [Moo82]. It also points out two characteristics to which optimum coil design for energy storage should tend:

- As only the winding sections submitted to tensile stress are actually storing energy, coil design for SMES application keep the volume submitted to compressive stress minimum.

- The conductor should have the highest possible strength, and should work as close as possible from its mechanical limits. If the conductor characteristics are uniform, the tensile stress to which it is submitted should be uniform also. On the contrary reinforcement may be added to the conductor to adapt it if it is non-uniform.

Once the geometry is fixed, the maximum energy which can be stored will be limited by the place where the conductor is submitted to the highest stress. Special attention must be paid to the superconducting wires mechanical limits, especially with composite wires such has HTS tapes (cf. § 1.2), as this kind of wires lose their superconducting properties before reaching their mechanical limit.

3.1.2 Classical SMES geometries

There is no clear consensus about the optimal coil geometry for SMES application, which depends on more factors than the sole mechanical point of view. Classically, SMES coils have either Solenoidal or Toroidal topologies (Figure 1-15). The benefits and drawbacks of each topology are presented Table 1-2.

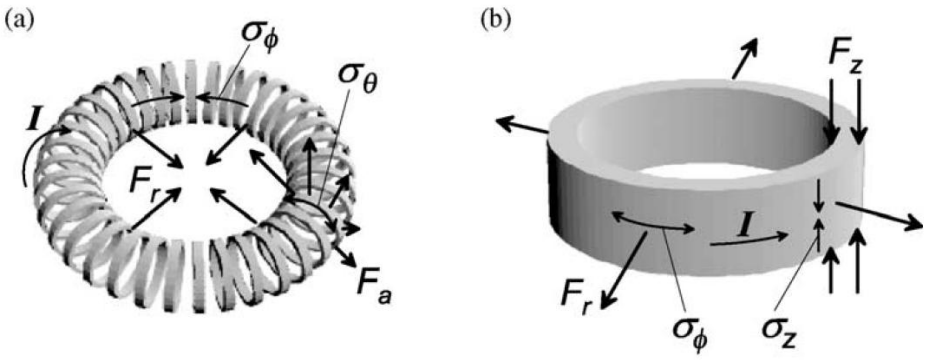

Figure 1-15 : (a) Toroidal and (b) solenoidal (segmented) geometries with induced stresses [NWS+05]

	Toroid (Figure 1-15a)	Solenoid (Figure 1-15b)
Forces (thin wall coils hypothesis)	Hoop force (Fa): tensile Centering forces (Fr): compressive	Hoop force (Fr): tensile Axial forces (FZ): compressive
Theoretical Energy per Volume ratio (E/V) [EB81]	$E/M_{toroid} \geq 1/3 \cdot \left(E/V_{optim}\right)$ At least three times lower than the Virial limit (cf. (1-9)	$E/M_{solenoid} = k \cdot E/V_{optim}, 1/3 \leq k < 1$ k = 1/3 when solenoid length is infinite (toroid case) k tends toward 1 (virial limit) when length goes to 0. Practically, k=1/2 is achievable
Observations	- Winding process more difficult - No or limited stray field - Stress may be optimized (see below)	- Winding process simpler - High stray field - Highly non-uniform stress

Table 1-2: Efficiency of Solenoidal and Toroidal topologies

In conclusion, if the design focuses on optimizing E/V, the result will be a short solenoid [SY80]. A toroid will be preferred for large scale devices were the stray field must be limited [Ull95]. However, adapted toroidal geometries may obtain more uniform stress distribution by using variable winding pitch [TTNS02]. In this case, the E/V ratio may exceed 1/3, and get closer to 1.

Figure 1-16: Force-balanced toroid with variable pitch winding [NWS+05]

These geometries, called force-reduced or force-balanced, are very interesting as they offer a good compromise between storage efficiency and electromagnetic compatibility. However, the complexity of the winding process makes it difficult to implement, especially with HTS materials.

3.2 Superconductors implementation

In order to design a coil using superconducting material, the mechanical considerations mentioned above must be completed by taking into account the superconducting characteristics of the conductor.

3.2.1 Critical surface

The superconducting material working point must remain below its critical surface but as close to the critical surface as possible, in order to optimize its use. If we remember that the current flowing through each turn is the same (the turns are in series) and under the assumption that the temperature is fixed and uniform, this problem comes down to either adapt locally the conductors to the magnetic flux density, by augmenting locally its superconducting section, or optimize the geometry to have uniform flux density on the conductor. This analysis is very similar to the one

presented above for mechanical stress, with similar conclusions. However, the parameter implicated is the superconducting section of the wire, not its total section.

3.2.2 Bi-axial study for HTS

For HTS wires not only the amplitude of the magnetic flux density but also its orientation with regard to the conductor has to be taken in consideration (cf. § 1.2). A good way of studying this problem is to decompose the flux density following the transverse and longitudinal directions and studying both independently, then considering the worst case of them.

For example, in a solenoid the field is essentially axial in the bore where it is maximal and tends to be partly radial at the extremities. The Superconducting tapes orientation is then practically imposed, they are to be placed on the edge to have their longitudinal axes (with the highest critical field) along the solenoid axis (Figure 1-17).

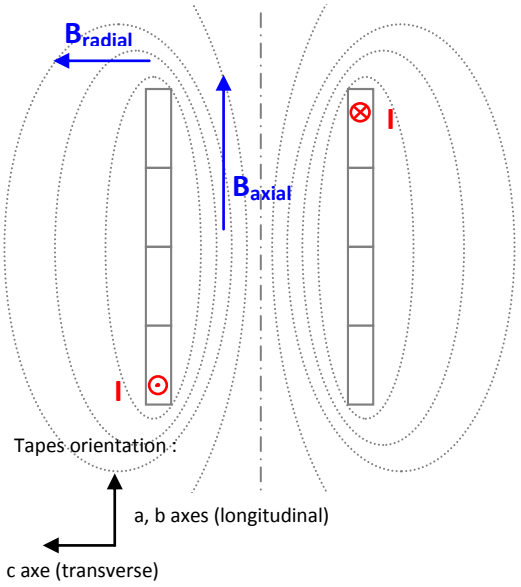

Figure 1-17 : Tape conductor orientation in solenoid winding

However in this case the tapes will be submitted to transverse field at the extremities. Even if the flux amplitude is lower in this place, the tapes could be closer to the critical field at the extremities than everywhere else. To solve this problem the turns at the extremities may have larger superconducting sections. Another solution is to geometrically optimize the solenoid ends, in order to attenuate the magnetic field locally [DVT03], leading to the design presented Figure 1-18a, or to tilt the upper turns of the coil in order to limit the transverse field, as shown Figure 1-18b:

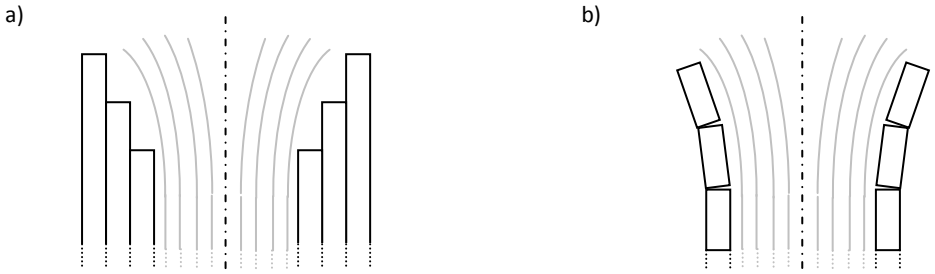

Figure 1-18: Optimized solenoid ends

3.3 Thermal design

3.3.1 Operating temperature

SMES are cryogenic devices, whose temperatures have to be maintained low enough to ensure non dissipative operation of the superconducting wires. The temperature is practically imposed by the cold source which is used and generally fixed before the SMES coil design.

Different types of cooling sources and cooling media are used depending on the temperature range and operation conditions (Table 1-3).

Cold source / Cooling media	Open cycle cooling	Closed cycle
gas/ fluid	Two-phase thermal exchange, suitable for helium cooling in the 1.2 to 10 K range. Commonly used in large scale LTS magnets using cable in conduit (LHC, ITER)	Similar cooling than in open cycle, except that the evaporated gas is re-liquefied continuously. The system consumes energy and is more voluminous but it is autonomous.
Liquid bath	Most commonly used system, but temperature range is limited: around 4.2 K with helium and around 77 K with nitrogen. Hydrogen (20 K) is too dangerous and Neon (27 K) is expensive and pose electrical isolation problems	
Conduction	More suitable for HTS coils with operating temperature over 15 K. The temperature gradients induced by conduction cooling could be problematic for lower operating temperature, though experimental devices at 4 K exists [MCK+09].	

Table 1-3: Most common SMES cooling methods

3.3.2 Temperature uniformity and stability

We have seen in § 3.2.1 that the coil electro-magnetic design is conducted under the assumption that the temperature is uniform and fixed. Practically, the coil cannot be isolated perfectly from the outside: heat losses are caused by radiation from the cryostat external surface, by conduction through the mechanical support of the coil the cryostat and the current leads to connect it electrically.

Moreover, current leads and connections between the superconducting wires are creating losses by Joule effect, while the coil superconducting winding itself generates heat during operation, when the conductor is close from its critical current (see § 1.1.2).

In consequence, a thermal system must be designed to ensure that the coil temperature is low enough to allow safe operation, with a reasonably homogenous and stable temperature.

LTS magnets

For LTS magnets, the heat dissipation is almost null until the transition, thanks to the high *n* value of this kind of superconductor. However at low temperature (around 4.2 K), the specific heat of the materials is more than 1000 times lower than at room temperature. The thermal inertia is then particularly low and even a very small event (vibration, cosmic rays, etc.) may cause a sufficient temperature increase to ignite the transition of the superconducting material and trigger a very brutal thermal runaway (a phenomenon called quench). A significant amount of non-superconducting material (generally copper or copper alloy) must be added in the LTS wires to increase the thermal inertia and make the temperature stable enough for reliable operation (Figure 1-19).

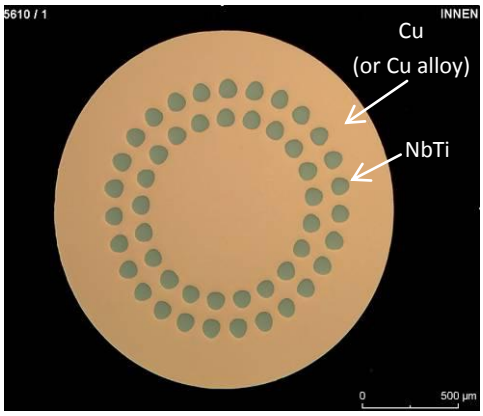

Figure 1-19: Typical LTS cable cross section (NbTi with copper matrix) by Bruker

The additional mass necessary to reach the stability is most of the time superior to what is necessary for mechanical reinforcement, except for very large scale devices.

HTS Magnets

For HTS magnets, the dissipation during operation is not negligible because the *n* value of those materials is lower. The cooling system has therefore to absorb this heat flux otherwise the temperature would slowly increase, which would progressively increase the heat dissipation and trigger a slow thermal runaway. However, the low thermal inertia is not an issue, the operating temperature being generally higher than for LTS. At 20 K for example the specific heat is already more than 70 times higher than at 4.2 K and the cable is intrinsically stable.

Even when HTS coil is used at very low temperature, the stability problem is easier to solve than with LTS because the transition is not as stiff so small events cannot throw the magnet off balance the same way it does with LTS.

3.4 Protection against quench

The thermal design is supposed to ensure that under normal operation the SMES coil does not quench. However quench may occur when experimentally testing the operational limits of the device and even during normal operation due to unexpected events. The coil must be protected against quench effects passively or actively, a quench detection system being necessary for the latter.

3.4.1 Quench protection methods

For the same reasons mentioned above concerning the thermal stability, the problems caused by quench are different in LTS and HTS coils and so are the solutions.

LTS devices

Intrinsic protection against quench may be obtained with LTS coils [Wil83]. In this case the low thermal inertia and good thermal conductivity makes heat propagation, thus quench propagation, very fast. The coil massively quenches and its stored energy is dissipated in all the coil volume, causing only a small elevation of the average temperature. Moreover the high thermal conductivity of the coil conductor materials limits the temperature gradient in the conductor.

However, intrinsic protection may be difficult to reach, due to design constraints or the very large system size [IS80]. For example if the system is a complex coil assembly, rapid current decrease due to quench condition in one of the windings could unbalance the mechanical forces equilibrium and controlled discharge of all the coil elements may be necessary to protect the system.

HTS devices

The protection of HTS magnets is an important issue [Iwa03], [SEL+08]. Because of the higher specific heat and the lower n factor compared to LTSs, the normal zone propagation speeds are very low, about several centimetres per second instead of several tenths of meters for LTSs [TPT+03], [ETWS08]. Energy is therefore being dissipated in small volumes, the so called hot spots, where temperature rises rapidly. Thermal expansion in the hot spots causes high mechanical stresses and possibly deformations to which HTS materials performances are highly vulnerable. Even if the conductor sustains the stress, when the temperature goes higher than 480 K the conductors soldering starts melting and the oxygen concentration in the superconducting material may be altered, which cause ultimately the loss of its superconducting properties. It is therefore necessary to limit the hotspots maximum temperature and the temperature gradients along the conductor, which requires an active protection.

Active Protection methods

There are two classical active protection methods. The first is to help the propagation of the normal zone to all the winding by heating the conductor when the quench starts in order to dissipate the stored energy in the total volume of the magnet, thus without creating hot spots. It requires adding heaters in good thermal contact to the winding, with enough heating power to guarantee a fast and uniform temperature rise. It is efficient on LTS systems because the heat necessary to induce a quench is limited, but not suitable for HTS magnets where the temperature margin may be very high. The second method is to discharge the magnet as soon as a quench occurs to dissipate the magnet energy in an external charge. This method requires a fast discharge, and therefore a high discharge voltage.

3.4.2 Transition detection systems

If an active protection is used, a detection system must be implemented to trigger the protection when it is needed. The detection system has to detect the apparition of a dissipative voltage on the coil, which is in the 10 – 100 mV range [Iwa03, IS80]. Of course a simple observation of the voltage across the coil is not sufficient, as the dissipative voltage will be masked during the charge by the source voltage and compensated by the coil inductive voltage if it is short-circuited. Two methods are commonly used to obtain a direct measurement of this signal.

Flux variation compensation

The inductive voltage may be compensated with an image of the flux variation obtained through a coupled measurement inductance (Figure 1-20). The output of such system is obtained through Eq. (1-10):

$$\begin{aligned} V_{output} &= k \cdot (L_{SMES} \frac{di}{dt} + V_{dissip}) - M_{mutual} \frac{di}{dt} \\ &= k \cdot V_{dissip} \ , \ if \ \ k \cdot L_{SMES} = M_{mutual} \end{aligned} \qquad \textbf{(1-10)}$$

Where k is an attenuation factor adjusted with the potentiometer, L_{SMES} the SMES inductance and M_{mutual} the mutual inductance between the SMES and the measurement coil called “mutual”.

It is clearly seen that such system should have the highest possible k value in order to have a good sensitivity. This is obtained if the measurement inductance has almost the same value than the SMES itself and is perfectly coupled to it.

This system is commonly used in large scale devices where the conductor is a cable made of several wires [Wil83]. In this case a small resistive wire is easy to add to the cable. It serves as measurement coil, with exactly the same inductance as the power wires and a perfect coupling. This coupling does not vary with vibrations, as the coils are mechanically interdependent. The resulting inductive voltage cancellation has therefore low noise levels.

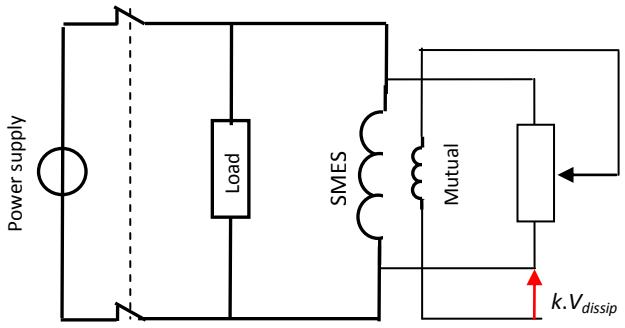

Figure 1-20: Compensation-based detection system

Bridge detection

Another efficient method to detect the apparition of quench-induced dissipative voltage is to compare the voltage between the two extremities of the coil and the middle [Wil83]. If a dissymmetry appears, it is due to the apparition of a voltage drop on one side or the other, which is

caused by a dissipative region. Of course a quench appearing symmetrically on the two halves of the coil could remain unnoticed, but this eventuality is unlikely. The comparison is usually made by mean of a Wheatstone bridge (Figure 1-21).

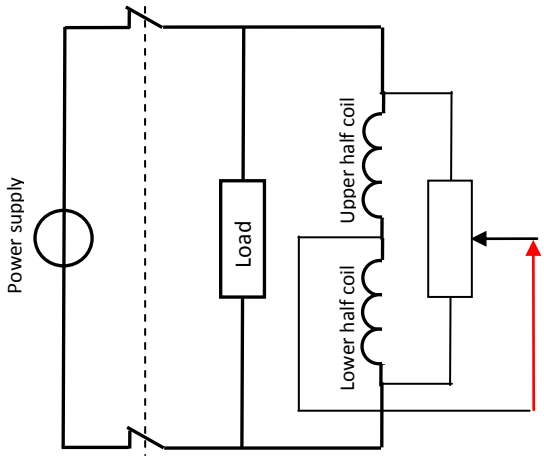

Figure 1-21 : Bridge-based detection system

HTS detection issues

Quench detection is not trivial in HTS magnets, for the same reasons that makes an active protection necessary (cf. § 3.4). As quench takes place in short lengths of conductors because of its slow propagation, the dissipative voltage that indicates its existence is small and grows slowly, the detector must therefore be especially sensitive, in the 10 mV range [Iwa03].

4. Conclusion

In this first chapter, the superconductivity phenomenon was introduced briefly, from an electrical engineer's point of view. Here are summarized the most important points:

- Superconductivity is the ability of some materials to present no losses when a continuous current is circulating in it, under certain conditions of temperature, magnetic flux density and current density.
- There are two types of superconducting materials, depending of their operating temperature range: Low Temperature Superconductors commonly operate around 4.2 K and up to 18 K, while High Temperature Superconductors operate commonly around 77 K and up to 100 K.
- LTS are alloys (NbTi, Nb_3Sn). They are easy to manufacture, have good mechanical properties and isotropic characteristics.

- HTS are complex ceramics (YBaCuO, BiSrCaCuO), whose characteristics are strongly anisotropic. They are brittle and complex processes are necessary to make wires with them, the resulting wires have limited mechanical properties.
- If operation well below the critical current I_c induces strictly no losses, when operating close below I_c a small dissipation appears. The resulting electric field follows a power law against the current density, until reaching the resistive state. The n factor of this power law determines the stiffness of transition (from several hundred for LTSs down to 10 in some cases for HTSs).

In a second time, the principle of magnetic energy storage was introduced. The interest of SMES as pulse power source was presented, and SMES magnet design issues were described. The key elements that were mentioned are:

- The energy density that is theoretically possible to store in a SMES is limited by mechanical considerations, through the virial theorem. On the contrary, the power output has no theoretical limit and very high values may be practically obtained. In consequence, SMES are suitable for high power pulse applications requiring a current source.
- The costs due to cryogenic operation limit their use to high value-added applications. Moreover, the cryogenic cost augmenting slower than the stored energy large scale applications are generally more interesting in terms of efficiency.
- Apart from the mechanical constraints, SMES coil design is governed by the necessity of maintaining the coil in its superconducting state. Studies must be conducted to determine in each location the operating conditions of the superconducting wire, and if necessary adapt the cross section to pass the rated current. The cryogenic system must insure a uniform and stable temperature in every operation phase.
- The coil must survive to a quench, either by designing it so that its temperature rise homogenously or by designing a protection system sensible enough to detect quench condition and protect the coil before its temperature rise too much.

In the following chapter, a specific application of SMES as pulse power source will be presented: SMES as Electromagnetic Launcher power supply.

CHAPTER 2 :
SMES AS POWER SUPPLY
FOR ELECTROMAGNETIC LAUNCHER

SMES are suitable for high power pulse applications, and especially when a current source is needed. It is a good candidate for electromagnetic launcher powering, as it was already mentioned in Chapter 1 § 2.3.2.

In this chapter are described in a first part the electromagnetic launcher principles and powering issues. SMES direct powering is compared with classical capacitor powering. The potential gains in energy efficiency are underlined and the limitations with present-day superconducting technology in terms of current amplitude are presented.

The possible ways to overcome this problem are discussed in the second part. SMES output current multiplication system, the so-called XRAM concept is described, and its possible implementations are studied. Electromagnetic launcher operating current reductions are also investigated, and a novel SMES-launcher integration concept is proposed, with preliminary results of optimization studies.

1. Electromagnetic launcher supply

In this part are described in a first section the electromagnetic launcher principle, and the practical implementations, focusing on the launcher technologies developed at Saint Louis Institute (ISL) with which we are cooperating in the framework of a DGA contract (cf. Chapter 3 § 1 for the project presentation).

1.1 Introduction to Electromagnetic launcher

1.1.1 Principle

The principle of an electromagnetic launcher (EML) is to accelerate a projectile by Lorentz force.

The launcher consists of two conducting parallel rails between which the projectile is placed, hence its other name "railgun". The projectile itself is electrically conducting, in sliding contact on each rail (Figure 2-1).

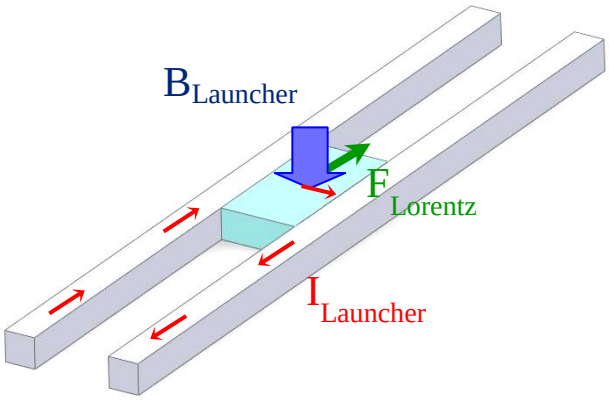

Figure 2-1: Electromagnetic launcher principle

The circuit formed by the two rails connected through the projectile is powered by a current pulse. This current circulating in the rails creates a magnetic flux density, thus creating a force on the projectile through Eq. (2-1).

$$F_x = I \cdot \int_{-d/2}^{d/2} B_z(y) \cdot dy \qquad \textbf{(2-1)}$$

Where F_x is the resulting force on the projectile, I the circulating current, d the distance between the rails and $B_z(y)$ the magnetic flux density component in z direction, created by the current between the two rails (which depends only of y for symmetry reasons).

This equation may be simplified by introducing the linear inductance dL/dx which gives Eq. (2-2):

$$F = \frac{1}{2} \frac{dL}{dx} \cdot I^2 \qquad \textbf{(2-2)}$$

In order to obtain high output velocity (up to several km/s) the current must be very high, ranging from 100 kA for a very small launcher to more than 1 MA for large launchers [LPW01].

1.1.2 EML practical implementations

Even though the EML principle is simple, there are major issues when it comes to practical implementations. Especially, the sliding contact between the rails and the projectile is difficult to maintain, as it reaches high speed under high current.

If the contact is partially lost, an electric arc is formed between the rails and the projectile. This may damage both the projectile and the rails, and decreases the launcher efficiency as part of the energy is dissipated in the resisting contact.

Two possibilities have been investigated against this problem:

- In the USA, the trend is to create plasma resistant projectile, and use the plasma as propellant, which leads to single-use launcher bores [WSPM09]
- At ISL, the trend is toward arcing reduction, by means of optimized contact brushes and rails. In this case the rails are re-usable.

In parallel to the investigations on rails and brush designs, developments are conducted at ISL on losses reduction. It leads to the concepts of distributed current input [LPW01] and segmented launchers (still unpublished):

- The distributed current concept (Figure 2-2 left) consists in feeding the rails in distributed locations along their length, following the projectile movement to reduce the total electrical resistance of the rails.
- In a segmented launcher (Figure 2-2 right), the projectile is successively powered through several rail segments, allowing the use of a new set of brushes in each segment.

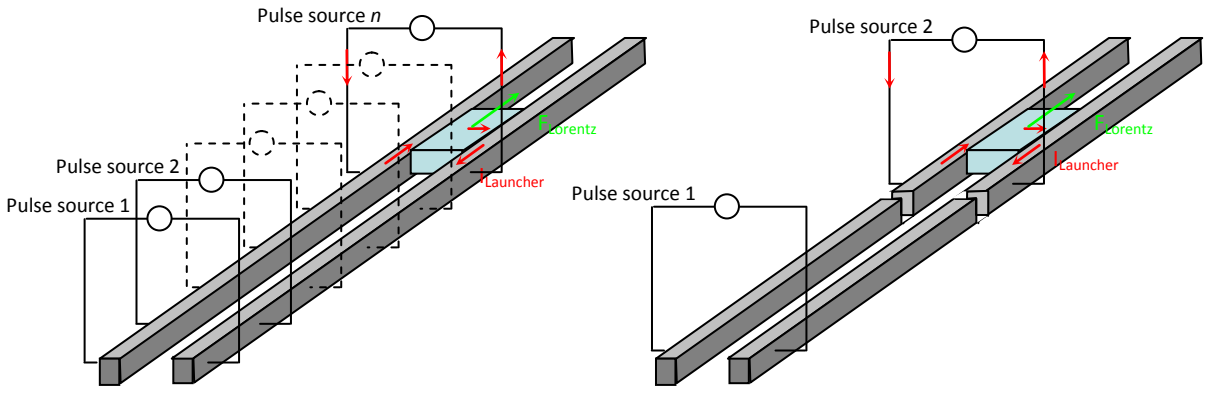

Figure 2-2 : Distributed powering concept (left) and segmented launcher concept (right)

1.1.3 EML applications

Military applications

The first application of EML is military: It may be used to launch kinetic energy penetrators (Figure 2-3), similarly to conventional guns. The interest is to obtain output speeds superior to what is obtained with conventional gas expansion-propelled penetrators (limited to 1.5 km/s) and comparable with the speed of shaped-charge rockets (up to 10 km/s). Moreover, the propellant not being included in the ammunitions, they are small, inert and less expensive. It enhances the operation safety and the firing capacity for on-board guns, and theoretically permits higher firing rates.

Figure 2-3: Pegasus 10 MJ launcher (from ISL)

Payload acceleration

Contrary to gas expansion-propelled systems, with EML the projectile acceleration is easy to adjust and may be maintained all along the launcher length. This property makes the use of EML as payload accelerator possible. The foreseen applications include suborbital or low orbital light-weight satellite or probe launching (Figure 2-4). The main interest is a drastic reduction of the ratio between the payload and the total load.

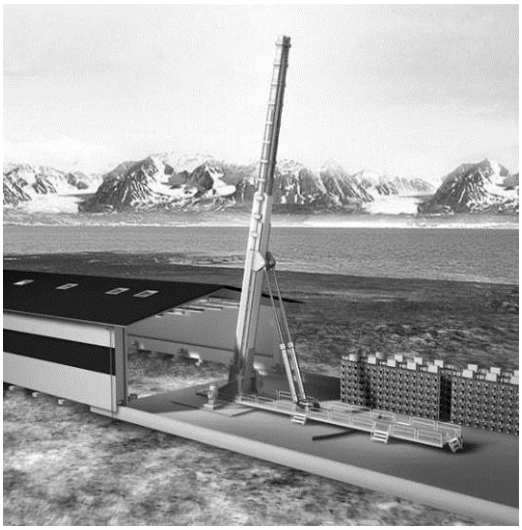

Figure 2-4: Artist view of payload suborbital launcher (from [LRVB07])

It requires long length launchers (more than 20 m) with reduced acceleration (lower than 15000 g or 147 km/s²) and velocities of about 2000 km/s at the launcher muzzle [LRVB07]. Several projects are on-going on this subject either for direct launching or two stage launching. In the last case the launcher accelerates a small rocket that is ignited at the end of the flight, to help reaching the desired altitude [BLGB05].

1.2 Launcher supply

Historically, some EML test devices were powered by homopolar generators but most of the time the power source consists of capacitor banks. In this section are first presented the principle of capacitor supply and its drawbacks. The potential interest of SMES supply is presented in a second time with its limitations. All the results comes from simulations based on the characteristics of an existing 2 m-length simple launcher developed at ISL, designed for a peak current around 160 kA and a projectile mass of 16 g. The qualitative conclusions derived from this example apply for any other launcher, even if the results would be quantitatively different.

1.2.1 Capacitor supply

Principle

The inductance of an EML at the beginning of a launch is almost zero, as the projectile is placed at the beginning of the rails. Even when the projectile reaches the end of the rails, the inductance remains low. For the launcher that is considered, the linear inductance is 0.45 µH/m.

By powering directly such load with capacitors which are voltage sources, the current would reach very high values, destroying the launcher and the projectile. In consequence, it is necessary to use a pulse forming unit limiting the current rise. This unit is a resistive inductance, whose value depends on the EML characteristics (linear inductance, maximal current) and the Capacitor banks (capacitance, charging voltage). The discharge circuit is presented Figure 2-5.

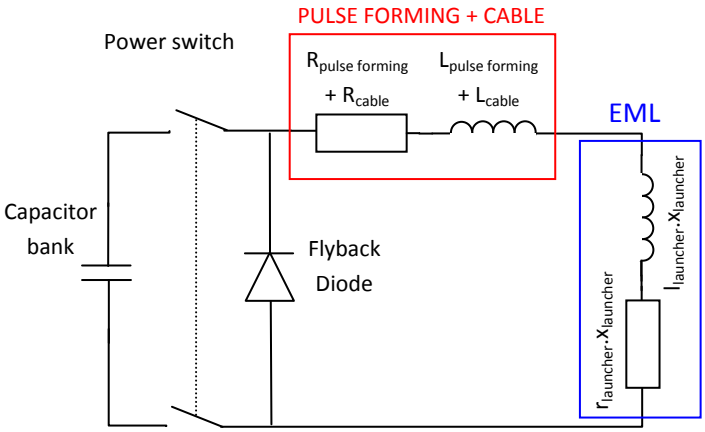

Figure 2-5: Capacitor powering circuit for EML

A flyback diode is used to prevent oscillations between capacitor and inductance.

Discharge efficiency

A numerical model was developed using Matlab® to study the energy transfers during a discharge. It solves numerically the differential equation system representing the electromagnetic and mechanical behavior of the system (cf. Appendix §°1.1).

For 110 kJ initially stored under 10 kV (capacitor bank of 2.2 mF), a pulse forming unit of about 7 µH is required to limit the current rise to its rated value (160 kA). The simulation results are in good agreement with the experimental values obtained at ISL, as shown Figure 2-6 on the left. From the simulated energy evolution presented on the right, it may be observed that the discharge has two

stages: In a first time, the energy stored in the capacitor is very quickly (around 0.2 ms) transferred to the inductance of the pulse forming coil. In a second time, part of the energy is transferred to the projectile, while the most of it is dissipated in the circuit resistances and the flyback diode.

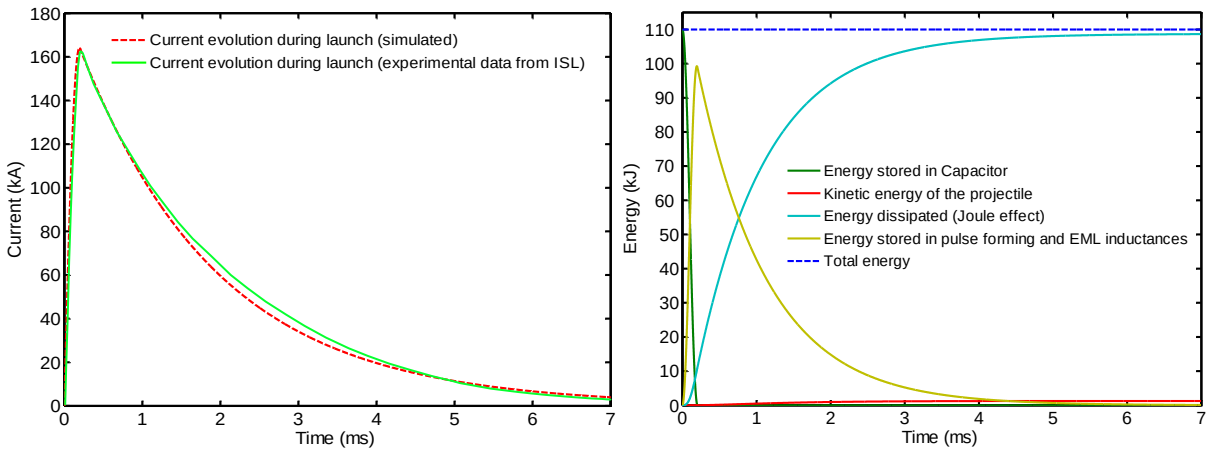

Figure 2-6: Simulated and experimental current evolution during launch at 400 m/s (left) and simulated energy transfer (right)

The projectile kinetic energy is around 1.4 kJ at the end of the launch, which gives a very low overall efficiency, about 1.3%. This launching overall efficiency is defined as the ratio between the energy transferred to the projectile and the energy lost by the storage system. An important part of the losses are due to the resistance of the pulse forming coil, which for a given maximal current cannot be reduced significantly.

It must be emphasized that if the operating current is increased the required pulse forming coil inductance, thus its resistance value, is lower. This explains why large scale launchers with very high operating currents have much higher efficiencies than small ones. Up to 30 % of overall efficiency was already achieved at ISL for 2 MA, 10 MJ discharges.

1.2.2 Direct SMES supply

Principle

The concept of direct SMES supply (Figure 2-7) is in first approximation the discharge of a constant inductance L_1 (the SMES) in a deformable inductance (the EML) whose value varies progressively form 0 to L_2 while the projectile advances between the rails.

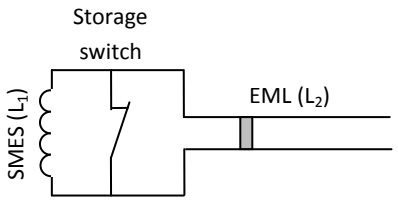

Figure 2-7 : Direct SMES supply principle

The short-circuit switch initiating the discharge is opened on an inductance which values is 0, thus another short-circuit. This short-circuit is then progressively converted into an inductance. In consequence, we may consider the whole system as a single closed current loop, whose value varies from L_1 to L_1+L_2.

The flux passing through a closed current loop is constant even if its geometry varies. The contrary would lead to an induced voltage appearing, which is impossible. From this observation, it is possible to derive the current variation during the launch, as shown in Eq. (2-3).

$$\Phi = L_1 \cdot I_{init} = (L_1 + L_2).I_{final}$$
$$\Rightarrow I_{final} = I_{initial} \cdot \frac{L_1}{(L_1 + L_2)} \quad \textbf{(2-3)}$$

The energy stored in the magnetic field is therefore reduced, as shown in Eq. (2-4). However, the energy is not dissipated (the voltage across the loop remains null) but converted into mechanical work deforming the loop, thus accelerating the projectile.

$$E_{mag\ init} = \tfrac{1}{2} \cdot L_1 \cdot I_{init}^{\ 2}$$
$$E_{mag\ final} = \tfrac{1}{2} \cdot (L_1 + L_2) \cdot I_{final}^{\ 2} = E_{mag\ init} \frac{L_1}{L_1 + L_2} \quad \textbf{(2-4)}$$

The energy efficiency of the launch, defined (similarly to § 1.2.1) as the ratio between the mechanical work transmitted to the projectile over the energy lost by the storage device, using direct SMES powering should thus be optimal (close to 100 %).

Influence of the EML initial inductance

The EML has necessarily an initial inductance, which is at the very least the inductance of the cables connecting it to the SMES. No current is circulating in this initial inductance as long as the SMES is short-circuited by the storage switch. However the currents in SMES and EML will necessarily become equal after this switch is opened, as they will be connected in series.

Under the assumption that the transient time required for these currents to equalize is short compared to the duration of an EML launch, the discharge may be divided in two phases:

- A “current equalizing phase”, which is a constant inductance-to-inductance discharge between the SMES and the EML initial inductance.
- The launch itself, where SMES and EML may be seen as a single deformable inductance (cf. above°§ 1.2.2 *Principle*).

The value of the total flux remains constant during an inductance-to-inductance discharge (Figure 2-8), as shown Eq. (2-5).

$$e(t) = -\frac{d\Phi_1(t)}{dt} = \frac{d\Phi_2(t)}{dt} \Rightarrow \Phi_1(t) + \Phi_2(t) = Cst \quad \textbf{(2-5)}$$

Where e is the voltage across the inductances and Φ_1, Φ_2 the flux produced by L_1, L_2.respectively.

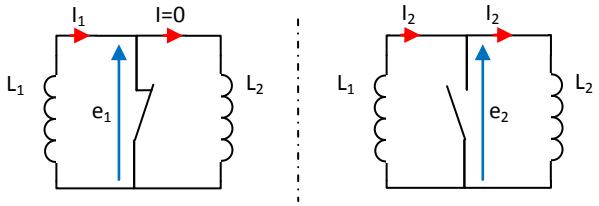

Figure 2-8: Initial (left) and final (right) states of constant inductance - inductance discharge

The value of the current at the end of the first phase is therefore obtained similarly as for a single deformable inductance using Eq. (2-3), with the total magnetic energy being reduced following Eq. (2-4). However, in this case the magnetic energy lost by the system is dissipated by Joule effect in

the switch instead of being converted into mechanical work (cf. Appendix § 2). The transient time only depends on the switch off-resistance and the inductances.

Modeling of a direct SMES supply

A numerical model of SMES-powered EML was developed using Matlab®, in order to quantify more accurately the obtainable efficiency as well as the electrical behavior during a launch. The simulated discharge circuit is presented Figure 2-9.

In order to prevent the voltage across the SMES to get higher than 10 kV (the initial voltage used for capacitor powering cf. 1.2.1) a very low off-resistance value of 0.2 Ω is considered for the storage switch. It may be obtained by adding the appropriate resistor in parallel with the switch. In this case, the transient time for the currents to equalize is lower than 10 µs (cf. Appendix § 2).

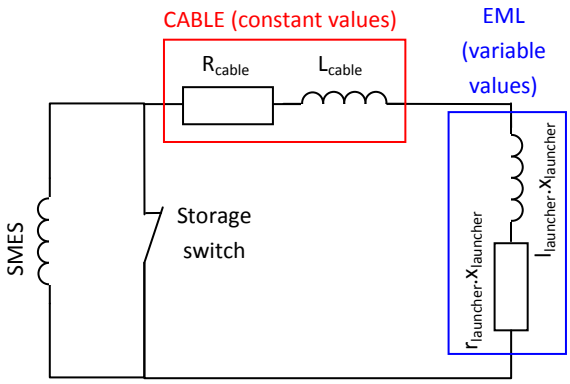

Figure 2-9: Simulated discharge circuit for EML direct SMES supply

This transient state is so short that it can be neglected in our studies, the losses and current drop when switching off the storage switch are therefore obtained analytically, under the hypothesis of instantaneous current homogenization.

The differential equation system representing the electromagnetic and mechanical behavior of the system during the launch is then solved numerically, using the same solving principles than for the capacitor powering model presented in § 1.2.1. (cf. Appendix §°1.1).

Discharge efficiency

The results presented Figure 2-10 are based on the same launcher and projectile characteristics than in § 1.2.1 with an identical initial storage, 110 kJ. The current is adapted so that the output speed is similar, about 400 m/s. The SMES inductance in this case is 61 µH.

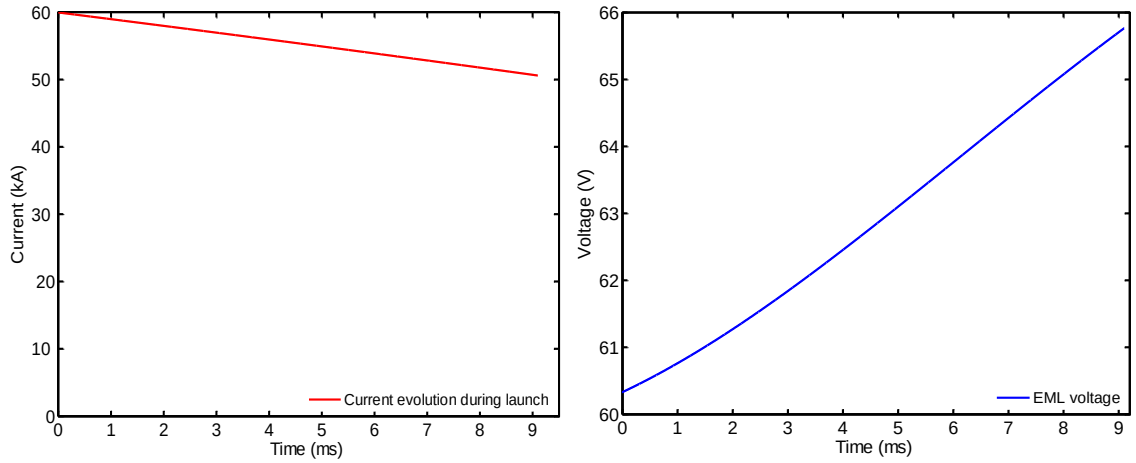

Figure 2-10: Current (left) and Voltage evolution (right) during SMES-powered launch at 400 m/s

The dissipated energy is lower than with capacitor powering, 29 kJ (26 %). As the losses are less important, the current decrease is only 10 % instead of 100 % with capacitors. The projectile is thus accelerated steadily along the launcher length. In consequence, a lower initial current (60 instead of 160 kA) is enough to obtain the same output speed. Most of the energy (78 kJ, 70 %) is still stored in the SMES coil at the end of the launch, and may be re-used afterward. The overall efficiency is thus about 73 %.

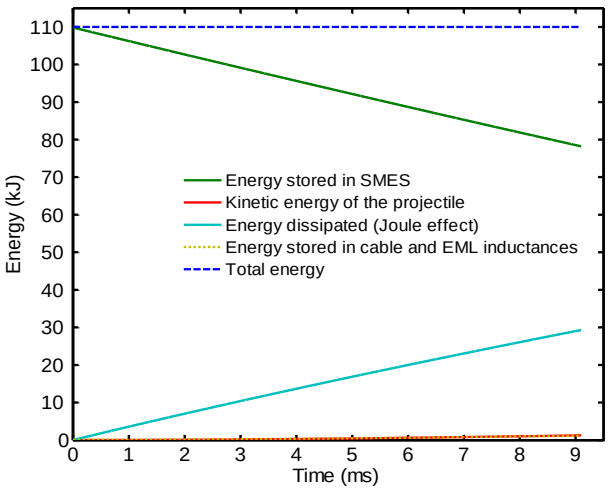

Figure 2-11 : Energy transfer during 110 kJ SMES-powered launch at 400 m/s

Of course, as the losses are lower, the initial energy could be reduced, in order to completely discharge the coil for each launch (Figure 2-12). However, in this case the maximal current required to reach a similar output speed will be higher (similar to what is required with capacitors powering) while the SMES inductance will be very low, 2.3 µH.

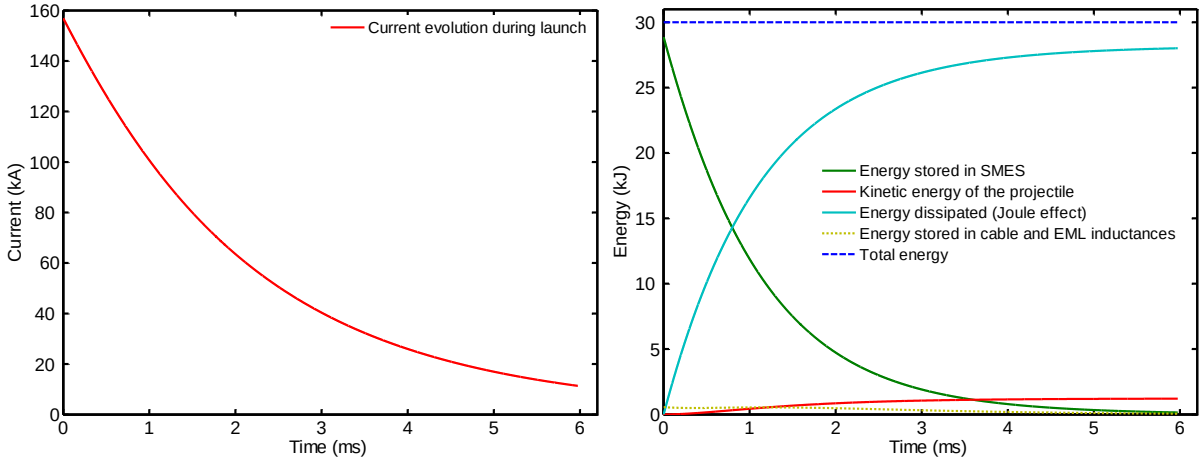

Figure 2-12 : Current evolution (left) and Energy transfer (right) during 30 kJ SMES-powered launch at 400 m/s

In this case the dissipated energy is similar (around 24 kJ) but the initial stored energy is lower than 30 % of the stored energy with capacitor system, which reduces the storage volume.

It should be noted that, contrary to capacitor powering where the pulse forming coil cannot be removed, the losses with SMES powering are only due to connection cables and may be reduced by proper design. In consequence, an almost perfect power transfer can be achieved. In this case the overall efficiency will be the efficiency of the launcher itself.

Realization issues

SMES powering is theoretically perfect for EML, however the kind of superconducting coils adapted for the applications are difficult to realize:

- Operating currents are above 50 kA even for small launchers, and easily reach several hundreds of kA. At present time, only few very large scale superconducting devices operating at very low temperatures (below 4 K) are able to carry such high currents, 200 kA for example in the SMES-ETM already presented in Chapter 1 [Ull95]. The cost (in money but also in volume) of cooling a SMES at such low temperature would be prohibitive. Moreover, thermal stability is lower at low temperatures, which may cause stability problems for pulse operations. These stability problems may be solved by increasing the mass of stabilizing material in the coil, but this would increase the mass and volume of cold material, thus the cooling costs.
- The ratio between operating current and stored energy leads to extremely small inductances. For the simulated SMES-Launcher systems presented above, 110 kJ under 60 kA and 30 kJ under 160 kA, the resulting inductances are respectively 61 and 2.3 µH as mentioned above. For a large scale launcher, and considering energy and operating current similar to those obtained with capacitor powering (10 MJ, 2 MA), the obtained inductance would be in the same order, 5 µH. Such small inductances would self-discharge very fast due to the resistances of the current leads and therefore cannot store energy efficiently.

1.3 Conclusion

Interest of high efficiency powering system

Optimizing the launcher electrical efficiency is critical, as it enhances its shooting rate and survivability, by lowering the rails overheating and arcing damages. At the same time, considering the rather modest energies involved in a launch (never exceeding a couple of MJ), it seems unnecessary to optimize the energy efficiency of the supply chain.

However, this energy must be discharged with a very high power output. As shown Figure 2-13 (cf. Chapter 1 § 2.2.1), high power storage devices have low energy densities. In consequence, even for small energies the storage volume is substantial and an increased efficiency will reduced it consequently.

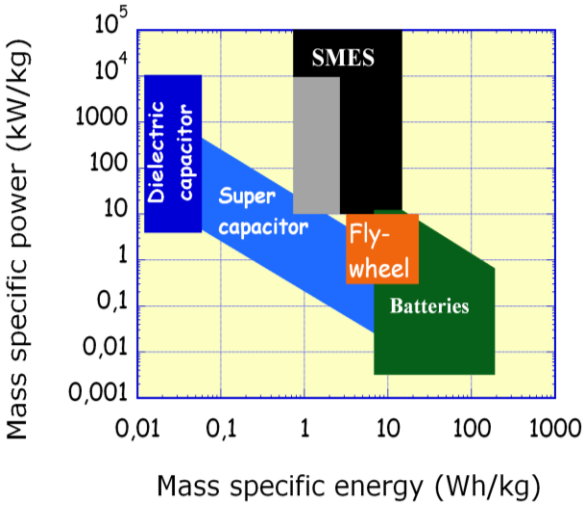

Figure 2-13: Energy and Power densities for classical electric storage (Ragone chart)

This is particularly interesting for on-board launchers and / or for rapid fire operation where enough energy must be stored in the power source to realize multiple shots without recharging time.

SMES integration in EML energy supply chain

As shown Figure 2-13, SMES systems are intermediate between capacitors and batteries in terms of energy density. In consequence, the first possibility is to use SMES as a buffer between low power / high energy source and high power / low energy discharge capacitors.

A multi-shot powering system may be designed using SMES storing enough energy to shot several tenths of projectiles, but with an output current lower than the EML operating current which makes realization easier.

In this case the SMES is used for fast capacitor reloading. The capacitor storage volume is thus only that of a single shot. This is especially interesting as Inductance to Capacitor discharge is theoretically very efficient. The major issue with this system is that the coil has to sustain the maximal capacitor storage voltage, which commonly reaches 10 kV. This possibility is investigated with the SMES II demonstrator (cf. Chapter 3 & 4).However, such supply chain being still capacitor-based, the overall efficiency will not be increased.

Simulation results show clearly that the most interesting way of using SMES is to directly power the launcher. As the efficiency is much higher, for the same stored energy the current drop during a launch is low (about 10 %). In consequence the accelerating force on the projectile is constant, and a lower current may be used for the same output speed.

However, the realization of a SMES with the required characteristics is difficult:

- Even if the operating current is reduced when compared to capacitor powering (because of the lower current drop during launch) it is still in the order of several tenths of kA for a small launcher. Obtaining such current is not trivial with existing superconductors, especially HTS.

- The required energy is low which, considering the operating current, leads to very low inductance values (several tenths of µH). A SMES designed to provide energy for several shots will have a higher inductance and this option seems very promising, but even in this case the inductance will remain below the mH range. While realizing a small inductance is not in itself an issue, it poses a problem of self-discharge. The losses in a superconducting coil being mainly due to the resistive part of the current leads, in first approximation they only depend on the current. In consequence, the self-discharge of a coil is faster if its inductance is low.

In order to overcome the problem posed by the high required current, studies must be conducted to either increase the output current of SMES systems or reduce the operating current of EMLs. This is the topic of the following section. The problem of the self-discharge will also be partly solved by reducing the current as the losses in the current leads, responsible of this discharge, will be reduced.

2. Toward direct SMES supply

In this section is first described the SMES output current multiplication using XRAM concept. Theoretical results are presented showing the interest of this method for EML powering. Possible practical implementations are presented with their benefits and drawbacks. In a second time, EML operating current reduction methods are studied. The so called “augmented railguns” designs are introduced. A novel SMES-EML integrated system is then presented, combining the interest of augmented railguns and SMES powering.

2.1 Current multiplication through XRAM

2.1.1 Principle

The XRAM principle is to charge several inductances in series and to discharge them in parallel to sum up their currents. It is the dual of the more widely used MARX system where capacitors are charged in parallel and placed in series to obtain higher voltage (which explains why its name is “MARX” spelled backward). The charging and discharging circuit principle is presented Figure 2-14.

During the charging phase, the switches 1 to *n* are closed and the discharge switches are open. The current circulates in the *n* inductances in series.

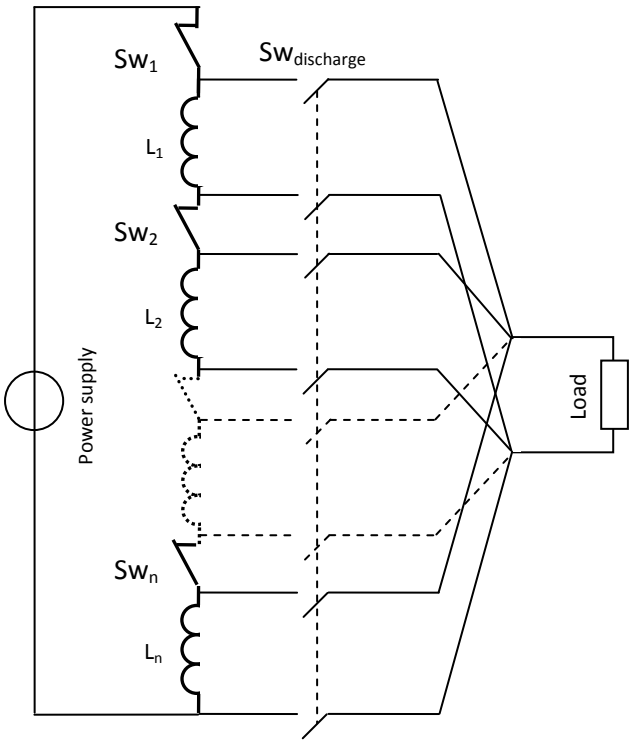

Figure 2-14: n-stage XRAM principle

When the system must be discharged, the discharge switches are first closed to establish the parallel discharge circuit. The switches 1 to n are then opened simultaneously which breaks the series circuit and triggers the discharge.

This system was already tested successfully at ISL with 8 resistive coils [DBS09a], and a 20-stage version was recently developed, demonstrating the possibility of directly powering a launcher. Superconducting XRAM was already proposed with LTS material with a maximal output current of 7 kA [WEM+99].

2.1.2 XRAM interest for direct SMES supply

As we have seen at the end of § 1.2.2 the two major issues for practical realization of SMES suitable for EML supply are a high required operating current and a low inductance. XRAM is a convenient solution to these two problems.

The *n* inductances displayed on Figure 2-14 are forming a SMES when connected in series, storing E_{stored} under I_{nom}. When connected in parallel, these inductances form an "equivalent" SMES storing the same energy but under a current n time higher ($I_{nom}.n$). The inductance of the equivalent SMES $L_{eq\ parallel}$ is given by Eq. (2-6):

$$E_{stored} = Cst = \frac{1}{2} L_{series} I_{nom}^{\ 2} = \frac{1}{2} L_{eq\ parallel} \left(I_{nom} \times n \right)^2$$
$$\Rightarrow L_{eq\ prallel} = L_{series} / n^2 \qquad \textbf{(2-6)}$$

In consequence, if powering the launcher requires a SMES with and inductance *L*=61 μH and an operating current *I*=60 kA (the values obtained in § 1.2.2 for a small launcher supply), using a 10-stages XRAM system will turn the problem into realizing a coil with an inductance $L.n^2$=6.1 mH, an operating current *I/n*=6 kA and made of 10 elements, which is much closer to what is possible with present day superconducting technology.

2.1.3 Preliminary study of XRAM supply efficiency

When using XRAM concept instead of single coil SMES, additional losses must be considered, in the connections and commutation system.

Current leads losses

For any kind of SMES, connections between the load at room temperature and coil at cryogenic temperature generate losses. These losses in the current leads cannot be reduced below a certain point, due to the necessary trade-off between the Joule losses and thermal losses by conduction. This topic will be discussed in details in Chapter 3 § 3. Typically the losses are about 40 W/kA for coil temperatures below 77 K, both electrically and thermally.

In consequence, the losses using an XRAM device will be similar to the losses a single coil device having the same output current. For example, the losses for a SMES with an operating current of 60 kA, or a 6 kA 10-stage XRAM device are both around 4.8 kW. It is negligible during the launch when compared to the 3 MW dissipated by the launcher itself. However, this dissipation also occurs when charging the device and storing energy.

Commutation system losses

The commutation system losses are on the contrary specific to XRAM devices and depend of the commutation technology. Solid-state switches (IGBT, GTO, etc.) should be preferred for their high switching speed. The launcher being a quasi-short-circuit, its voltage under operation is low, as it was observed from the simulation in § 1.2.2. High current / low voltage switches may thus be used.

During the charge, the switches 1 to *n* are on. Classical on-state voltages at 6 kA are about 4 V for solid state switches, which gives 240 kW losses for a ten-stage device. In consequence the output power of the charging unit will have to be much higher with XRAM system than for single coil system. Of course the power dissipated in the switches varies with the current. The rough estimation that we make here for power dissipation is therefore only valid if the current variation is small. This assumption should in principle be verified in practical systems, as it was stated in°§ 1.3.

During the discharge, the losses are doubled, as there are two discharge switches for each stage. 4 kJ are dissipated in the commutation systems during the discharge, and the overall efficiency is only reduced from 73 to 70 %.

Conclusion

The outcome of this primary study about superconducting XRAM efficiency as direct SMES supply is uneven. The use of *n*-stage XRAM makes it possible to divide the current in the SMES coils by *n* without reducing significantly the overall efficiency, but the losses due to the current leads are not reduced. They still correspond to the losses induced by the EML operating current, which is very high.

Moreover, if the discharge efficiency is not modified, the charge efficiency is substantially reduced. A powerful charging source is required to reach the desired current, due to the voltage drops induced by the switches. For the same reason, the self-discharge time constant of such SMES is very short (a few seconds).

2.1.4 Cryogenic XRAM concept

Cooling power reduction

The idea of cryogenic XRAM concept is to include the switching system in the SMES cryostat (Figure 2-15). In this case only 4 current leads are needed, 2 for the series charging circuit (on the left) and 2 for the discharge in parallel (on the right).

For the charging system, the current leads are designed classically, for continuous operation at the coil segments rated current. However, the discharge time being short, there is no need to design the parallel discharge current leads for continuous operation. They may be significantly under-sized which will reduce drastically the cooling power required to cool them.

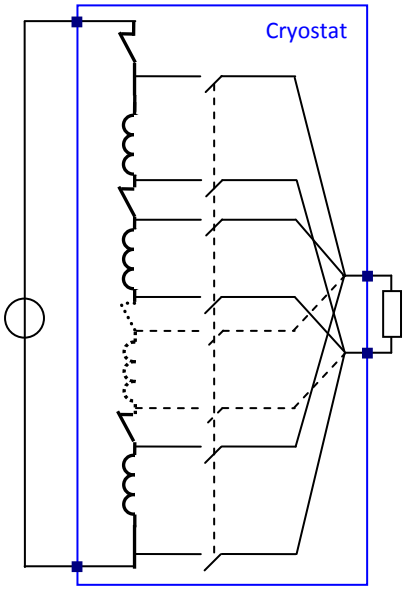

Figure 2-15: Cryogenic XRAM layout

Considering the ten-stage 6 kA XRAM system already presented above, the cooling power required by the current leads could be reduced from 4.8 kW (cf. § 2.1.3) to 0.96 kW by using identical current leads optimized for 6 kA for both the charging series circuit and the parallel discharge circuit.

The major drawback with this method is that the losses in the switching units are occurring at cryogenic temperature. If we consider similar losses at cryogenic temperature than at room temperature (240 kW cf. § 2.1.3), the additional cooling power required to remove them is much higher than the cooling power spared.

Such system may therefore have an interest only if the losses in the switching units can be reduced by two orders of magnitude, to a level similar to the current leads losses. The paragraphs below briefly present some possibilities that may be considered to reach such low losses on switching units.

Use of superconducting switches

In order to have very low switching losses, the use of superconducting switches for superconducting XRAM at 4.2 K was already proposed with Low Temperature Superconductors [WEM+99]. The obtained layout is represented Figure 2-16, with the superconducting witches *Sc1* to *Sc6* for charging, and *Sp1* to *Sp6* for parallel discharge.

Such switches are in fact superconducting wires whose temperature is controlled using heaters. When the heaters are off, the switch is superconducting and the current passes through it without any losses. When the heaters are on, the wire temperature increases and it returns to the normal state. The switch resistance ceases to be zero and the current flows through the load, provided that the load resistance is much lower than the resistance of the switches in their resistive state.

Fast switching may be obtained with LTS material, due to the very low specific heat at low temperature and the stiffness of the transition. It seems however difficult to implement with HTS the higher specific heat and higher temperature margins lowering the switching speed. In consequence, cryogenic solid-state switches are the only practical solution for XRAM SMES designed with HTS.

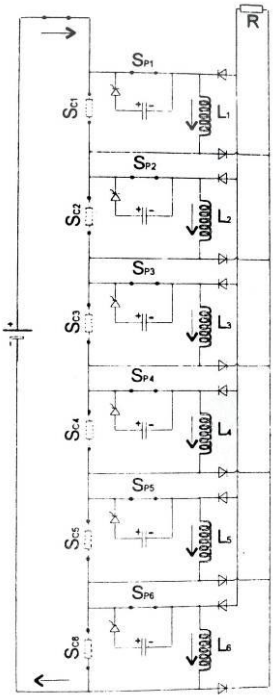

Figure 2-16: LTS 6-stage XRAM with superconducting switches (from [WEM+99])

Expected losses reduction with cryogenic semi-conductor switches

At cryogenic temperature (down to 30 K), the threshold voltages of power electronic components increase, while their on-state resistances decrease [HYE+05]. The on-state losses of Thyristor-based switches (such as GTO and GCT) and IGBTs being essentially due to their threshold voltages, no losses reductions are expected by operating such devices at cryogenic temperatures.

On the contrary, Power MOSFETs are ohmic devices whose losses are only due to the on-state resistance. They are not commonly used as room temperature for high power switching, but studies on Cryo-MOSFETs at 77 K [KRSS91], [YLR+07] showed reduction of the on-state resistance about one

order of magnitude, and several studies are on-going on integrated high power cryo-MOSFETs switching units, showing promising results [YLSH09].

Assuming that large cryo-MOSFET switching arrays will be developed in the near future, it will be possible to reduce almost at will cryogenic XRAM on-state losses, by increasing the size of the switching arrays.

Conclusion

Cryogenic XRAM, by lowering the thermal losses on the coil and improving at the same time the switching devices efficiency, is theoretically a perfect solution for EML powering. Overall efficiencies about the same order than with direct SMES supply are expected (70 %). However, additional studies are necessary to consider all the potential side effects, before testing such system at large scale.

2.2 Operating current reduction

2.2.1 Augmented launchers principle

The Lorentz force accelerating the projectile in an EML is of the form $F_{Lorentz} = I_{launcher} \cdot l_{projectile} \cdot B$. For classical launchers, the magnetic flux density B is only induced by the current circulating in the rails so that B and $I_{launcher}$ are correlated. However, an external source could be used to increase B, as shown by Eq. (2-7). This is the "augmented railgun" principle (Figure 2-17).

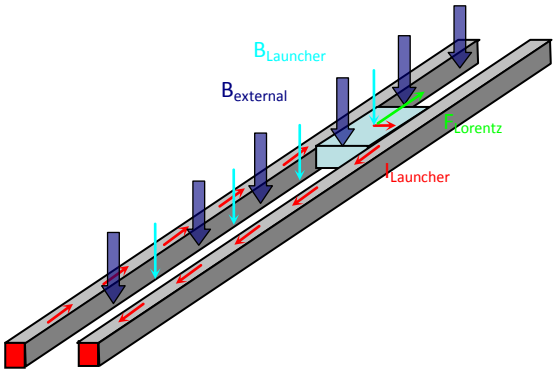

Figure 2-17: Augmented railgun principle

$$F_{Lorentz} = I_{launcher} \cdot l_{projectile} \cdot \left(B_{launcher} + B_{external} \right) \quad \textbf{(2-7)}$$

With this principle, the desired projectile acceleration may be obtained with a lower operating current than using classical launcher, making EML SMES powering easier. Moreover, the lower current makes it easier to realize long-life/low-losses sliding contacts. Finally, the magnetic flux being partly de-correlated from the current, a steadier acceleration may be obtained when compared to classical launchers were both current and magnetic flux density are decreasing along the launch.

2.2.2 Existing augmented launcher concepts

Different methods were investigated to generate the external field. The most widely studied is the concept presented Figure 2-18. It features an additional set of rails powered by an external source.

This system was tested at ISL [GL05], and an enhancement of the launcher capability was demonstrated. However, the launching overall efficiency was not clearly increased, due to the losses in the secondary rails

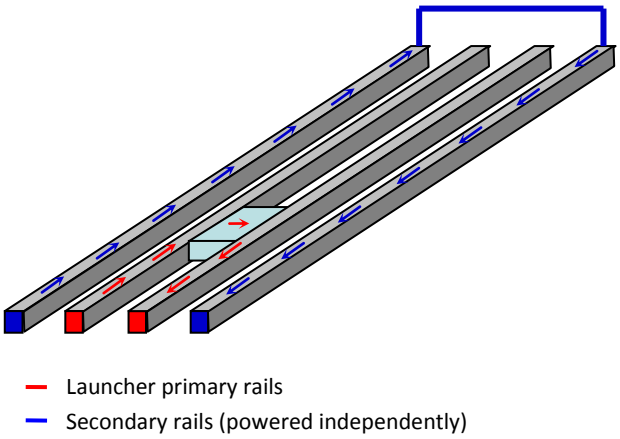

Figure 2-18: Augmented launcher concept, proposed in particular by ISL

Other augmentation solutions were proposed:

- Permanent magnets, leading to the Augmented Rail Gun Permanent Magnet concept (ARGPM [KAE+95])
- Sets of successively-powered short resistive dipoles distributed along the rails length (the STAR concept [NTES04])
- SARG concept (Superconducting-Augmented Rail Gun) where the external magnetic field is produced by a long single dipole used as permanent electro-magnet [HCF86].

These solutions systematically separate the magnetic flux density generation from the rail powering, which is insured by capacitor banks. The best result obtained with SARG was a launching efficiency increased by a factor two. However, the device volume is not reduced, as the reduction of the capacitor storage volume is compensated by the additional volume of the augmenting system.

2.3 The S3EL concept

The S^3EL concept (Superconducting Self-Supplied Electromagnetic Launcher) aims to get high EML performances and efficiency, similar to what could be obtained with direct SMES powering, but with an increased feasibility. A patent was filed by the DGA/CNRS for this concept [TBA11].

The principle is to use the Magnetic flux density produced by the SMES to augment the flux density in the launcher, thus combining the benefits of launcher augmentation and direct SMES powering. Such self-augmentation makes it possible to obtain, with significantly lower operating currents, performances similar or even higher than what is obtained with a non-augmented launcher. The use of XRAM current multiplication may also be used in this configuration, to reduce the coil nominal current even further.

For such SMES-Launcher integration, coil geometries insuring that the magnetic flux from the coil passes between the rails of the launcher should be privileged. S^3EL coils will thus have dipole-like

geometries (Figure 2-19) instead of classical solenoidal or toroidal SMES geometries presented Chapter 1 § 3.1.2.

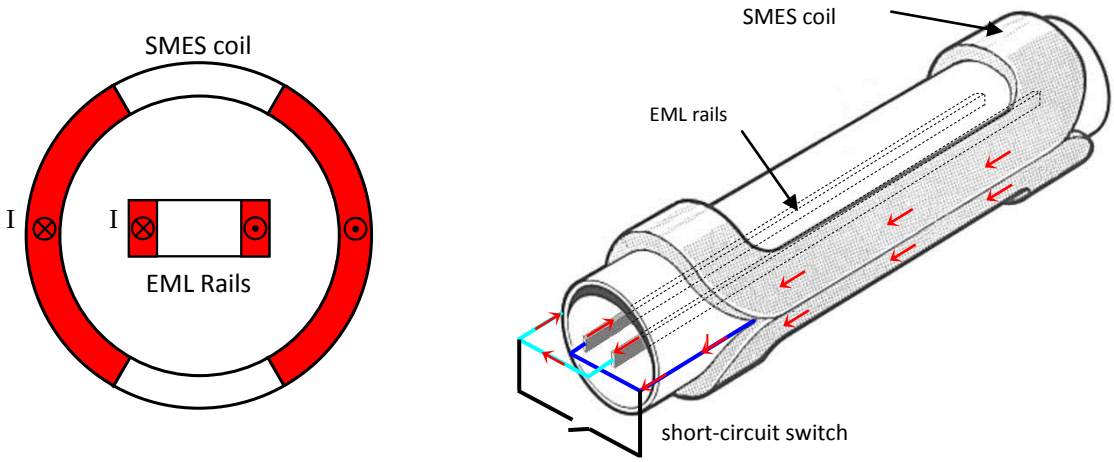

Figure 2-19: Possible SMES-launcher integration for S³EL concept with dipole-type coil. Cross section (left) and perspective view (right)

2.3.1 Preliminary evaluation of S³EL efficiency and feasibility

In order to evaluate theoretically the benefits of such integration, the numerical model that was developed to simulate the behavior of SMES-powered EML (cf. § 1.2.2) was upgraded to integrate a magnetic coupling between SMES and launcher. This coupling changes with the position *(x)* of the projectile in the launcher, following Eq. (2-8):

$$k(x) = k_{\max} \cdot x / x_{launcher} \quad \text{, with} \quad k_{\max} = \frac{M^2}{L_{Launcher} L_{SMES}} \qquad \textbf{(2-8)}$$

Where $L_{launcher}$ is the total inductance of the launcher, which is reached when current is circulating in the whole length of the rails, thus when the projectile is about to leave the launcher. L_{SMES} is the SMES inductance and M the mutual between these two inductances. $x_{launcher}$ is the length of the launcher.

In a first time, k_{max} is treated as an arbitrary simulation parameter varying from 0 to 1, independent from the SMES coil shape and inductance.

With launching conditions similar to § 1.2.1 & 1.2.2 (a 16 g projectile, with an output speed around 400 m/s and an initial stored energy of 110 kJ) the simulations demonstrate a drastic operating current reduction of S³EL when the coupling k_{max} increases (Figure 2-20).

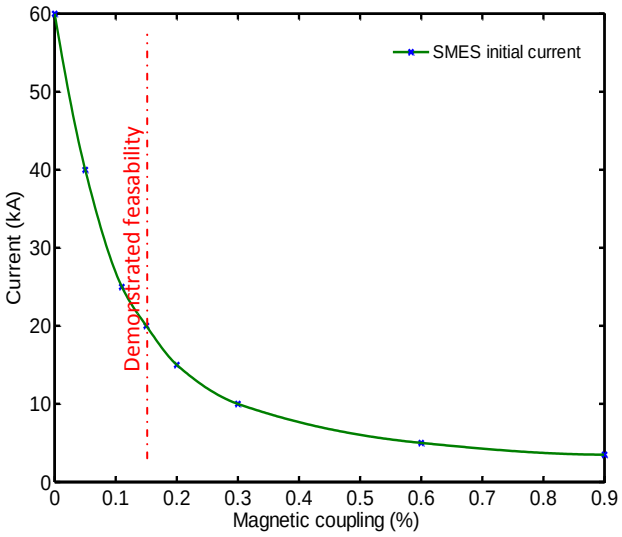

Figure 2-20 : EML Operating current for increasing SMES-Launcher coupling (k_{max} value)

Obtaining very high coupling values will be practically difficult due the shape of the launcher which is a very long and thin current loop. Some realistic scaling ideas may however be derived from the results of the SARG experiments mentioned above in § 2.2.2. In these experiments, a superconducting dipole was used to provide an augmenting magnetic flux. Even if the coil was not used to power the launcher, its coupling to the rails was similar to the one present in a S^3EL system. A coupling of 13 % was obtained: this is the limit of "demonstrated feasibility" placed on Figure 2-20.

The dipole that was used in the SARG experiments was not specifically optimized for integration around a launcher. A refined integration between the coil and launcher could probably give coupling values up to 15 %, but significantly higher coupling seems difficult to reach, at least with warm launcher structure. Detailed S^3EL simulation results obtained for plausible coupling values are compared with classical capacitor powering and SMES powering configurations in Table 2-1.

	Capacitor powering		SMES powering (no coupling)		SMES powering 11% coupling		SMES powering 15% coupling	
Initial Energy	110 kJ							
Initial current	165 kA		60 kA		25 kA		20 kA	
Inductance			0.061 mH		0.35 mH		0.61 mH	
Dissipated energy	108 kJ	98 %	31.5 kJ	28 %	7 kJ	6.4%	4.6 kJ	4.2%
Projectile kinetic energy	1.4 kJ		1.4 kJ		1.39 kJ		1.42 kJ	
Stored energy after the launch	≈0	≈0%	78 kJ	70 %	100 kJ	91%	102.5 kJ	93.2%
Current after the launch			50 kA	83 %	23.9 kA	95.6%	19.3 kA	96.5%

Table 2-1 : Launching overall efficiencies for Capacitor, SMES and S^3EL powering

The conclusion drawn from these preliminary simulations is that S^3EL system may indeed operate with a much lower current when compared to non-coupled SMES powering, even if the coupling between the launcher and the SMES is rather low (divided by 3 for k=0.15). Moreover, in this configuration the SMES inductance is augmented (up to 10 times) for an identical initial storage, which increases the self-discharge time constant.

Finally, the overall efficiency of the launch is also improved, due to lower losses by Joule effect in the launcher. The current and energy evolution for S^3EL with 15 % coupling are presented Figure 2-21.

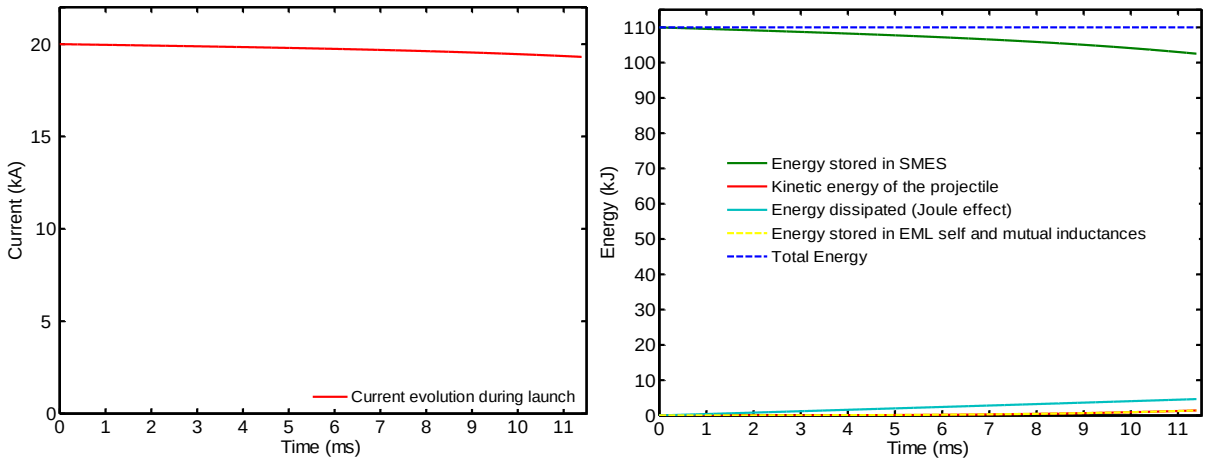

Figure 2-21: Simulated current (left) and energy transfer (right) for 15 %-coupled S^3EL launch at 400 m/s

2.3.2 SE^{3}L geometry optimization principle

As it was already mentioned, the promising simulation results presented above for S^{3}EL concept are obtained by considering arbitrary coupling values between coil and launcher, and some bibliographic results obtained with a dipole coil [HCF86]. However, the very small inductance value of the SMES coil that corresponds to our application (below *1 mH*, as shown in Table 2-1) implies a low number of coil turns. Realizing a dipole in these conditions may not be practical, and even if it was, such coil shape may not be optimal for this specific application. It is therefore necessary to conduct a study determining the coil geometries optimally adapted to the S^{3}EL concept.

The objective of this optimization study is, for given launching characteristics (launcher length, projectile mass and output speed), to obtain the coil configurations insuring:

- Lowest possible operating current, in order for the coil realisation to be easier with existing superconducting material (especially HTS), at the highest temperature possible.
- Smallest possible coil in order for the system to remain compact.

Increasing the magnetic flux passing between the rails for a given current is possible by simply increasing the SMES coil inductance, but in this case the volume of the system is not optimized. In order to consider the compactness as part of the objectives, it is the proportion of the SMES magnetic flux that passes between the launcher rails that must be optimized, thus the magnetic coupling between coil and rails, as defined in the previous paragraph by Eq. (2-8).

The main constraints on this study are geometric (Figure 2-22):

- Launcher topology (distance between rails, size of the rails mechanical support, direction of the current and magnetic flux density, etc.).
- Cryostat and coil thermal insulation.

Considering that our objective is to maximize the coil/rail coupling value, the zone where the coil winding is to be placed will likely be the closest possible from the rails, around the forbidden zone representing the cryostat, thermal insulation and rails mechanical support.

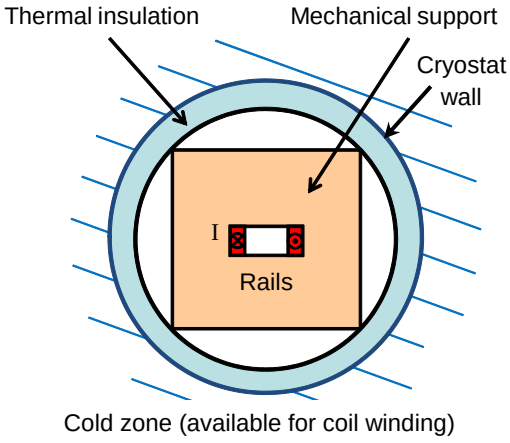

Figure 2-22 : Constraints on the coil winding localization

2.3.3 First optimization results

Coil coupling optimization tool

A simulation tool is being developed using Matlab® for fast processing of the coupling between the launcher and adjustable SMES coil geometries. The study is conducted in 2D, for a cross-section of the S^{3}EL system, with an out-of-plane simulation depth corresponding to the launcher length

(about 2 m). The coupling is calculated analytically by evaluating the magnetic flux passing through the rails and the inductance of the coil, for each configuration coil configuration. This calculation is made using the potential vector $\vec{A}$ and taking advantage of the symmetries in the study.

Each tested coil configurations is defined as the combination of a given number of round wires with a fixed cross section. These round wires are considered connected in series, thus with equal current flowing through them. Varying the number of wires allows optimizing the geometry for various coil volumes and inductances.

The wires may theoretically be placed anywhere outside the forbidden zone which represents the room necessary to fit both the launcher rails, their mechanical housing, the coil cryostat and its thermal insulation (Figure 2-22). This zone was considered in our experiment as a cylinder with a diameter consistent with the existing launcher dimensions. Later studies could easily be conducted with other forbidden zone shapes, if for example the realization of a cryostat with a square hole was considered.

Following the observations presented in the previous paragraph, the study of the possible coil configurations is restricted to the area that is closest from the rails. This area, which is of annular shape, is discretized in order for the number of possible configurations to be finite. This discretization forms a “grid of possible positions” for the coil wires, as shown Figure 2-23.

Moreover, the repartition of the wires must respect the symmetries of the system with respect to the vertical and horizontal planes:

- In order to insure that the net force on the projectile is in the out-of-plane direction, the number of wires on the left and the right side must be equal, with the current flowing inward on one side and outward on the other.
- Symmetry considerations indicate also that the optimal repartition of the wires above and below the horizontal plane must be even.

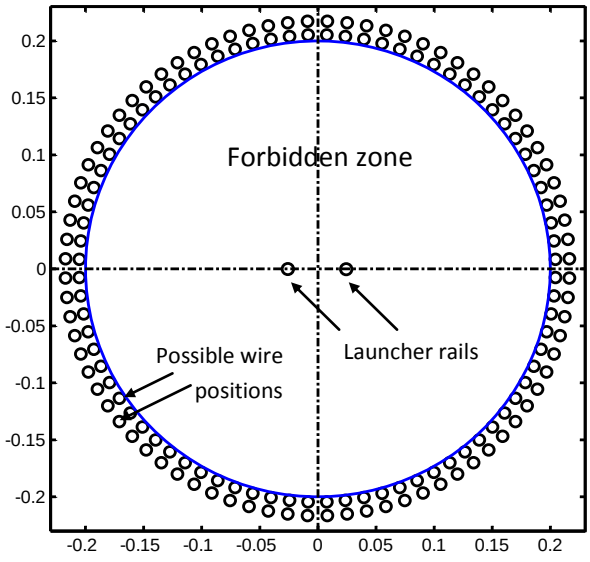

Figure 2-23: Simulated geometry

First results

The first studies using this simulation tool were conducted testing all the grid positions, which is possible for low wire numbers, but induce exponential solving times when the number of wire increase. It leads to the results presented Figure 2-24.

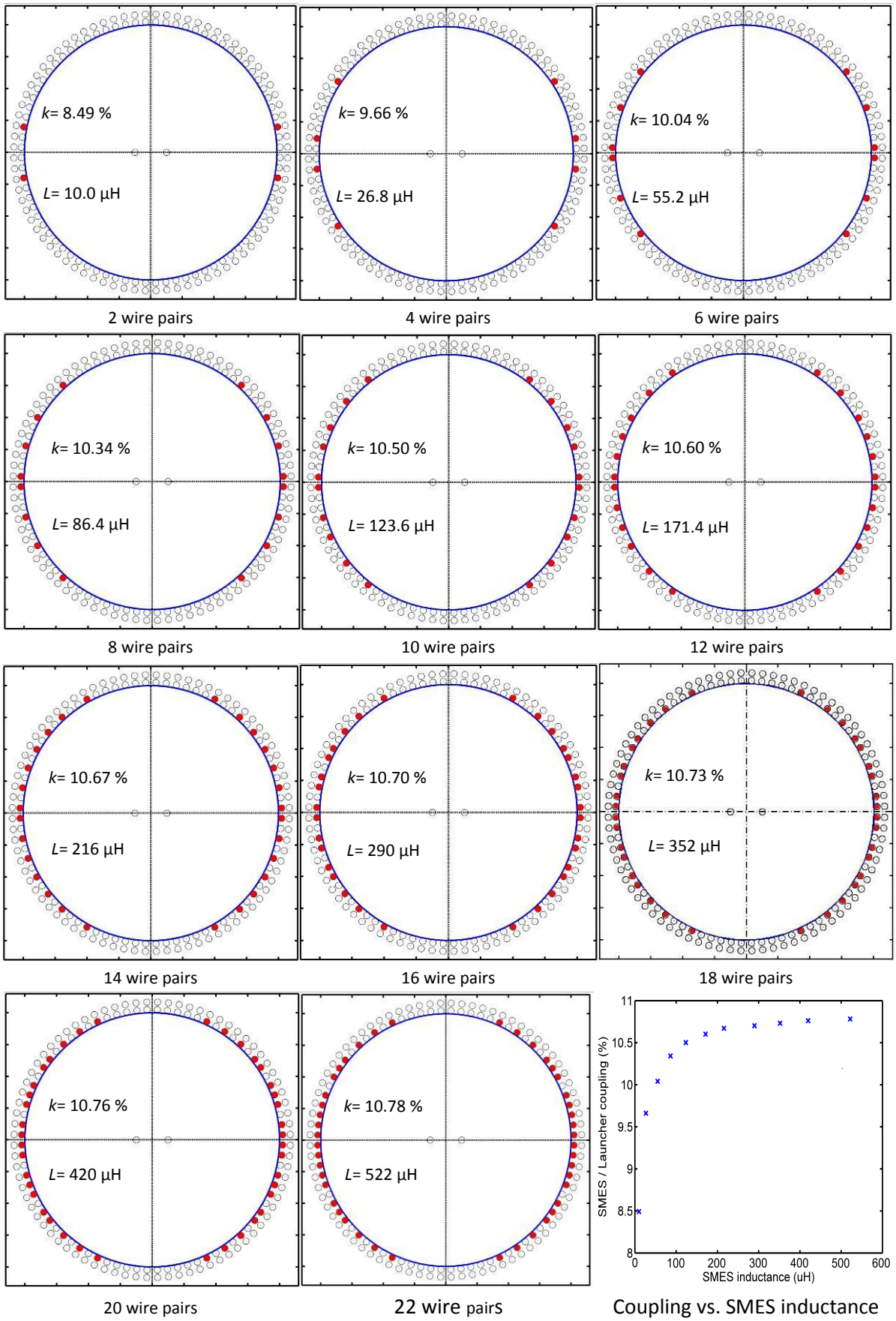

Figure 2-24: Optimal geometries for increasing number of wires (2 to 22) and resulting coupling values

The results indicates that if the coupling value increase rapidly for low number of wires it tends to saturate above 6 (around 200 µH), when the obtained geometry takes a dipole-like shape. The maximal possible value seems to be around 11 %, but additional simulations will be necessary to investigate the behaviour of the coupling when the inductance is higher than 600 µH.

Considering the simulation times (1 day for 20 wires, 3 days for 22 wires), testing all the configurations with higher number of wires will be difficult. Optimization methods such as genetic algorithm could be used to select the configurations to be simulated, which would reduce substantially the solving time. The integration of this simulation tool with existing general-purpose optimization tool available at G2Elab (General Optimization Tool) is being conducted.

The most important conclusion that can be drawn from this study is that a suitable S^{3}EL coil configuration may be obtained for coil inductances higher than 200 µH. Lower inductances will not offer interesting gains when compared to classical uncoupled SMES-Launcher configurations.

2.3.4 Launching simulation results with optimized geometries

Once the optimized geometry for a given number of wires is obtained, the resulting magnetic coupling and inductance may be injected in the S^{3}EL powering simulation code presented in § 2.3.1.

For example, if we consider the optimal geometry with 11 wires, and a launcher similar to the one simulated previously (with 2 m-long rails), the SMES coil has an inductance *L*=522 µH. With 10.78 % coupling, the required current for an output speed of 400 m/s is 22 kA, and the stored energy is thus around 126 kJ (Figure 2-25).

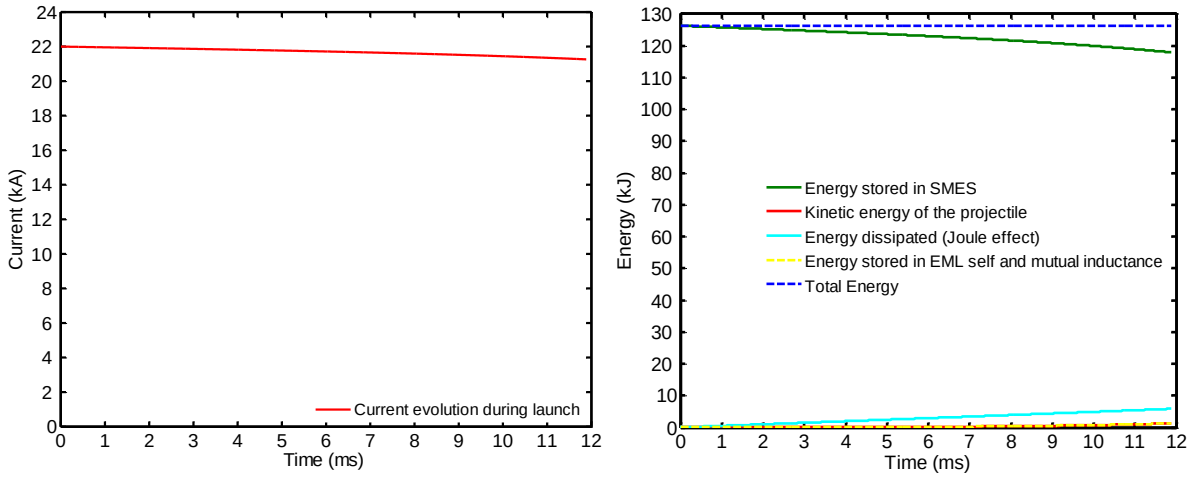

Figure 2-25 : Current (left) and Energy (right) evolution for optimized S^{3}EL configuration (output speed 400 m/s)

Similarly, the minimal operating current and corresponding initial stored energy that is required to reach the launcher specifications in terms of launching speed and kinetic energy may be obtained for all the configurations. Its evolution against the coil turn number (a coil turn is, in our configuration simply a wire pair), is presented Figure 2-26. The coil turn number is related to the superconducting material volume that will be required for the coil realization.

The required operating current gives insights about the feasibility of the device with the existing superconductor technology and, if realization is possible, the maximal temperature of operation. In case XRAM method is used, it helps determining the required number of stages.

In conclusion, it seems that to make S^3EL realization possible with present-day HTS technology, a minimal inductance of about 350 µH is required so that the coil operating current does not exceed 25 kA, which corresponds to 18 turns in our example.

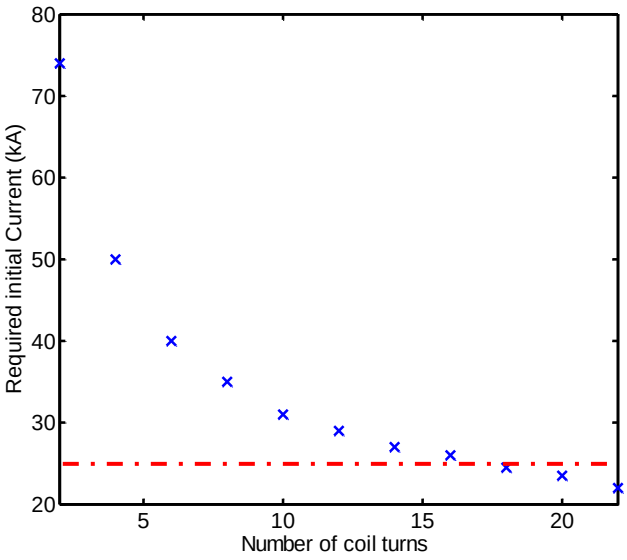

Figure 2-26 : Operating current reduction with the coil turn number increase

3. Conclusion

In this chapter, the possibilities of integrating a SMES in an EML supply chain were presented.

The possibilities offered by indirect powering, which consist in reloading the discharge capacitors between the launches was only mentioned. It will be tested with the SMES II demonstrator, whose design and tests will be presented in the following chapters.

The interest of SMES direct powering for the EML overall efficiency was underlined. To overcome the realization issues of such high current SMES, two possibilities were studied: Multiplying the current output using the XRAM principle, and reducing the current required by the launch, by using EML augmentation method.

This last study led to the very promising patented concept S^3EL (Superconducting Self-Supplied Launcher). With this method, a quasi-constant acceleration force is obtained on the projectile, while the operating current is divided by eight when compared to its classical capacitor-based counterpart, with an efficiency reaching 90 %.

This work being only theoretical, the calculated efficiencies are probably too optimistic. However, the magnitude of the expected benefits convinces us to develop the studies on the subject and obtain experimental data to confirm the behaviour of SMES-powered launcher and S^3EL.

Experimental tests of superconducting XRAM are possible with SMES II, though at much lower current (600 A). The results of these tests are presented in Chapter 4. On the contrary, testing the S^3EL concept will require a new prototype, with an adapted geometry. This is one of the most promising perspectives of this work.

It should be noted that XRAM principle and S^3EL concept are complementary, and a full S^3EL demonstrator could be designed featuring 10 overlapping dipole-like coils having a rated current of only 22/10=2.2 kA.

Finally, a variant of the S^3EL system could be proposed for rapid-fire railgun application, using several coupled launcher forming a segment torus with their powering coils (Figure 2-27). With this configuration, the coupling between the coil elements enhances the energy density of the system, thus its autonomy when compared to single-launcher S^3EL configuration. In the meantime, the stray field is reduced by the torus-like topology.

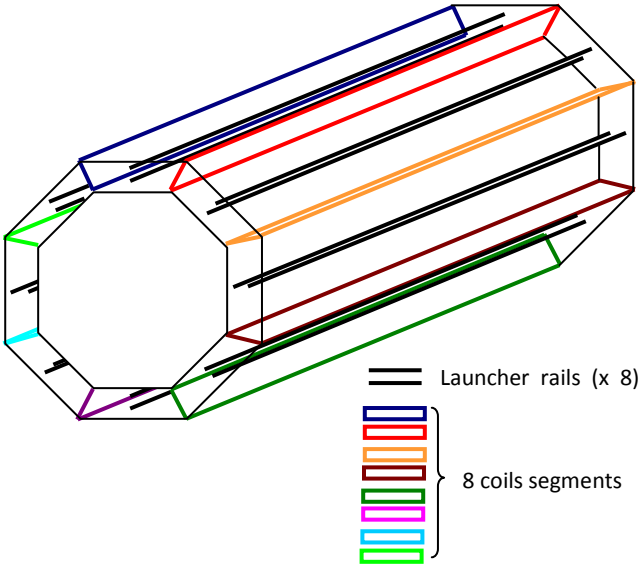

Figure 2-27: S^3EL variant with several coupled launchers

CHAPTER 3 :
SMES II DESIGN

The SMES II demonstrator is an upgrade of a previous device, SMES I, which was successfully tested in 2007. In this chapter the contribution of this thesis to the design of SMES II is presented.

In the first part, the characteristics of SMES I are briefly recalled, after that the specifications and design constraints for SMES II are described along with their consequences on the thermal design. A presentation of the magnetic design, conducted by K. Berger, is included for a good understanding of the device characteristics. The second and third parts present respectively the electro-thermal optimization of the superconducting and resistive current leads segments. The fourth and last part describes the thermal design of the coils cooling system.

The mechanical design (the pieces and elements definitions and assembly, mechanical structure resistance, etc.) was done by M. Deleglise, engineer and projector. His work on mechanical design will not be presented extensively later on, but all the studies presented were of course conducted in close cooperation with him. The CAD views presented were also obtained by him.

1. Demonstrator origin, specifications and design issues

In this part are first presented the main characteristics of the SMES I demonstrator, on which SMES II is based. SMES II specifications and its foreseen modes of operation are described in a second time. The resulting magneto-electric design is then detailed. This part is concluded by a general description of the cooling principle and design choices, introducing the design issues that will be addressed in the following parts.

1.1 The SMES I demonstrator

Studies were conducted on HTS SMES since 2003 at Neel Institute / G2ELab, in the framework of a DGA contract with Nexans. A scale 1 demonstrator called SMES I (Figure 3-1) was realized as proof of concept for HTS SMES operation. It had also to demonstrate the possibility of being operated without any specific cryogenics skills, thus without cryogenic fluid handling. The design and realisation of this first demonstrator were the subject of Boris Bellin's PhD thesis [Bel06], defended in 2006.

Figure 3-1 : SMES I demonstrator under test

1.1.1 SMES I main characteristics

SMES I was a short solenoid consisting in a stack of 26 pancakes connected in series, for a total inductance of 17 H. It was designed for an operating current of 300 A and therefore expected to store about 800 kJ.

HTS Conductor

The conductor used for this device was provided by Nexans. It is made of several BSCCO-2212 tapes (cf. Chapter I, Figure 1-5) soldered one on top of the others, allowing the current density to be shared between them (Figure 3-2). The resulting assembly is then insulated with kapton®.

Figure 3-2 : Nexans conductor structure

The 26 pancakes were formed by winding the conductor (about 450 m for each) on epoxy-coated copper. The winding was glued to the plate using Redux®, an epoxy film with low curing temperature.

In order to use efficiently the conductor, it is oriented so that the longitudinal direction of the superconductor material follows the coil magnetic flux density main orientation (the coil axis). In consequence, the tapes are wound on the edge on the copper plates (zoom on the right Figure 3-3).

To optimise further the use of superconducting material, the number of tapes forming the conductor was adapted to the local magnetic field orientation: 3 in the areas where it is mainly longitudinal and 4 in the areas with higher transverse component (the coils extremities). The tapes were also reinforced with stainless steel tape to withstand the stress induced by the magnetic flux during operation in the areas where it is maximal. The conductor types used in the different pancakes is presented Figure 3-3.

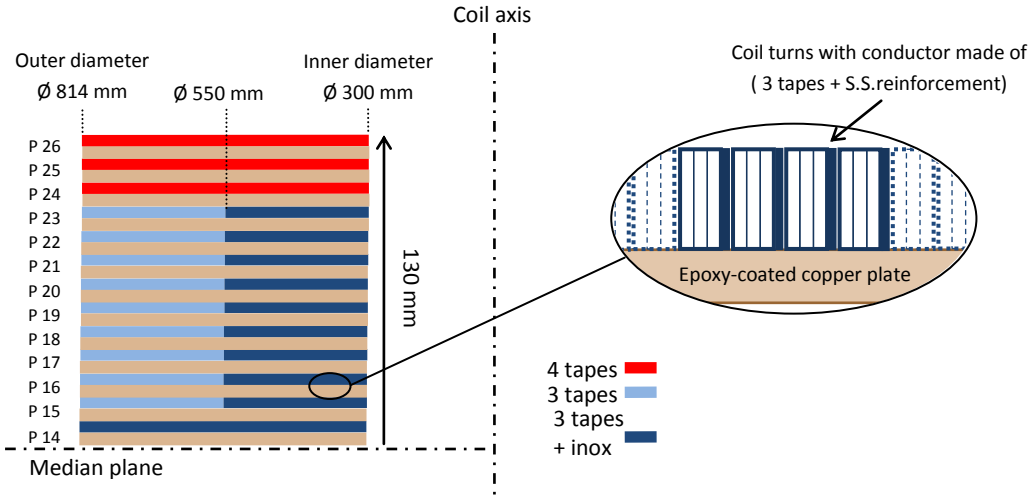

Figure 3-3 : Conductor types in SMES I lower-half coil (upper-half is symmetrical)

In order to be easily operated without specific knowledge about cryogenics, the SMES I did not use any cryogenic fluid. Its magnet was conduction-cooled at 20 K by two Gifford-MacMahon cryocoolers, one cooling the coil and the other cooling the current leads and the thermal shield. The cooling power was transferred to the coil by conduction through a massive croissant-shaped copper plate. Flexible copper elements connect it to the pancakes copper plates in order to isolate the coil pancakes from the cryocooler vibrations and absorb the differential thermal expansions (Figure 3-4).

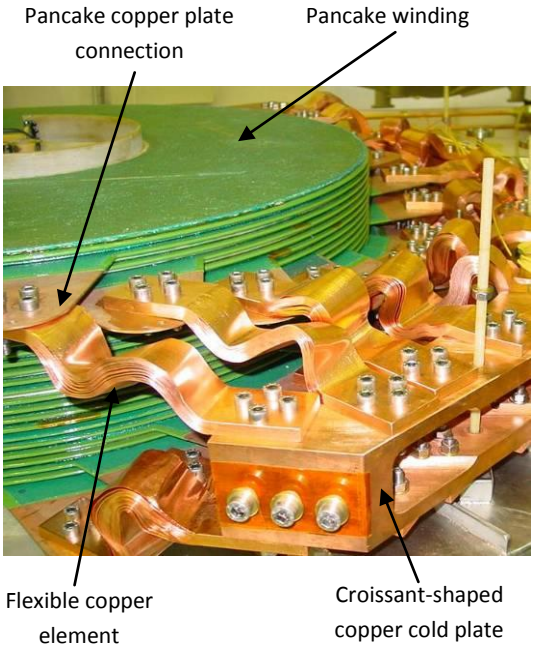

Figure 3-4 : Pancake stack and cooling plates

1.1.2 SMES I test and results

The SMES I demonstrator test campaign was conducted in 2007 [TDB+08]. The cooling down was successful, and the magnet reached 200 A before quenching. This quench was not detected early enough and one of the pancakes (the next-to-last of the stack) was damaged. We bypassed the two last pancakes to continue the tests and the 24 remnant pancakes reached 250 A, storing more than 400 kJ with a maximum power of 175 kW under 700 V (Figure 3-5).

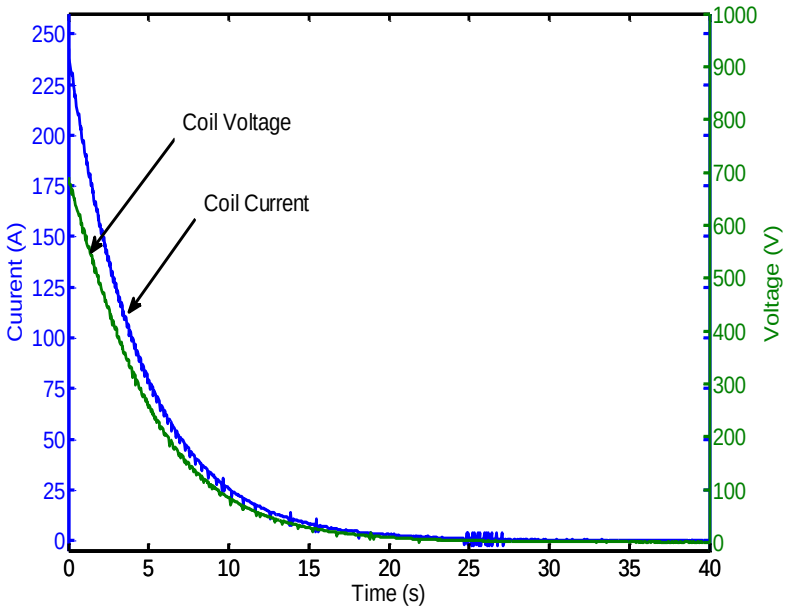

Figure 3-5 : SMES I discharge in a 2.8 Ohm resistor

The magnet temperature under operation was about 16 K, lower than the nominal value (20 K). This was due to the lower than expected operating current (250 instead of 300 A), creating lower heat dissipation in the coil.

While the tests were globally successful, two points were requiring improvements:

- The coil was not protected well enough, which caused damages on the pancake during the first quench. The detection device sensitivity has to be improved.

- The maximal power was limited to around 200 kW due to the limitation in current (250 A) and voltage (800 V). The limitation in current is due to the superconducting wires characteristics. It is intrinsic and cannot be improved without rewinding the coil. The limitation in voltage is essentially due to the current leads insulation, which may be improved significantly.

1.2 SMES II demonstrator, objectives and specifications

The DGA contract funding the SMES I project was extended to continue the studies on SMES, more specifically as pulse power source for electromagnetic launchers. The study of an upgraded demonstrator was decided along with the theoretical studies presented in the second chapter. This new version, the SMES II, re-uses the same set of 26 pancakes than the SMES I, with 2 additional pancakes wounded using the same method. The operating current is therefore the same, 300 A.

The objectives of SMES II as part of an electromagnetic launcher supply chain are the following:

- Demonstrate the possibility of rapidly and efficiently reloading the capacitors powering a segmented launcher, in order to fire several shots in a short time.
- Test the XRAM current multiplication method, which is an essential step toward direct SMES powering (cf. Chapter 2).

As for SMES I, SMES II cooling system must also be as transparent as possible for the user, thus without complex cryogenic fluid handling.

1.2.1 High Voltage operation for fast capacitor reloading

The idea consists in using the SMES as a buffer: First loaded using low power source (the electrical grid) to store energy for several shots, then used to reload the discharge capacitors quickly between the launches, taking advantage of its high power capability. To get enough energy in the capacitors, it is necessary to reach high voltage. MARX concept may be used for this purpose, the capacitors being charged by the SMES in parallel and discharged in series in the launcher.

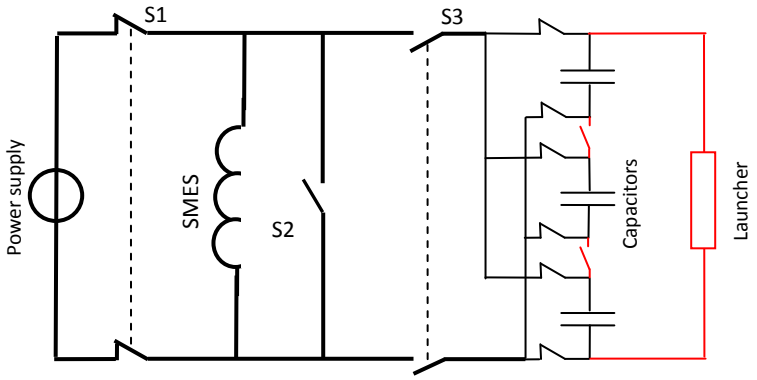

Figure 3-6: Railgun supply chain using SMES and discharge capacitors

Figure 3-6 presents a diagram of this concept. It includes a SMES coil with its charging circuit through the switch S1 and its storage short-circuit switch S2 (bold black lines), the preliminary discharge circuit between the SMES and three capacitors in parallel through S3 (thin black lines), and the capacitor series discharge circuit in the launcher (thin red lines).

The electrical insulation of the SMES II has to be reviewed to obtain an operating voltage of 4 kV, in order to charge the capacitors at a sufficient level for launcher operation.

1.2.2 Sequential discharge

Segmented launchers (cf. Chapter 2 § 1.1.2) are very promising for long-life/low losses launchers development. They consist of several launcher segments placed one after the others. The load is accelerated successively by the different segments that must be powered sequentially. This technology, developed at ISL, makes it possible to use a different set of contact brushes in each segment and therefore a better electrical contact between the load and the rails throughout the launch.

An objective of SMES II is also to demonstrate the possibility of reloading the two sets of capacitors powering a 2-segments launcher by discharging sequentially the same energy from 2 coupled coils. The 28 pancakes were thus divided in two groups, placed one on top of the other in the same cryostat (Figure 3-7). The interest when compared with powering successively the two loads with the same coil, is that the current in each coil may be adapted independently.

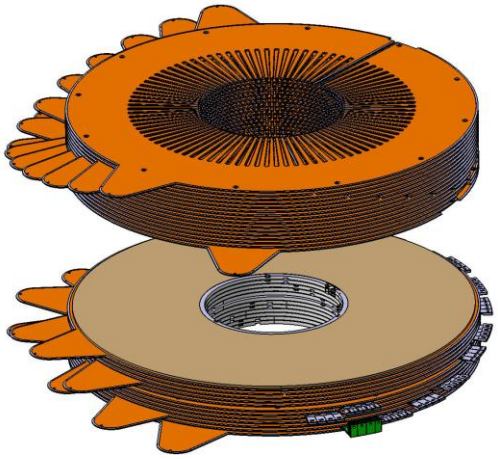

Figure 3-7 : CAD view of SMES II pancake stacks (only the copper backing of each pancake is shown)

The size of the coils, the distance between them and their rated current were optimized to get 200 kJ from each coil discharge. This optimization was realized by K. Berger, the resulting specifications are described below in §1.3.2.

1.2.3 High current output via XRAM system

As it was mentioned in Chapter 2, the most efficient way of powering a launcher is through direct SMES supply, but in this case high current output is necessary. The XRAM concept (cf. Chapter 2 § 2.1.1) may be used to increase the output current. In order to test this concept, the pancakes of the lower winding of the SMES II are not connected in series to form a single solenoid but grouped to form a 6-stage XRAM system (Figure 3-8).

The XRAM commutation system is developed at ISL [DBS09b]. Named ICCOS (Inverse Current Commutation using Semiconductor devices), it consists of thyristors and diodes, forming solid states counter-current switches. It will be presented more in details in Chapter 4 § 2.4.2.

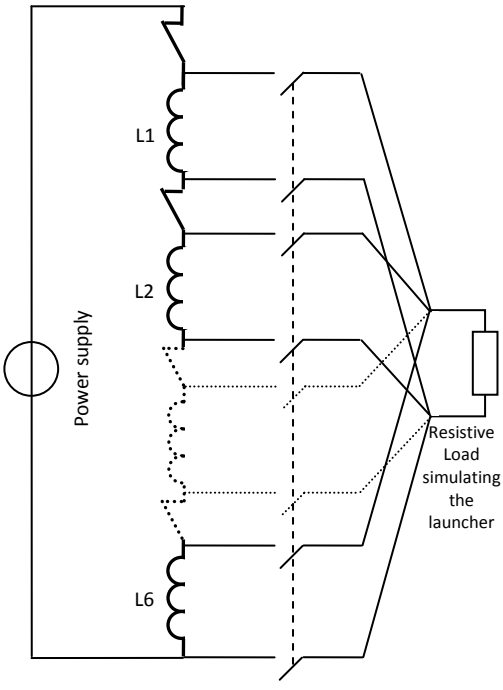

Figure 3-8: Lower coil XRAM layout

This system is implemented outside of the cryostat; this is why operation requires two current leads for each stage. Some of the current leads are however unpluggable, in order to test the feasibility of such systems for potential use in XRAM configuration with cryogenic commutation systems (cf. Chapter 2 § 2.1.4).

With a rated current of 300 A and a 6-stage XRAM multiplier, 1.8 kA could be obtained. It is still much too low to power a real launcher, but it is an interesting proof of concept for superconducting XRAM system.

1.3 SMES II magnetic and electric specifications

The SMES II electro-magnetic design is based on the characteristics of the already existing pancakes. Their arrangement is optimized to comply with the objectives presented above.

1.3.1 Coupled coils energy discharge

In order to discharge sequentially the same energy from two short circuited coils, either the coils are magnetically uncoupled, or an energy exchange is induced by the coupling during the first discharge that must be considered. In the second solution the total amount of energy per volume is higher as the energy is stored not only in the two inductances but also in the mutual.

	Energy in L_1	Energy in $M_{1\text{-}2}$	Energy in L_2
Before L_1 discharge	$E_{1init} = \frac{1}{2} L_1 I_1^2$	$E_{mutinit} = M_{1-2} I_1 I_2$ $M_{1-2} = k\sqrt{L_1 L_2}$	$E_{2init} = \frac{1}{2} L_2 I_2^2$
After L_1 discharge	$E_{1discharged} = E_{1init} \cdot (1-k^2)$ $E_{1stored} = 0$	$E_{mut\,stored} = 0$	$E_{2stored} = E_{2init} + E_{mut\,init} + E_{1init} \cdot k^2$ Currentovercharge: $\Delta I_2 = k\sqrt{L_1/L_2}\, I_1^2$

Table 3-1: Energies stored in the coils before and after the first coil discharge

As shown in Table 3-1, the only relevant parameters to adjust the energy available for the two discharges are the two coils inductances, their respective operating currents and the magnetic coupling coefficient.

1.3.2 Parametric study of the pancake arrangement

With our already existing set of 28 pancakes assembled two by two, the possibilities for the two coil inductances are limited. The seven possible combinations were investigated using finite element software Flux®, varying the distance (gap) and the operating currents to find an optimal solution satisfying the three following constraints:

- The energies available during the two discharges have to be equal; this is the original purpose of the device.

- The conductor must operate below 80% of its critical current, to ensure that the coil temperature does not drift due to excessive energy dissipation in the conductor. This condition must be guaranteed during the four phase of operation – coils charging, energy storage, first coil discharge and subsequent overcharge of the second coil, and then second coil discharge –. This is particularly critical during the lower coil overcharge if the magnetic coupling is high.

- The gap between the two coils has to be kept as small as possible to obtain the most compact system possible.

This work was led by K. Berger, the results for 2 x 200 kJ discharges are summarized in Table 3-2:

pancake number in upper | lower coils	26	2	24	4	22	6	20	8	18	10	16	12	14	14
Inductances (H)	16.0	0.14	14.0	0.53	12.1	1.16	10.3	2.00	8.57	3.00	6.98	4.18	5.51	5.51
Gap (mm)	1		24		55		103		176		313		**1000**	
Coupling coefficient (%)	64		55		46		37		26		14		2	
Initial currents (A)	207	264	203	292	205	279	212	272	223	269	242	266	269	264
Lower coil current after upper coil discharge (A)	**1695**		**865**		**588**		**449**		**365**		309		269	

Table 3-2 : Magnetic optimization results for 200 kJ discharges

The first five solutions are impossible due to the excessive current (in red) in the lower coil after the upper coil discharge. The last solution requires almost de-coupled coils, thus a very high distance (in red) between them.

In conclusion, the only practical solution is a 16 – 12 pancakes arrangement respectively charged at 242 and 266 A, with 0.31 m between the two windings (in green). After the first coil discharge the current in the lower coil reaches 309 A, which is still below the critical current as the magnetic flux density is lower in this configuration. The Flux® simulations of the magnetic flux density in the demonstrator, before and after the discharge of the upper coil are presented Figure 3-9.

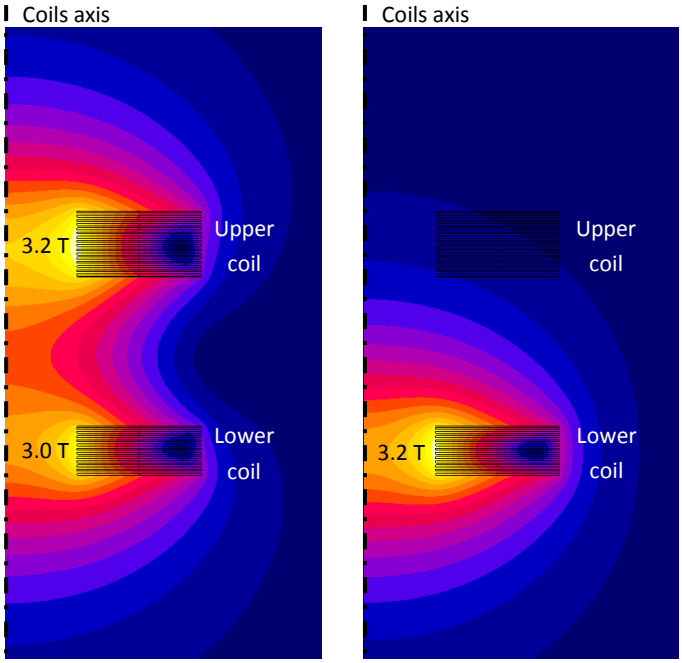

Figure 3-9 : Magnetic flux density (modulus): before (left) and after (right) the upper coil discharge

1.3.3 Pancakes positions and connections

Considering the magnetic flux density orientation, it is necessary to organize the pancakes so to have pancakes with higher superconducting sections each extremity of the two coils. The pancake organization is presented Figure 3-10.

The 2 new pancakes are wound with Nexans conductor made Sumitomo BSCCO-2223 tapes. These tapes have better characteristics at 20 K than those used for the previous pancakes. Only two tapes soldered together are enough to pass the rated current, even in the transverse field existing at the coils extremities.

Each pancake has a different number of turns, essentially due to the difference of thickness between the conductor types. The inductances of the upper and lower coils, taking into account the real number of turns, are thus slightly different from the hypothesis made during optimization. They were re-calculated to obtain the final ratings of SMES II presented Table 3-3.

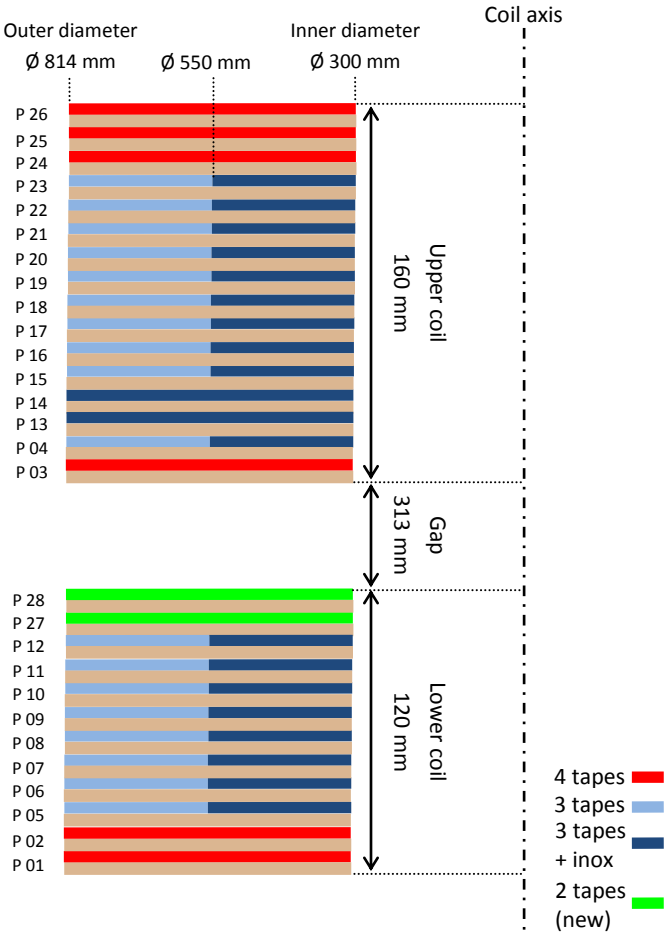

Figure 3-10: Pancakes organization in SMES II (not to scale)

	Inductance	Coupling coef.	Operating current before / after upper discharge
Upper coil	6.6 H	14 %	250 A / 0 A
Lower coil	4.3 H		261 A / 305 A

Table 3-3: SMES II final rating

The upper coil pancakes are connected in series. For the lower coil, which will also be used to test the XRAM concept, the pancakes are only connected two by two, forming six coils segments. The connections between the six segments, either in series or in parallel for XRAM discharge, will be done outside the cryostat.

1.4 SMES II thermal design overview

This section is a rapid overview of the SMES II thermal design and its issues, introducing the studies presented later (§ 2, 3 & 4). Thermal design principles for conduction-cooled SMES are first reminded. The specific problem of the current leads is introduced in a second part. In the last part, the design choices for SMES II are presented.

1.4.1 Thermal design principle for conduction-cooled SMES

In conduction-cooling systems the cooling power is available on a cold plate, in our case the cold head of cryocoolers. It is therefore localized and limited when compared to classical bath cooling. Thermal plates must be designed to bring this cooling power to the cold mass, consisting of the coils and current leads. Special attention must be paid to the heat losses localization (distributed or localized) for the design of the cooling plates, in order to guarantee a suitable temperature uniformity and stability. The heat incomes on the cold mass of a cryogenic device are divided in two groups: heat produced inside the cold mass, such as losses by Joule effect, and heat from the outside, by conduction or radiation. All these heat incomes have the same effect on the cryogenic system: they tend to increase its temperature. In consequence, they will be considered systematically as "losses" later on (conduction losses, radiative losses, etc.).

Heat incomes from the outside:

The cryostat of a conduction-cooled device is basically a vacuum chamber. The vacuum quality (around 10^{-6} mbar) keeps the losses by conduction and convection in the remaining gas negligible. The only losses left to consider are therefore:

- The radiative losses between the cryostat and cold mass surfaces, which are distributed on all the cold mass surface and may be reduced by proper shielding.
- The losses by conduction, in the mechanical structure and through the current leads, which are localized. The mechanical structure losses can be reduced by proper design and material choice, they are generally low. On the contrary, current leads losses are important and cannot be reduced below a certain point. Current leads design issues will be detailed in the next paragraph.

Heat generated in the cold mass

Heat is generated in the cold mass only when the SMES is under operation. It includes dissipation in the superconducting wires, distributed in the whole superconducting volume, and Joule effect in the resistive elements and connections that are localized. The heat generated during pulse discharge may be ignored for the cooling system design as it is a transient phenomenon.

1.4.2 Current leads losses reduction

Resistive leads issues

Normal current leads induce heat losses by conduction from the outside and at the same time generate heat by Joule effect under operation. Thermal and electrical conductivities being correlated, the objectives of reducing the conduction losses and reducing the dissipated heat are contradictory. For example, reducing the conduction losses requires increasing the equivalent thermal resistance, which will result in an increased heat generation by joule effect under operation.

An optimum exists for this trade-off, depending of the material that is used. It is generally in the order of 40 W/kA for a conduction-cooled system. The detailed description of the problem and its solution will be presented in § 3.1.1.

Superconducting lead: use and limitations

Superconducting material does not have the same constraints, as their thermal and electrical conductivity are not correlated. The heat dissipation due to the circulating current being null, the only losses are due to thermal conduction, which may be reduced through an adapted geometry (especially by increasing the length). However, the leads material must remain superconducting to operate, which cannot be achieved when the temperature gets close to the critical temperature.

In consequence, current leads are usually made in two parts: The first part is resistive, down to an intermediary thermalization, and only the second part is superconductive. The temperature of the intermediate thermalization determines the maximal temperature of the superconducting part, thus its critical current, which in turns determines the minimal cross section of the superconducting lead necessary for the rated current. For a given length, this section determines the thermal losses induced by the superconducting leads on the coil. If the length is not imposed, knowing the cross section makes it possible it calculate the required length to obtain the desired losses on the coil.

With this method, most of the heat losses created by the current leads are absorbed at the intermediary thermalization, which is especially suitable for cryocooler-cooled devices, as the cooling power of cryocoolers is higher when their operating temperature increases.

1.4.3 SMES II thermal design choices

For the SMES I demonstrator, two AL 330 cryocoolers were used: one was cooling the magnet (20 K) and the other was cooling both the current leads and the active thermal shield reducing the radiative losses on the coils, to an intermediate temperature low enough for superconducting leads operation, around 40 K. As SMES II re-uses the pancakes of SMES I and some of its other elements, the cooling concept of the two demonstrators is very similar. The main additional constraints are:

- Higher number of current leads, 2 for the upper coil and 12 for the XRAM concept implementation on the lower coil, instead of two for SMES I
- Limited room around the coils to place the cooling system and current leads. The SMES I cryostat bottom and upper flange being re-used, the diameter cannot be extended.
- Imposed number of cryocooler, 3 in total instead of 2 for SMES I, due to the high cost of such devices.

In SMES II, the distance between the two windings (0.3 m) makes their cooling difficult to realize with only one cryocooler. It is then decided to cool each coil with its own cryocooler, the one cooling the upper coil mounted on the upper flange and the one cooling the lower coil mounted upside down on the lower flange (Figure 3-11).

For each coil the cooling power supplied by the cryocooler is distributed following the method successfully tested on SMES I and already presented in § 1.1.1.

The cryocooler cold head is mounted on a croissant-shaped (in red Figure 3-11) copper piece, the pancakes being connected to it by flexible copper elements.

As a consequence of this design, there is one cryocooler left to ensure the current leads intermediate thermalization cooling, as in the previous version, but their number has been multiplied by 7. An adapted design must be found to ensure the current leads cooling at a temperature low enough to allow superconducting leads use. This is the main issue of SMES II thermal design.

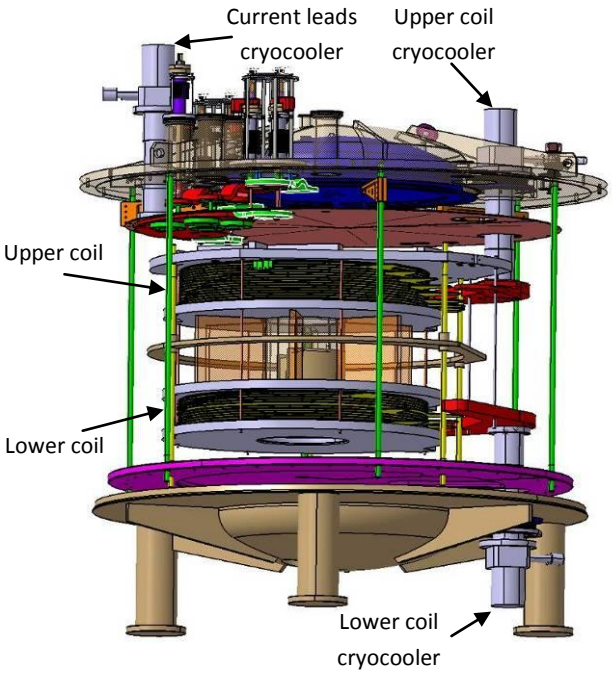

Figure 3-11: SMES II CAD view

2. High Tc Superconducting current leads design

The objective of the superconducting lead design is to obtain the highest possible operation temperature, in order to have the highest possible cooling power at the intermediate thermalization. However the losses on the coil must stay reasonable, which limits the superconducting leads cross section. The “reasonable” hypothesis chosen for the thermal losses brought by the current leads on the coil is the value calculated for SMES I current leads, around 20 mW. The upper end thermalization temperature was fixed at 40 K in SMES I, which was very conservative. The objective for SMES II is if possible to work at higher temperature.

For the upper coil, the closest from the cryostat upper flange, the current leads are as short as for SMES I, about 0.2 m. We re-use the Nexans® bulk BSCCO leads implemented in the previous version. Their operation is possible at least up to 60 K. The lower coil consists of six stacked coil elements. Twelve leads have to be designed to connect it, with much longer lengths as their output is also on the cryostat upper flange (from 0.57 to 0.66 m).

2.1 Lower coil superconducting leads design choices

2.1.1 Distribution around the coil

For the lower coil we decided to build our own leads because of the implementation specificities in our system, with not much room available to insert them. The lower coil pancakes are arranged as presented above in § 1.3.3, and connected two by two. These connections, on the inner diameter are constraining the pancakes angular orientation. This orientation was chosen to minimize the superposition of current leads connections
(on the outer diameter). Only the 1st and 5th pancakes connections are superposed, as shown Figure 3-12.

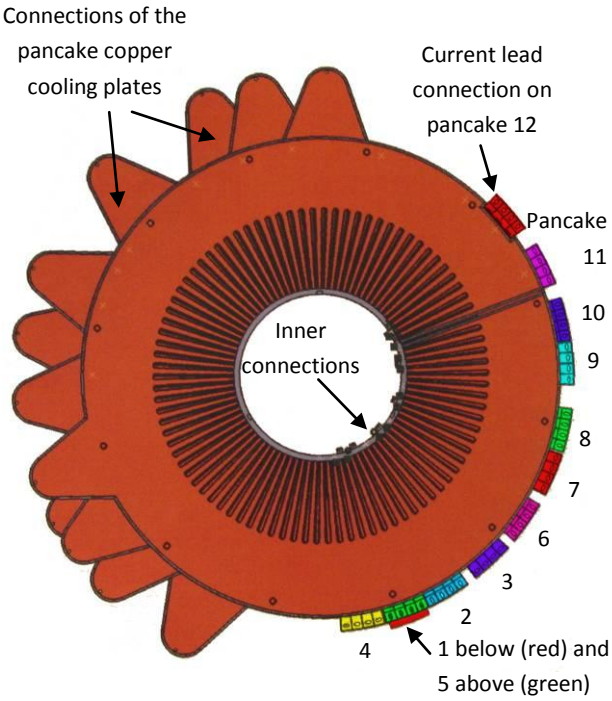

Figure 3-12 : Lower coil pancake stack view (from above) with current leads connections

2.1.2 Superconducting material and leads connections

Bulk superconductor is not suitable in this case because it is brittle and potentially vulnerable to thermal expansion effects over long lengths. We used AMSC® PIT BSCCO tapes with a Gold/Silver alloy matrix. This kind of tapes is specifically designed for current leads, with much lower thermal conductivity when compared to pure silver matrix tapes (only 25 W/K/m at 25 K). Its critical current against magnetic field is presented Figure 3-13.

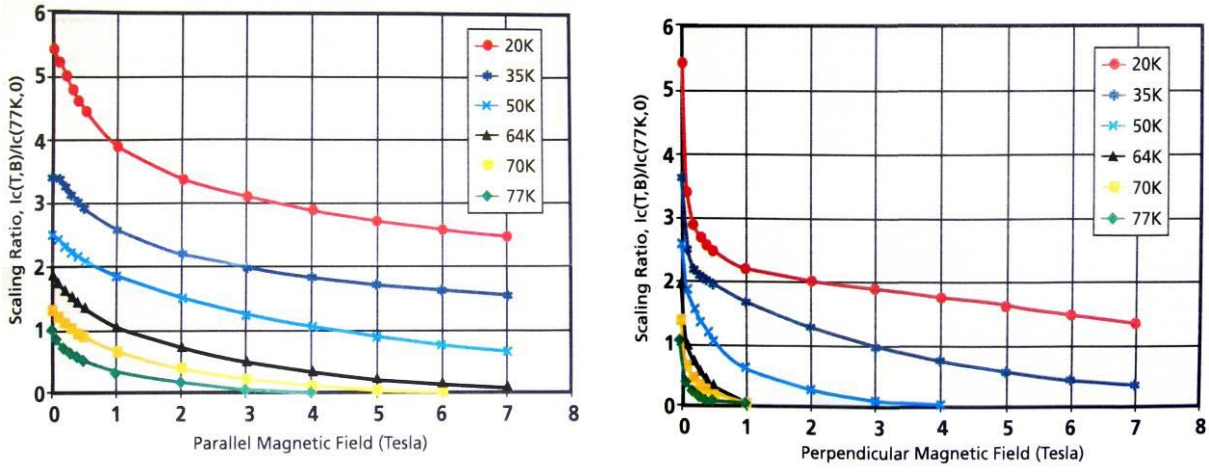

Figure 3-13: Critical current of the AMSC current leads tapes ($Ic_{77\,K}$=100 A)

To support the stress induced by Lorenz forces and thermal contractions, the tapes are housed in a grooved fiber glass rod presenting a low thermal conductivity. The tapes are soldered together at each extremity with custom-made copper connectors.
The design of the lower end connector includes a thermalization surface in order to evacuate the heat losses directly through the coils cooling system, without heating the winding itself (Figure 3-14). The exact area of this contact surface is optimized in the coils cooling system design (cf. § 4.3.3).

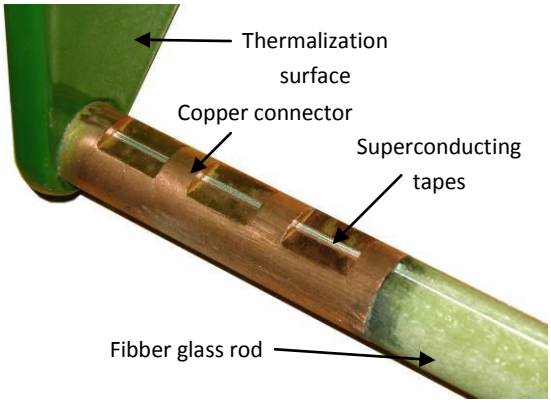

Figure 3-14: Lower end of a superconducting current lead with its connectors

2.2 Superconducting tapes implementation

2.2.1 Orientation in the coils field

The lower coil current leads are placed along the coil stack. They are therefore in the field of the lower coil itself close to their lower end and in the upper coil field close to their upper end. This is a major issue as the critical current of the superconductor is reduced when temperature increases and also when magnetic flux density increases. Moreover, as it was already mentioned in the SMES II specification presentation (cf. § 1.2.2), in sequential discharge operation the lower coil is overcharged up to 345 A after the upper coil discharge. The design of these leads must then be adapted to this higher operating current.

If the tapes (in red Figure 3-15) are oriented following the radial direction of the coils (in blue), the two components of the coil magnetic flux density (axial and radial) are both in the longitudinal or axial directions for the tapes. The only transverse field left to consider is the resultant of the tapes self-fields.

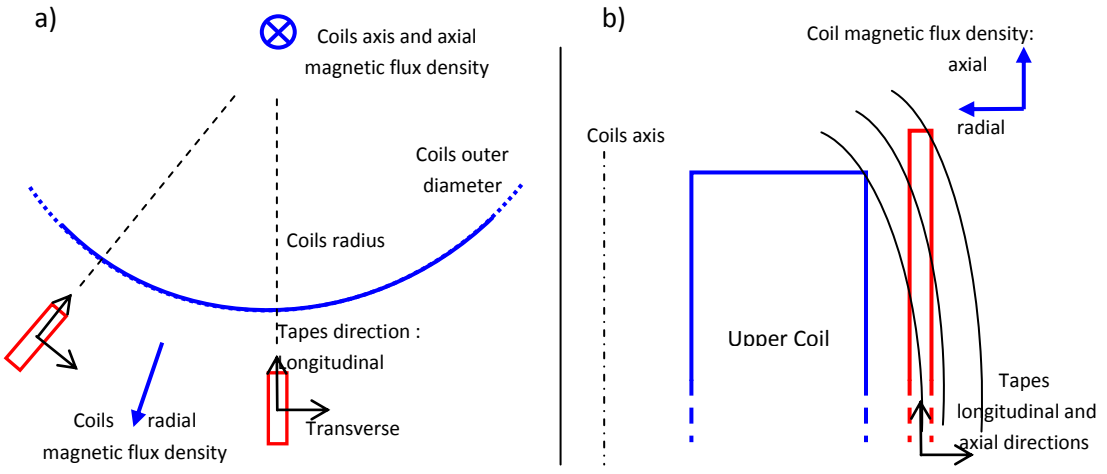

Figure 3-15: Current leads tapes orientation a) coil axis view b) coil radial view

2.2.2 Tapes magnetic and thermal operating conditions

Once the position of the superconducting leads in the cryostat is fixed, their magnetic operating conditions can be estimated, through finite element simulations. Thermal simulations are also conducted in order to help determining the worst operation conditions with regards to the tapes characteristics.

Magnetic operation conditions

As it was mentioned in the previous paragraph, the field created by the coils is longitudinal (or axial) for the current leads tapes. Numerical simulations using Flux® where conducted in order to evaluate the magnetic flux density along the current leads path (Figure 3-16).

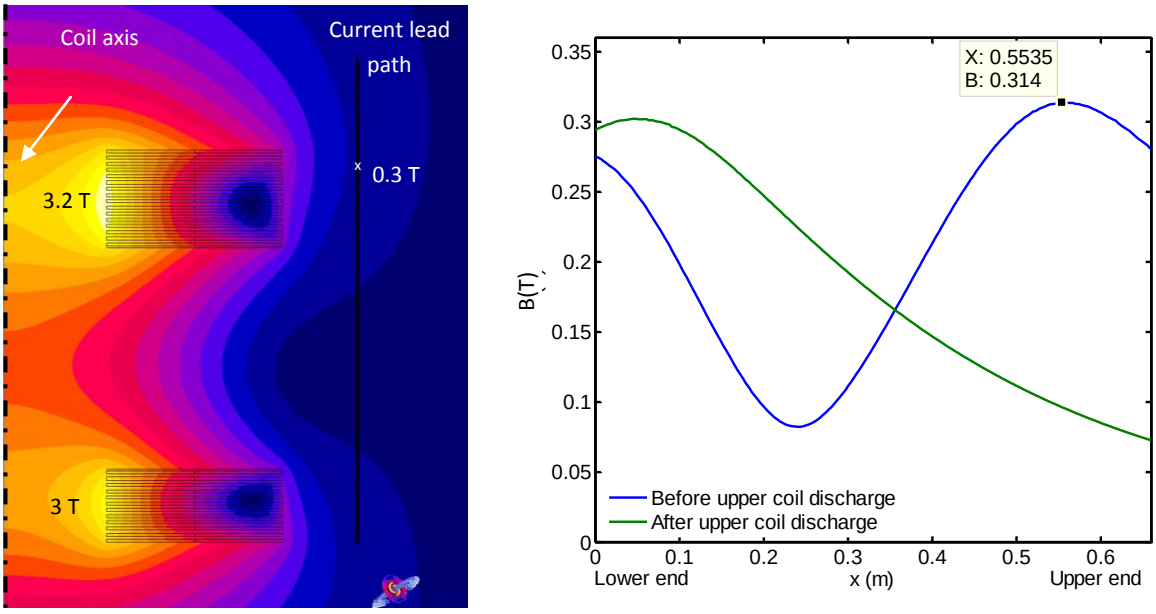

Figure 3-16: Map of the magnetic flux density before upper coil discharge (left) and Magnetic flux density along the leads path before and after the first coil discharge (right)

As mentioned above, the only transverse field to which the current lead tapes are subjected is created by the tapes themselves (Figure 3-17). It is constant along the lead length, which means that the worst condition is found at the hottest temperature, at the top of the leads. At 305 A, the maximum value reached by the lower coil current after the upper coil discharge, it reaches 45 mT.

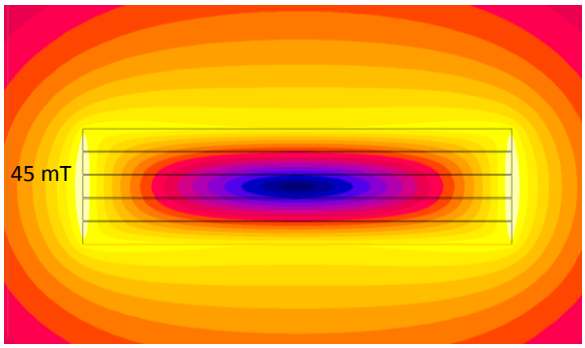

Figure 3-17: Self transverse field on the superconducting leads

Temperature profile along the leads length

The leads temperature profile is not linear, due to the variation of the tapes thermal conductivity with the temperature. Simulations were conducted for different upper end temperatures to help determining the number of tapes to be used, using a Matlab® code (Figure 3-18). The model only takes into account the thermal conduction, radiation effect being negligible as the elements surrounding the leads are roughly at the same temperature.

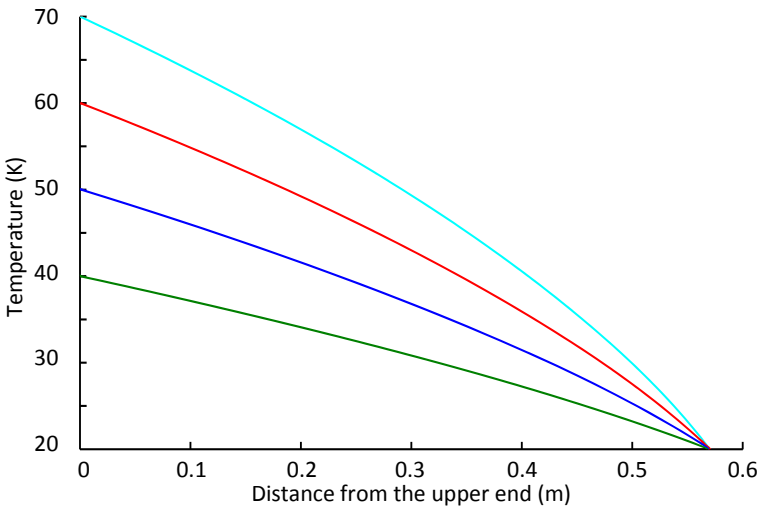

Figure 3-18: Temperature profiles along the shorter current lead length for 4 upper end temperatures

2.2.3 Temperature / tapes number trade-off

Knowing the magnetic flux density conditions and the different possible temperature profiles, the tape number and upper end temperature are determined in order to limit the losses on the coils, to a value of 20 mW for each current lead.

A Matlab® code was also developed to simulate the thermal losses induced by the leads on the coil, depending on the number of tapes used and the hot end temperature (Table 3-4). The results are given in the worst case, corresponding to the shortest length (0.57 m).

Tapes / Temperature	3	4	5	6
40 K	5	6.4	7.8	9.1
50 K	8.4	10.7	13	15.3
60 K	12.4	15.8	19.2	22.57
70 K	17.1	21.8	26.5	31.3

Table 3-4: Thermal losses induced by one current lead (mW)

In grey are the impossibilities due to the tape critical current limit. This limit was chosen at 0.7 I_c in order to guarantee negligible heat dissipation in the superconductor. The configurations producing more losses than the criterion are in red. In green are the possible configurations.

In accordance with the objectives presented at the beginning of this section, the configuration offering the highest operating temperature for the current leads thermalization while producing acceptable heat losses is chosen. The superconducting leads therefore contain 5 tapes each, and the thermalization maximal temperature is fixed at 60 K.

3. Resistive current leads and associated thermalization system

For the upper part of the current leads operating between 300 K (room temperature) and the intermediate thermalization system, resistive conductor must be used. To conduct the design, the temperature expected on the lower end of these current leads will be fixed at 50 K in order to have a substantial (10 K) safety margin on the superconducting leads operation. This high margin is necessary for two main reasons:

- The cooling power against temperature profile of the cryocooler, which is a critical parameter to determine the operation temperature, is not exactly known. A lot of parameters may affect it, particularly the helium input and output pressures of the compressors. The actual behavior of the cryocooler may thus differ significantly from the calibration chart provided by the constructor.

- The equivalent thermal conductivity of the thermalization interface is a critical parameter of the design, as it will be detailed in §3.2.1. Even if it can be measured precisely on a given sample (cf. Chapter 4 § 1.3.2), when realizing several interfaces the realization process will induce a consequent spread of the characteristics. This spread is difficult to quantify without realizing and testing a large number of samples, which is not practically possible. Pessimistic hypothesis must therefore be adopted to guarantee the system operation.

The current leads optimization principles and the code developed for this task is presented first. In a second time the results of this optimization and the technical solutions chosen for the current leads integration are described.

3.1 Current leads and thermalization system simulation tool

3.1.1 Optimization principles

The purpose of the current leads optimization is to obtain a minimal heat income on the lower end while ensuring that the temperature of this lower end remains stable under the rated current (cf. § 1.4.2). In this case the heat flux on the hot end is zero under the rated current; meaning that the heat generated by Joule effect exactly compensate the thermal losses. Writing the thermal equilibrium makes it possible to derive the minimal cooling power required on the cold end and the leads aspect ratio respectively through Eq. (3-1) & (3-2), under the hypothesis that the only thermal losses are by conduction on the extremities.

$$Q_0^* = I \times \sqrt{2 \cdot \int_{T_0}^{T_1} \lambda(q) \cdot \rho(q) \cdot dq} \qquad \textbf{(3-1)}$$

$$L/S^* \cdot I = \int_{T_0}^{T_1} \frac{\lambda(T)}{\sqrt{2 \cdot \int_{T_0}^{T} \lambda(q) \cdot \rho(q) \cdot dq}} \cdot dT \qquad \textbf{(3-2)}$$

With λ the thermal conductivity and ρ the electrical resistivity of the current lead material, T_0 the temperature of the cold end and T_1 on the hot end, Q_0 the minimal thermal flux on the cold end, I the rated current and L/S the optimized form factor of the current lead.

If the temperatures on both ends are not yet known, the equations cannot be solved directly. A numerical iterative method may be used.

3.1.2 Simulation tool

A simulation code has been developed using Matlab® to realize the current leads optimization.

Current lead and thermalization model

Due to the heat flux in the thermalization interfaces and cooling plates, the temperature on the lower end of a current lead is not that of its cooling source. The simulation model must therefore consider the different electrical and thermal interfaces, the cooling plates, as well as the cooling power against temperature characteristic of the cold source. A schematic view of the model implemented in our simulation code is presented Figure 3-19.

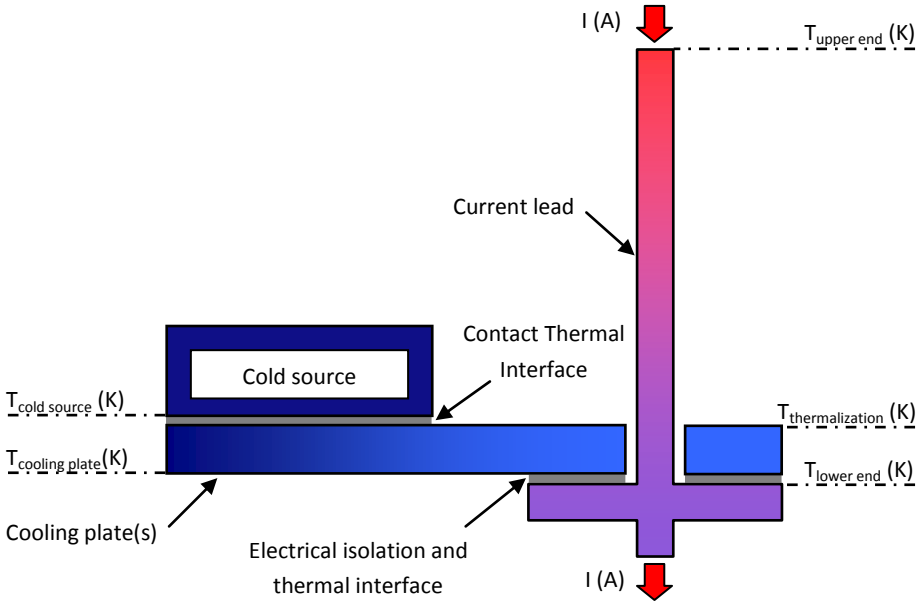

Figure 3-19: Current lead and thermalization model

Solving process

From temperature on the upper end temperature and the operating current, the code calculates the temperature and heat flux on the lower end using an iterative method. In the first step the lower end temperature is calculated as if there was no heat flux, meaning that the thermalizations and cold source are supposed perfect. For example if the cold source is a cryocooler, the initial temperature chosen is its no-load temperature. If the cold source is a liquid nitrogen tank, it will be considered at 77 K.

The optimization equations are then solved, and the obtained heat flux is used to calculate the actual temperature of the cold source, taking into account its response to the heat load. The temperature drops in the various cold plate and thermalizations interfaces are also calculated with this heat flux value.

In the next step the new value for the lower end temperature is calculated, which is then used to re-calculate the optimized heat flux. The process is repeated until the variation of the obtained thermal flux between two steps is lower than a given criterion (Figure 3-20). The convergence is very fast, less than ten iterations are usually enough to reach a 0.05 W criterion.

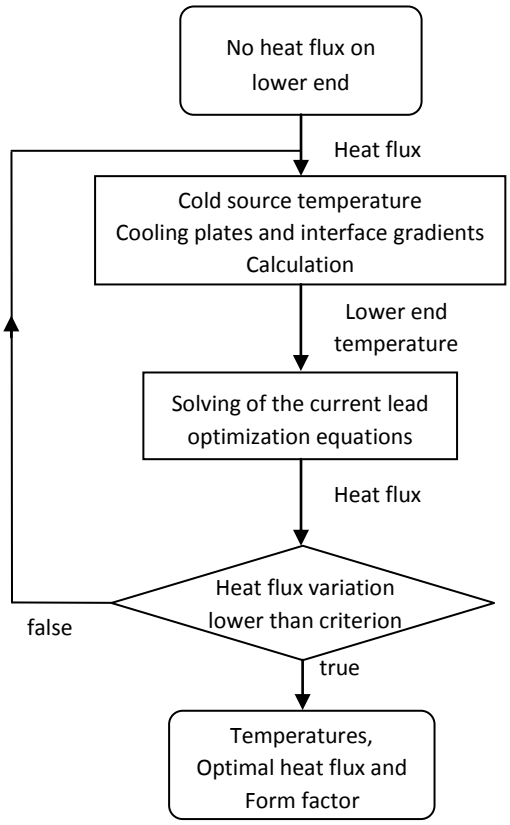

Figure 3-20: Solving process

3.2 Current leads optimization

3.2.1 Thermalization interfaces for SMES II

The temperature gradient existing in thermalization interfaces imposes to the cold source -the cryocooler cold head in our case- a much lower temperature than the current lead lower end temperature. The cryocooler cooling power is therefore consequently reduced.

An interface with high thermal conductivity would reduce this gradient and therefore the loss of cooling power. This interface must however isolate electrically the lead, which may reach high voltages during operation, from the cold plates which are grounded. This is especially true for pulse power operation devices such as SMES II which operates up to 5 kV.

These two constraints, a good thermal conductivity and a high breakdown voltage, are contradictory as good electrical insulators are usually poor thermal conductors. The notable exceptions to this rule are materials being electrical insulators while having a crystalline structure, such as diamond and sapphire. Their use is however impossible in conduction-cooled devices as they are brittle and does not resist to the vibrations induced by cryocooler operation.

In SMES I, the current leads contact surfaces were coated with epoxy, and Redux (an epoxy film with low curing temperature) was used to glue the surfaces together with the cold plates, using the same method than for the pancakes backing (cf. § 1.1.1). This interface is suitable for operation up to 5 kV but its thermal surface conductivity is quite low, around 100 $W.K^{-1}.m^{-2}$ at 20 K and 200 at 77 K.

A better interface was considered for SMES II as a way of gaining cooling power by reducing the temperature gradients in thermalizations. This was expected to make possible the cooling of a higher number of leads with the same cryocooler.

The most satisfying result of the experiments conducted in this perspective (cf. Chapter 4) was to replace the Redux® film by a thin layer of Eccobond®. The interface conductivity around 77 K is two times higher.

3.2.2 Simulation results

Single stage current leads

The first estimations given by the optimization tool showed that even using the new thermalization interface, it was impossible for a single cryocooler to cool the top of the current leads lower than 105 K, taking into account the restrictions imposed on the design in terms of available space in the cryostat for thermalizations (Table 3-5).

Cooling source	Cryocooler (Al330)
Material	brass
Upper end temperature	300 K
Lower end temperature	105 K
Aspect ratio (L/S)	2500
Heat flux under operation (for each lead)	15 W
Heat flux without current	8 W
Temperature gradient in isolation layer	12 K
Temperature gradient in cooling plates	4 K
Temperature of the cooling source	95 K

Table 3-5 : Optimization results for single stage current leads

To solve this problem, we studied the possibility of implementing multi stage thermalizations for the current leads.

Double stage current leads

As the optimum for a simple current lead having one thermalization is to have no heat flux on the hot end, the optimum for a current lead having more thermalizations is obtained by considering as many current leads segments as there are thermalizations, and to optimize them one after the other.

The simulation tool already presented may be used for multi stage current leads following this idea: The first segment calculated is the hottest one, whose temperature on the upper end is known (room temperature). This first optimization gives the temperature of the second segment upper end which is then optimized, and so on until the last segment.

Simulations show that a two stage system is sufficient to meet the specifications. The first stage is cooled by conduction from a liquid nitrogen tank; the second stage is cooled by the cryocooler. With this system, the temperature of the superconducting leads is below 50 K. The simulation results are summarized Table 3-6.

Optimization results for current leads and thermalization		
Cooling	Liquid Nitrogen	Cryocooler
Material	brass	brass
Upper end temperature	300 K	93 K
Lower end temperature	93 K	42 K
Aspect ratio (L/S)	2466	1092
Heat flux under operation (for each lead)	14.6 W	4.8 W
Heat flux without current	7.7 W	2.5 W
Temperature gradient in isolation layer	10 K	10 K
Temperature gradient in cooling plates	2 K	2 K
Temperature of the cooling source	80 K (LN2 tank cold plate)	32 K

Table 3-6 : Current lead optimization results

If using the same thermalization interface than for SMES I, the lower end temperature goes up to 66 K, the use of the new thermalization interface is therefore necessary. It gives a comfortable margin of almost 20 K when compared to the maximal temperature acceptable for the superconducting leads. The resulting total current leads system is represented Figure 3-21.

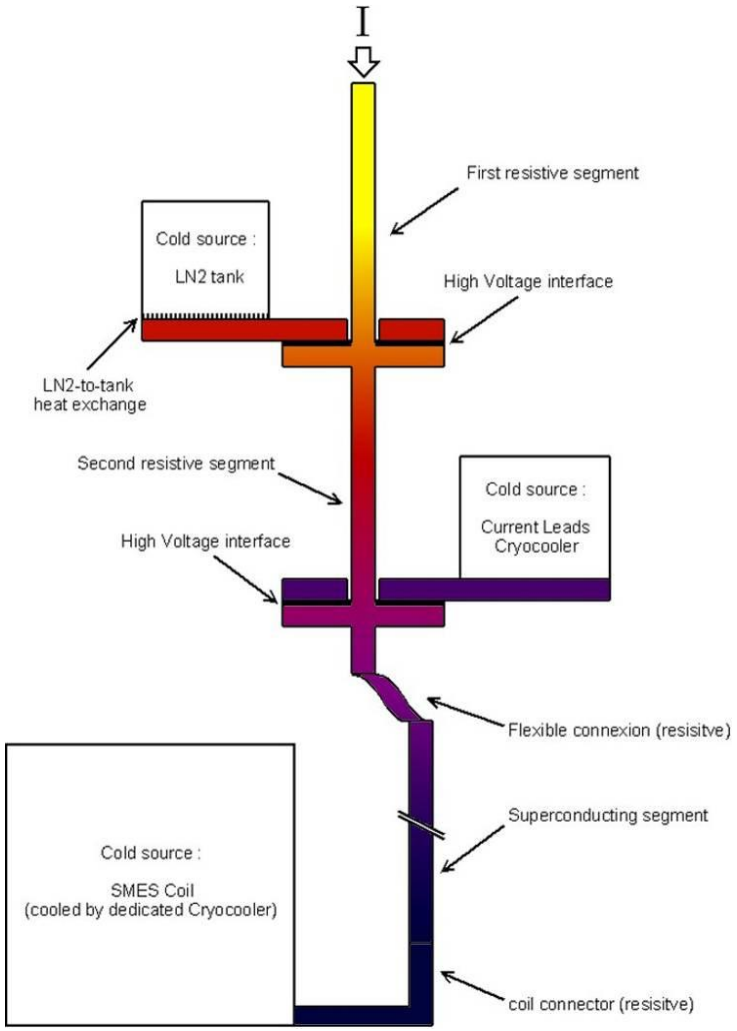

Figure 3-21 : Schematic view of a complete current lead, with two-stage thermalization of the resistive segment (thermal gradient is only indicative).

3.2.3 Optimized current leads Implementation

There are two major issues for designing a current lead thermalization system following the results of this optimization and fitting it in the existing cryostat: The high number of current leads thermalizations to be juxtaposed, and the integration of the intermediate nitrogen thermalization stage.

Current leads integrations

Due to the shape of the existing cryostat flange, only 8 out of 14 leads may have their dedicated connection on the upper flange. For the last six of them, the only practical solution is to re-use existing holes in the cryostat and to group them three by three. This set up reduces their thermalization surfaces but this was considered during the optimization process. It was decided to integrate an additional functionality to these two groups of 3 leads. They are “unpluggable” at the LN2 thermalization level. This is not necessary for our system but it is a proof of concept for potential XRAM applications with cryogenic commutation (cf. §1.2.3).

Intermediate nitrogen cooling

For the LN2 tank integration, the preferred solution is to fit the tank in the back of the upper dished head of the cryostat upper flange. The room in this part of the cryostat is large enough to integrate a 65 liter tank, which should allow about 24 hours of cooling power (following the optimization results for heat generation at the LN2 thermalization).

However with this architecture, the tank is not exactly close to the current leads, which means that cold plates must be designed to bring the cooling power to the current leads intermediate thermalizations.

The CAD view of the total cooling system is presented Figure 3-22. It summarizes the different design choices.

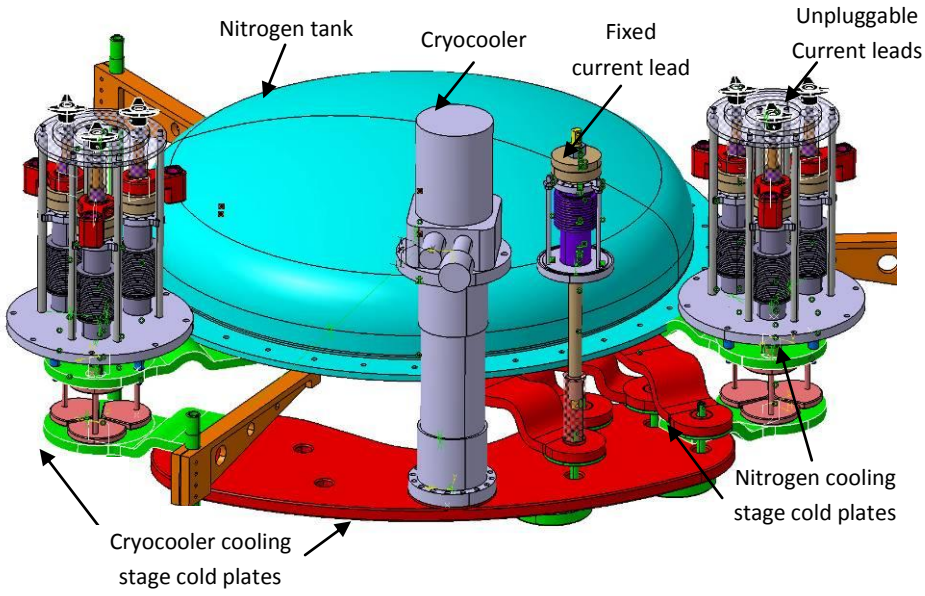

Figure 3-22 : Current leads thermalization system (cryostat upper flange removed)

Some of the elements are not visible on the figure, in order to simplify the comprehension. The 2 groups of three unpluggable leads are completely represented, but the 8 fixed current leads symmetrically placed on the red cryocooler cooling plate are not.

Only one upper segment (from 300 K to nitrogen cooling) is visible, but the others are similar. Concerning the intermediate segments (between nitrogen cooling and cryocooler) 4 are shown with their thermalization plates, on the right side of the cryocooler. The left side is of course identical.

Temperature gradients in the cooling plates

The equivalent thermal conductivities of the different thermalization cold plates presented above are calculated using Flux®, the results being integrated in the simulation tool. The results of these simulations for the cryocooler cooling plates are presented Figure 3-23.

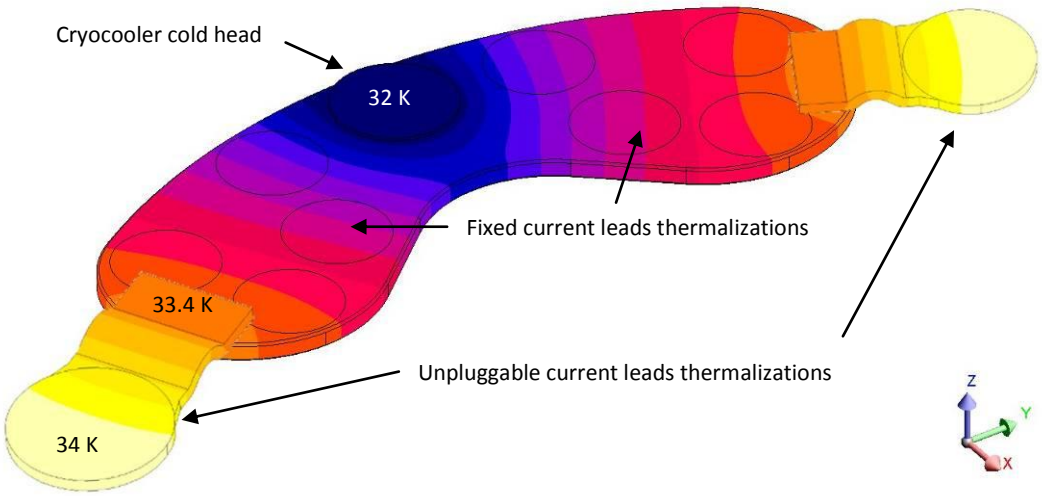

Figure 3-23: Temperature gradients in current leads cryocooler cold plates

4. Coils cooling system

Once the critical influence of the current leads on the thermal design is quantified, the design of the coils cooling system is possible. As it was already mentioned in § 1.4.1 apart from the leads-induced losses, the thermal losses due to radiation and conduction in the mechanical structures must be considered, as well as the heat generated in the coil under operation.

In this part the active thermal screen design is presented first. The evaluation of the losses on the coils is described in a second time. Finally, the cooling chain design based on the losses evaluation is presented.

4.1 Active thermal screen

The radiative losses on the coils are limited by an active copper thermal screen, cooled by the current lead cryocooler. In this section the active thermal screen is designed to ensure that the thermal screen temperature is below 50 K, for the losses on the coil to be reduced as much as possible. The losses on the screen are first evaluated, considering a uniform temperature at 50 K. The screen thickness is then estimated to obtain a maximal gradient of 10 K between the cold source at 40 K and the thermal screen hot spot. As we have seen in § 3, this value is very conservative, as the cryocooler operating temperature should be below 40 K.

4.1.1 Thermal losses by radiation

Multi-layer passive thermal screening, the so called Superisolation, is used between the cryostat surface and the thermal screen to reduce the radiative losses. It consists in thin aluminum-coated films separated by synthetic meshes.

As the thermal losses obtained using Superisolation are partly due to radiation and partly to conduction between the layers, its effect is best described by an equivalent conduction.

Following the classically admitted optimum of 20 layers per cm of available space [AP88], 80 layers will be used, for an equivalent surface conductivity of about 5 mW/m²/K between 300 and 50 K.

The total losses on the active screen are obtained by the classical equations of thermal conductivity, in our case they are about 10 W. This value was actually considered in the current leads optimization tool to define the cryocooler working point. We did not mention it at the time to simplify its description.

4.1.2 Thermal losses by conduction in the structure

A schematic view of the mechanical structure supporting the coils is displayed in § 4.2 on Figure 3-24. The thermal screen is hanging from the upper flange of the cryostat using six G10 fiber glass tubes (inner diameter 13 mm, outer diameter 21 mm and length 0.97 m), representing an equivalent cross-section of 1.28 10^{-3} m².

As the thermal conductivity of this material changes with the temperature, the total thermal conduction losses caused by these tubes are defined by Eq. (3-3):

$$Q_{conduction} = \int_{50}^{300} \lambda(T) dT \cdot \frac{S_{equivalent}}{l_{tubes}} \qquad \textbf{(3-3)}$$

Where $\lambda(T)$ is the thermal conductivity of the material at the temperature T and $S_{equivalent}$ is the total cross-section presented above. They are very low, about 200 mW in our case.

4.1.3 Temperature homogeneity

The thermal shield bottom must sustain the weight of the coils; its material and thickness are thus imposed: it is a 30 mm thick plate of aluminum-alloy. The walls and the top of the shield are made of copper plates, whose thickness has to be defined.

Numerical simulations using software Flux® were conducted to evaluate the temperature gradient on the entire shield. An 8 K total gradient may be obtained using 3 mm-thick CuC1 copper plates for the shield wall, which satisfies the constraints introduced above at the beginning of § 4.1.

4.2 Thermal losses on the coils

The coils thermal losses due to conduction and radiation may be evaluated following the same method used for the thermal screen. The losses under operation will be presented separately.

4.2.1 Thermal losses by radiation

The thermal screen at 60 K radiates on the coil which is at 16 K. Once again, Superisolation is used to reduce this thermal loss. It is placed between the active screen and the coils. At this range of temperature, the equivalent surface conductivity of Superisolation is lower, about 2.5 mW/m²/K in our case (40 layers in 20 mm). The total radiative losses are then expected to be around 1 W, the percentage going to each coil being calculated using their surface ratio.

4.2.2 Thermal losses by conduction

The coils are supported from the bottom of the thermal shield (Figure 3-24) by 4 G10 fiber glass tubes similar to those hanging the shield to cryostat upper flange but shorter, 0.72 m. They represent an equivalent section of 8.5 10^{-4} m².

The thermal conduction losses caused by these tubes are only 10 mW. These losses mainly go to the upper coil, as shown Figure 3-24.

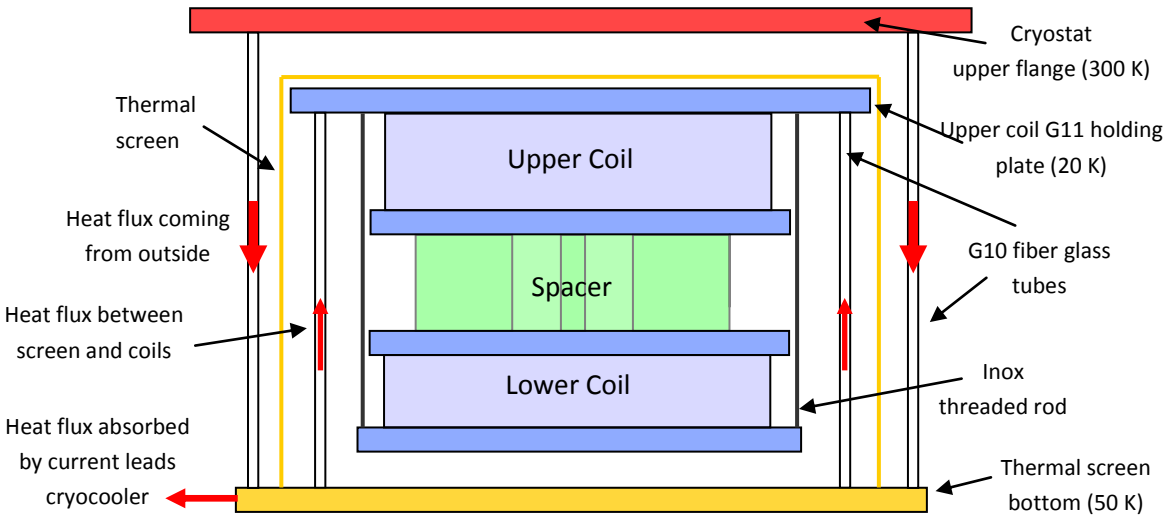

Figure 3-24 : Schematic view of the mechanical structure supporting the coils

The superconducting leads which are not mentioned Figure 3-24 have also to be considered. They were calculated in § 2 around 20 mW each. It represents 40 mW for the upper coil, and 240 mW for the lower coil, due to its 6 current lead pairs.

4.2.3 Heat generated under operation

Two operation phases must be distinguished: current charge and storage which are continuous or quasi-continuous, and discharge which is a transient state. Transient losses are not relevant for the magnet cooling design, as the magnet thermal inertia is high enough to guarantee the temperature stability during discharges.

Heat is dissipated during continuous operation in the resistive connections (Figure 3-25) but also in the superconductor when it is operating close to its critical current.

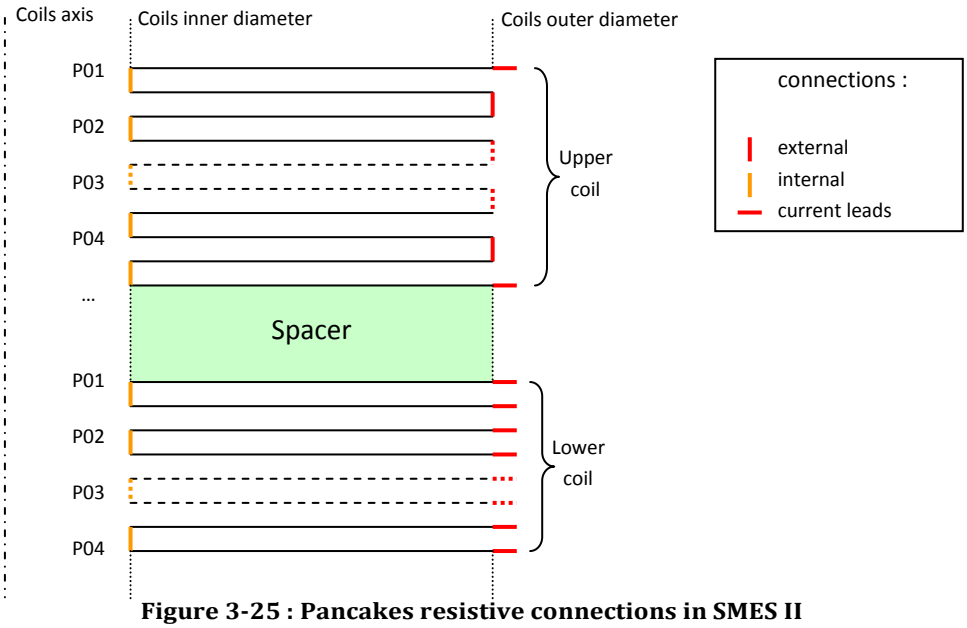

Figure 3-25 : Pancakes resistive connections in SMES II

Resistive connections

The resistance of the pancakes internal and external connections was investigated during SMES I design. They have similar values, about 0.3 µΩ. In consequence, each of them dissipates 20 mW under 250 A.

In our case, there are 15 connections on the upper coils (16 pancakes) and 6 connections on the lower coil (12 pancakes). The heat generated are therefore respectively 340 mW and 120 mW.

Moreover, there are 12 current leads connections on the lower coil, which were measured at 1.3 µΩ. This resistance includes the soldered contact between pancake and current lead copper connector, the resistance of the copper connector itself and the contact resistance between the copper connector and the current leads tapes. The total heat generated by these connections is 960 mW.

As we will see in Chapter 4 § 1.4, superconducting straps are soldered on the copper connector to reduce its equivalent resistance, which was not considered in this evaluation. The real value should thus be slightly lower.

Dissipation in superconductor

The effect of dissipation in the superconductor is difficult to evaluate. The SMES I design was made under hypothesis that the conductor was homogenously close from its critical current, at 0.8 Ic. It is pessimistic as only part of the conductor is submitted to the maximum magnetic flux density. Under this conservative hypothesis the heat produced is about 0.5 W in each pancakes, therefore the total heat loads induced on the two cryocoolers are respectively 7.8 W and 5.8 W.

In fact when testing the SMES I, it was observed that continuous operation at this level of dissipation is practically impossible, the protection system (cf. Chapter 4 § 2.1) will activate the discharge even before any temperature elevation may be observed due to dissipation run out. The design was done anyway using this hypothesis, in order to have large temperature margins for safe operation.

4.2.4 Summary

The results obtained for coils cooling design are synthesized in Table 3-7, along with the results previously obtained for current leads and thermal shield cooling. As it was already said in introduction to the resistive leads design § 3, the cooling power against temperature profile of the cryocooler is not known very precisely. Especially at low power the potential variation of temperature due to the cryocooler operation conditions is high, the temperature values for upper and lower coils cryocooler are therefore only indicative.

Cryocooler	Upper coil	Lower coil	Current leads and thermal shield
Thermal losses (W):			
Radiation	0.58	0.42	10
Conduction (structure)	0.01	0	0.2
Conduction (leads)	0.04	0.24	35
Total without current (W)	0.63	0.66	45.2
Cryocooler minimal temperature (K)	≈ 11	≈ 11	≈ 24
Heat generation (W):			
Resistive connections (or resistive conductor)	0.34	1.08	32
Conductor dissipation	7.8	5.8	0
Total under operation (W)	8.77	7.54	77
Cryocooler temperature under operation (K)	≈ 13	≈13	≈32

Table 3-7: Expected heat load on the cryocoolers

4.3 Design of the coils cooling chain

The heat flux and resulting cryocooler temperatures evaluated in the previous section are used for the design of the coils cooling cold plates, in order to guarantee a suitable temperature of operation for the superconducting wires. The objective for this temperature is to be lower than 16 K, as it was the operating temperature observed during SMES I tests.

4.3.1 Cooling architecture

As it was already mentioned in the general thermal design presentation § 1.4.3, the architecture of the cooling chains for the two SMES II coils are similar, and based on the one design for the SMES I. It is schematized Figure 3-26.

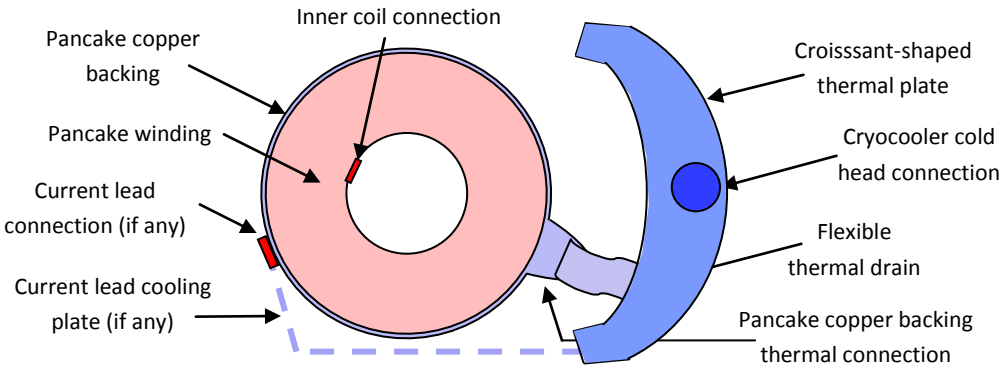

Figure 3-26 : Pancake cooling chain schematic view (from above)

Concerning the cooling of the winding, the maximal gradient between the winding and its copper backing thermal connection was fixed in the pancakes design at about 1 K under operation at the rated current [Bel06]. In order to have the superconducting tapes working below 16 K, the different coils cooling plates must therefore induce a temperature drop lower than 2 K.

Concerning the heat brought by the current leads (in red Figure 3-26), it may create a localized rise of temperature in the pancakes where they are connected: the upper and lower pancakes of the upper coil, and all the pancakes of the lower coil. A thermalization of the superconducting leads lower end is therefore necessary to evacuate these losses directly to the cooling system (represented in dotted blue line Figure 3-26). It must be designed for the temperature of the leads connection not to be higher than the winding temperature (16 K).

4.3.2 Coils cooling chain

The coils cooling chains consists of the flexible thermal drains, and the croissant-shaped cold plates.

Flexible thermal drains

The flexible drains design was already conducted for SMES I (Figure 3-27). Their measured equivalent thermal resistances are around 1 K/W. The connection interfaces, with the croissant-shaped cold plate on one side, and the pancakes copper backing on the other were also measured at 0.1 K/W

each. These values were obtained with annealed copper presenting a very good thermal conductivity around 15 K, their treatment will be described Chapter 4 § 1.2.2.

Figure 3-27: Flexible thermal drains and connections

The total temperature gradient in these elements is therefore 0.6 K under the assumption that 0.5 W are dissipated in each pancake and 20 mW in the inner connection, under operation at the rated current.

Croissant-shaped cold plates

The interface between the cryocooler and the croissant-shaped plate has been measured for SMES I design. Its equivalent thermal resistance is about 0.01 K/W. Under operation the temperature gradients in the upper and lower cryocooler interfaces are thus both lower than 0.1 K.

The croissant-shaped plates distribute the cooling power through the thermal drains, which are connected all along their lengths. They were optimized using Flux® to create a temperature difference lower than 0.5 K (Figure 3-28) under operation, considering the localization of each flexible drains connection. For the lower coil, the current leads thermalization connections were also considered (cf. below).

The croissant-shaped plates create temperature gradients lower than 0.3 K, sensibly lower than the maximal acceptable value.

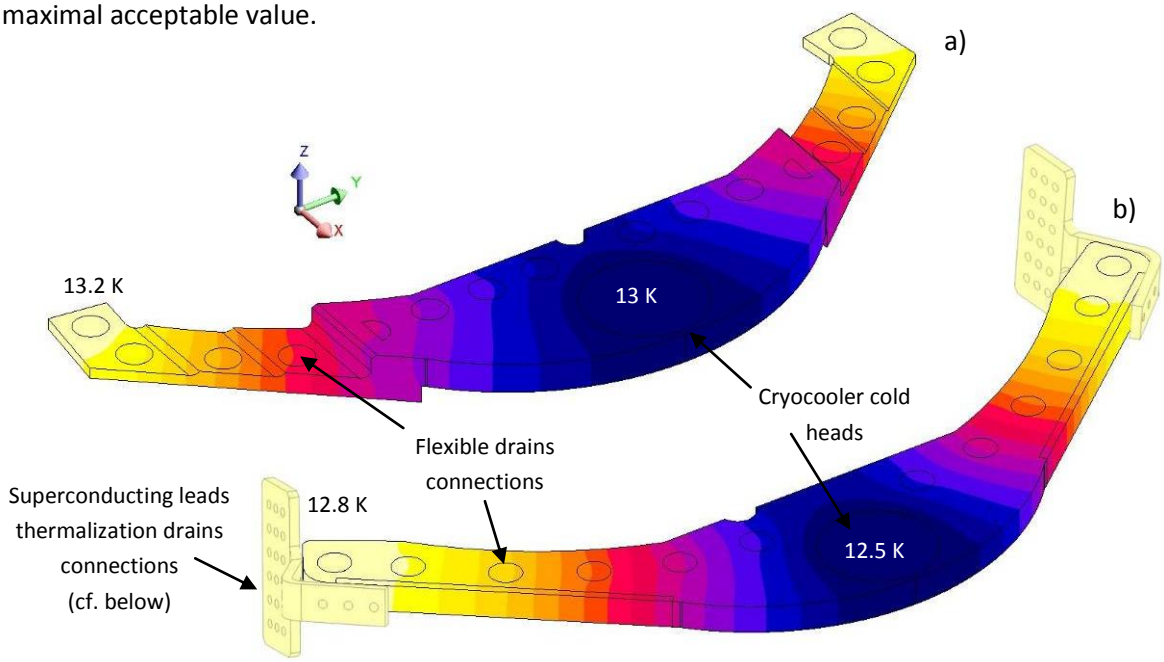

Figure 3-28: Temperature gradients in the croissant-shaped cold plates a) upper b) lower

4.3.3 Cooling of the superconducting leads lower end

The leads cooling chain consists of the high voltage thermalization interface and the thermal drain bringing the cooling power from the croissant-shaped cold plate to the leads lower ends.

Superconducting lead thermalization interface

As it was mentioned in the superconducting lead design § 2.1.2, the leads lower end connectors are designed to be thermalized. The thermalization interface is similar to that of the resistive current leads that was detailed in § 3.2.1.

A thermalization surface of 9.10^{-4} m² (3 x 3 cm) gives an equivalent thermal resistance of 2.8 K/W. The resulting temperature gradient is less than 0.4 K if we consider 80 mW of heat dissipation. This value corresponds to the 20 mW of thermal losses, as it was designed in § 2, and 60 mW due to the Joule effect in the current leads resistive connections, for a conservative value of 0.5 μΩ.

Thermal drain

The thermals drain must be designed for the temperature of the leads connectors to be effectively lower than the winding maximum temperature. Considering the elements already calculated above, thermal drains with an equivalent thermal resistance around 7 K/W are suitable. It will create a temperature gradient of 0.5 K under 80 mW.

To make assembly easier, the thermal drain cooling the leads lower ends consists of flexible copper braids connected at the extremities of the lower coil croissant-shaped cold plate. The number of copper braids was optimized for each drain length according to the copper quality. The results of this optimization for the longest drain (1.1 m) are presented Figure 3-29.

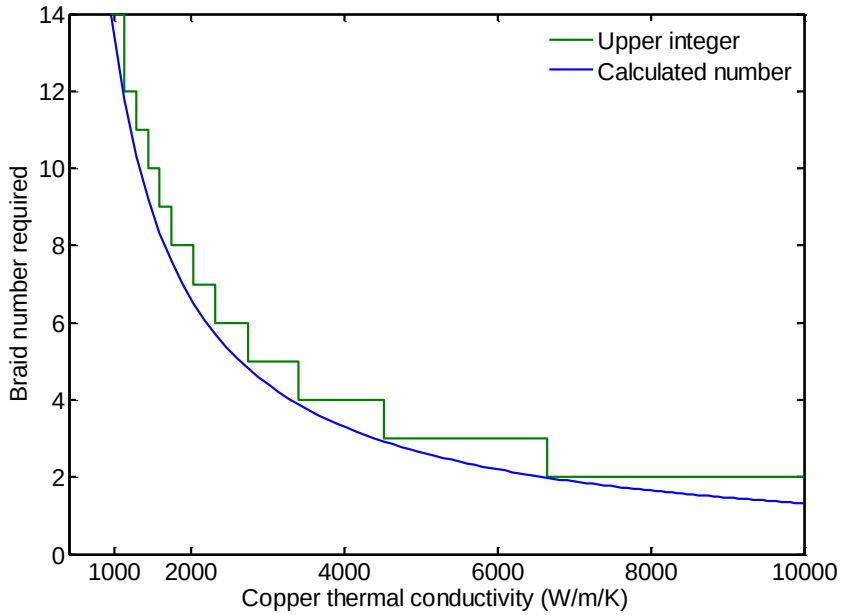

Figure 3-29 : Copper braid number depending on the copper thermal conductivity (for the longest length 1.1 m)

The copper thermal conductivity increases when the temperature decreases. At a given temperature, it also depends of its level of purity and the quality of its crystalline structure. This dependency is particularly important around 15 K. The results Figure 3-29 starts for a conductivity of 400 W/m/K because it is the worst possible case corresponding to the copper at room temperature. Conductivities in the order of 7500 W/m/K are classically obtained at 20 K. The studies on the thermal conductivity of the copper braids will be presented in Chapter 4 §1.4.3, along with the final number of braids for each drain.

5. Conclusion

In this chapter, the studies conducted for the design of SMES II were presented. With the existing elements from SMES I, and considering the practical constraints (cost, volume, etc.) the design studies were conducted to obtain the desired operating specification (rated current, stored energy, power consumption).

The result is satisfying, particularly concerning the current lead system which was one of the major issues. The proposed multi-stage thermalization allows considerable savings in terms of cooling power, and occupied volume. With this design, SMES II is not completely autonomous and requires liquid nitrogen transfer. This drawback is acceptable as liquid nitrogen, contrary to liquid helium, is cheap and widely available, so that the demonstrator may still be operated in “industrial” conditions, without specific knowledge about cryogenics.

However, a lot of engineering solutions have yet to be developed to make this design possible, essentially for the current leads and their thermalizations. The tests of these solutions and their use for the prototype realization are presented in the first part of the next and last chapter.

CHAPTER 4 :
SMES II REALIZATION AND TEST

In this chapter are first described the experimental studies that were conducted to test engineering solutions for SMES II demonstrator realization. The objective of these studies is to maintain the demonstrator operating conditions as close as possible to the design described in the previous chapter. The realization phases are also described, illustrating the practical implementation of the preferred solutions. The problems encountered during this phase are detailed, along with the choices that were made to solve them.

In a second part are presented the tests conducted with SMES II. Two tests campaigns were conducted:

- The first in Grenoble to validate the operation conditions and the agreement between theoretical and actual characteristics.
- The second at ISL to test the operation modes presented at the beginning of Chapter 3, in terms of operation limits and efficiency.

1. Preliminary studies and Realization

In this part are detailed the experimental studies that were conducted on technical solutions considered for the prototype, and how they were implemented.

The first section presents the test device developed for experiments at variable temperature, the studies on temperature measurements and their conclusions for SMES II instrumentation.

The next 4 sections describe the different phases of the prototype assembly, presenting for each the related studies and their results. Are successively described:

- The coils and cooling chains assembly
- The resistive current leads system with its thermalizations
- The superconducting leads and their connections
- The final assembly

1.1 Test device for cryogenic temperature measurement

The results of SMES I showed us that it was problematic not to be able to differentiate the temperature evolution of each pancakes. The objective for SMES II is therefore to increase drastically the number of temperature sensors on the coil, which pose the problem of their price, calibration and measurement. A test device for the sensors test and calibration was therefore developed, it is presented first. The tested sensors are then presented, followed by the measurement methods. The developed acquisition systems conclude this section.

1.1.1 Test device for measurements at variable temperature

In order to quickly build an experimental setting operating at variable temperature, the simplest way was to equip a small existing cryostat with one of the cryocoolers designated for the SMES II cooling. The cryocooler having a cold head temperature varying with the heat load, the operating temperature may be changed by using heating resistors on the cold head. This is the method used during the tests conducted for SMES I design. However, a large temperature range is difficult to obtain because of the very high cooling power of our cryocooler (330 W at 77 K).

Design of a variable temperature head

In order to limit the amount of heating power necessary to obtain a large temperature range, an adapted “head” was designed for the cryocooler (Figure 4-1), with a voluntarily reduced thermal conductivity obtained by reducing the cross section and selecting a suitable material (aluminium alloy).

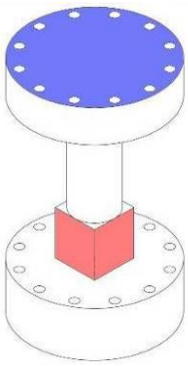

Figure 4-1 : Variable temperature head

The face mounted on the cryocooler cold head is in blue and the faces on which heating resistors are mounted in red. The face with the desired temperature is below.

The variable head was simulated using Flux®. Good temperature uniformity on the lower face is necessary for accurate measurement that is why the heating resistors are mounted on the cylinder and not on the lower face. The temperature gradient on this face was simulated at less than 0.1 K.

Using this method the temperature range was extended from 15 K up to room temperature with a heating power of 0 to 100 W (Figure 4-2).

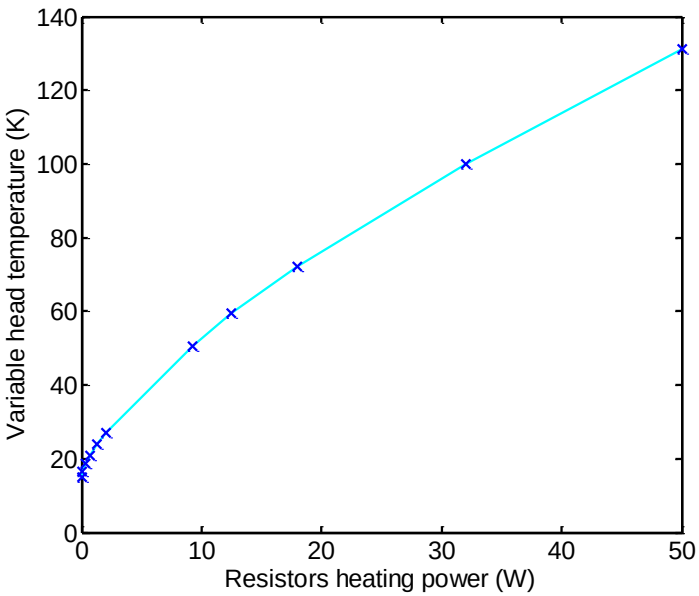

Figure 4-2: Temperature against resistors heating power (experimental data)

Device implementation

The implementation in the existing cryostat is shown Figure 4-3. It features a small liquid nitrogen tank, that will is used to cool an active thermal shield. It will also be used to thermalize the current leads of the heating resistors and the instrumentation connections. The tank has a ring shape which allows the cryocooler head to pass through it.

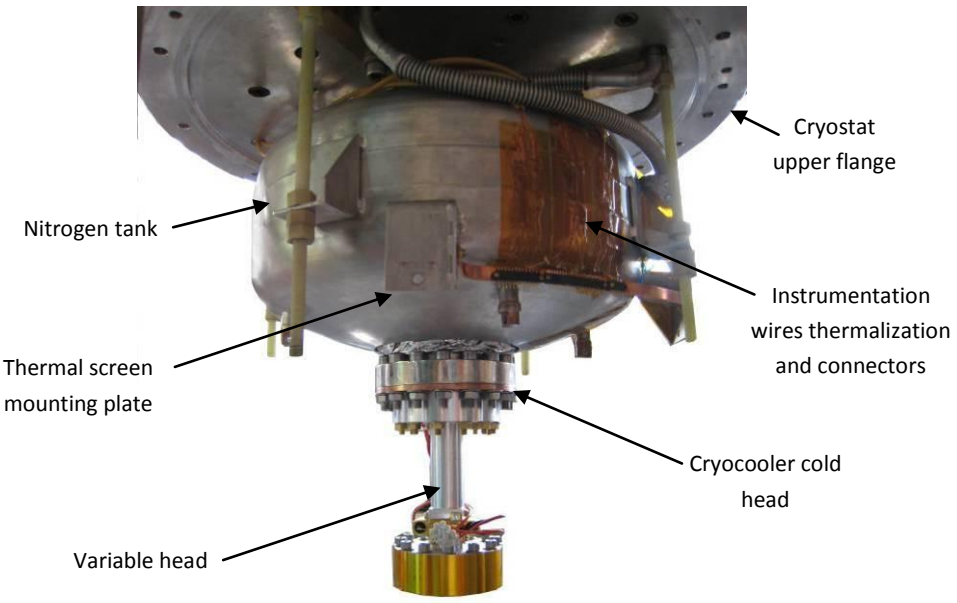

Figure 4-3: Test device implementation

The device is thermally isolated by maintaining a good vacuum level during the test. Superisolation is also used on both side of the active screen to reduce the heat losses.

1.1.2 Temperature sensors

Sensor choice

The most commonly used sensors in our range of temperature (from 300 K to 10 K) are both resistive:

- Platinum sensors are cheap and easy to implement, the platinum resistivity being proportional to the temperature. However its temperature coefficient is positive, which means that platinum sensors sensitivities get lower when temperature goes down. Moreover, lower than 50 K resistance cease to be proportional to temperature, the temperature coefficient decrease and tends to reach progressively zero at temperatures below 4.2 K. The resistance is then almost constant: it is the so called “residual resistance”. For these two reasons this kind of sensors is normally used only down to 50 K. In this range the sensors characteristics are relatively homogenous, standard calibration may thus be used. The most common platinum sensors are Pt100, which have a 100 Ohms resistance at 273.15 K (0°C), their residual resistance at low temperature is about 1 Ohm.
- Cernox sensors have negative and variable temperature coefficients. Their resistance is low at high temperature and then augments exponentially when the temperature lowers, which means that their sensitivity at low temperature is high. However, each sensor has its own resistance values and standard calibration cannot be used. They are also very expensive, about 300 € each without calibration, and 400 € more with calibration values. Cernox are the most classically used sensors for cryogenic applications in the 1 K – 50 K range.

For precise temperature measurements below 30 K, for example in thermal characterizations, Cernox are perfect. Several Cernox were available and we calibrate them using a certified calibrated sensor (a carbon sensor, whose resistance against temperature profile is similar to that of a Cernox) as primary reference.

However for SMES II the temperature of 28 pancakes (operating around 16 K) should be measured. Using Cernox for all of these sensors is impossible due to their cost that is why the operation of platinum sensors at low temperatures is investigated.

Platinum sensors calibration at low temperature

We studied the possibility of extending the platinum sensors range of use by calibrating them carefully down to 13 K. For this purpose we tests Pt1000 sensors which are as their names indicate, 10 times more resistive than Pt100, thus providing more sensitivity. Their calibration was conducted using the same reference than for Cernox (Figure 4-4), the 4.2 K point being obtained by measurement in liquid helium.

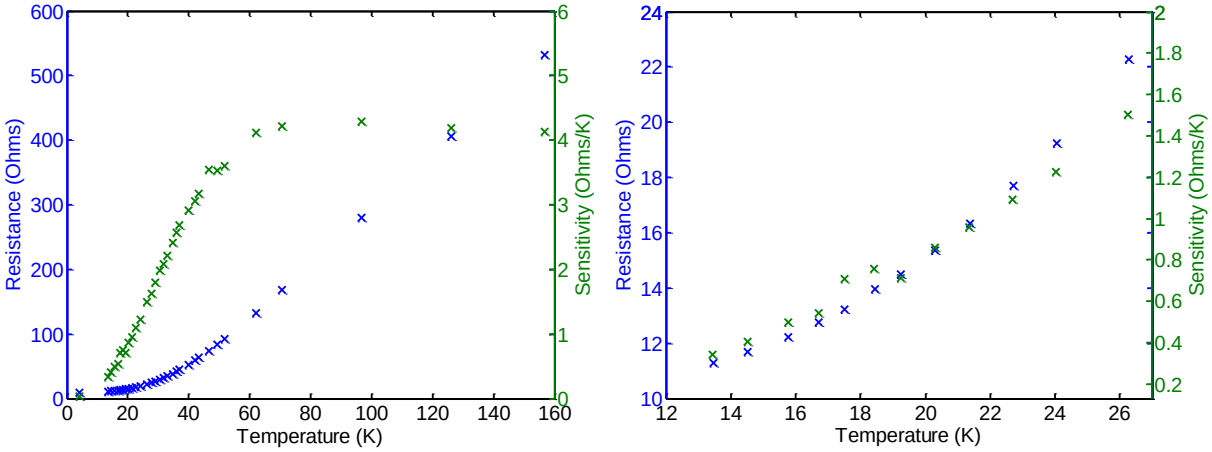

Figure 4-4 : Pt 1000 R vs. T calibration

Around 13 K, the sensor sensitivity is about 0.4 Ω/K, when this sensitivity is above 50 K almost constant at about 4.2 Ω/K. The same calibration data may be used for all the sensors, and the results are reproducible in this range of precision.

These experiments demonstrate that measurement using Pt1000 around 13 K is possible. Even if the precision is reduced when compared to Cernox, precision of ± 0.5 K is possible, which is enough for the SMES II instrumentation where temperature sensors are used for process control.

1.1.3 Sensor measurement

4 wires measurement

For precise resistance measurement, and especially when the sensor is placed in a cryostat with long wires and multiple connections, 4 wires method is necessary. The resistance is fed using a stabilized current source and the voltage across the sensor is measured through a separated circuit. Using this method the resistance measurement is independent from the wires resistance, at least if the voltage measurement has a suitable input impedance.

The current source can be used for more than one sensor, if they are connected in series (Figure 4-5).

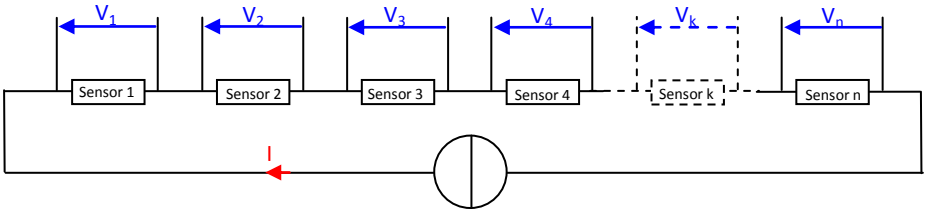

Figure 4-5: Multiple sensor 4 wires measurement

In this case good electrical insulation between sensors and measured surfaces is necessary; the fortuitous grounding of some measurement wires creating otherwise short-circuits between the series connected sensors. Differential voltage acquisition is also necessary.

Heat dissipation

To obtain a correct temperature measurement, the temperature difference between the measured surface and the sensor must be minimized. In order to do so, it is necessary to have a suitable interface between them, as well as careful thermalization of the measurement wires in order to cancel the losses coming through them. It is also critical to create as little heat as possible in the sensor. That is why sensors with high resistance values are suitable: As $V_{measured} = R \cdot I$ while $P_{sensor} = V_{measured}^{\ 2} / R_{sensor}$, for the same heat dissipation the voltage, the precision will be lower if R is lower.

For example, around 13 K Cernox resistance will be around 1 kΩ. Fed with 0.01 mA, it will dissipate only 1 µW and the measured voltage will be around 10 mV, which is easily measurable.

At the same temperature when using Pt1000 the resistance is around 10 Ω. For the same heat dissipation the measured voltage will be reduced ten times, to only 1 mV, which requires a more accurate and sensitive acquisition.

Thermoelectric voltage offset

Another problem for measurements in cryogenic systems is the thermoelectric voltages created by temperature gradients in the wires and at the connections. These voltages are in the 1 to 10 µV range, which is not negligible if the measured signal is in the 1 mV range. To get rid of this signal, the simplest way is to invert periodically the current source. In one direction the thermoelectric voltage will be added to the sensor voltage, while it will be subtracted in the other. The subtraction of the two signals will give the true sensor output, as shown in Eq. (4-1).

$$V_+ = I \cdot R_{sensor} + V_{thermo} \quad ; \quad V_- = -I \cdot R_{sensor} + V_{thermo} \quad ; \quad V_{sensor} = \frac{V_+ - V_-}{2} \qquad \textbf{(4-1)}$$

1.1.4 Acquisition systems

For the acquisition system choice, the problematic is the same than for sensors. A very sensitive and accurate system may be developed but it will be difficult for it to measure a large number of sensors. Two systems were therefore used:

Acquisition for thermal characterization

An acquisition system for precision 8 channel measurement in real time was developed, featuring 1 Hz periodic inversion of the current source, and based on an AD-Win® data acquisition board. The software development was conducted by P. Toledo during his practice period.

The total imprecision on the acquisition channel is about 0.1 Ω under 0.1 mA. It was used to realize the calibration presented above and the measurements of thermal conductivities presented below in § 1.3.2 & 1.4.4.

SMES II Acquisition

For SMES II instrumentation where a lot more channels have to be scanned, but only for process control purpose, such acquisition system is not necessary. The sensors voltages will be measured sequentially using a switching unit, the results being transferred to the PC and displayed using a Labview® program. The current source will only be inverted manually from time to time to check the thermoelectric values, the data being reprocessed afterward considering the offset if necessary.

1.2 Coils and cooling chains assembly

The first step for the prototype realization is to assemble the pancakes stacks, and to connect them electrically and thermally to the cooling plates. In this section are first presented the results of the pancakes dielectric tests and their consequences on the stacks organization. The copper annealing treatment insuring the flexible drain characteristics is described in a second time. The result of this first realization step concludes the section.

1.2.1 Coils assembly

The pancakes built for SMES I are re-organized following the order presented in the SMES II magnetic design (Chapter 3 § 1.3.3, Figure 3-10). This organisation is reproduced Figure 4-6.

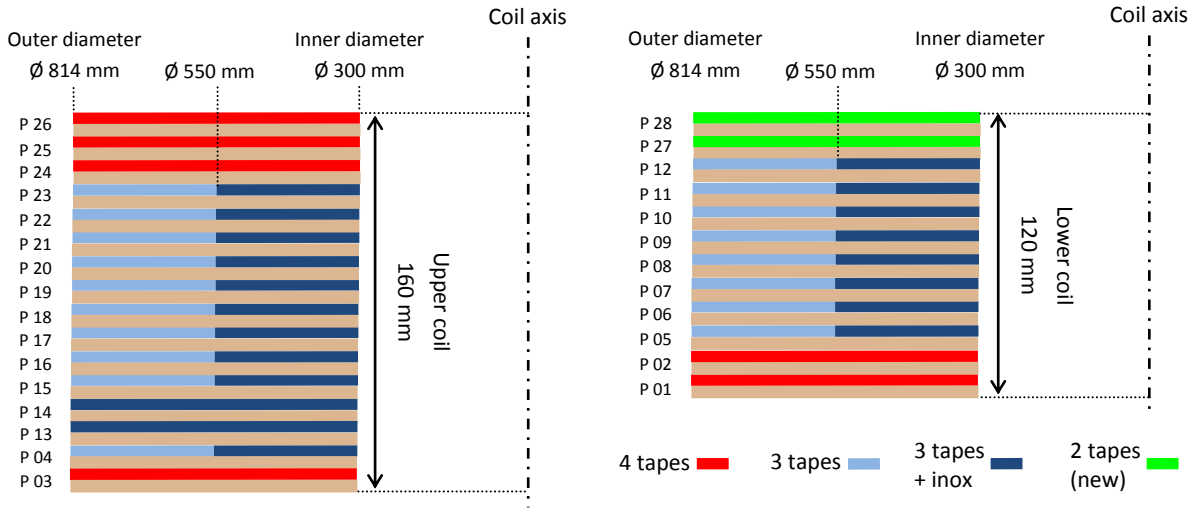

Figure 4-6: Pancakes organization in SMES II upper coil (left) and lower coil (right)

Pancakes High Voltage compliance

When operating in sequential discharge, the different pancakes are submitted to maximum voltages from almost 0 at the middle points of the stacks to 5 kV at the extremities. The breakdown voltage of each pancake was tested by grounding the thermal plate and submitting the winding to an increasing voltage using a high voltage source protected by a very high resistance (several MΩ), until a leak current appears and/or breakdown occurs. The tests were therefore potentially destructive and several pancakes had to be repaired (especially around the inner and outer connections) afterward to improve their characteristics. The results of the last tests (after repair) are presented Table 4-1.

Upper coil

Middle point

Pancake	3	4	13	14	15	16	17	18	19	20	21	22	23	24	25	26
$V_{required}$ (kV)	5	4.5	3.9	3.4	2.8	2.3	1.8	1.2	1.2	1.8	2.3	2.8	3.4	3.9	4.5	5
V_{tested} (kV)	5	5	5.5	5.5	2.9	5	3.2	4	3	5.5	4.5	5.2	6	4.5	4.7	3.7

Lower coil

Inner connections

Pancake	1	2	5	6	7	8	9	10	11	12	27	28
$V_{required}$ (kV)	5	4.3	3.5	2.8	2	1.3	1.3	2	2.8	3.5	4.3	5
V_{tested} (kV)	5	5	4.7	4.7	5	4.1	3.6	3.6	3.8	3.8	4.3	5

Table 4-1: Pancakes breakdown voltages

The only pancake that does not meet the requirements is the last of the upper coil (the 26th). It must be wounded with wires made of 4 tapes, and sustain the maximum voltage 5 kV. The only possible replacement is pancake 24, which is also wounded with 4 tape wire and sustains 4.5 kV. This voltage will thus be the maximal operating voltage for the upper coil.

Considering the lower coil in XRAM operation, the different double pancakes elements are in parallel, thus submitted to the same voltage. The characteristics of the worst pancake pair, 3.6 kV are limiting the operation. It is however much larger than the maximal voltage expected with this operation mode (around a hundred volts), as the objective is to discharge in a very low resistance simulating a launcher.

Pancakes connections and assembly

The pancake stacks organization being decided, they were connected electrically to form the upper coil and the six lower coil elements.

On the outer diameter, the copper connectors of adjacent pancakes are assembled 2 by 2 using 4 M5 screws then soldered using Sn-Pb (Figure 4-8). On the inner diameter the same method is used but the copper connectors are smaller, only one M5 screw is used (Figure 4-7). Small superconducting straps are soldered across the connectors in order to reduce the resistance of the connection (not visible on Figure 4-7).

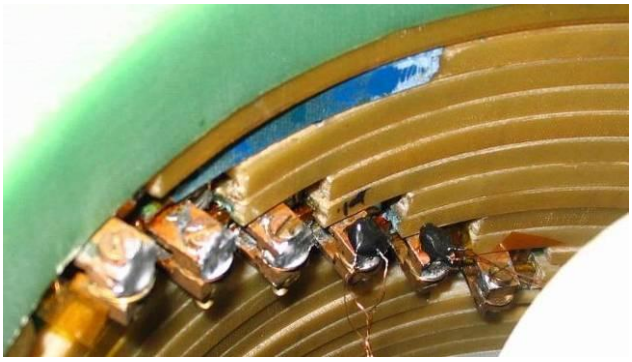

Figure 4-7: Inner connections

The two stacks being completed, they were placed between fiber-glass flanges, one on top of the other. A fiber-glass spacer is placed between them (300 mm) and threaded stainless steel rods maintain the coils in position.

The resulting assembly was mounted on the thermal screen lower plate using 4 fiber-glass tubes, following the design presented in Chapter 3 § 4 (Figure 4-8).

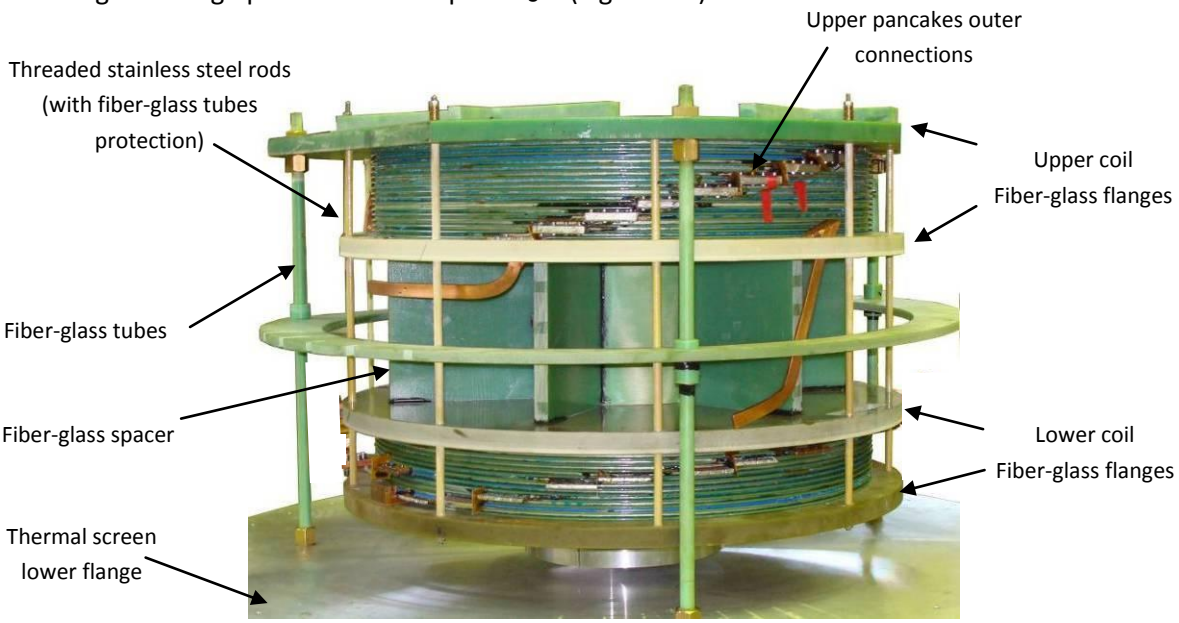

Figure 4-8: Coils assembly

1.2.2 Cooling chain assembly

Annealing treatment of the flexible thermal drains

Concerning the cooling chain presented in Chapter 3 § 4.3, the key elements are the flexible thermal drains (Figure 4-9). They are made of thin layers of CuC1 quality copper (pure at 99.9 %), soldered by pressure at the extremities. In order to obtain the best possible thermal conductivity in these elements, each of them was annealed following a process already tested for SMES I.

The elements are placed in a tubular oven in which a good quality vacuum is established, in order to avoid oxidation. They are heated up to 900°C, during 12 hours. This process was re-used for the thermalization plates used for the resistive current leads cooling.

Figure 4-9: Flexible thermal drain

RRR ratio

Samples annealed using this process were tested electrically to measure their RRR, the Residual Resistance Ratio. This ratio is obtained by dividing the resistance of the copper element at room temperature, with its residual resistance at 4.2 K.

Before treatment, this ratio is around 100 for massive elements. After treatment, it reaches 800. Thermal conductivity in pure metals is related to electrical resistivity through the Wiedman-Franz law: a high RRR value thus insures a high thermal conductivity (Figure 4-10).

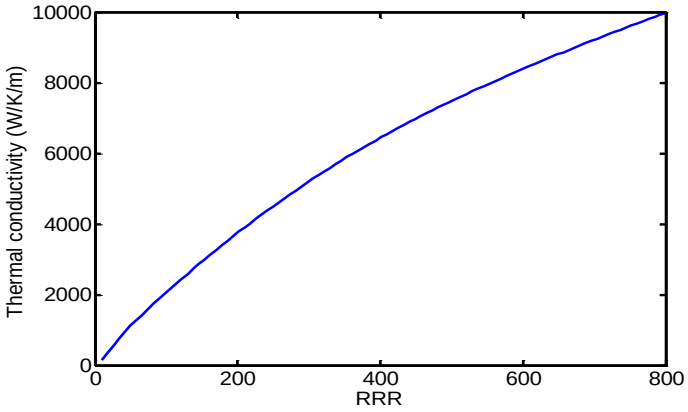

Figure 4-10: Interpolated values for thermal conductivity of copper vs. RRR at 15 K

Assembly

The croissant shaped thermal plates, whose design were presented at the end of the thermal system optimization (Chapter 3 § 4.3.2), are fixed to the upper coil fiber-glass flange, through threaded fiber-glass rods. The thermal drains are then connected to theses plates on one end, and to the pancakes cooling plates on the other. The resulting assembly is presented Figure 4-11.

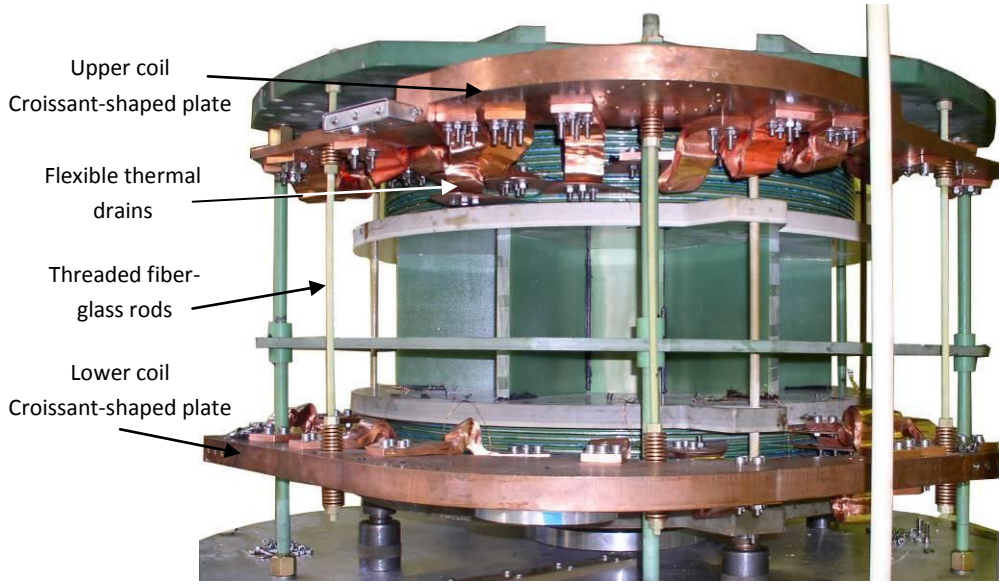

Figure 4-11: Coils assembly with cooling chains

1.3 Resistive leads system

In this section are first presented the tests which led to the current leads segments realization method. The studies conducted on the high voltage thermalization interface are then detailed, before describing the thermalization realization issues. The final thermalization setting and its consequences are presented in conclusion.

1.3.1 Studies on copper – copper interfaces for current leads assembly

As their machining out of a massive block is not practical, the current leads resistive segments are systematically made of two elements: A cylindrical part carrying the current and a disk or sector-shaped part for thermalization purpose (Figure 4-12).

When connecting these two elements, an electric and thermal interface is created that was not considered during the design. The objective of the realization process is to minimize this interface resistance, both thermally and electrically.

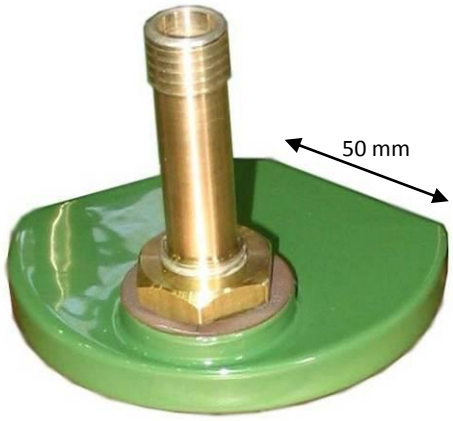

Figure 4-12: Current lead segment

Test samples

We tested four different methods for the elements assembly. These methods and the electrical resistance obtained experimentally for each are presented in Table 4-2.

Interface	Sn-Pb soldering	Indium soldering	Thermal Press fitting	Screw-pressed contact
Resistivity at 300 K	0.16	0.8	2.1	3.5
Resistivity at 77 K	<0.04	0.12	1.9	1.0

Table 4-2: Electrical resistivity of different assemblies ($\mu\Omega.cm^2$)

Realization of the Current leads segments

Sn-Pb soldered interface produce clearly less Joule losses, and results obtained for other purpose (see below copper braids connections § 1.4.4) tend to prove that it is also optimal thermally. In consequence the current leads elements were systematically soldered. For mechanical reasons, this soldering was sometimes completed with screwing or thermal press fitting.

1.3.2 Characterization studies for High Voltage thermalization interface

This interface was identified as a key point for the thermal design of SMES II (Chapter 3 §3).

Interface materials

The interface originally used for high voltage thermalization interfaces consist of two layers:

- A thin (0.2 mm) epoxy layer deposited on one of the surfaces (either the cooling plate or the current lead surface) by electrostatic projection, following the same method already used for the pancakes.
- A Redux® film, which glues the epoxy-coated surface to the other surface when cured over 120°C.

The Redux film is problematic because it is meshed and does not necessarily guarantee a good contact on the whole surface. We studied the possibility of changing this layer for another type of glue, in order to ameliorate the equivalent surface conductivity.

In order to do so, the glue layer must be as thin as possible while insuring a good contact on the surface. It must also be strong enough mechanically at low temperature to support the weight of the thermalization plates, resist to vibrations created by the cryocoolers and sustain the additional stress induced by thermal contractions during cooling. Finally the glue must have good electrical isolation properties.

The reflection was oriented toward the Emerson & Cumming epoxy-based glues already used in cryogenic devices in the laboratory: Eccobond® and three different types of Stycast® (black, transparent and blue). They were first tested mechanically and electrically in thin layers (Table 4-3).

	Layer homogeneity	Mechanical strength	Electrical isolation (for 1mm)
Stycast 2651 (black)	Bad (too sticky)	Modest	Low : leakage current over 2 kV
Stycast 2850 FT (blue)	Bad (fluid but contain grains)	Modest	Good, higher than 10 kV
Stycast 1264 B (transparent)	Very good (extremely fluid)	Low (brittle)	Good, higher than 10 kV
Eccobond	Correct (see below)	Good	depending on the sample, 2-10 kV

Table 4-3: Test results of existing glues for thermalizations

Eccobond is the best potential substitute to Redux film. However, small bubbles tend to appear in the layer during polymerization, which may reduce drastically its voltage breakdown. A process was developed to solve this problem.

Interface assembly Process

We developed a process to insure the quality of the Eccobond layer: 0.2 mm fiber glass wedges are placed at the edge of one of the contact surface, which is then covered with Eccobond. After that, the two surfaces are pressed together, the wedges guaranteeing the Eccobond layer thickness (Figure 4-13).

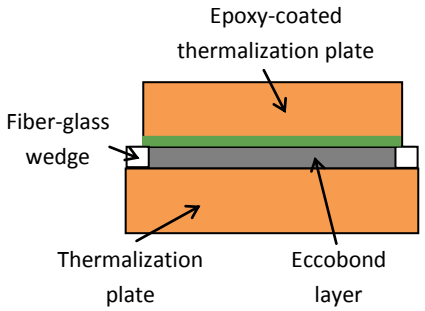

Figure 4-13: High voltage interface realization (cut view)

The assembly is maintained mechanically and placed in a vacuum chamber. Vacuum helps extracting gas bubbles in the Eccobond layer which insures its electrical properties.

Test samples characteristics

Two identical test samples were realized: one with Redux used as a reference, and the other with Eccobond (Figure 4-14 right). They were tested using the variable temperature device already presented § 1.1.1. The measurement consists in heating one side of the sample while the other side

is thermalized at the desired temperature on the variable temperature head. The equivalent thermal resistance is obtained by measuring the resulting temperature gradient. A schematic view of the experimental settings is shown Figure 4-14.

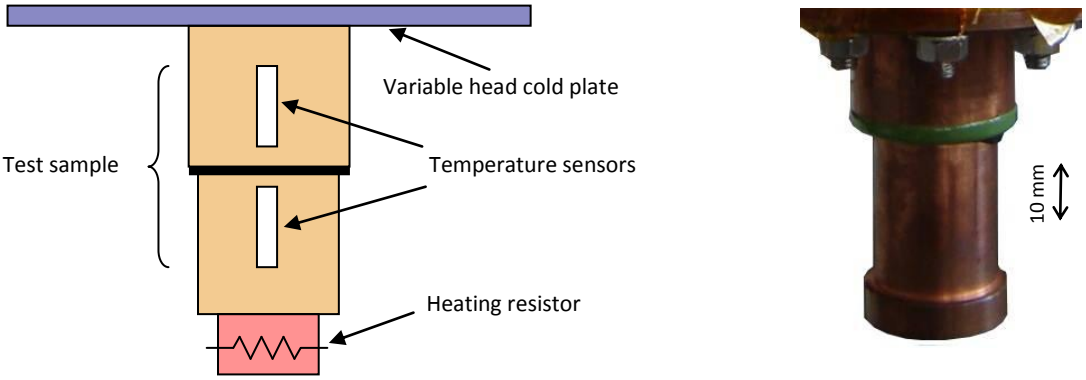

Figure 4-14: Schematic view (left) and sample mounting (right) for conductivity measurements at variable temperature

The results obtained for the reference sample confirmed the values already obtained during SMES I design. The sample with Eccobond have better surface thermal conductivity, especially at lower temperatures, its characteristics at the operating temperatures are presented in Table 4-4.

Surface conductivity (W/K/m²)	15 K	60 K
Reference : epoxy / Redux	100	200
epoxy / eccobond	450	500

Table 4-4: Surface thermal conductivity of high voltage interfaces

High Voltage compliance

The breakdown voltage of the sample with Eccobond was also tested in real conditions, using the test device. For this test the sample instrumentation was removed, and a high voltage electrical connection was placed on the sample lower end, the upper end being grounded through the cryocooler cold head. The breakdown voltage was initially 5 kV, which is enough for our use.

Moreover, after this first breakdown the voltage have been successfully augmented up to the limit of the voltage source (10 kV), without further problems. This kind of behaviour was already observed for some of the pancakes. It is probably due to the repartition of the electric field in the multi-layer interface. If the time required for the evening of the electrical field in the multi-layer interface is higher than the voltage rise time, then a fraction of the interface thickness may be submitted temporarily to a higher field than expected, leading to a partial breakdown. After this partial breakdown occurs, the field is more uniform and a higher breakdown value may be reached.

1.3.3 Thermalization realization issues

The thermalizations are realized using the method described above, and tested electrically. The electrical isolation between current leads and thermalization plates was tested up to 5 kV without problems. The interfaces mechanical strengths are tested by lowering them slowly in a liquid

nitrogen bath. This test was realized without problems for the smaller surface thermalizations, but on some of the larger ones, the Eccobond® layer cracked.

In order to understand the problem, we re-tested mechanically the test sample after several thermal shocks. The sample was submitted to shear stress up to 280 N/cm² without damage, thus not presenting the same problems than the large thermalizations. However, it was easily destructed by applying a peeling force. Our conclusion is that the higher mechanical contractions on larger surfaces create larger peeling forces than what was observed on the sample, overstepping the maximal peeling strength of the glue.

The only solution was to replace the Eccobond® layer on large thermalizations by Redux® film, in order to insure the safety of operation at low temperature. The final result is presented Figure 4-15.

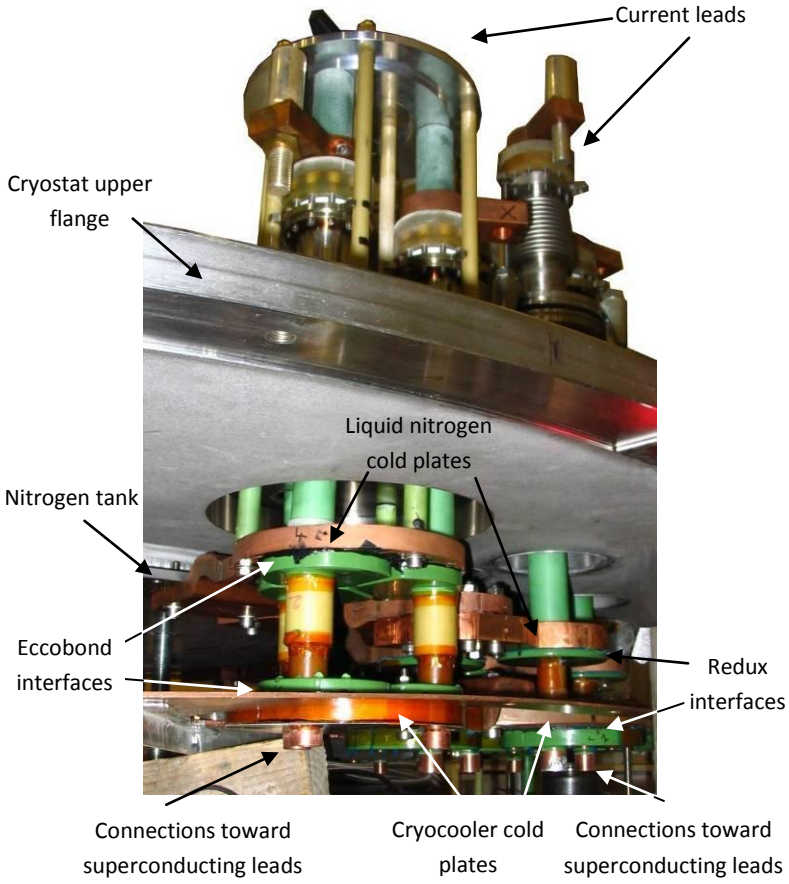

Figure 4-15: Resistive current leads system

1.3.4 Consequences

Due to this thermalization problem, the thermal design presented previously is not followed, and the safe operation of the superconducting leads at 50 K is impossible to guarantee.

The only practical solution was to reduce the heat load on the cryocooler, and therefore the number of current leads. Instead of connection the pancakes two by two on the lower coil to create a six stages XRAM, the connection was done four-by-four, to create a three stages system only. We this modification, only 6 current leads are necessary, which reduce the heat load on the cryocooler.

Taking into account the modified Redux-glued thermalization interfaces and an 8 leads system, the simulation tool developed for the resistive leads optimization gives the results presented Table 4-5.

Results for 8 current leads and modified thermalization		
	Liquid Nitrogen	Cryocooler
Upper end temperature	300 K	108 K
Lower end temperature	108 instead of 93 K	47 instead of 42 K
Heat flux under operation (for each lead)	18 instead of 14.6 W	7.5 instead of 4.8 W
Heat flux without current	8 instead of 7.7 W	2.8 instead of 2.5 W
Temperature gradient in isolation layer	10 K	9 instead of 8 K
Temperature gradient in cooling plates	Similar, 2 K	Similar, 2 K
Temperature of the cooling source	Similar, 80 K (LN2 tank cold plate)	34.4 instead of 34 K

Table 4-5: Simulation results for modified thermalization system

The three additional outer pancake connections on the lower coil are realised using copper parts on which are soldered superconducting tapes, following the method developed to reduce the resistance of the resistive connections on the inner contacts. The result is presented Figure 4-16.

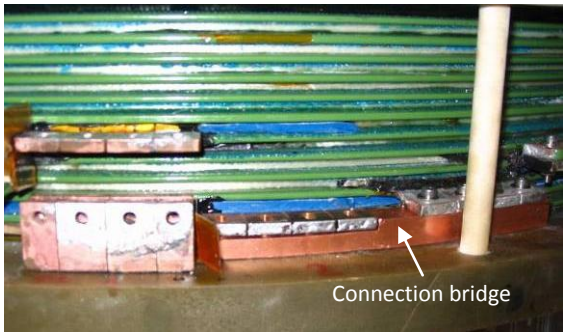

Figure 4-16 : Additional connection on the lower coil for three stage XRAM

1.4 Superconducting leads

This section presents successively the superconducting leads realization and their electrical connections. It presents then the thermalization copper breads treatment and their interfaces.

1.4.1 Superconducting leads realization

As it was mentioned in their thermal design (Chapter 3 § 2.1.2), the 5 superconducting tapes necessary for each lead are housed in a grooved fiber glass rod, and soldered together at each extremity with custom-made copper connectors. A process was developed to insure reliable soldering without damaging the tapes.

Copper connectors

The copper connectors are similar on each side. They are grooved copper rods with similar diameter than the fiber-glass rod used to maintain the tapes. For the lower end that must be thermalized, this cylinder is fitted in a plate whose extremity is adapted to be connectable to the pancakes outer connections (Figure 4-17).

This fitting is made by thermal contraction, following the method previously tested for the resistive current leads segments (cf. § 1.3.1).

This method is used because the tapes must later be soldered to these connectors, which have to sustain the subsequent temperature rise without being disassembled.

In order to insure the lowest possible resistive losses in the connectors, the thermalization plate is also grooved to place superconducting tapes.

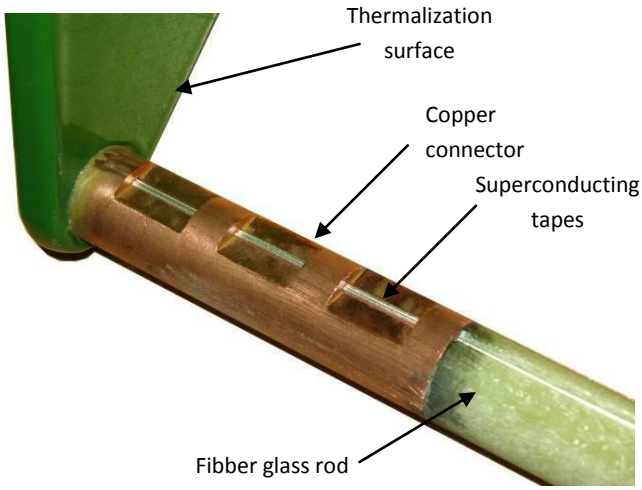

Figure 4-17: Superconducting tapes lower end connector

Soldering method

A soldering process was developed to insure a proper soldering without heating the tapes over 200°C, temperature after which there are risks of deterioration of the superconducting characteristics.

The soldering is made with Indium, with a specific flux. Instead of locally heating the elements, the whole leads were placed in a regulated oven to reach 200°C, after what all the soldering where made simultaneously (Figure 4-18).

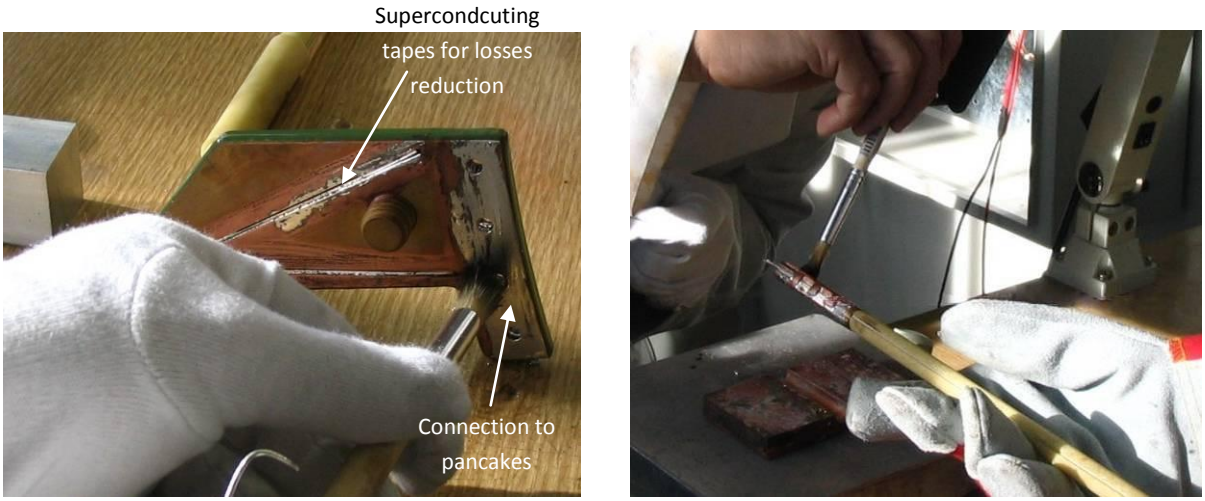

Figure 4-18: Lower (left) and upper (right) connectors soldering

Mechanical reinforcement

In order to protect the tapes from shear stress at the limit between the copper connector and the fiber-glass rod, the assembly tapes + connectors + fiber-glass rod was fitted in an adjusted fiber-glass tube, which was glued at the extremities using eccobond. The final result is presented Figure 4-19.

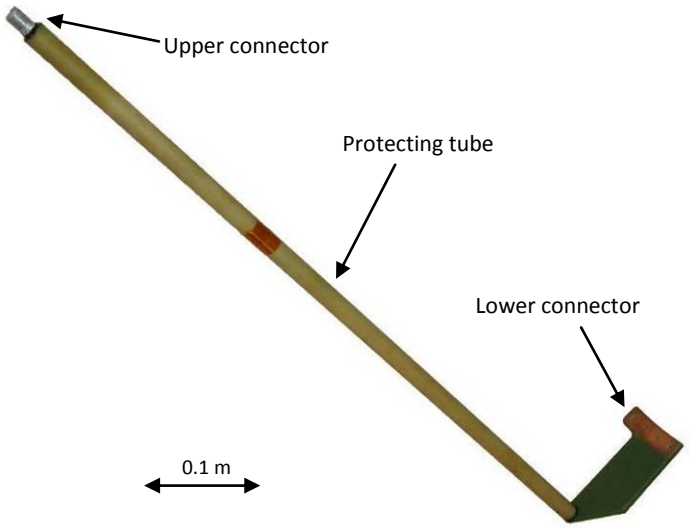

Figure 4-19: Superconducting current leads

1.4.2 Superconducting leads electrical connections

On the lower end, the electrical connection to the pancakes is similar to the other outer pancakes connections. The lead connector is fastened on the pancake connector with 4 screws (M6) and soldered with Sn-Pb.

On the upper end, the connection must be flexible to isolate the superconducting leads from the cryocooler vibrations and to sustain the thermal contractions. Flexible connectors were realized using copper braids with an adapted section (Figure 4-20).

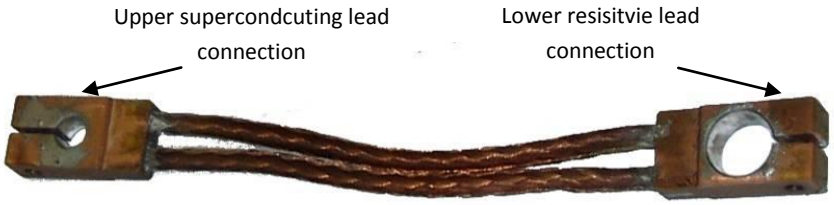

Figure 4-20: Flexible connection between resistive and superconducting leads

The interfaces consist in cylindrical bores adjusted to the superconducting leads upper connector on one side, and the resistive leads lower connector on the other. Before final assembly, the connectors were protected with a fiber-glass braided sheath. The result of the superconducting leads assembly is presented Figure 4-21.

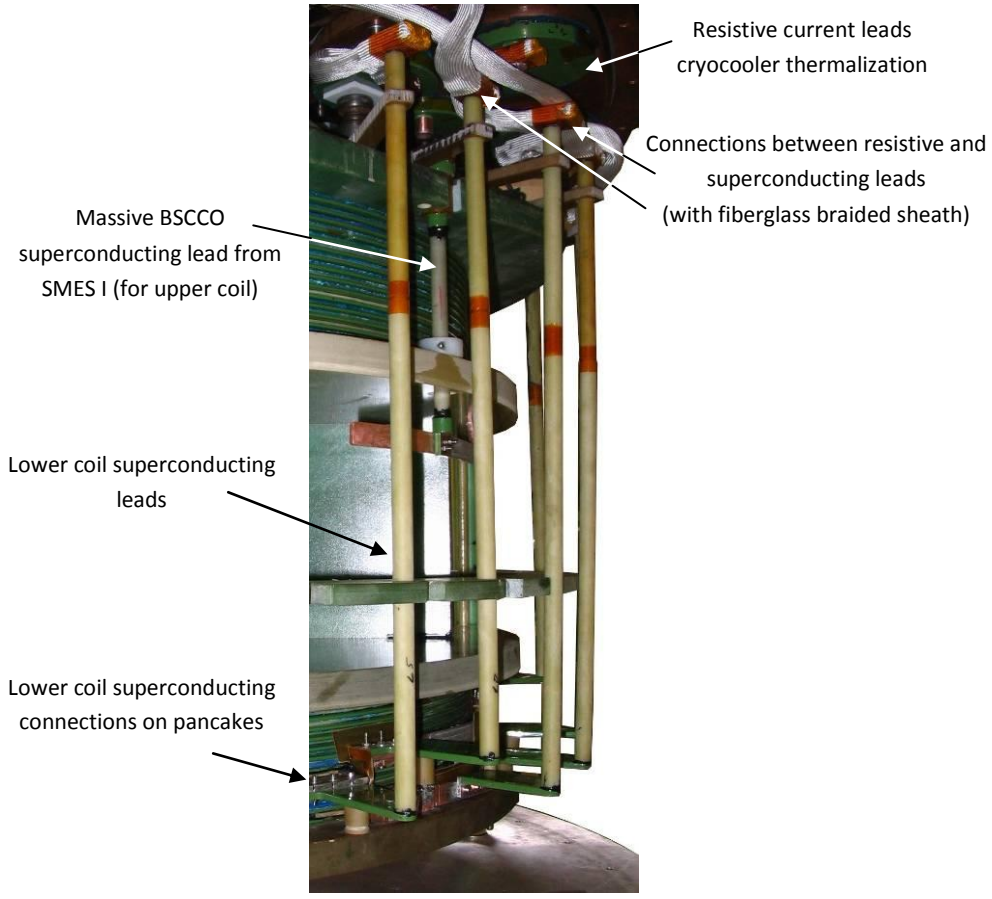

Figure 4-21: Superconducting leads assembly

1.4.3 Thermalization Copper braids annealing treatment

The lower end of the superconducting leads is thermalized using very flexible copper braids in order to make assembly easier. As it was presented in the thermalization design (Chapter 3 § 4.3.3), the conductivity of copper determines the number of braids to be used for each thermalization. As for the flexible drains presented above (cf. § 1.2.2) annealing treatment was studied in order to increase the copper braids thermal conductivity.

Braids annealing issues

Annealing process is much more complex for braids than for bulk pieces, due to their structure:

- The braids are composed of small copper wires (Ø 0.1 mm) obtained by drawing. This process causes a lot of dislocation in the crystal structure, which induce a much lower RRR. The flexible drain presented earlier had an RRR of around 150 before treatment, but the braids wires RRR is only around 50, for the same copper quality (CuC1 pure at 99.9 %).
- When the annealing process is conducted the structural stress induced by drawing is released, which cause each wire to take a corrugated shape. The already breaded wires are then overlapping even more, which reduces the braid flexibility. Moreover, the annealing temperature is by definition close from the melting temperature, the overlapping wires thus tend to sinter to each other's, which rigidify the braid even more.

- As the surface/volume ratio is much higher for thin wires than bulk pieces, the effect of copper vaporization during the annealing treatment in vacuum is much more important, with a substantial loss of material. The oxidation of copper must therefore be prevented using other methods.

Different treatments were tested; the results are presented in Table 4-6.

Atmosphere	Remark	Temp. (°C)	Duration (hour)			RRR	Conclusion
			rise	max	fall		
Vacuum	Classical	900	1	12	1	500	RRR ok but high losses and stiffness
Vacuum	Short treatment & lower temperature to reduce vaporization	800	1	2	1	308	Ok but RRR is not satisfying
Vacuum	Short treatment to reduce vaporization & higher temperature to increase RRR	850	1	2	1	330	idem
Ar 95% H_2 5% + Ti chips	First test in controlled atmosphere	900	1	0.3	1	233	Ok but RRR not satisfying
Ar 95% H_2 5% + Ti chips	Lower temperature for rigidity reduction	750	1	12	1	483	Good

Table 4-6: Annealing treatment results for copper braids

The best treatment is clearly the last one. With an RRR value of 480 the thermal conductivity of copper is approximately 7000 W/K/m (see Figure 4-10 in § 1.2.2). Following the results of the thermalization design two braids for each thermal drain are enough to obtain a satisfying equivalent thermal resistance.

Considering the length necessary for thermalization (12 m) and the length used to realize the connections between resistive and superconducting leads, around 20 m has to be annealed.

Annealing oven

Classical ovens for annealing treatment in controlled atmosphere or vacuum are tubular, with cold extremities, which make the use of standard gas / vacuum connections possible. This kind of oven has however limited diameter and only the middle part of the tube has good temperature homogeneity. In consequence, they are not suitable for the annealing of voluminous or lengthy parts, like the braids used for thermalization.

In consequence, the annealing was done in a standard large-size oven, in which an airtight vessel was placed to create a controlled atmosphere (Figure 4-22).

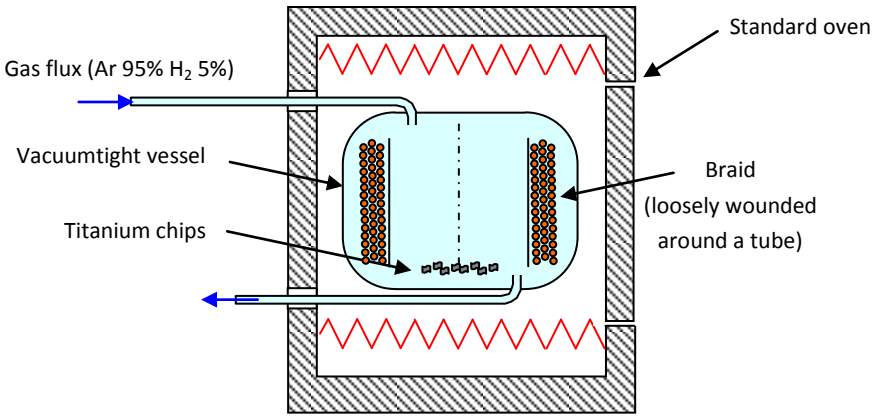

Figure 4-22: Schematic view of annealing oven

The vessel being placed in the oven, it must sustain 900°C while remaining airtight. As airtight opening systems are difficult to implement at such high temperatures, the elements to be annealed are placed in the stainless steel vessel which is closed by welding the upper dished head using TIG. The vessel must therefore be sawed to extract the elements and re-welded each time it is used. The gas inlet and outlet are also stainless steel tubes, with metallic seals.

This annealing oven was also used for the bulk copper elements too large to enter in the existent tubular ovens, especially the connection elements that are used to connect the braids on the croissant-shaped cold plate (see below § 1.4.4). It was graciously provided by C. Warth-Martin from the Laboratoire National des Champs Magnétiques Intenses (LNCMI).

Annealing results

For the breads treatment, the vessel atmosphere was purged two times using a vacuum pump, and then replaced by the gas flow, which was around 10 litres per hour. The result was not as good as what was obtained on short samples: the braid was oxidized in some locations and it was generally stiffer than expected. The reason was probably an insufficient gas flow for the amount of material treated.

The RRR was measured around 300, depending on the location. The number of braids for each thermalization was therefore increased to 3.

1.4.4 Copper braids connections

Connection equivalent resistances

To connect the braids on the lower coil croissant-shaped cold plate on one end, and on the current leads thermalizations plates on the other end, different methods were studied. Classical soldering using Sn-Pb was compared to Magneto-formed connections with or without indium insert. Magneto-forming consist in pressing the braid and the end-connector together with the magnetic pressure created by a small exploding coil wounded around them and fed by a short high current pulse.

The three samples were instrumented and placed in the test device already presented, to test their thermal conductivity, following the same measurement methods than for thermalization interfaces. As the operating temperature is already defined (around 15 K), the test samples were directly connected on the cryocooler cold head in the test device (Figure 4-23).

The result of this experiment is that around 15 K the magneto-formed interface and the soldered interface gives similar results, with equivalent resistances around 0.2 K/W, whereas the magneto-formed interface with indium insert as higher resistance, 1 K/W.

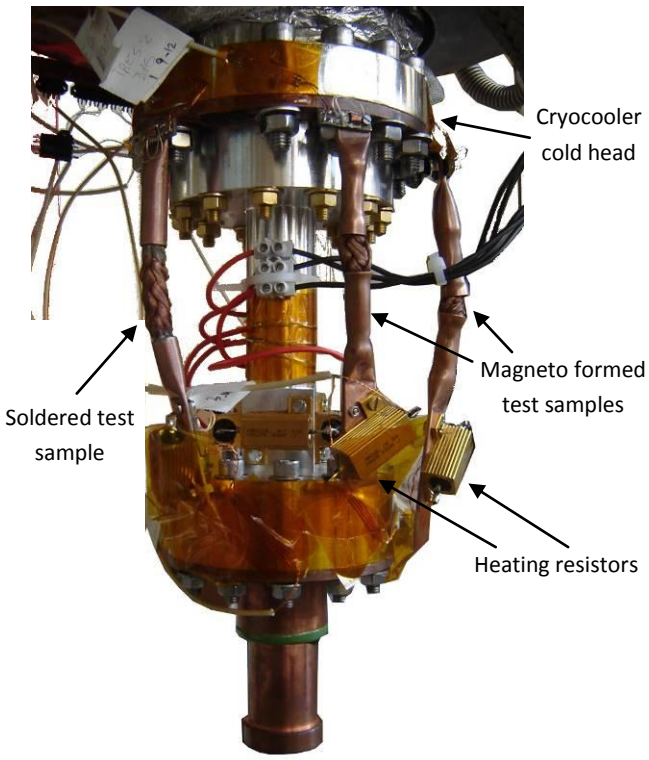

Figure 4-23: Breads connectors in test device

Realization process

The soldered interface being easier to implement, it was selected. However, the process actually used for SMES II is slightly better than the one that were tested. Instead of soldering a bulk copper connector on the braids, we considered the possibility of creating the connection directly using the braid with soldering in it. Using this method the equivalent thermal resistance is better as there is less interfaces: instead of Copper (braid) – Soldering – Copper, the interface is now Copper (braid) – Soldering only.

To realize such interface, the braid is first pressed in a die, then filled with soldering, and pressed again to obtain the final shape. The die is schematically represented Figure 4–25 and the result Figure 4–26.

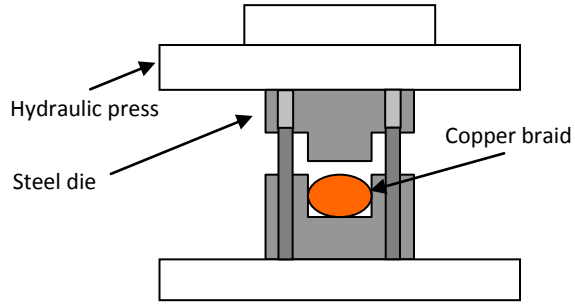

Figure 4-24: Die system for braids connection

Figure 4-25: Resulting braid connection

Assembly

On the cryocooler side, the braids connections are pressed on two T-shaped plates that are fastened on each extremities of the lower coil croissant-shaped cold plate as shown Figure 4-26.

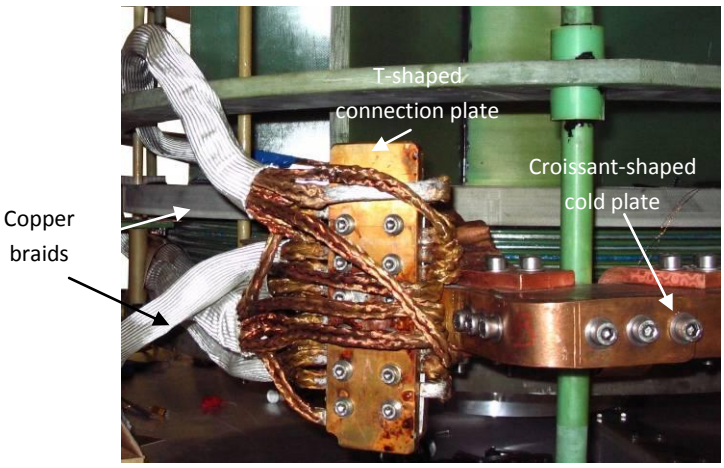

Figure 4-26: Copper braids connections on the croissant-shaped cold plate

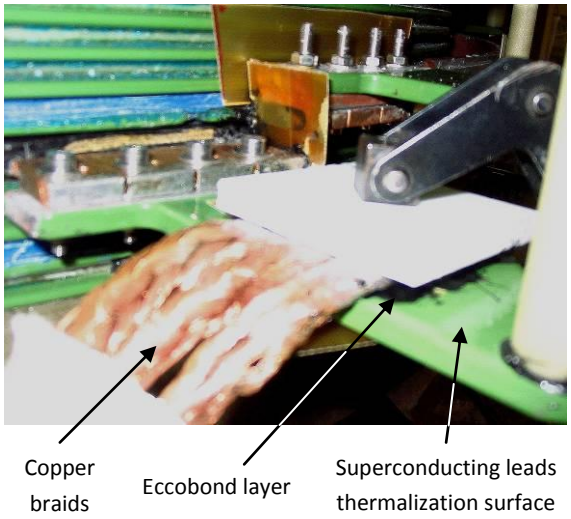

Figure 4-27: Braids / Thermalization interface

On the leads thermalization side, the breads connections are glued on the thermalization surface with eccobond, using the same process than for the other thermalization interfaces (Figure 4-27).

1.5 Conclusion of SMES II assembly

After connecting the instrumentation and mounting the cryocoolers, the SMES II assembly was concluded by mounting the active thermal screen with its Superisolation layers. The device was then placed in its cryostat (Figure 4-28) and sealed. The vacuum-tightness of the cryostat was checked before starting the first cool down.

Figure 4-28: Last step of assembly

2. SMES II experimental setting and tests

In this part are described the tests conducted with the prototype and their results. We present in the first section the protection device used for these experiments. The second section describes the behaviour of the prototype cryogenics and comparisons with the expected results are proposed. The third section presents the characterization tests, concerning the coils inductances, their coupling and the maximal operation current obtained. The last section details the operations conducted to test the electromagnetic launcher supply chains investigated: indirect through fast capacitors reloading, direct through XRAM current multiplier and the sequential discharge capability.

2.1 Protection device

The SMES II coils requires an active protection system against quench for safe operation (cf. Chapter 1 § 3.4). The protection is based on the fast discharge of the coils in resistors, taking advantage of the high voltage operation capability. However, it requires a sensible transition detection to detect the problem and discharge the coil early enough for its temperature not to increase too much.

2.1.1 Detection issues

The detection system is based on bridge compensation principle (cf. Chapter 1 § 3.4.2): The voltage between the two extremities of the coil and the middle is compared by mean of a Wheatstone bridge (in blue Figure 4-29). The output of the bridge (in red) is amplified and compared with an adjustable threshold. When the signal oversteps this threshold during a given time, adjustable between 0 and 200 ms, the coil discharge is triggered.

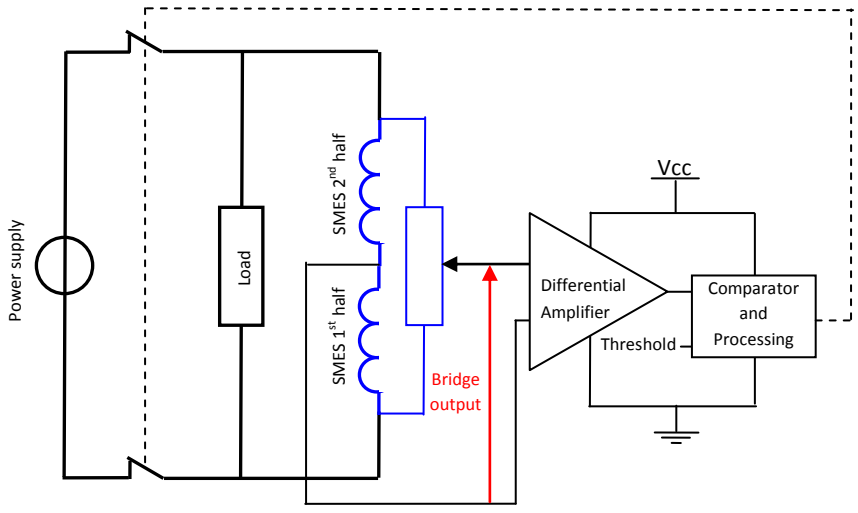

Figure 4-29: Bridge-based transition detection

Detection level

The dissipation voltage level above which the protection should be triggered is not easy to determine, especially for HTS devices (cf. Chapter 1 § 3.4). As transitions tend to appear on short lengths and propagate slowly, the voltage induced is difficult to detect.

During SMES I tests, one of the pancakes was damaged during operation. When this pancake was repaired only a few turns (around 20 m) had to be removed from the winding 450 m long pancake winding. The damages were thus highly localized, which demonstrates the low propagation speed of the transition and the necessity of detecting even a short length of transited conductor to protect the pancakes.

Based on the literature mentioned in Chapter 1 § 3.4 and our experience with SMES I, we decided to build a detection system with threshold adjustable between 30 mV and 300 mV, and stetting by default at 40 mV. It corresponds to 5 cm of transited conductor dissipating under 300 A at Tc.

High voltage issue

The bridge transition detector presented Figure 4-29 is easy to implement if the middle of the coil is grounded. In this case even during a high voltage discharge the differential amplifier input voltage will stay close to zero. However, if the coil is grounded by one of its extremities, during the discharge the amplifier sees a common-mode voltage of half the total coil discharge voltage, which in our case could reach 10 kV.

Usually this problem is solved either by reducing the voltage before the bridge, to acceptable levels for classical electronic devices or by using isolation amplifiers. These are rather expensive and are also limited in voltage, to around 4 kV. For higher voltage operation, the only way is to attenuate the signals.

With attenuated signals, detection of voltages levels of some tenth of millivolts become a major issue [Sch02] and very sensitive amplifiers must be used, as well as advanced noise filtering methods.

Protected direct detection concept

The solution we implemented is to build a direct detection system without high voltage capability or voltage attenuation. The measurement of the imbalance being full scale, it can be made very sensitive. When a quench is detected, the coil must be discharged quickly. During the discharge the voltage will rise to the point of being destructive for the detection system, but the quench having already been detected, it is not indispensable to keep observing the imbalance of voltages anymore. The system will therefore place itself offline via high voltage fast switches, shortly before starting the discharge. Being isolated from the coil, it will not be subjected to the high voltage caused by discharge.

In normal operation, when the operator wants to discharge the coil, the detection system also isolates itself shortly before operating the discharge switches (Figure 4-30).

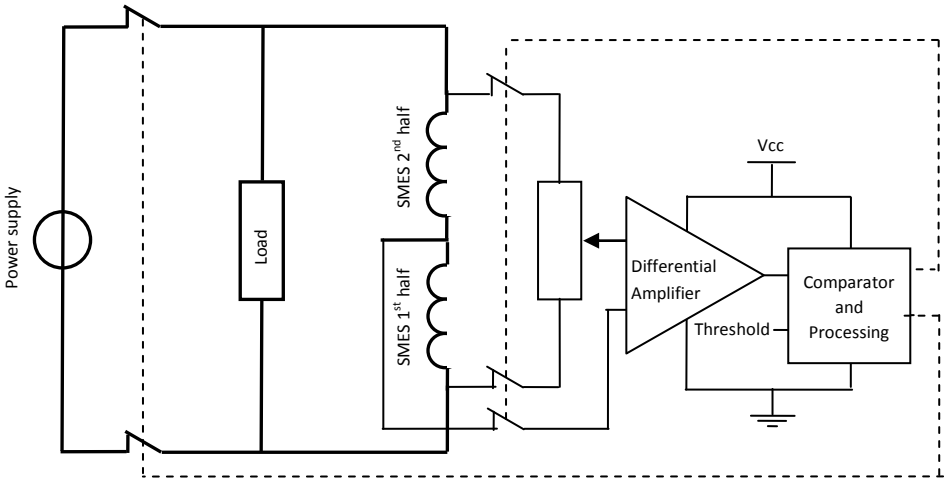

Figure 4-30 : Protected direct Quench Detection implementation

With this active protection of the detector the use of standard electronic system without any attenuation is possible, even if the coil is not referenced to earth by its middle or is part of a complex assembly of coils. The galvanic isolation during pulse discharge also enhances the safety of operation for the system managing the power switches, without need of additional isolation devices such as optocouplers.

The protected detection device is therefore less expensive than classical systems and easier to implement, without any need of isolation amplifiers or high voltage compliant electronic. Because it is not attenuated, the voltage detection is more sensitive. The level of detection being above the noise, there is no need of high noise rejection to ensure the reliability. A patent was filed for this concept [BT10].

2.1.2 Coupled coils protection

For SMES II, there are two coils to protect. Each of them has its own bridge detection system but as they are magnetically coupled, the influence of one coil on the other has to be considered.

The two coils being placed one on top of the other, the coupling between the first coil and the two halves of the second coil are different. A fast discharge of the upper coil (coil 1) could therefore unbalance the detection bridge of the lower one (coil 2) following Eq. (4-2), and reciprocally a fast discharge of the lower coil could unbalance the bridge of the upper one.

$$V_{bridge\,2} = V_{q2}/2 + (L_{21} - L_{22} + M_2 - M_2)\, di_2/dt + (M_{21\_1} - M_{22\_1})\, di_1/dt \;,\; L_{21} \approx L_{22},\; M_{21\_1} \neq M_{22\_1}$$
$$\Rightarrow V_{bridge\,2} = V_{q2}/2 + (M_{21\_1} - M_{22\_1})\, di_1/dt \qquad \textbf{(4-2)}$$

With L_{21} and L_{22} being respectively the inductance of the first and second half of the lower SMES coil, M_{21_1} and M_{22_1} being the mutual inductances between these and the upper coil, M_2 the mutual inductance between the two halves of the lower coil and V_{q2} representing the dissipative voltage appearing in case of quench on the lower coil.

In our case, the upper coil will always be discharged first. The only bridge we have to protect against this problem is thus the lower coil bridge. To compensate the influence of the coupling on this coil -third term of Eq. (4-2)-, we need to subtract to the signal of its detection bridge $V_{bridge2}$ an image of di_1/dt, which gives Eq. (4-3).

$$V_{compensated\,2} = V_{bridge\,2} - k \cdot di_1/dt = V_{q2}/2 + (M_{21\_1} - M_{22\_1} - k)\, di_1/dt \qquad \textbf{(4-3)}$$
$$\Rightarrow V_{compensated\,2} = V_{q2}/2 \quad if \quad k = M_{21\_1} - M_{22\_1}$$

$k \cdot di_1/dt$ is adjusted so that it compensates exactly the difference between the two mutual inductances.

To obtain an adjustable image of di_1/dt, using voltage dividers on V_1 is possible but it does not isolate the detection system during the pulses and makes it impossible to choose the voltage reference of each coil separately.

We preferred the use of a small resistive coil, placed in the bore of the upper coil to be magnetically coupled with it. It provides an image of the upper coil voltage, with galvanic isolation. Of course, this small coil is coupled not only with the upper coil but also with the lower one. This additional coupling is however low enough to have no sensible influence on the compensation equilibrium. The subtraction of $k \cdot di_1/dt$ to $V_{bridge2}$ may be obtained by using a secondary bridge (in red Figure 4-31). The resulting diagram is presented au-dessous, with the mutual coil placed in the upper SMES coil in blue.

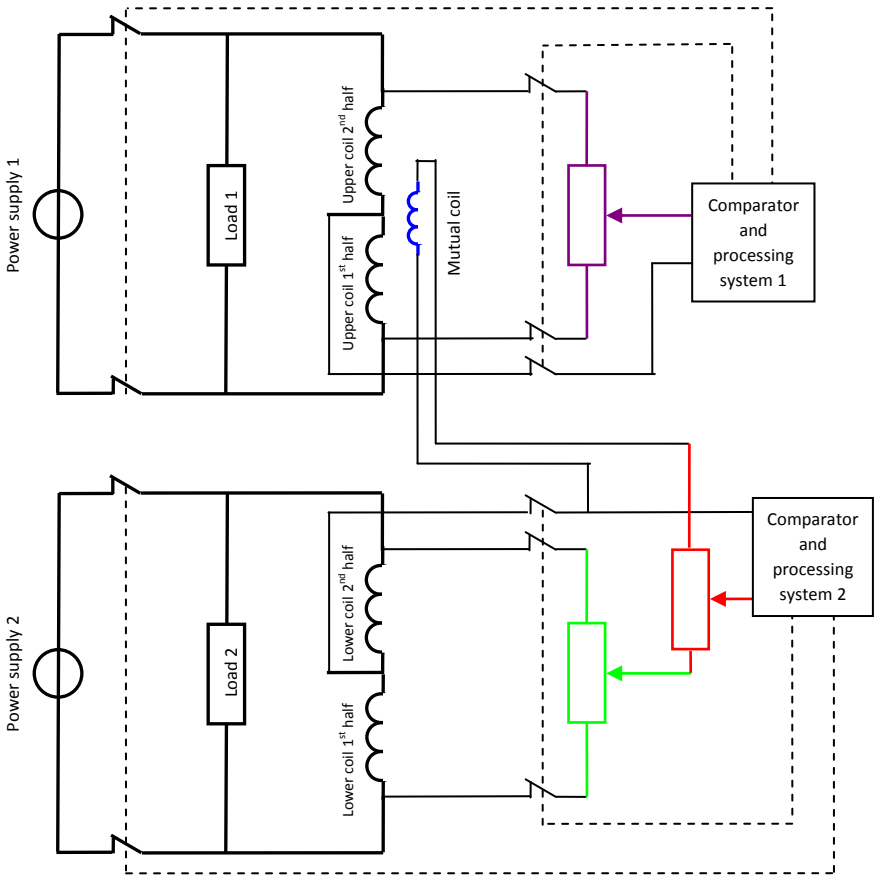

Figure 4-31: SMES II detection system

2.1.3 Practical implementation

Practically, the detection system we implemented consists of two separated electronic devices Figure 4-32). The first one is analogical and contains the detection bridges. Its inputs are the voltages of the four coil extremities, protected by high voltage switches and the voltage of the mutual coil inductance placed in the bore of the upper coil. Two potentiometers adjust the balance of the coils detection bridges. Another one sets the compensation of the lower coil protection by the mutual inductance. The signals of the bridges are amplified and normalized to provide two -15/+15V analogical outputs being images of the dissipative voltage in the two coils. These signals are transmitted to the second device.

Figure 4-32: Detection bridges (above) and process control device (below)

In the second device, those two analogical inputs are first compared to stabilized values, independently adjustable for each coil between 30 and 300 mV. When one of the signals exceeds its threshold, a digital countdown is started. If the value is still above the threshold at the end of the timer the system reckons that a quench is starting. This delay prevents the system to trigger on sudden voltage peaks appearing in the noise, for example during switch handling. The countdown time is programmable independently for both channels between 0 and 150 ms. The countdowns are executed by a microcontroller that also checks the values of various other parameters, including a the threshold value of the cryostat vacuum gauge, and the current in the two coils. The FPGA performs the logic controlling the charge/discharge and short-circuit switches for both coils and the switches protecting the detection bridges. It prevents the management of the power switches if all the parameters are not correct. These two devices were developed and realized at Neel Institute, by G. Simiand and O. Exshaw.

2.2 Cryogenics behaviour

SMES II cryogenics was first tested in April 2009. 40 temperatures were measured using the acquisition system presented § 1.1: on each pancake cooling plate, close to the cryocoolers, on the different thermalizations, on the thermal screen, etc. During the cooling, the current source powering the sensors was set to increasing values, from 10 µA to 500 µA, to ensure enough precision without heating the sensors too much. Frequent inversions of the current source were performed to check the existence of thermoelectric voltages, for this offset to be considered when re-processing the data.

2.2.1 Cooling time and minimal temperature

The cooling-down takes approximately one week, about the same time as with the first version. Nevertheless, the cooling of the coil itself is much faster: it takes around 2.5 days to have the coil windings below 15 K as shown Figure 4-33.

The remnant time is necessary to get the thermal screen and current leads thermalizations to their minimal temperatures and to fully stabilize the coils, whose final temperature is at the limit of our sensors calibration, around 12 K.

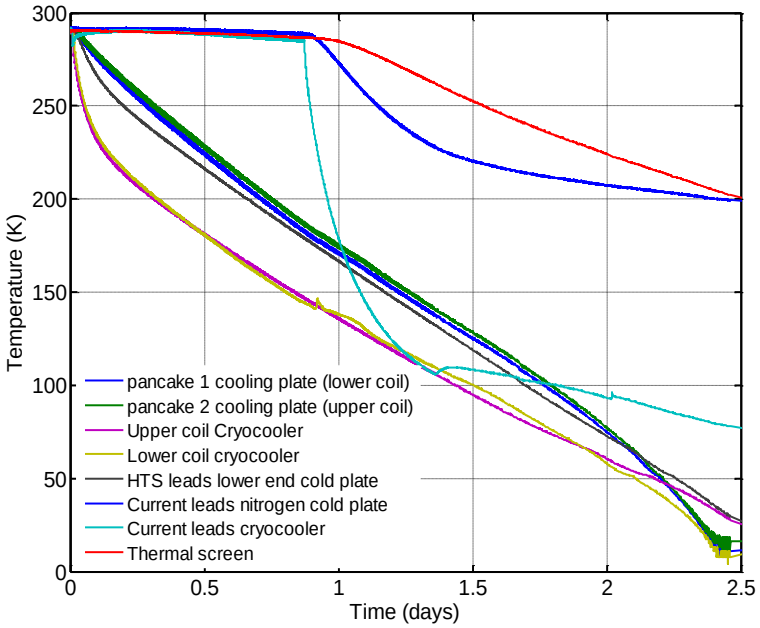

Figure 4-33: SMES temperatures during cooling

This is consistent with the minimal temperatures estimated between 11 and 12 K during the design presented in Chapter 3 § 4.2. As it was already mentioned, the cooling power of the two AL330 cooling the coils is not known with a high precision but this operation temperature indicates at least that the estimation of the losses on the coils were correct.

2.2.2 Nitrogen consumption

Temperature evolution with liquid nitrogen

As it was foreseen, operation without liquid nitrogen is possible only with limited current, the current leads thermalization cold plate being above 50 K. The additional cooling power provided by LN2 lower this temperature below 35 K (Figure 4-34), while the coils temperatures do not change perceptibly. This is again very close to the expected value, which was 34 K.

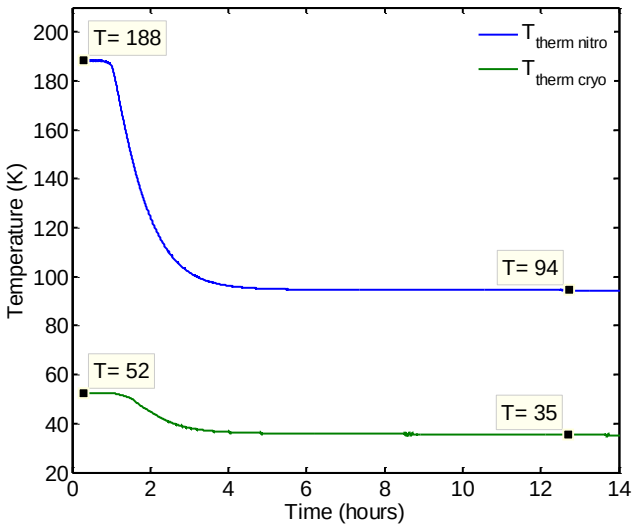

Figure 4-34: Nitrogen cooling

As seen Figure 4-34 the nitrogen cooling is fast, only a couple of hours are necessary to obtain a suitable operating temperature (below 40 K).

Liquid nitrogen consumption

The heating power on the nitrogen tank is due to the current leads and the thermal losses by radiation. There are 8 current leads, whose heating power was evaluated during the design at 8 W, their total heating power is thus 64 W.

The losses due to radiation are not negligible, due to the lack of thermal shielding between the tank and the cryostat upper dished head. They are evaluated about 32 W.

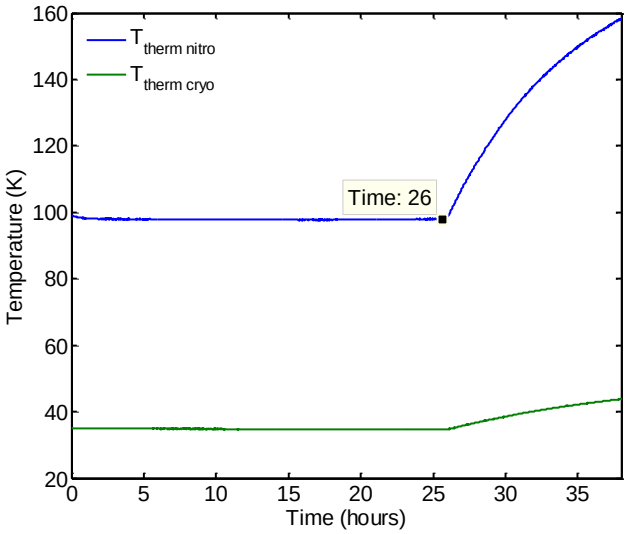

Figure 4-35: Nitrogen tank cooling capacity (graph starts immediately after refilling)

The energy necessary to evaporate 1 liter of liquid nitrogen being around 160 kJ, the 65 liters tank should provide around 30 hours of cooling power when the coil is not in use. It has practically to be refilled only every 26 hours (Figure 4-35).

Considering the inaccuracy on some of the critical design parameters (cryocooler cooling power, exact volume of the nitrogen tank, exchange between nitrogen and cold plates, etc.), the agreement between the design and the experimental values is satisfying.

2.3 Magnetic and Electric characterization tests

2.3.1 Detection / Protection device setting up

The first tests were conducted at low energies in order to adjust the detection / protection system. There are three parameters to be adjusted in our system: the two detection bridges corresponding to the two coils (in purple and green Figure 4-31), and the secondary compensation bridge for the lower coil (in red).

The two detection bridges were adjusted first and separately in order not to be influenced one by the other. For the lower coil, the input corresponding to the mutual coil was short circuited in this first test.

The equilibrium of each bridge is of course only adjustable when it is submitted to a voltage, thus when the coil is in transient state. This was obtained by ramping slowly the current up and down between 0 and 40 A under 5 V. During this setting up, the detection bridges (Figure 4-31a) were disconnected from the data processing device (Figure 4-31b) to prevent false detection. The bridges were adjusted so that the bridge output stays below the limit (40 mV) even during steep transients such as coil discharges.

After that, the compensation bridge was adjusted by short-circuiting the lower coil and varying the current in the upper coil. The results are presented Figure 4-36.

For a charging voltage of 5 V the upper coil bridge output $V_{unbal\ sup}$ in green is influenced by the charge of the lower coil. It reaches almost 50 mV without any current in the upper coil (from t=0 to t=30 s).

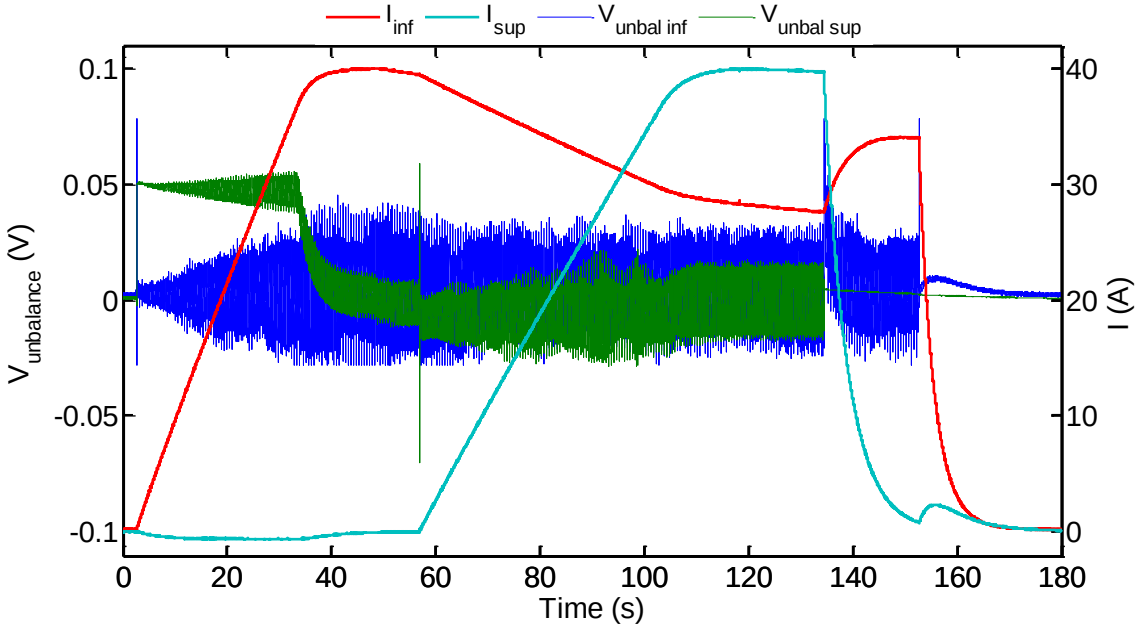

Figure 4-36: Detection outputs during coils charge and discharge

On the contrary, the lower coil detection bridge output, $V_{unbal\ sup}$ in blue is only slightly modified during the upper coil fast discharge around t=130 s, which demonstrates the efficiency of the compensation bridge.

2.3.2 Inductances and coupling evaluation

Measuring accurately the inductance is critical for SMES characterization. It gives the stored energy and, when compared to the energy transferred to the charge, the device efficiency. In order to obtain consistent evaluation, the evolution of the inductance with the circulating current and its derivative is first studied theoretically. An appropriate measurement method is selected in a second time, in order to minimize the measurement biases.

Influence of the current and its derivative on the coil inductances

As no magnetic material is used in our system, the value of the coil inductance is essentially determined by its topology and the distribution of current density in it. Two parameters may induce a modification of this value: The current density distribution in the wires, and the geometric deformations due to mechanical stresses.

a) Influence of the current density distribution

The current density distribution in a normal wire depends on the current derivative (the frequency), due to the skin effect, which is negligible in our case, due to the rather low frequencies (below 10 Hz) and the small section of the conductors. However, for a superconducting wire, it also depends on the

current value, as the current density in the cross-section is not homogenous even in quasi-static state.

Following the simplified Bean model commonly used for superconductors, we consider that the current density can only take two values: J_c (the critical current density) and 0. The section of wire submitted to J_c is the external layer, which is penetrated by the magnetic flux density. The wire critical current is reached when the entire wire section is penetrated, thus submitted to J_c (Figure 4-37).

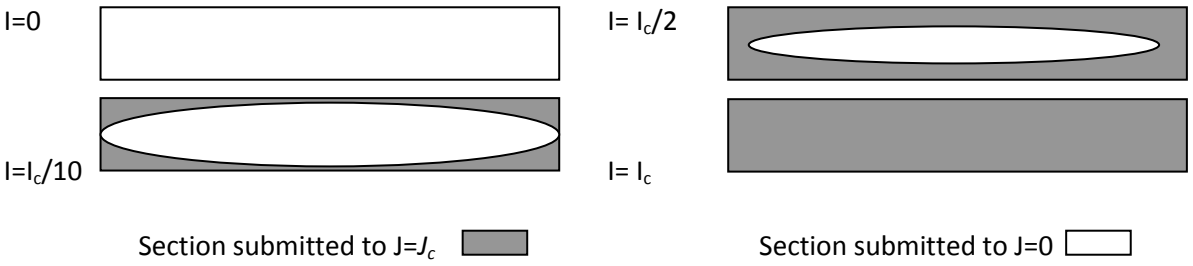

Figure 4-37: Repartition of the current density in a tape cross-section following the simplified Bean model (only the tape self-field is considered here)

To investigate the influence of the current density distribution (induced both by the current and its derivative) on the total inductance, a coil model was simulated using finite elements software Flux®. The study was conducted in axisymmetric 2D; each coil turn being represented by two areas with different current densities following the model presented Figure 4-37, though the repartition in the conductor is different. As the tapes are not only submitted to their self-field but also to the field of the coil, the current density will be concentrated on one side of the conductor, the side that is submitted to the higher field. Various current repartitions were studied, corresponding to different magnetic configurations.

This study requires a mesh sharp enough to accurately render the current repartition in the wires, this is why meshing the whole set of pancake is impossible. Only one pancake was simulated: it features 250 turns, the average turn number of the SMES II pancakes. The pancake inductance evolution with the current is represented Figure 4-38. The results shows that the current dependency is very small, and greatly below the level of accuracy that we could possibility achieve during measurements.

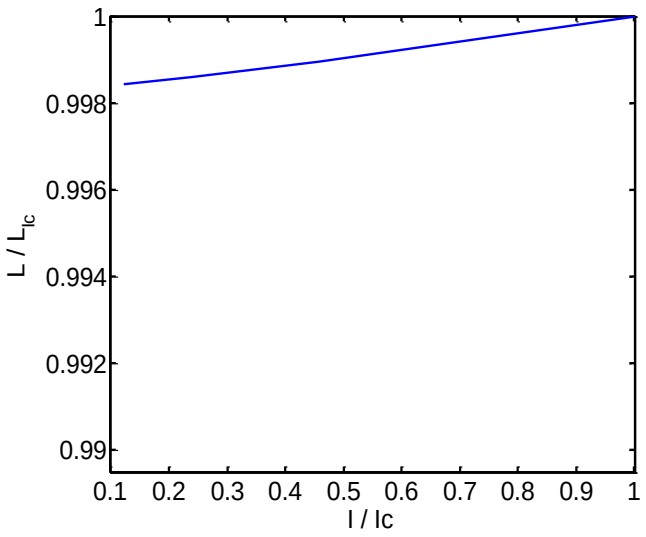

Figure 4-38: Simulated pancake inductance evolution

Other simulations were conducted with lower number of turns, showing that the influence of the current density repartition gets lower when the turns number increases. The inductance variation of the coils is thus probably even lower than that of a single pancake.

b) Influence of the mechanical stress

It is very difficult to obtain an accurate equivalent model of the coil mechanical behaviour, due to its complex composite structure. However, a pessimistic evaluation of the inner and outer diameter evolution may be obtained, under the following hypothesis:

- The turns are independent
- They are only made of the material having the lowest Young modulus (silver, 91 GPa at 20 K)
- The inner turn is submitted to the highest possible tensile stress before losing its superconducting properties, (120 MPa, cf. Chapter 1 § 1.2.4)
- The outer turn is submitted to compressive stress, also maximal (120 Mpa)

Under these hypothesises, the length of the inner turn increases by around 1 mm, while the length of the outer turn is reduced by about the same length, leading to radiuses variations below 0.1 mm. These variations have no measurable influence on the coils inductances.

Measurement method and results

In transient state, losses due to eddy currents and hysteresis affect the measurement accuracy. It must therefore be conducted in quasi-static state. However, if the coil reactive impedance is low its resistance cannot be neglected and must be measured at the same time. For this evaluation to be precise enough, reasonably high currents are necessary, though the current should remain well below the wires critical current for the superconductor itself not to dissipate.

Three inductance evaluation methods are commonly used: the first two methods are based on coil current ramping. The inductance is then obtained either by integrating the power to get the stored energy or differentiating the current to get the impedance. The third method is to use sinusoidal powering to evaluate directly the impedance.

In our case, the third method is not suitable, as it would require a power source providing low frequency / high current signal, which is difficult to achieve. Taking into account the highly perturbed electro-magnetic background due to the vibrations induced by the cryocoolers on the coil and measurement cables, the first method is preferred to the second, as integration provides a better noise reduction.

For this measure, both current and voltage on the coil are measured to obtain the power input. This power is integrated numerically to obtain the energy given to the coil (E_{input}). Under the assumption that both the inductance and resistance of the coil are constant, part of this energy is stored and part is dissipated, following Eq. (4-4). The energy E_{input} is then fitted to obtain bit *L* and *R* parameters.

$$E_{input} = \frac{1}{2} L \cdot I^2 + R \cdot I^2 \cdot t_{charge} = E_{stored} + E_{dissipated} \quad \textbf{(4-4)}$$

Of course this equation is only valid in quasi-static state, as hysteretic and eddy current losses are neglected. In order to validate this assumption measurements were conducted for low currents under constant voltages of 2, 10, 20 and 40 V. In fact, A.C. losses are not exactly negligible; this is why the measured inductance is slightly lower when the voltage is increased. However, this variation is lower than 1 % which is in the same order than our measurement precision.

Using higher voltages improves the safety of operation at high currents. As the coil reaches its limits faster, the amount of heat generated before the protection system triggers the discharge is lower and the coil temperature drift is therefore lower. In consequence, as the influence of the charging voltage on the inductance evaluation is negligible, measurements are conducted under 40 V. The results for the lower and upper coils are presented Figure 4-39.

The measured inductances for the lower and upper coils are respectively 4.23 H and 6.56 H, while the simulated values obtained using Flux® were 4.3 and 6.6 H. The higher resistance for the lower coil (4.2 mΩ instead of 1.52 mΩ) is due to the connections between the three coils segments, which are outside the cryostat.

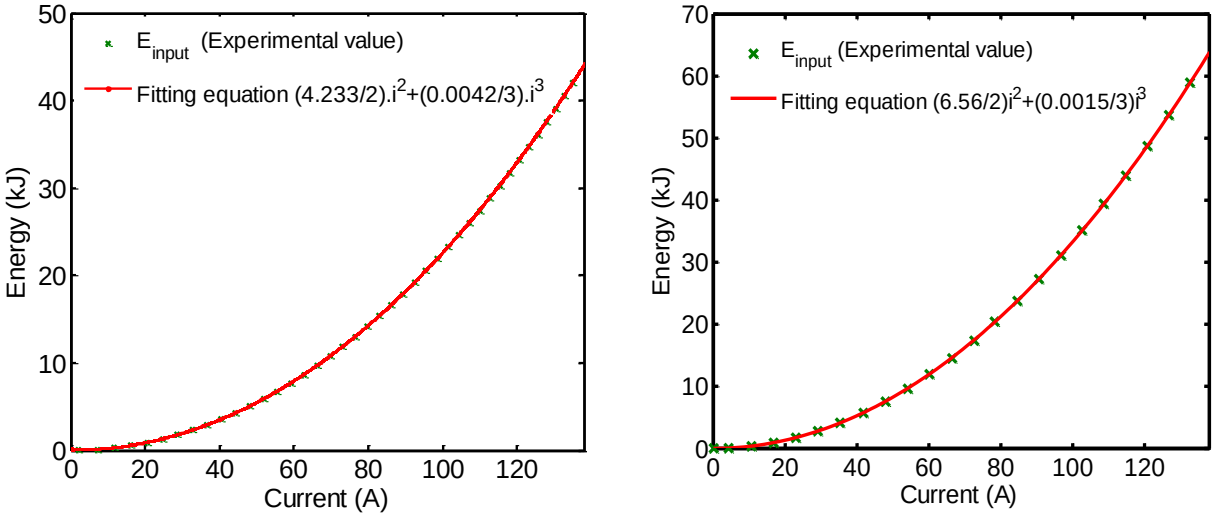

Figure 4-39: Energy charge on the lower (left) and upper (right) coils

Coupling Measurements

The magnetic coupling between the upper and lower coils may be obtained simply by using the two coils as a transformer. The upper coil is charged and discharged while the lower coil is in open circuit, and the ratio between the voltages on the two coils is measured (Figure 4-40). Knowing the inductances values, the coupling coefficient *k* is obtained through Eq. (4-5). For SMES II it is around 15.5 %.

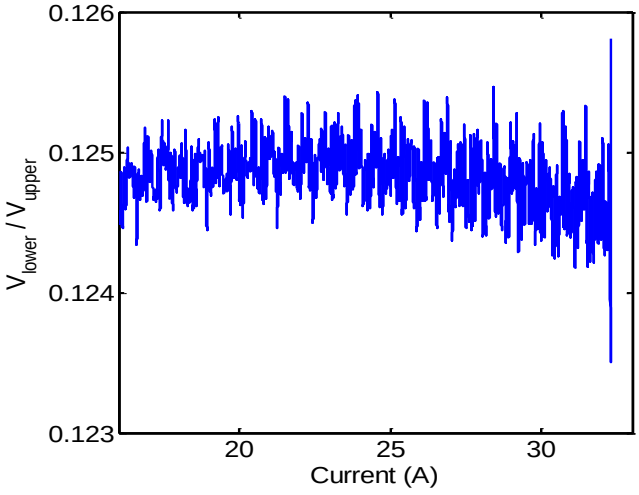

Figure 4-40: Ratio between upper and lower coils voltages during upper coil discharge

$$V_{lower}/V_{upper} = k \cdot \sqrt{L_{lower}/L_{upper}} \qquad \textbf{(4-5)}$$

This value is sensibly higher than what was expected (14 %, cf. Chapter 3, § 1.3.2). Thermal contraction was not considered when designing the fiber-glass spacer between the two coils, the distance between the coils is thus smaller than expected (about 0.25 %, 0.7 mm), which cause the magnetic coupling to be higher.

2.3.3 Operation limits and maximal stored energy

Each coil was tested at its limit fixed in a by the protection system for a dissipation level of 50 mV in a first time. The results on each coils were similar, around 200 A (Figure 4-41).

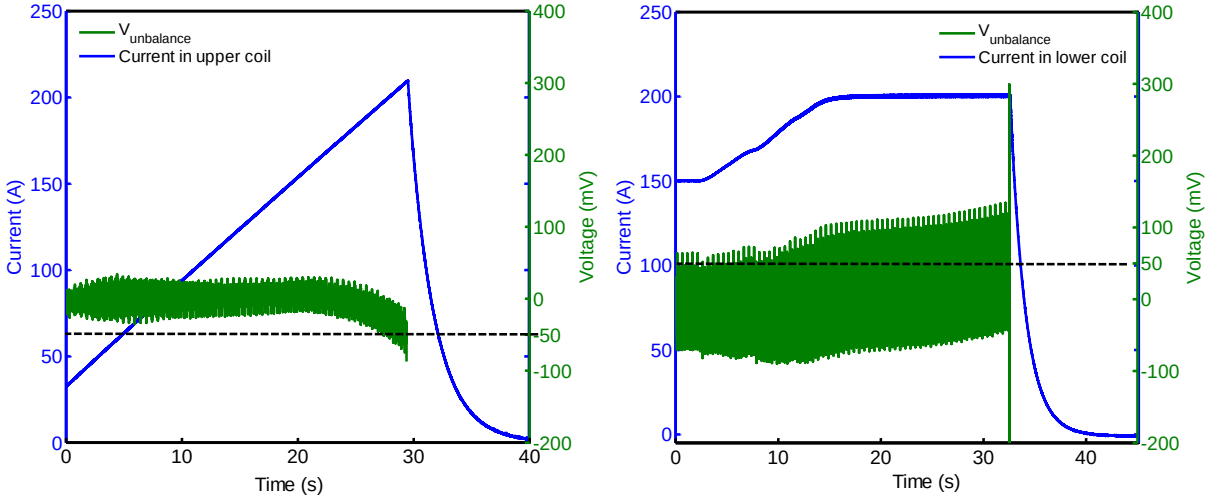

Figure 4-41: Upper (left) and Lower (right) coil maximal operating currents for 50 mV dissipation

However, the coils may be operated at higher currents for a short time. Operation was tested on the upper coil up to 255 A without any damage (Figure 4-42). Though the dissipation reach 200 mV, no sensible variation of the operating temperature is observed.

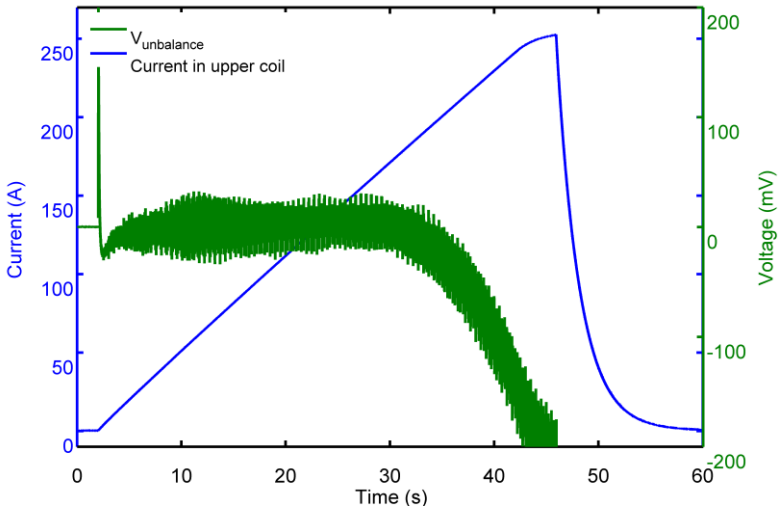

Figure 4-42 : Upper coil maximal operating current for 200 mV dissipation

These operating current values are consistent with the results obtained with SMES I. It proves that the pancake damaged during SMES I tests was correctly repaired. Considering the inductances measurements presented above, the maximal stored energy in the two coils are respectively 210 and 130 kJ on the upper and lower coils, when used separately.

2.3.4 First losses evaluation

Quasi-static losses and time constant

In quasi-static state the only existing losses are resistive losses and dissipation losses in superconducting material. The minimal losses are obtained when the current is low enough to have almost no dissipation in the superconductor, below 200 A. In this case the time constant is simply the *L/R* ratio: respectively 4316 and 769 s (72 min and 12 min 48 s) for the upper and lower coil.

As it is clearly visible for the lower coil on the right Figure 4-41, above 200 A even if the current value is constant, the dissipation voltage increases. It means that the dissipation that appeared locally in the superconductor produces enough heat to increase the wire temperature. The length of wire dissipating thus increases progressively, which leads to higher heat generation and temperature rise. In consequence, above 200 A operation ceases to be perfectly stable, and if the current is maintained for a long time the coils will ultimately quench. In any case, the protection system activates when the dissipating voltage reaches 40 mV, thus when the losses in the winding reaches 8 W under 200 A.

Transient losses

During discharges, the variation of the magnetic flux density induces eddy current in all the resistive elements (pancake copper plates, thermalization plates, thermal shield, cryostat, etc.). These losses increase in a first time with the frequency squared, then linearly due to the skin effect. They were studied for SMES I, whose design was optimized for them to remain negligible for a 2 s discharge (below 0.2 % of the total stored energy).

As the wires are superconducting, another kind of losses must be considered, due to the hysteretic behaviour of the material with regard to magnetic flux density. These losses are difficult to evaluate precisely, it requires a multi-domain numerical model integrating the electrical, magnetic and thermal behaviour of the whole coil winding. However, these losses are independent from the discharge speed, as a complete hysteretic cycle is made for each charge - discharge operation.

For SMES II, these losses were evaluated experimentally for the two coils by comparing the stored energy with the energy obtained during a discharge, the current being around 200 A (Figure 4-43).

- For the upper coil, the initial energy was 144 kJ, and the discharged energy 141.3 kJ. The total losses were thus about 2.7 kJ (1.8 %).
- For the lower coil; the initial energy was 88.9 kJ. 84.2 kJ were discharged and 1.6 kJ was lost (1.7 %).

This demonstrates the good efficiency (98 %) of SMES storage, at least for low speeds where eddy currents losses are negligible. Additional measurement would be necessary to investigate the behaviour of the device at higher frequencies, but this will require very powerful 4 quadrants voltage/current source that are not available for now.

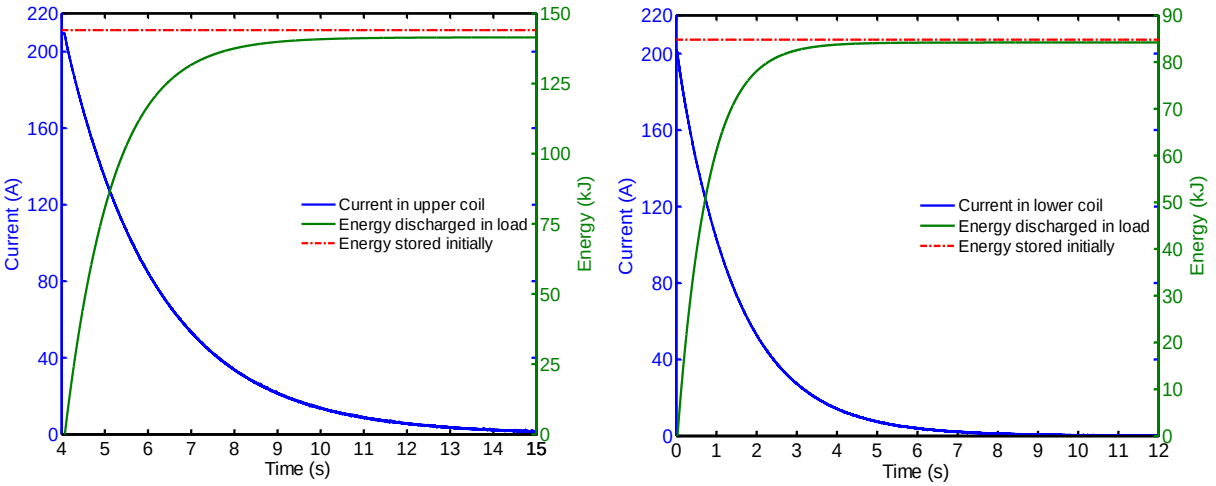

Figure 4-43: Energy losses during discharge in upper (lower) and lower (right) coil

2.4 Power operation

SMES II tests as electromagnetic launcher power source were conducted in cooperation with Saint Louis Institute (ISL). In this section are presented the results obtained for capacitor reloading (indirect powering) and XRAM discharge (direct powering). SMES II sequential discharge capability was not tested at full power due to the potential risk of damage, but preliminary results demonstrate its effectiveness for such operations.

2.4.1 Fast capacitor reloading

As it was already mentioned at the beginning of Chapter 3, indirect powering through capacitors is at present time the only possible way of integrating SMES in an electromagnetic launcher power chain. Moreover, such energy transfer is interesting to study for three reasons.

- The discharge frequency is constant, which is convenient for A.C. losses evaluations.
- Instead of having a voltage pulse like with resistive discharge, the voltage value starts from 0 and evolves smoothly which is safer for the insulation system.
- The maximal voltage being reached at the end of the discharge, if a breakdown occurs it will happen at the end of the discharge, when the left stored energy in the coil is lower. The electric arc induced will thus dissipate less.

Experimental setting

The electric circuit implemented for the tests is presented Figure 4-44, along with the experimental setting:

The SMES upper coil is initially charged using a flywheel (not represented), under approximately 40 V. The power source is then disconnected which cause the energy stored in the SMES to be transferred to the capacitors. There are nine of them, measuring 970 µF each, for a total of 8.73 mF. A diode prevents the energy to oscillate between coil and capacitors.

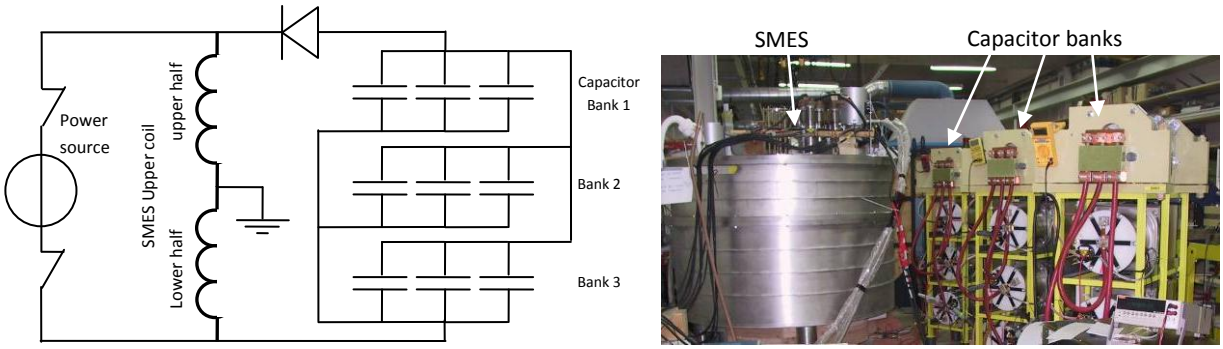

Figure 4-44: SMES - Capacitor transfer circuit (left) and practical implementation (right)

Results

The coil maximal operating voltage was theoretically 9 kV (+ 4.5 kV on one end, -4.5 kV on the other). As a breakdown of the coil and/or current leads insulation would lead to its destruction, a very high safety margin is kept during tests. In consequence, the operating voltage is limited at one third of the rated value, 3 kV (Figure 4-45).

During this test the voltage reached 2.7 kV, the upper coil being initially charged at 102 A.

The energy initially stored in the coil was about 34.4 kJ, while the energy transferred to the capacitor bank was 31.8 kJ.

The total efficiency of this transfer is thus about 92 %.

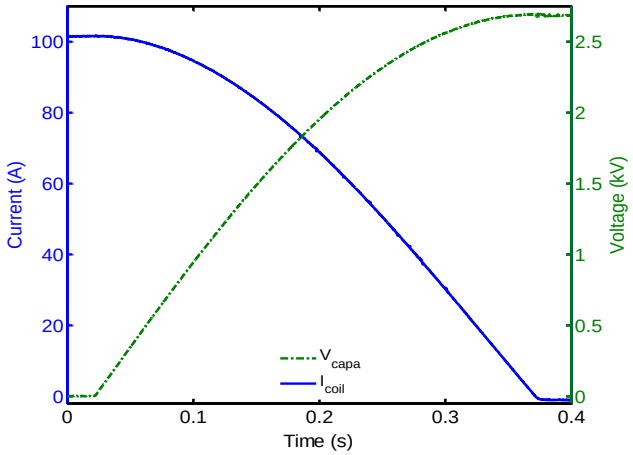

Figure 4-45: Upper coil discharge in capacitors

This lower efficiency when compared to what was evaluated above in § 2.3.4 may be explained by the losses in the transfer circuit (multiple resistive connections between the capacitors banks).

2.4.2 XRAM operation

As it was already mentioned, the operating current of SMES II is too low to directly power a launcher. However, the concept may be tested using a load having a resistance comparable to a real launcher (about 5 mΩ). The objective of this test is to evaluate the behaviour of the superconducting coils in XRAM operation and the discharge efficiency.

Experimental setting

The XRAM commutation system tested with the 3 lower coil segments is presented Figure 4-47. As mentioned in Chapter 3 § 1.2.3 it features counter-current solid-state switches developed at ISL (ICCOS system). Operation is divided in three phases:

- Initially, the small capacitors C_1 C_2 and C_3 are charged up to and adapted voltage (a few tenth of Volts) which depends of the expected current value and the impedance of the load.
- By triggering Th_1, Th_2 and Th_3, the coils series charging circuit is closed and their current starts to increase
- When the current in the coils segments reach the desired value, Th_4 is triggered. It closes the capacitors $C_{1,2,3}$ circuits through the load, which block $Th_{1,2 \text{ and } 3}$ by cancelling the current passing through them for a short time (hence the name, counter-current switch). Once the series circuit is open, the currents of the coil segments circulate through the parallel discharge circuit, including the three sets of diodes, Th_4 and the load.

The main interest of such system is that all the series-circuit switches are opened by triggering only one element (Th_4). The very good synchronisation obtained using this method makes possible to use the XRAM concept with a very high number of elements (cf. Chapter 2 § 2.1): up to 20 stages were already tested at ISL with resistive inductances.

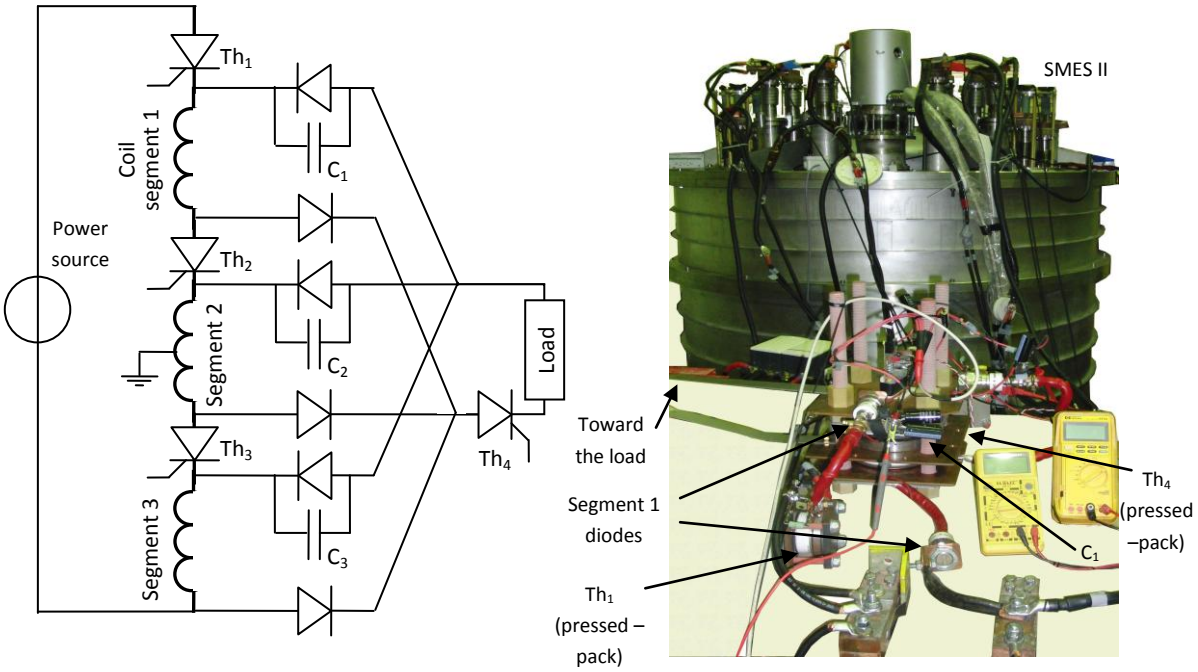

Figure 4-46 : XRAM discharge circuit (left) and practical implementation (right)

Current discharge profiles and discharge efficiency

The coupling coefficients between the three segments being different, the evolutions of their currents will also differ. Moreover, the inductances of the segments are not exactly equals. They are respectively of 542, 595and 505 mH for the upper middle and lower segments.

The evolution Figure 4-47 shows that the middle segment is overcharged. The lower segment discharge is faster than the upper segment one. Spice simulations of a simplified layout, including the segments inductances, their coupling and the discharge diodes but with perfect switches instead of thyristors shows the same kind of current waveforms.

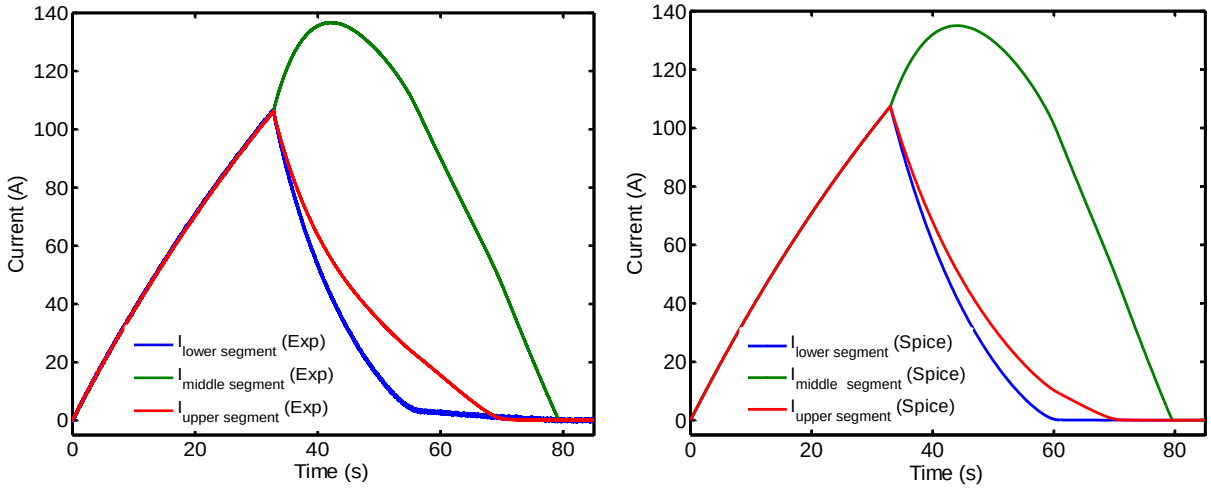

Figure 4-47: Evolution of the current in the coils segments. Experimental (left) Spice simulations (right)

Spice simulations with other coupling values also demonstrate that the current circulating in the load I_{output} does not change significantly with the coupling balance between the three segments. In consequence, I_{output} may be fitted using Eq. (4-6), the equation for equilibrated XRAM discharge.

$$I_{output} = \left(3 \cdot I_{\max} + V_{threshold} / R_{eq}\right) \cdot e^{-R_{eq}/L_{eq} \cdot t} - V_{threshold} / R_{eq} \qquad \textbf{(4-6)}$$

Where I_{max} is the current reached by the coil segments at the discharge beginning, $V_{thershold}$ is the sum of all the voltage drops induced in each parallel branch by the two diodes and Th_4. R_{eq} is the equivalent resistance of the parallel circuit (mainly the load). L_{eq} the equivalent inductance (cf. Chapter 2 § 2.1.2) which is the total inductance of the three segments, $L_{lower\ coil}$ divided by 9.

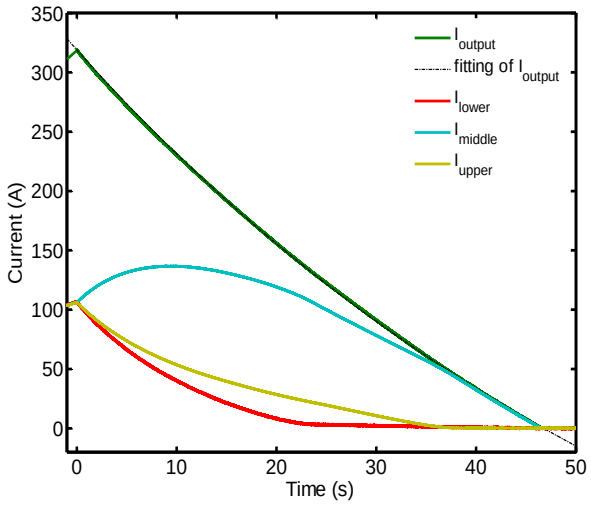

Figure 4-48: XRAM discharge currents

The fitting result is shown Figure 4-48 (green dotted line), with the following coefficients:

I_{max} = 106 A; L_{eq} = 0.470 H; R_{eq} = 7 mΩ; $V_{thershold}$ = 2.26 V.

These values are in perfect agreement with the experimental setting: The load resistance is 5 mΩ.

The fitting of I_{output} makes it easy to determine the discharge efficiency. From the initial energy E_{stored}=24 kJ, the energy discharged in the 5 mΩ load is E_{load}=6.4 kJ, while 2.5 kJ are dissipated in the connection cables and 15 kJ are dissipated in the commutation system.

The total efficiency is thus about 27 %. This rather low value when compared to the first efficiency studies (70 %) on XRAM presented in Chapter 2 § 2.1.3 may be explicated by the fact that the tests

are conducted at much lower currents, where the losses due to the commutation system are predominant.

XRAM operating limits

The only problem with unbalanced magnetic coupling is that the middle segments may quench when overcharged. However, the current reaches its maximum in the middle segment when the two other segments are already partially (or totally, depending on the load resistance value) discharged. The operating limits are thus determined by the maximal current of the middle segment alone, 337 A (Figure 4-49).

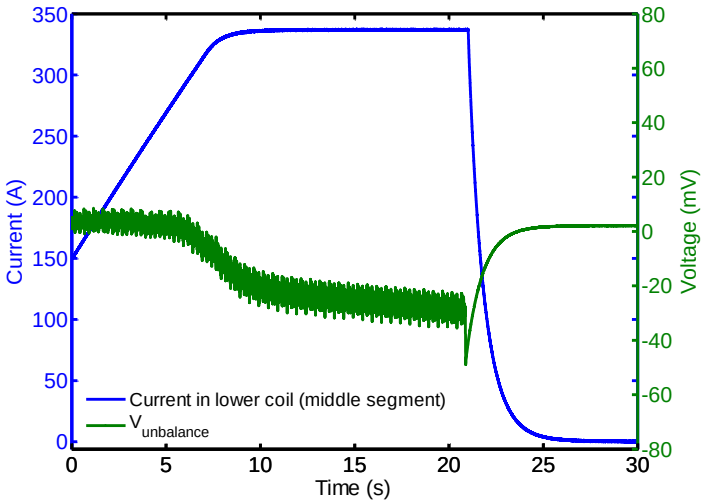

Figure 4-49 : Operating limits of the middle segment

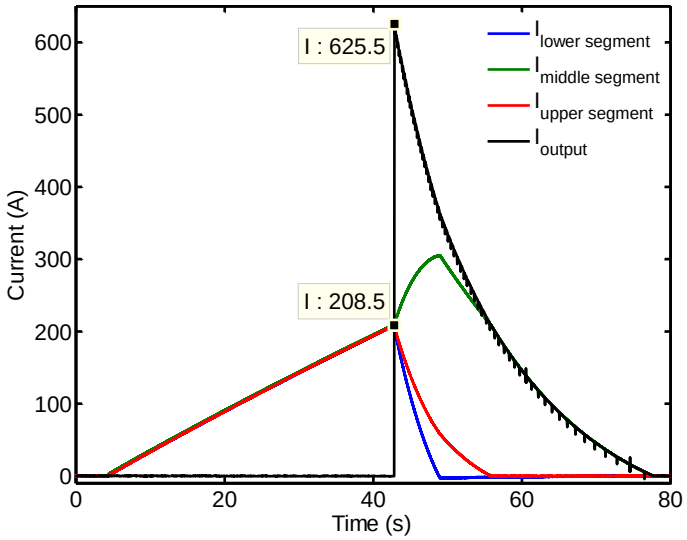

Figure 4-50: Maximal discharge current with SMES II XRAM system

The system was tested with a maximal current of 300 A for the middle segment, and with a higher load resistance, 27 mΩ, to insure a faster discharge and limit the temperature rise in the superconducting wires in case of quench when the maximal current is reached. Considering this new resistance value, the current overcharge is higher, it reaches 50 %. The initial charging current is thus be limited above 200 A. The maximal output current obtained during this test is 625.5 A (Figure 4-50).

The discharge resistance being higher, the efficiency is increased. During this test, 89 kJ were stored at the beginning, and 60 kJ were dissipated in the load. The efficiency reaches 67 %.

2.4.3 Sequential discharge

Sequential discharge was only tested up to 100 A, to reduce the chances of damaging the coils in case of problem with the compensated protection system. However, the results Figure 4-51 makes it possible to compare the lower coil overcharge with the theoretical value given by Eq. (4-7).

$$\Delta i_{lower\ coil} = k\sqrt{L_{upper} / L_{lower}} \cdot (i_{upper\ coil})_{init} \qquad \textbf{(4-7)}$$

Where $(i_{upper\ coil})_{init}$ is the current circulating in the upper coil at the beginning of its discharge, k the coupling coefficient between the two coils, and $\Delta i_{lower\ coil}$ is the current over-charge in the lower coil.

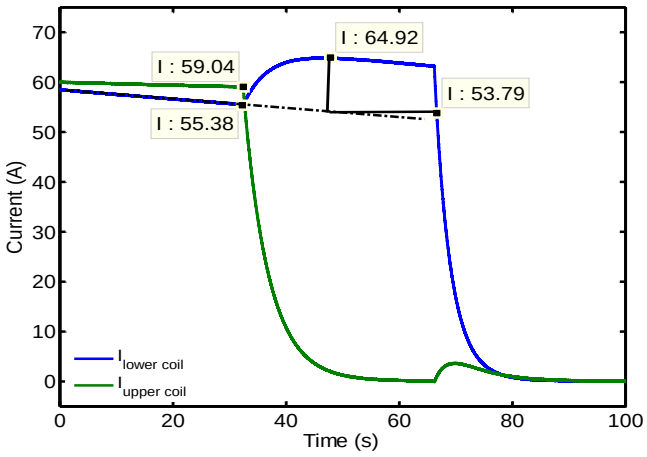

Figure 4-51: Sequential discharge

If we estimate the current overcharge on the lower coil taking as reference the lower coil current value when the upper coil discharge starts, $\Delta i_{lower\ coil}$ = 9.5 A.

However, as the discharge is slow, part of the energy stored in the lower coil is dissipated during the overcharging time, which led to an underestimation of Δi.

The current overcharge may also be calculated under the hypothesis of a constant slope for the lower coil current (see Figure 4-51), which leads to a higher value, 11.1 A closer to the expected one obtained using Eq.(4-7), 11.5 A. Sequential operations may thus be obtained with identical energy discharged from the two coils. Additional tests will be necessary to reach full power in this configuration.

3. Conclusion

The realization of SMES II was a long and sometimes difficult process that took almost three years. A lot of small practical problems where encountered that were not mentioned in this work, requiring quick and pragmatic solutions. Its completion was possible thanks to the experience obtained with SMES I and the know-how that was accumulated in the laboratory by all the team members: the technicians, especially A. Boulbès, G. Barthelemy, G. André and L. Germani, and the engineer M. Deleglise.

In the main this realization was a success, most of the specifications that were defined during the design were obtained. The only unsolved problem was the high voltage thermalization interface, which led us to reduce our expectations for the number of XRAM stages, from 12 to 6. However, this choice made it possible to obtain the expected operating temperature and rated current.

Realizing a test campaigns at ISL made it possible to demonstrate the possibility of transporting the device without damages, which was not straightforward as the coil is hanging from the cryostat upper flange and thus very sensible to tilting. It demonstrates also that operating it in an “industrial” environment is possible: the device was operated for a relatively long time (several weeks) by ISL

staff members with no particular knowledge in cryogenics. Its operation was also monitored remotely, which allowed us to verify its behaviour during the whole time.

The tests in themselves were also successful. The upper coil operating voltage was tested up to 2.7 kV, and the operating current reached 255 A, which gives a maximal available power of 680 kW, about four times higher than with SMES I. The energy transfer to power capacitors is efficient 92 %, which demonstrates the possibility to use SMES in an EML supply chain, as an intermediate storage to rapidly reload (about 0.5 s) the discharge capacitors.

With the lower coil, the feasibility of XRAM concept with HTS coils and solid-state switches was demonstrated, even though the output current (625 A) was reduced compared to the original specifications, due to the lower number stages. These results may be used as basis for preliminary studies of larger scale devices with output currents enabling direct EML powering.

Sequential discharge of both coils was tested at low currents, with results in good agreement with what was expected. However, this operation mode was never tested at full power, additional tests will be necessary to determine the operating limits of SMES II in this operation mode.

Finally, the tests of the SMES II coils in all the possible configurations have demonstrated the efficiency of the detection and protection system, and the considerable gains that were obtained compared with SMES I version. The operating limits were reached on both coils several times without damages, and number of false detection events was drastically lowered, thanks to the increased signal-noise ratio.

General Conclusion

The results of this work on High Temperature Superconducting Magnetic Energy Storage let expect considerable gains for Electro-Magnetic Launcher powering, through optimized SMES – EML integration and gives some preliminary experimental results confirming the feasibility of such system.

The activities that were conducted may be grouped in two complementary domains: theoretical studies on optimal SMES configurations on one hand, and studies for practical SMES design and realization on the other.

Concerning the studies on optimal SMES configuration, the proposed Superconducting Self-Supplied Electromagnetic Launcher (S^3EL) design reduces the operating current eight times when compared to classical capacitor-based powering. The launcher characteristics (length, width, projectile mass and output speed) and the initial stored energy being identical in both configurations.

Moreover, the preliminary results on cryogenic XRAM indicate that the overall energy efficiency of SMES powering using XRAM principle is not reduced considerably when compared to single coil SMES, even if the number of XRAM elements in parallel is high.

At the same time, using XRAM induces substantial savings in terms of required cooling power, which reduces considerably the volume occupied outside of the cryostat by the SMES cooling system, and its power consumption.

In consequence, and considering the possibilities offered by second generation HTS conductors such as YBaCuO Coated Conductor tapes, a small scale functional S^3EL demonstrator seems practically feasible, and such device would be an essential step toward large scale high efficiency launcher development.

With the studies conducted for the design and realization of the demonstrator SMES II, a lot of experience and know-how has been accumulated, which will make the design and realization of future demonstrators easier. An efficient optimization tool for current leads system was developed, and experience was gathered in the field of high voltage insulation with good thermal properties.

The results obtained with SMES II upper coil demonstrate the possibility to discharge a conduction-cooled SMES under high voltage (3 kV); it gives us a proof of concept for SMES-based high-efficiency fast capacitor reloading (0.5 s).

The lower coil successful XRAM operation at 625 A demonstrates the possibility to operate a HTS-based XRAM system. The efficiency is of course lower to what could be expected at higher current, but these first results give an experimental basis to the future theoretical works on cryogenic XRAM systems.

Finally, the design and realization of a set of two coupled coils give and insight of what could be the future S^3EL powering systems, as inductive reloading of the S^3EL discharge coil by means of a secondary coupled coils will be investigated in the future.

References

[Abe99] T. R. Abel. D-SMES for Wisconsin. *Modern power systems*, 19(10):28–29, 1999

[AP88] G. Antonini and J. P. Pain. Low-temperature thermal insulants. *Revue De Physique Appliquee*, 23(11):1755–1760, November 1988.

[Bel06] B. Bellin. *Contributions a l etude des bobinages supraconducteurs : le projet DGA du SMES HTS Impulsionnel*. PhD thesis, INPG, 2006.

[BKK+09] J. H. Bae, S. H. Kim, H. J. Kim, M. H. Sohn, K. C. Seong, and H. M. Kim. Design, fabrication and evaluation of a conduction cooled HTS magnet for SMES. *Physica C-superconductivity and Its Applications*, 469(15-20):1794–1798, August 2009.

[BLGB05] O. Bozic, J.M. Longo, P. Giese, and J. Behrens. High-end concept based on hypersonic two-stage rocket and electro-magnetic railgun to launch micro-satellites into low-earth orbit. *Proceedings of the Fifth European Symposium on Aerothermodynamics for Space Vehicles*, pages 451–456, 2005.

[BT10] A. Badel and P. Tixador. Détecteur de transition de bobine supraconductrice, PCT Patent FR2011/050318, 2011.

[Car08] T. Carrof. *Développement de conducteurs à base d'YBaCuO sur des substrats flexibles par MOCVD*. PhD thesis, INPG, 2008.

[DBS09a] P. Dedie, V. Brommer, and S. Scharnholz. Experimental realization of an eight-stage xram generator based on ICCOS semiconductor opening switches, fed by a magnetodynamic storage system. *IEEE Transactions On Magnetics*, 45(1):266–271, January 2009.

[DBS09b] P. Dedie, V. Brornmer, and S. Scharnholz. IcCCOS countercurrent-thyristor high-power opening switch for currents up to 28 ka. *IEEE Transactions On Magnetics*, 45(1):536–539, January 2009.

[DVT03] G. Donnier-Valentin and P. Tixador. Optimisation du SMES 10 MJ. Technical report, CNRS, 2003.

[EB81] Y. Eyssa and R. Boom. Considerations of a large force balanced magnetic energy storage system. *IEEETransactions On Magnetics*, 17(1):460–462, 1981.

[ETWS08] T. Effio, U. P. Trociewitz, X. Wang, and J. Schwartz. Quench induced degradation in $Bi_2Sr_2CaCu_2O_{8+x}$ tape conductors at 4.2 k. *Superconductor Science & Technology*, 21(4):045010, April 2008.

[Fer69] M. Ferrier. *Stockage d'énergie dans un enroulement supra-conducteur*. International institute of Refrigeration, Low temperatures and Electric power, 1969.

[GL05] J. Gallant and P. Lehmann. Experiments with brush projectiles in a parallel augmented railgun. *IEEETransactions On Magnetics*, 41(1):188–193, January 2005.

[HCF86] C. G. HOMAN, C. E. CUMMINGS, and C. M. FOWLER. Superconducting augmented rail gun (sarg). *Ieee Transactions On Magnetics*, 22(6):1527–1531, 1986.

[HYE+05] P. Haldar, H. Ye, H. Efstathiadis, J. Raynolds, M. J. Hennessy, O. M. Mueller, and E. K. Mueller. Improving performance of cryogenic power electronics. *IEEE Transactions On Applied Superconductivity*, 15(2):2370–2375, June 2005.

[IS80] Y. Iwasa and M.W. Sinclair. Protection of large superconducting magnets: maximum permissible undetected quench voltage. *Cryogenics*, 20(12):711–714, December 1980.

[Iwa03] Yukikazu Iwasa. HTS magnets: stability; protection; cryogenics; economics; current stability/protection activities at FBML. *Cryogenics*, 43(3-5):303–316, March 2003.

[Iwa06] Yukikazu Iwasa. HTS and NMR/MRI magnets: Unique features, opportunities, and challenges. *Physica C: Superconductivity*, 445-448:1088–1094, October 2006.

[KAE+95] S. KATSUKI, H. AKIYAMA, N. EGUCHI, T. SUEDA, M. SOEJIMA, S. MAEDA, and K. N. SATO. Augmented railgun using a permanent-magnet. *Review of Scientific Instruments*, 66(8):4227–4232, August 1995.

[KRSS91] R. KARUNANITHI, A. K. RAYCHAUDHURI, Z. SZUCS, and G. V. SHIVASHANKAR. Behavior of power mosfets at cryogenic temperatures. *Cryogenics*, 31(12):1065–1069, December 1991.

[KSC+06] H. J. Kim, K. C. Seong, J. W. Cho, J. H. Bae, K. D. Sim, K. W. Ryu, B. Y. Seok, and S. H. Kim. Development of a 3 MJ/750 kVA SMES system. *Cryogenics*, 46(5):367–372, May 2006.

[LLC10] Tres Amigas LLC. http://www.tresamigasllc.com, 2010.

[LPW01] P. Lehmann, H. Peter, and J. Wey. First experimental results with the ISL 10 MJ railgun pegasus. *IEEE Transactions On Magnetics*, 37(1):435–439, January 2001.

[LRVB07] P. Lehmann, B. Reck, M. D. Vo, and J. Behrens. Acceleration of a suborbital payload using an electromagnetic railgun. *IEEE Transactions On Magnetics*, 43(1):480–485, January 2007.

[MCK+09] T. Mito, H. Chikaraishi, A. Kawagoe, R. Maekawa, R. Abe, T. Baba, K. Okumura, A. Kuge, M. Iwakuma, and F. Sumiyoshi. Summary of a 1 MJ Conduction-Cooled LTS Pulse Coil Developed for 1 MW, 1 s UPS-SMES. *IEEE Transactions On Applied Superconductivity*, 19(3):1999–2003, June 2009.

[MKK+03] R. Mikkonen, T. Kalliohaka, A. Korpela, J. Lehtonen, and R. Perala. A 0.2 MJ cryogen free Nb3SnSMES in UPS application. *Superconductor Science & Technology*, 16(8):946–950, August 2003.

[Moo82] Francis C. Moon. The virial theorem and scaling laws for superconducting magnet systems. *Journal of Applied Physics*, 53(12):9112–9121, 1982.

[NHM+06] S. Nagaya, N. Hirano, H. Moriguchi, K. Shikimachi, H. Nakabayashi, S. Hanai, J. Inagaki, S. Ioka, and S. Kawashima. Field test results of the 5 MVA SMES system for bridging instantaneous voltage dips. *IEEE Transactions On Applied Superconductivity*, 16(2):632–635, June 2006.

[NTES04] W. C. Nunnally, J. E. Thompson, T. G. Engel, and C. V. Smith. An improved, linear homopolar, electro-magnetic launcher: Star. *12th Symposium On Electromagnetic Launch Technology*, pages 91–95, 2004.

[NWS+05] Shinichi Nomura, Naruaki Watanabe, Chisato Suzuki, Hiroki Ajikawa, Michio Uyama, Shinya Kajita, Yoshihiro Ohata, Hiroaki Tsutsui, Shunji Tsuji-Iio, and Ryuichi Shimada. Advanced configuration of superconducting magnetic energy storage. *Energy*, 30(11-12):2115–2127, 2005.

[Sch02] J. H. Schultz. Protection of superconducting magnets. *IEEE Transactions On Applied Superconductivity*, 12(1):1390–1395, 2002.

[SEL+08] J. Schwartz, T. Effio, X. T. Liu, Q. V. Le, A. L. Mbaruku, H. J. Schneider-Muntau, T. M. Shen, H. H. Song, U. P. Trociewitz, X. R. Wang, and H. W. Weijers. High field superconducting solenoids via high temperature superconductors. *IEEE Transactions On Applied Superconductivity*, 18(2):70–81, June 2008.

[SMH+05] K. Shikimachi, H. Moriguchi, N. Hirano, S. Nagaya, T. Ito, J. Inagaki, S. Hanai, M. Takahashi, and T. Kurusu. Development of MVA class HTS SMES system for bridging instantaneous voltage dips. *IEEE Transactions On Applied Superconductivity*, 15(2):1931–1934, June 2005.

[SY80] I. N. Sviatoslavsky and W. C. Young. Structural design features for commercial fusion power reactor magnet systems. *Nuclear Engineering and Design*, 58(2):207–218, May 1980.

[TBA11] P. Tixador, A. Badel, and M. Amiet. Lanceurs électromagnétiques à rails et procédé associé de lancement d'un projectile, French patent N° 11/00111, 2011.

[TDB+08] P. Tixador, M. Deleglise, A. Badel, K. Berger, B. Bellin, J. C. Vallier, A. Allais, and C. E. Bruzek. First tests of a 800 kJ HTS SMES. *IEEE Transactions On Applied Superconductivity*, 18(2):774–778, June 2008.

[TPT+03] F. Trillaud, H. Palanki, U. P. Trociewitz, S. H. Thompson, H. W. Weijers, and J. Schwartz. Normal zone propagation experiments on HTS composite conductors. *Cryogenics*, 43(3-5):271–279, March 2003.

[TTNS02] H. Tsutsui, H. Tsutsui, S. Nomura, and R. Shimada. Optimization of SMES coil by using virial theorem. *IEEE Transactions On Applied Superconductivit*, 12(1):800–803, 2002.

[Ull95] G. W. Ullrich. Summary of the DNA SMES Development Program. *IEEE Transactions On Applied Superconductivity*, 5(2):416–421, June 1995.

[WAN+09] K. Watanabe, S. Awaji, G. Nishijima, S. Hanai, and M. Ono. Cryogen-free 23 T superconducting magnet with a 7.5 T $YBa_2Cu_3O_7$ insert coil. *Applied Physics Express*, 2(11):113001, November 2009.

[WEM+99] W. Weck, P. Ehrhart, A. Muller, H. Scholderle, and E. Sturm. Demonstration of a superconducting inductive pulsed power supply at simulated load conditions. *IEEE Transactions On Magnetics*, 35(1):383–387, January 1999.

[Wil83] Martin N. Wilson. *Superconducting Magnets*. Clarendon Press, 1983.

[WSPM09] D. A. Wetz, F. Stefani, J. V. Parker, and I. R. Mcnab. Advancements in the development of a plasma-driven electromagnetic launcher. *IEEE Transactions On Magnetics*, 45(1):495–500, January 2009.

[XWD+08] L. Y. Xiao, Z. K. Wang, S. T. Dai, J. Y. Zhang, D. Zhang, Z. Y. Gao, N. H. Song, F. Y. Zhang, X. Xu, and L. Z. Lin. Fabrication and tests of a 1 MJ HTS magnet for SMES. *IEEE Transactions On Applied Superconductivity*, 18(2):770–773, June 2008.

[YLR+07] H. Ye, C. Lee, J. Raynolds, P. Haldar, M. J. Hennessy, and E. K. Mueller. Silicon power mosfet at low temperatures: A two-dimensional computer simulation study. *Cryogenics*, 47(4):243–251, April 2007.

[YLSH09] H. Ye, C. Lee, R. W. Simon, and P. Haldar. Development of cryogenic power modules for superconducting hybrid power electronic system. *International Journal of Materials & Product Technology*, 34(1-2):188–199, 2009.

Table of Figures

Table of Tables

Appendix

1. Modeling of a Capacitor and SMES supply for EML launch

1.1. Capacitor powering

The equations governing the behavior of the system when $V_{capa} > 0$ are :

$$\left\{\begin{array}{l} m.a(t) = \frac{1}{2} l_{launcher} \cdot i(t)^2 - \alpha \cdot v(t) \\ di/dt = -\frac{\int i(t)}{C \cdot L_{tot}(t)} - \left[\frac{R_{tot}(t)}{L_{tot}(t)} + \frac{l_{launcher} \cdot v(t) \cdot i(t)}{L_{tot}(t)}\right] \cdot i(t) \end{array}\right\} \quad \text{(A-1)}$$

With :

$$R_{tot}(t) = R_{constant} + r_{launcher} \cdot x_{launcher}(t)$$
$$L_{tot}(t) = L_{constant} + l_{launcher} \cdot x_{launcher}(t)$$

Where m is the mass of the projectile, a its acceleration and v its speed, $l_{auncher}$ and $r_{launcher}$ respectively the linear inductance and resistance of the launcher and α the friction coefficient. $L_{constant}$ and $R_{constant}$ represent respectively the inductance and resistance of both the connection cables between capacitor and launcher and the pulse forming unit, while C is the capacitor value.

When V_{capa} reaches 0, the flyback diode starts conducting current, short-circuiting the capacitor. The first term of Eq. (A-1) is therefore equal to 0, at least under the assumption of a null forward voltage. The equations become Eq. (A-2).

$$\left\{\begin{array}{l} m.a(t) = \frac{1}{2} l_{launcher} \cdot i(t)^2 - \alpha \cdot v(t) \\ di/dt = -\left[\frac{R_{tot}(t)}{L_{tot}(t)} + \frac{l_{launcher} \cdot v(t) \cdot i(t)}{L_{tot}(t)}\right] \cdot i(t) \end{array}\right\} \quad \text{(A-2)}$$

These differential systems are numerically solved using Matlab® built-in algorithm ODE45. This algorithm implements the Dormand-Prince method, an explicit type of Runge-Kutta formulation.

1.2. SMES powering

Under the assumption that the current in the SMES and the launcher are equal, the simulation of SMES-powered EML is exactly similar to the second phase of capacitor powering, when the flyback diode is passing, cf. Eq. (A-2). The only difference is that $L_{constant}$ is now the inductance of the SMES and connection cables, while $R_{constant}$ is only the resistance of the connection cables (the SMES coil being superconducting).

2. Inductance-to-inductance discharge

In order to understand how the currents in the two inductances become equals after the short-circuit is opened (Figure A-1), the easiest way is first to consider that the switch as a finite and constant off-resistance. The behavior of an ideal switch is then obtained by letting this resistance tend to infinite.

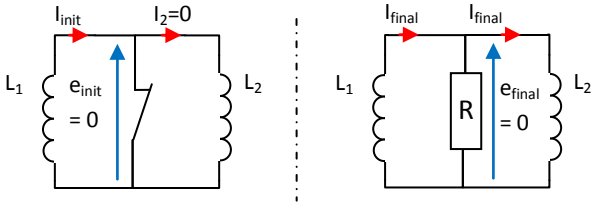

Figure A-1: Initial (left) and final (right) states of constant inductance - inductance discharge

The differential system obtained (A-3) may be solved exactly as it may easily be simplified into a single first order differential equation.

$$\begin{cases} -L_1 \dfrac{di_1(t)}{dt} = R \cdot \left[i_1(t) - i_2(t) \right] \\ L_2 \dfrac{di_2(t)}{dt} = R \cdot \left[i_1(t) - i_2(t) \right] \end{cases} \qquad \text{(A-3)}$$

The evolution of the currents in both inductances may be derived from this equation, considering the initial conditions: $i_1(0)=I_{init}$, $i_2(0)=0$. The result (A-4) demonstrates that the transient time, for given inductances, only depends on the switch off-resistance. If the switch is considered perfect, the transient time tends two zero, but the voltage across the switch tends to infinite, the energy dissipated staying constant.

$$\begin{cases} i_1(t) = \dfrac{I_{init}}{L_1 + L_2} \left(L_1 + L_2 \cdot e^{-t \cdot \left[R \cdot \left(1/L_1 + 1/L_2 \right) \right]} \right) \\ i_2(t) = \dfrac{L_1}{L_2} \left[I_{init} - i_1(t) \right] \end{cases} \qquad \text{(A-4)}$$

The steady state obtained using these formulas is of course the same that the one that was derived from the flux conservation:

When t tends toward infinite, both $i_1(t)$ and $i_1(t)$ tend toward $I_{init} \cdot \dfrac{L_1}{L_1 + L_2}$.

It should be noted that this case is the dual of the more commonly studied case of capacitor-capacitor energy exchange, in which case the invariant quantity is the electric charge Q, instead of the flux Φ.

UNIVERSITE DE GRENOBLE

INSTITUT POLYTECHNIQUE DE GRENOBLE

SUPERCONDUCTING MAGNETIC ENERGY STORAGE

Haute Température Critique comme Source Impulsionnelle

Résumé en Français

Sommaire

Introduction

L'objectif de ce travail est d'étudier les possibilités des SMES (Superconducting Magnetic Energy Storage) utilisant des matériaux supraconducteurs à haute température critique, comme source de courant impulsionnelle. L'alimentation de lanceurs électromagnétiques est plus spécifiquement visée.

Ce travail a été conduit dans le cadre d'un contrat DGA, en coopération avec l'Institut Saint Louis qui étudie ces lanceurs et les alimentations pulsées qu'ils nécessitent. Il repose sur l'expérience et le savoir-faire acquis à Grenoble, au sein du G2Elab et de l'Institut Néel, sur les applications supraconductrices haute température critique.

Le premier chapitre introduira brièvement la supraconductivité, du point de vue des applications. Les spécificités des supraconducteurs haute température critique, découverts en 1981 et dont l'utilisation dans les applications n'a commencé que dans les années 2000, seront soulignées. Le principe des SMES, leurs caractéristiques et leurs applications principales seront présentées dans une deuxième partie.

Dans le deuxième chapitre, l'utilisation de SMES pour l'alimentation de lanceur sera étudiée d'un point de vue théorique. Des simulations de lancement avec alimentation conventionnelle et par SMES seront comparées, afin de mettre en évidence les gains potentiels liés à l'utilisation de SMES. Les contraintes pour la réalisation de SMES ayant les caractéristiques requises pour cette application seront rappelées. Par la suite, des solutions nouvelles pour faciliter la réalisation de lanceurs alimentés par SMES seront introduites et discutées, elles permettent d'utiliser de manière optimale les caractéristiques des SMES, et d'accroître à la fois la faisabilité des dispositifs ainsi que leurs performances.

Le troisième chapitre présente les études conduites pour la conception du démonstrateur SMES II. Celui-ci est une version transformée du SMES I, prototype déjà testé en 2007 dans le laboratoire. Ce nouveau démonstrateur a pour objectif de tester l'utilisation de SMES comme source impulsionnelle, et de tester des solutions technologiques préfigurant l'alimentation de lanceurs par SMES. Ses caractéristiques seront tout d'abord présentées et discutées, après quoi les travaux de conception seront détaillés.

Le quatrième chapitre décrit la réalisation du démonstrateur et les tests effectués avec celui-ci. Les résultats expérimentaux sont interprétés et comparés avec les caractéristiques attendues.

Enfin des conclusions sont tirées, concernant l'intérêt et la faisabilité de lanceurs alimentés par SMES haute température critique et le savoir-faire acquis dans ce domaine au cours de ces travaux.

CHAPITRE 1 : INTRODUCTION AUX SMES

4. Les matériaux supraconducteurs

4.1 Introduction

Les matériaux supraconducteurs présentent la caractéristique de ne pas dissiper d'énergie lorsqu'ils sont parcourus par un courant, tant qu'ils restent dans l'état supraconducteur. Celui-ci est gouverné par trois paramètres définissant une surface critique : Température, Induction magnétique et Densité de courant (Figure 1-1). Le passage entre l'état supraconducteur et l'état normal, appelé « transition », est très brutal, il peut être modélisé par une loi en puissance.

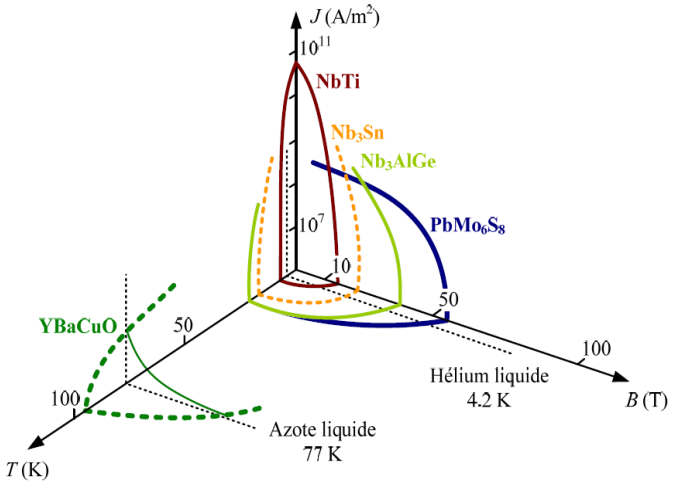

Figure 1-1 : Surfaces critiques pour différents matériaux supraconducteurs (ordre de grandeur)

On distingue deux familles de matériaux supraconducteurs suivant leurs plages de température d'utilisation. Les matériaux basse température critique (bTc) comme le NbTi sont les plus couramment utilisés, ils opèrent aux alentours de 4.2 K. Les matériaux haute température critique (hTc), de compositions plus complexes comme le BiSrCaCuO (BSCCO) ou l'YBaCuO, permettent une utilisation à des températures plus hautes, allant jusqu'à 90 K.

4.2 Les matériaux haute température critique

Les matériaux haute température critiques sont comme on l'a vu des céramiques de structures assez complexes qui sont sous leurs formes massives très dures et cassantes. Les propriétés supra de ces matériaux ne se développent à grande échelle que si la structure cristalline est régulière. La réalisation de conducteurs avec ce type de matériaux est donc un défi considérable, ce qui explique le temps qu'il a fallu attendre entre leur découverte au début des années 80 et l'apparition de conducteurs commerciaux dans des longueurs suffisantes pour la réalisation d'applications, dans les années 2000.

L'une des spécificités de ces matériaux est d'avoir une structure fortement anisotropique, anisotropie qui se retrouve dans la forme des conducteurs qui sont en général des rubans plats et non pas des conducteurs ronds (Figure 1-2). Ceci implique des techniques de mise en œuvre spécifique pour le bobinage.

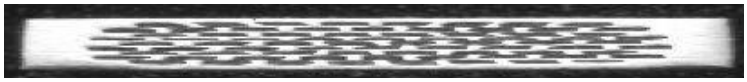

Figure 1-2 : Conducteur BSCCO Nexans. Les filaments de supraconducteurs sont visibles en noir, dans la matrice en argent (les proportions sont respectées)

Cette anisotropie se retrouve dans les caractéristiques supraconductrices du conducteur. Ainsi le courant critique, au-dessus duquel le conducteur commence à dissiper, dépend non seulement de l'intensité de l'induction magnétique mais également de l'orientation de celle-ci (Figure 1-3).

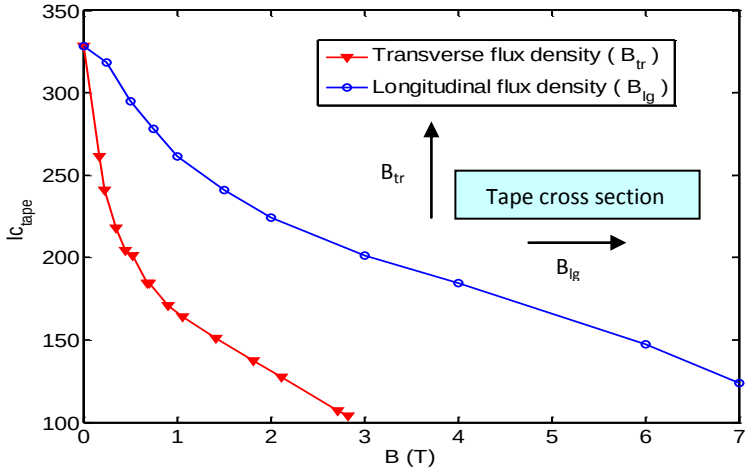

Figure 1-3 : Influence de l'orientation de l'induction magnétique sur le courant critique d'un ruban BSCCO Nexans (à 20 K)

Les caractéristiques présentées Figure 1-3 sont celles des rubans utilisés pour former le conducteur du SMES II (Chapitres 3 & 4). Ce conducteur consiste en 3 rubans BSCCO soudés les uns sur les autres, 4 dans les zones où l'induction est transversale par rapport aux rubans, car alors leur courant critique est réduit.

5. Introduction aux SMES

5.1 Principe

Le principe d'un SMES (Superconducting Magnetic Energy Storage) est de stocker de l'énergie sous forme magnétique dans un électro-aimant court-circuité (Figure 1-4).

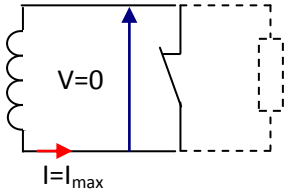

Figure 1-4 : Principe du stockage inductif (circuit de décharge en pointillé)

La bobine est réalisée avec un conducteur supraconducteur et ne dissipe donc pas l'énergie stockée, qui reste constante. La densité d'énergie stockable dans ce type de dispositif est modérée, limitée en dernier ressort par les contraintes mécaniques admissibles par le conducteur (théorème du viriel). Par contre, la puissance de sortie peut être très élevée. Le diagramme de Ragone (Figure 1-5) permet de comparer les SMES avec les principaux autres dispositifs de stockage.

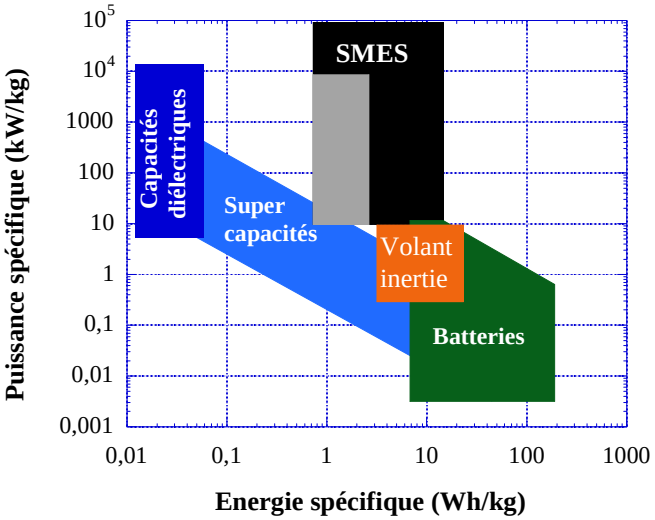

Figure 1-5 : Densité d'énergie et de puissance de différents dispositifs de stockage.

En considérant que la valeur du courant est donnée, cette puissance n'est limitée que par la tenue diélectrique de la bobine. Un SMES est donc une source impulsionnelle de courant. Ceci en fait un très bon candidat pour l'alimentation de lanceurs électromagnétiques car ceux-ci nécessitent une alimentation en courant de très forte valeur (centaines de kA) sur une durée courte (quelques ms).

5.2 Utilisation de conducteur haute température critique

L'utilisation de supraconducteurs hTc pour un SMES permet de réduire la puissance nécessaire au refroidissement et d'accroître la stabilité thermique, grâce à leurs températures d'utilisation plus élevées. Cependant les conducteurs hTc sont difficiles à mettre en œuvre sur de grandes longueurs du fait de leur faible résistance mécanique et de l'anisotropie de leurs caractéristiques. De plus, leur grande stabilité thermique les rend vulnérables en cas de transition, car l'échauffement induit reste très localisé et peut engendrer la destruction du bobinage. Une protection active de la bobine contre la transition est donc nécessaire. Elle consiste à décharger rapidement la bobine dès que l'apparition d'une tension dissipative sur la bobine est détectée. Cette tension peut notamment être détectée grâce à un montage en pont comme illustré Figure 1-6.

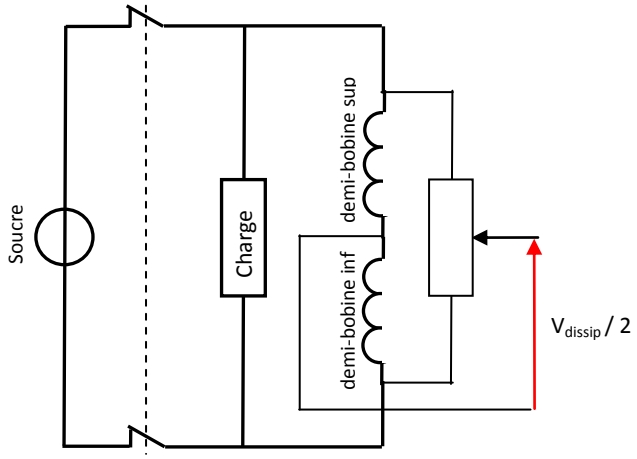

Figure 1-6 : Montage de détection de transition en pont

5.3 Applications

Historiquement le concept du SMES a été imaginé comme solution de stockage à très grande échelle de l'énergie électrique, avec pour objectif de niveler la charge journalière sur le réseau. Vu la faible densité d'énergie atteignable cela nécessiterait des bobines toriques de plusieurs kilomètres de diamètre, à l'image du LHC au Cern par exemple. Cette application a été quasiment abandonnée à l'heure actuelle et des applications de taille plus réduite mais à forte valeur ajoutée sont privilégiées.

Connecté au réseau d'une installation sensible, un SMES peut être utilisé pour offrir une protection contre les pics ou chutes de tension transitoires liés par exemple au démarrage ou à l'arrêt de gros dispositifs. Cette application a été testée, notamment sur des sites de production de micro-électronique, mais aucun dispositif commercial n'est disponible.

Il peut également être utilisé pour la réalisation de FACTS (Flexible AC Transmission System). Il permet alors de stabiliser les lignes hautes tension longue distance et/ou dont les charges sont fortement déséquilibrées, en absorbant/fournissant de la puissance réactive. Ce type d'application a fait l'objet d'une commercialisation, avec une bobine basse température critique (Figure 1-7).

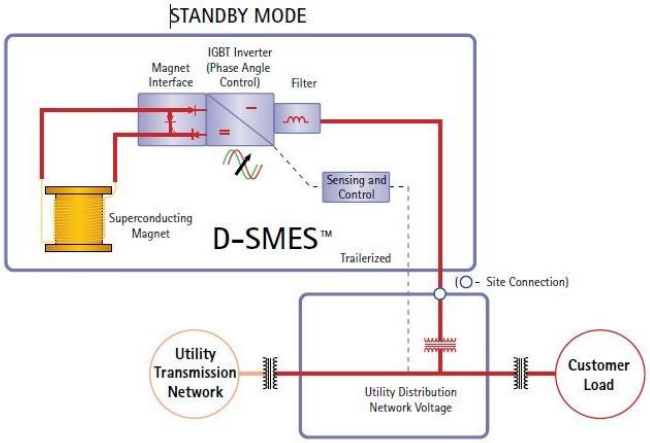

Figure 1-7 : SMES FACTS commercialisé par American Supraconductor

Le SMES peut enfin être utilisé en tant que source impulsionnelle, grâce à la grande densité de puissance atteignable. En particulier, c'est un bon candidat pour l'alimentation d'applications nécessitant une source de courant, pour lesquelles l'utilisation de condensateurs est mal adaptée. C'est le cas notamment des lanceurs électromagnétiques (Chapitre 2), mais aussi des dispositifs de magnétoformage, ou des catapultes pour l'aéronautique.

CHAPITRE 2 : SMES COMME SOURCE D'ALIMENTATION POUR LANCEUR ELECTROMAGNETIQUE

6. Les lanceurs électromagnétiques

6.1 Principe

Le principe d'un lanceur électromagnétique consiste à placer un mobile conducteur en contact glissant entre deux rails également conducteurs. Lorsque le circuit constitué par les rails et le mobile est parcouru par un courant, celui-ci est soumis à une force de Laplace qui l'accélère (Figure 2-1).

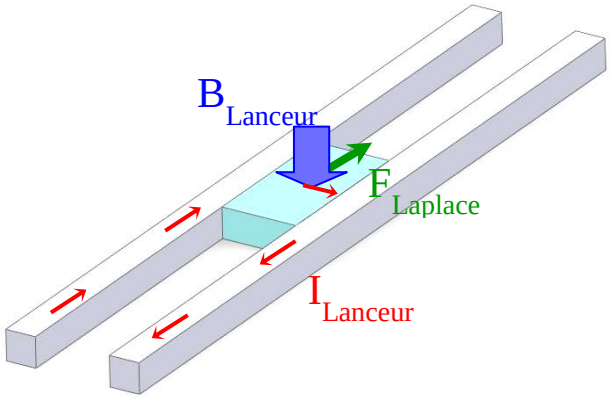

Figure 2-1 : Schéma de principe d'un lanceur électromagnétique

L'intérêt d'un tel système est de pouvoir obtenir des vitesses de sortie plus élevées que par une accélération classique par détente de gaz, et de pouvoir parfaitement calibrer l'accélération subie par le projectile. De nombreux types de lanceurs basés sur ce principe ont été étudiés, notamment à l'Institut Saint Louis, afin d'optimiser le rendement. Lanceurs segmentés, alimentation en courant distribuée spatialement et temporellement, etc.

6.2 Alimentation conventionnelle des lanceurs

L'alimentation de ces lanceurs est en générale assurée par des condensateurs, qui permettent de fournir les très forts courants nécessaires (centaines de kA). Cependant les condensateurs sont des sources de tension et les lanceurs sont quasiment des courts-circuits, particulièrement au début du tir quand le mobile est à l'entrée des rails. Un dispositif de mise en forme est donc nécessaire pour limiter la montée du courant lors de la décharge des condensateurs. Ce dispositif est essentiellement une inductance résistive, qui dissipe une part très importante de l'énergie stockée dans les condensateurs (Figure 2-2). Sachant que les condensateurs ont des densités d'énergie faibles ce faible rendement entraîne un volume élevé, ce qui est problématique pour les applications embarquées et/ou les applications destinées à assurer de nombreux tirs à la suite.

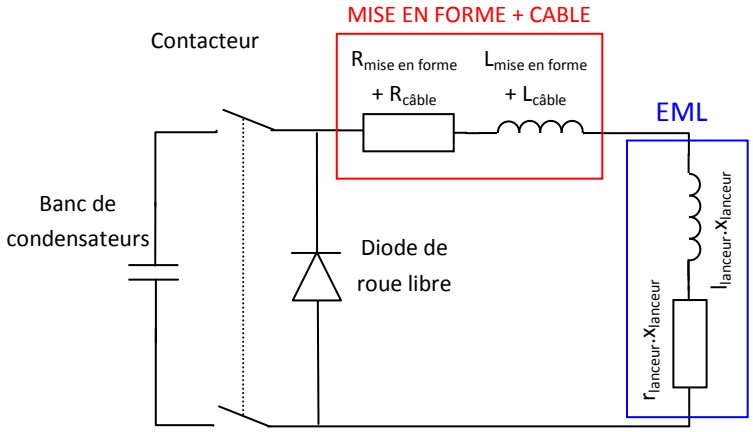

Figure 2-2 : Circuit d'alimentation d'un lanceur par condensateur

7. Utilisation d'un SMES pour l'alimentation de lanceur

7.1 Alimentation indirecte : Recharge rapide de condensateur

L'utilisation d'un SMES pour l'alimentation de lanceur peut s'envisager de deux manières. Tout d'abord en tant que stockage « tampon », pour effectuer une recharge rapide des condensateurs entre deux tirs (Figure 2-3).

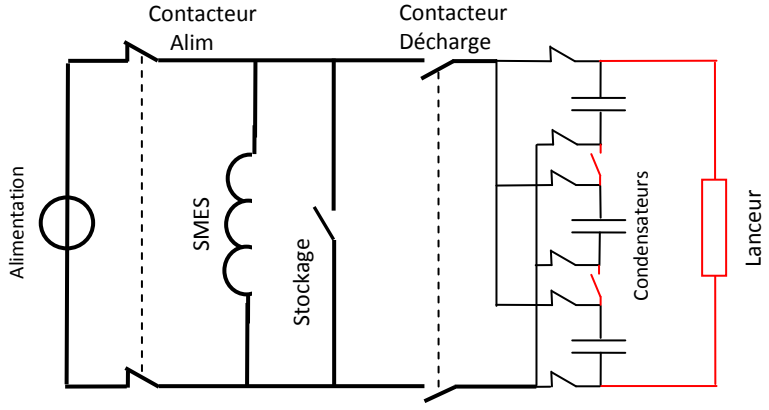

Figure 2-3 : Recharge rapide de condensateur

Cela permettrait de gagner en compacité pour des systèmes destinés à tirer en rafale, car la densité d'énergie stockée dans un SMES est supérieure à celle atteignable avec des condensateurs.

7.2 Alimentation directe de lanceur par SMES

L'utilisation d'un SMES pour l'alimentation de lanceurs peut s'imaginer en connectant directement le SMES au lanceur (Figure 2-4). Cette configuration semble plus prometteuse, car elle permet de s'affranchir de tout dispositif de mise en forme (le SMES étant une source de courant).

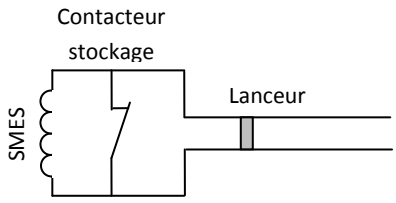

Figure 2-4 : Alimentation directe par SMES

On peut démontrer que le transfert d'énergie d'un SMES (bobine parfaite) à un lanceur est théoriquement optimum. Pour quantifier plus exactement les rendements atteignables avec une alimentation par SMES, un code de simulation a été développé. Il permet une étude comparée des alimentations par condensateur et par SMES (Figure 2-5).

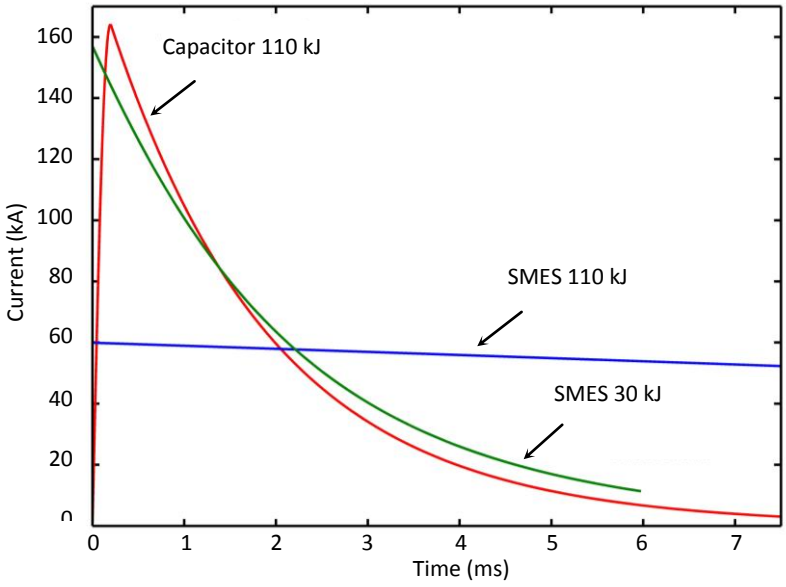

Figure 2-5 : Simulation de l'évolution du courant lors du tir par condensateur et SMES

Il ressort des simulations que pour un petit lanceur, l'alimentation par SMES permet d'obtenir un rendement total (défini comme le rapport entre l'énergie cinétique gagnée par le mobile et l'énergie perdue par le dispositif de stockage) de 70 % contre 2 % avec une alimentation par condensateur (Tableau 2-1).

	Condensateur	SMES	
Energie initiale (kJ)	110	110	30
Courant maximal (kA)	160	60	160
Inductance (uH)	Sans objet	61	2.3
Energie dissipée par effet Joule (kJ)	108	30	28
Energie cinétique acquise (kJ)	1,4 kJ		

Tableau 2-1 : Résultats de simulation pour un petit lanceur alimenté par condensateur et SMES

Dans le cas d'un lanceur de grande taille le rendement d'une alimentation par SMES serait probablement similaire, mais l'alimentation par condensateur a un rendement meilleur, de l'ordre de 30 %. L'alimentation directe par SMES pose cependant des problèmes de réalisation, car le courant nécessaire est très élevé, et difficilement atteignable avec les conducteurs supraconducteurs disponibles aujourd'hui. De plus l'inductance de ces dispositifs est très faible ce qui pose des problèmes d'auto-décharge. Enfin le refroidissement d'une bobine ayant un tel courant nominale demande une puissance thermique importante, donc un système de refroidissement volumineux.

8. Augmenter la faisabilité de l'alimentation directe

8.1 Augmentation du courant de sortie par le principe XRAM

La première solution étudiée pour rendre l'alimentation de lanceur par SMES faisable en pratique, est d'augmenter le courant de sortie du SMES en utilisant le principe XRAM, qui consiste à charger plusieurs bobines en série et à les décharger en parallèle pour sommer leurs courants (Figure 2-6). Deux cas peuvent être considérés, selon que la commutation série/parallèle s'effectue en dehors du cryostat ou à l'intérieur à basse température.

Les études préliminaires conduites à partir de données bibliographiques montrent que, si une commutation à chaud permet d'augmenter le courant de sortie tout en gardant un rendement électrique convenable, elle ne permet pas de diminuer la consommation de puissance thermique pour le refroidissement qui reste très élevée. Au contraire, l'utilisation de commutateurs semi-conducteurs cryogéniques permet de réduire celle-ci, pour un rendement électrique sensiblement identique. La mise en œuvre de commutateurs dans un environnement cryogénique reste toutefois délicate et des travaux plus poussés devront être conduits pour envisager une réalisation concrète.

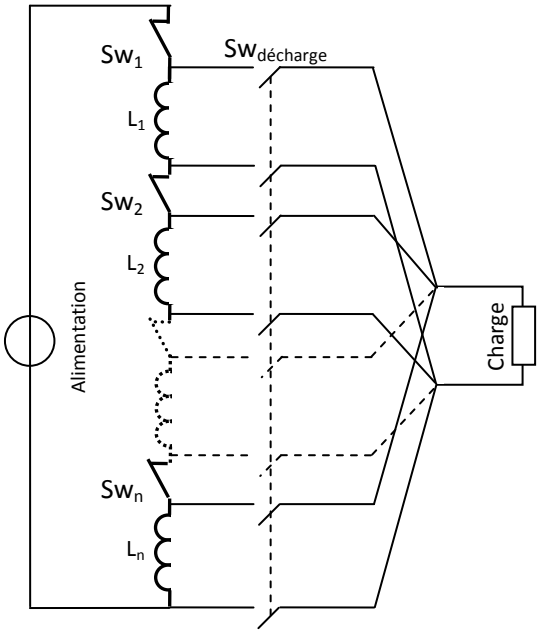

Figure 2-6 : Principe XRAM

8.2 Intégration SMES – Lanceur

La deuxième solution étudiée est de réduire le courant nécessaire à l'accélération du mobile, en réalisant l'intégration SMES – lanceur. L'idée d'utiliser un dispositif pour augmenter l'induction magnétique dans le lanceur et ainsi augmenter la force d'accélération à courant égal a déjà été envisagée et testée avec succès, notamment à l'aide d'un dipôle supraconducteur. La solution proposée et étudiée ici consiste à utiliser l'induction magnétique du SMES lui-même comme source externe et donc de réaliser un lanceur augmenté auto-alimenté (Figure 2-7). C'est le concept S^{3}EL (Superconducting Self Supplied Electromagnetic Launcher) qui a fait l'objet d'un dépôt de brevet.

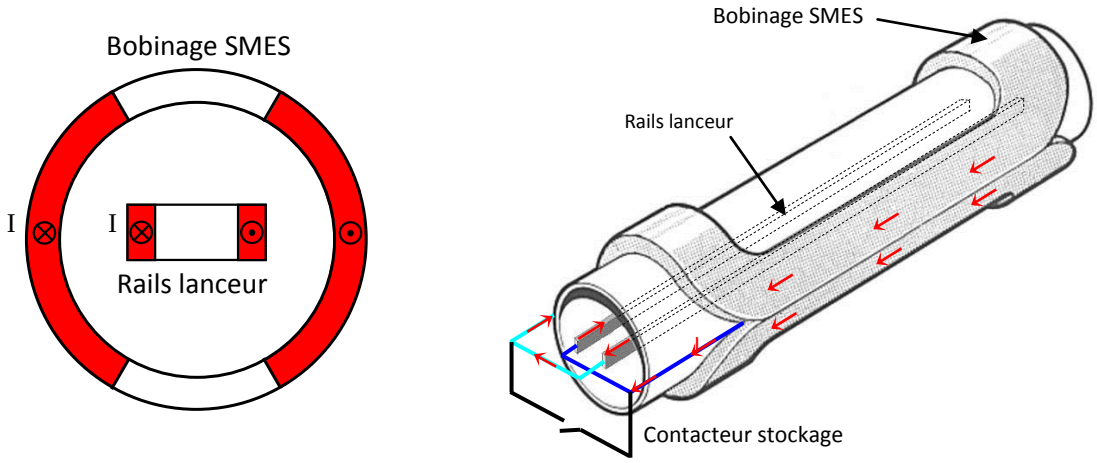

Figure 2-7 : Schéma de principe du concept S^{3}EL d'intégration SMES - Lanceur

Des simulations ont été conduites pour démontrer l'intérêt de ce concept, en prenant pour base le petit lanceur déjà considéré dans les simulations précédentes. Les résultats indiquent que le courant

nécessaire à l'accélération du mobile décroît très rapidement lorsque le couplage magnétique entre le SMES et le lanceur augmente. Il est ainsi divisé par 3 lorsque le couplage atteint 15 % (Figure 2-8).

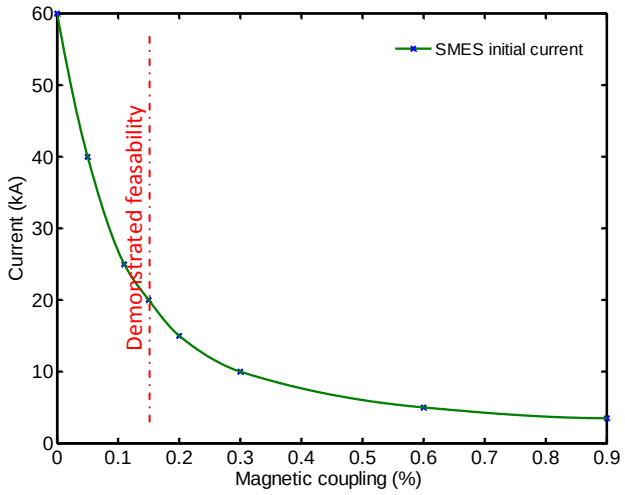

Figure 2-8 : Evolution du courant d'alimentation d'un lanceur en fonction du couplage entre le lanceur et le SMES qui l'alimente.

Cependant la réalisation d'un bobinage pour le SMES ayant un bon couplage magnétique avec le lanceur et une petite inductance (inférieure au mH) adaptée à l'énergie requise pour les tirs n'est pas forcément possible. En effet le SMES opère à température cryogénique et doit donc être isolé des rails, il n'est donc pas possible de rapprocher le bobinage du SMES des rails pour réaliser un couplage optimal (Figure 2-9).

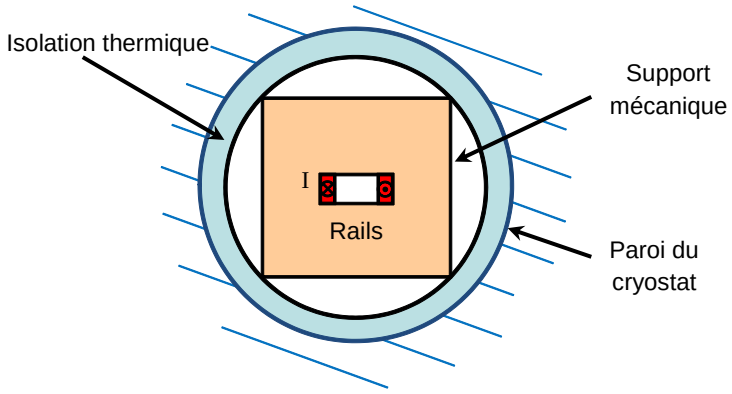

Figure 2-9 : Contraintes pour l'implantation du bobinage du SMES.
Hachures : zone froide disponible pour le bobinage

Un code d'optimisation géométrique de la bobine de SMES a donc été développé pour déterminer le couplage maximal atteignable pour une inductance donnée. Celui-ci calcule analytiquement le couplage entre les rails du lanceur et différentes géométries possibles pour la bobine de SMES. Ces possibilités sont représentées par une grille de positions disponibles pour les différentes spires de la bobine, toutes les spires étant considérées en série.

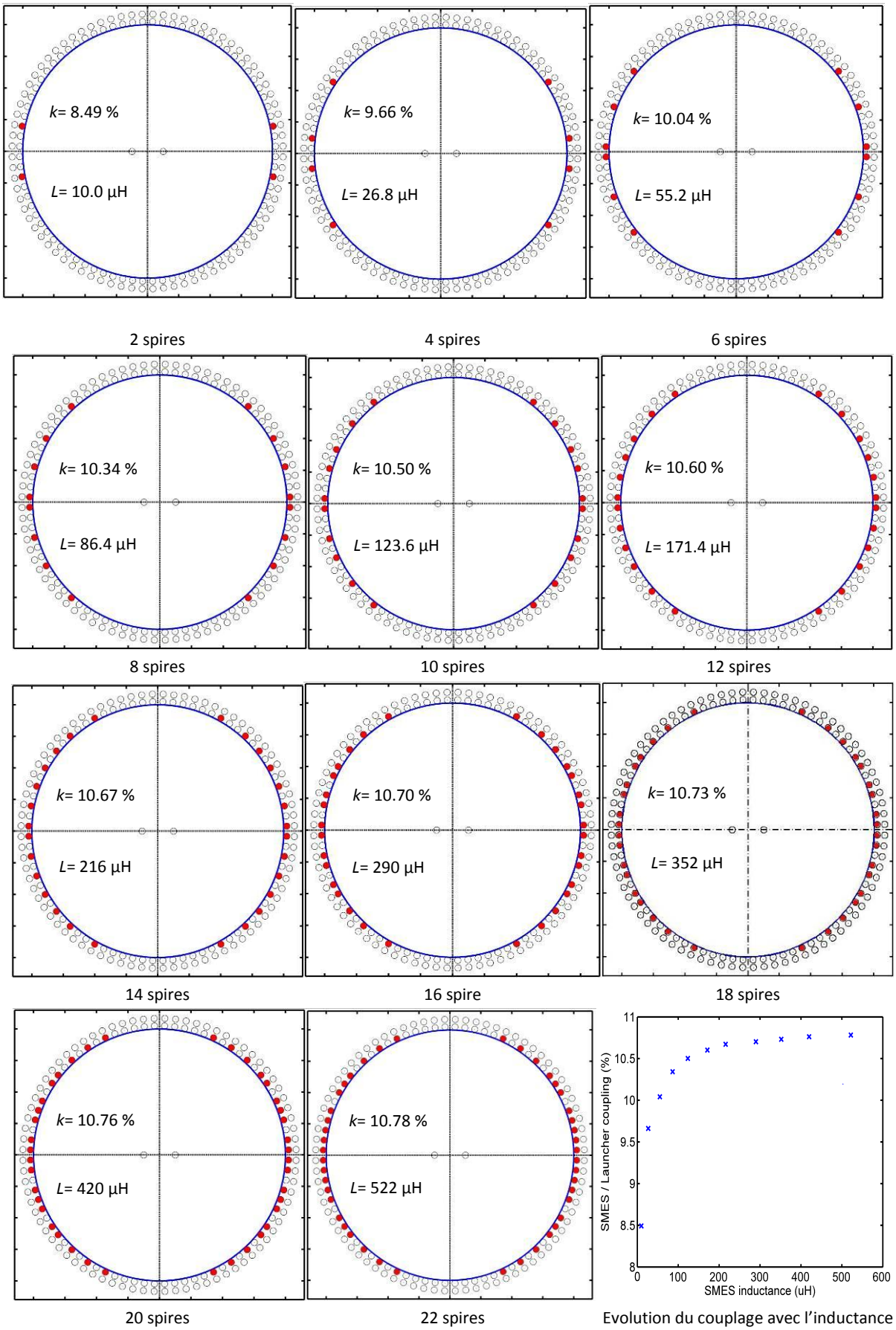

Figure 2-10 : Géométries optimales de bobines avec un nombre de spires allant de 2 à 22, avec les inductances et couplages associés (Les point rouges sont les positions occupées par les spires)

Ce travail d'optimisation a permis de montrer la faisabilité de bobines ayant des couplages de l'ordre de 11 % avec le lanceur, pour des inductances inférieures à 1 mH. La Figure 2-10 représente les positions optimales des spires et l'évolution de la répartition lorsque le nombre de spires augmente. Les inductances et couplages résultants sont également indiqués.

En conclusion, l'alimentation directe de lanceur par SMES paraît extrêmement prometteuse, même si les résultats présentés sont théoriques. L'utilisation du concept S^3EL, en combinaison avec le principe XRAM, permet d'envisager la réalisation pratique de ce type de dispositifs avec les technologies de supraconducteurs actuels.

CHAPITRE 3 : CONCEPTION DU DÉMONSTRATEUR SMES II

En parallèle des études théoriques, un démonstrateur a été développé pour tester à échelle réduite la faisabilité des différents modes d'alimentation de lanceur par SMES : recharge rapide de condensateurs et alimentation directe. Ce démonstrateur appelé SMES II est une évolution du SMES I développé auparavant au sein du laboratoire.

9. Objectifs et Spécifications du démonstrateur SMES II

9.1 Démonstrateur SMES I

Le SMES I (Figure 3-1) était une bobine en conducteur haute température critique BiSrCaCuO (BSCCO) stockant 400 kJ sous 250 A, réalisée en partenariat avec Nexans dans le cadre d'un contrat DGA. Sa grande spécificité était son refroidissement à 16 K uniquement par conduction, sans fluide cryogénique, permettant une utilisation sans connaissances particulières en cryogénie.

Figure 3-1 : Démonstrateur SMES I en test

Il a été testé avec succès en 2007 et a permis de valider certains choix technologiques, notamment la technique de bobinage du conducteur BSCCO en galette, l'isolation électrique et le refroidissement par conduction, à partir de cryoréfigérateurs. Cependant sa tension maximale limitée à 800 V ne permet pas d'envisager la recharge de condensateurs pour l'alimentation de lanceurs et son courant de sortie est trop faible pour une alimentation directe.

9.2 Projet SMES II

9.2.1 Objectifs

L'objectif du démonstrateur SMES II est de réutiliser les éléments du SMES I, notamment les galettes de conducteurs, pour réaliser un dispositif ayant des caractéristiques supérieures. Les choix technologiques validés sont réutilisés, notamment le principe de refroidissement par conduction. L'objectif est de pouvoir tester :

- La recharge de condensateur, en augmentant la tension admissible
- La décharge séquentielle de deux sources d'énergie identique, préfigurant l'alimentation de lanceurs segmentés
- Le concept XRAM permettant la multiplication du courant de sortie.

9.2.2 Caractéristiques

- Courant nominal 250 A (réutilisation des galettes du SMES I)
- Bobinage scindé en 2 bobines indépendantes mais couplées (situées sur le même axe), avec des caractéristiques adaptées pour obtenir deux décharges successives d'énergies identiques, 2 x 200 kJ.
- Tension maximale de décharge portée à 4 kV sur la bobine supérieure pour permettre la recharge de condensateur
- Bobine inférieure formée de 6 segments adaptés au concept XRAM
- Puissance de refroidissement imposée : 3 cryoréfrigérateurs AL330 permettant d'absorber 330 W à 77 K, et aux alentours de 10 W à 20 K, alors que 2 étaient utilisés pour SMES I

9.3 SMES II: Dimensionnement magnétique

Les deux bobines du SMES II étant couplées, la décharge de la première bobine a tendance à surcharger la deuxième. Obtenir deux décharges successives de même énergie nécessite donc d'avoir des bobines d'inductance différentes, et d'adapter la distance entre elles. Ce travail de dimensionnement a été conduit par K. Berger.

Sachant que les galettes de conducteur constituant les bobines étaient déjà existantes, le nombre de possibilités était réduit et chaque configuration a été simulée. De plus, des contraintes existent sur le positionnement des galettes, dont certaines ont été conçues spécialement pour être placées aux extrémités, avec une meilleur tolérance au champ radial, alors que d'autres ayant un renfort

mécanique du conducteur sont conçues pour être placées au milieu des bobines, là où les contraintes sont les plus fortes.

Le courant nominal de 250 A peut être dépassé si l'induction magnétique est réduite, car alors les capacités de transport de courant du conducteur sont accrues. Ceci a également été pris en compte dans l'évaluation des solutions possibles, présentées dans le Tableau 3-1

Nombre de galettes Bobine haute | basse	26	2	24	4	22	6	20	8	18	10	16	12	14	14
Inductances (H)	16.0	0.14	14.0	0.53	12.1	1.16	10.3	2.00	8.57	3.00	6.98	4.18	5.51	5.51
Distance (mm)	1		24		55		103		176		313		1000	
Coefficient de couplage (%)	64		55		46		37		26		14		2	
Courant initial (A)	207	264	203	292	205	279	212	272	223	269	242	266	269	264
Courant bobine basse après décharge bobine haute (A)	1695		865		588		449		365		309		269	

Tableau 3-1 : Résultats du dimensionnement magnétique pour deux décharges de 200 kJ. En rouge sont indiquées les impossibilités, en vert la solution retenue

La solution retenue, une bobine supérieure composée de 16 galettes (6.6 H) et une bobine inférieure de 12 galettes (4.3 H) distantes de 31 cm est présentée (Figure 3-2).

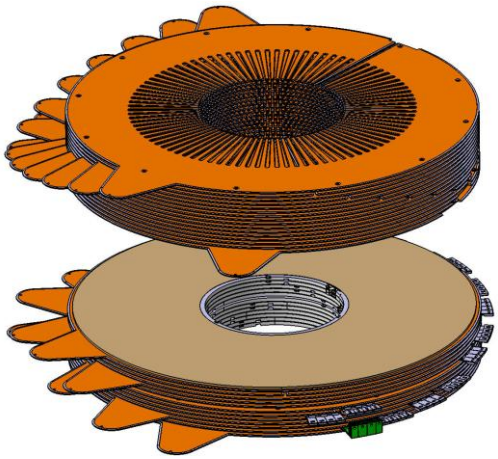

Figure 3-2 : Vue CAO des deux bobinages du SMES II (seuls les supports en cuivre des galettes sont visibles, le conducteur n'est pas représenté)

10. Dimensionnement Thermique et Electrique

L'une des contraintes principales pour la conception de ce démonstrateur est la puissance de refroidissement disponible très limitée, avec 3 cryoréfrigérateurs. Sachant que les deux bobines sont distantes de 31 cm, il est nécessaire de prévoir un cryoréfrigérateur par bobine, et il n'en reste donc qu'un pour refroidir les 14 amenées de courant (12 étant nécessaires pour la connexion XRAM de la bobine inférieure, et 2 pour la bobine supérieure). L'implantation prévue pour les cryoréfrigérateurs est présentée Figure 3-3.

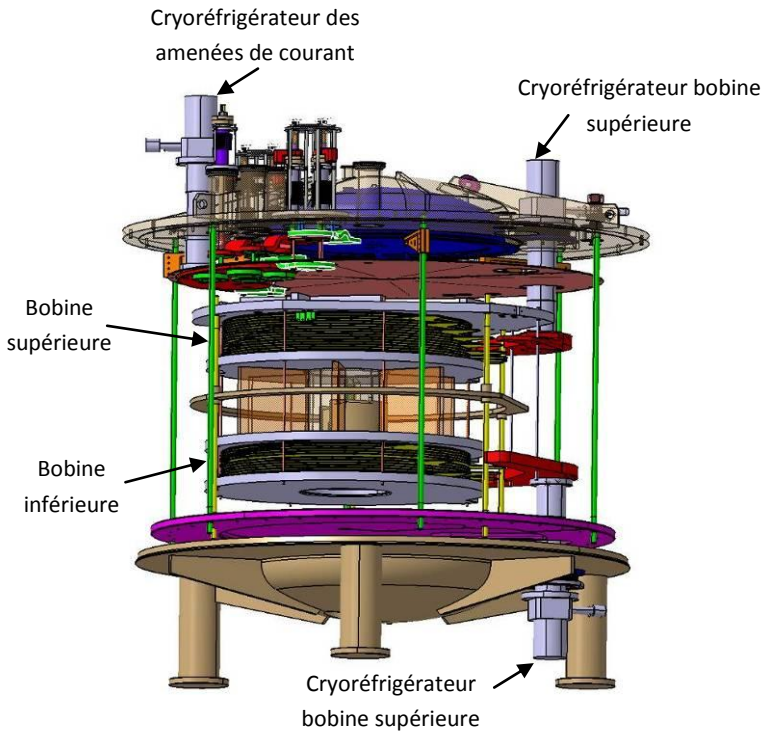

Figure 3-3 : Vue CAO générale du SMES II

L'essentiel du travail a donc porté sur l'optimisation thermique du démonstrateur et particulièrement des amenées de courant et de leur refroidissement. Ces travaux ont été conduits en étroite collaboration avec les autres membres de l'équipe, en particulier M. Deleglise, l'ingénieur en charge de la conception mécanique générale du projet et de sa mise en œuvre.

10.1 Conception des amenées de courant

Les amenées de courant sont constituées de deux segments, un segment résistif depuis l'extérieur du cryostat (300 K) jusqu'à une thermalisation intermédiaire (50 K) puis un segment supraconducteur depuis 50 K jusqu'à la bobine opérant à 16 K (Figure 3-4).

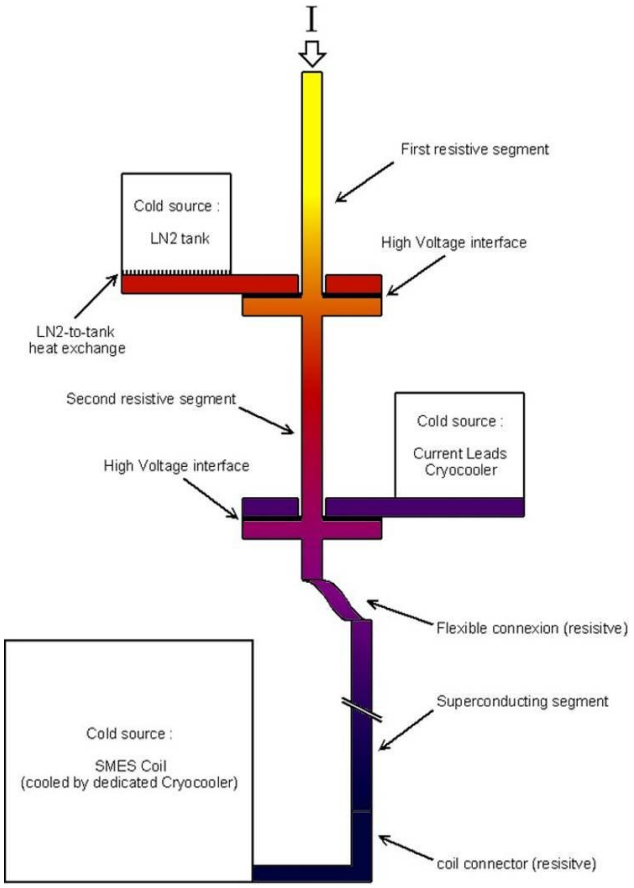

Figure 3-4 : Schéma de principe des Amenées de courant

Pour le dimensionnement électrothermique des amenées de courant, des simulations magnétostatiques des bobines ont tout d'abord été menées (Flux 2D et 3D) pour définir les conditions d'opération des segments supraconducteurs, en termes d'induction magnétique et de densité de courant (Figure 3-5).

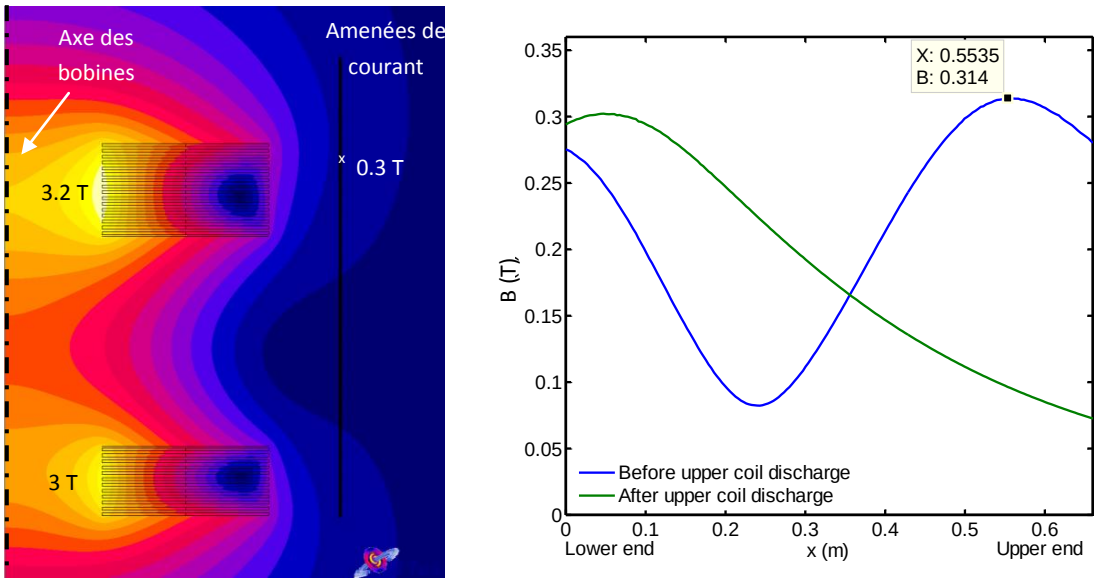

Figure 3-5 : A gauche, Induction magnétique créée par les bobines au courant nominal. A droite, induction magnétique vue par les amenées de courant.

Cela a permis de définir la section minimale de supraconducteur et donc les échanges thermiques associés. La température maximale admissible pour la thermalisation intermédiaire a ainsi pu être définie à 50K.

L'optimisation des segments résistifs et de leur refroidissement a été conduite afin de garantir la température de la thermalisation intermédiaire définie. Un outil de simulation thermique a été développé et utilisé (Figure 3-6) pour obtenir itérativement la configuration optimale pour le segment résistif (matériau, section, longueur).

Les interfaces de thermalisation par conduction de ces amenées doivent garantir à la fois une bonne conductivité surfacique et une isolation électrique suffisante (4 kV), elles sont donc cruciales. Les caractéristiques de ces interfaces, obtenues expérimentalement ont été intégrées dans les simulations (voir Chapitre 4).

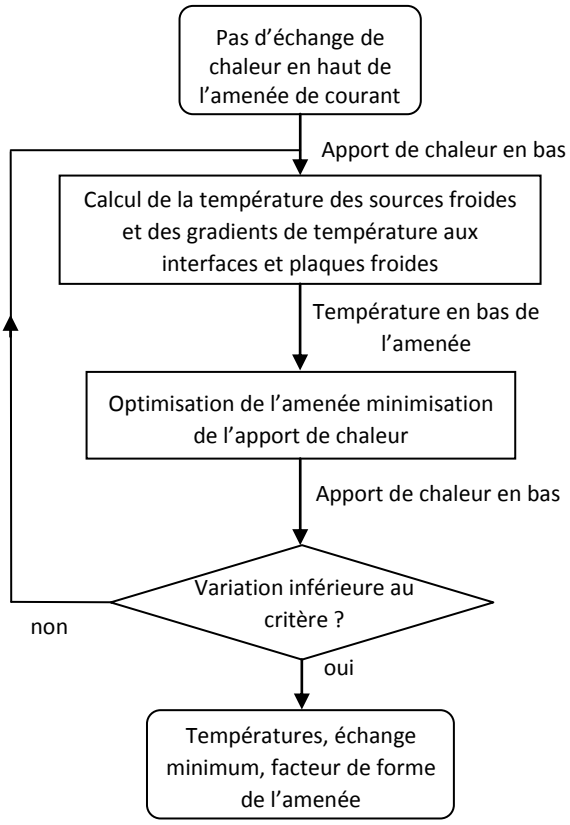

Figure 3-6 : Principe de fonctionnement du code d'optimisation

Cet outil a mis en évidence la nécessité d'utiliser une deuxième thermalisation intermédiaire, avec pour source froide un réservoir d'azote auxiliaire. Il a permis de fixer les caractéristiques des différents éléments de cette chaîne additionnelle de refroidissement. La chaîne de refroidissement complète est présentée Figure 3-7.

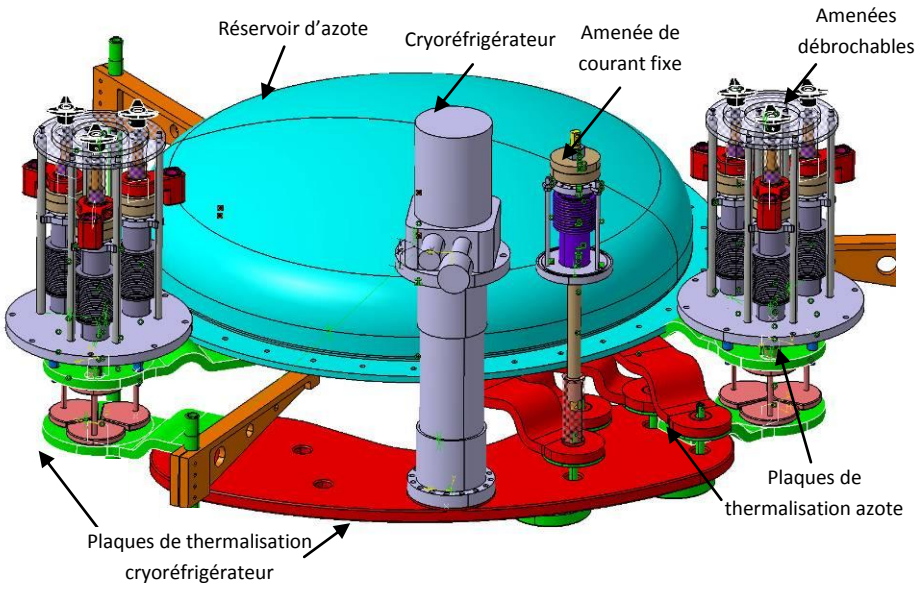

Figure 3-7 : Vue CAO du système de refroidissement des amenées de courant (la bride supérieure du cryostat a été enlevée).

11. Etude thermique des bobinages

Au niveau du bobinage, les apports thermiques générés par les amenées de courant ont été évalués, ainsi que les apports par radiation et par conduction à travers les éléments de maintien mécanique. La charge thermique calculée pour chacun des cryoréfrigérateurs est présentée dans le Tableau 3-2.

Cryoréfrigérateurs	Bobine supérieure	Bobine inférieure	Amenées de courant (et écran thermique)
Apport thermique (W):			
Radiation	0.58	0.42	10
Conduction (structure)	0.01	0	0.2
Conduction (amenées)	0.04	0.24	35
Total à courant nul (W)	0.63	0.66	45.2
Température minimale du cryoréfrigérateur (K)	≈ 11	≈ 11	≈ 24
Dissipation de chaleur (W):			
Connexions résistives (et amenées résistives)	0.34	1.08	32
Dissipation conducteur supra	7.8	5.8	0
Total en fonctionnement nominal (W)	8.77	7.54	77
Température du cryoréfrigérateur en fonctionnement nominal (K)	≈ 13	≈13	≈32

Tableau 3-2 : Charge thermique prévue pour chacun des cryoréfrigérateurs et température d'opération attendue

Contrairement au cas du SMES I, les apports de chaleur par les amenées de courant ne sont pas négligeables, du fait de leur nombre élevé. Des drains thermiques ont donc été dimensionnés pour absorber cet apport de chaleur au niveau de chaque connexion entre amenée de courant et bobine.

Ce dimensionnement prend en compte les caractéristiques thermiques obtenues expérimentalement pour les tresses de cuivre utilisées et les interfaces de contact tresse/amenée de courant et tresse/plaque froide.

Enfin, des simulations thermiques 3D ont été conduites avec le logiciel Flux®, pour optimiser la géométrie des 2 secteurs en cuivre répartissant la puissance de refroidissement depuis les têtes froides des cryoréfrigérateurs vers les galettes des 2 bobinages (Figure 3-8).

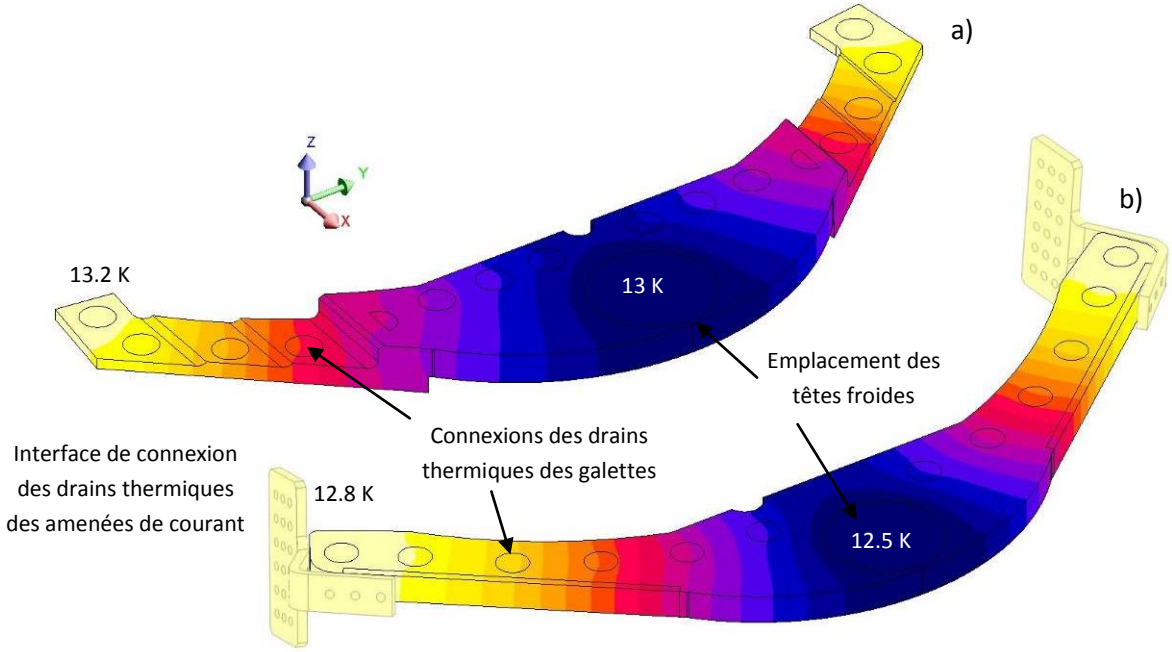

Figure 3-8 : Gradients de température dans les secteurs de refroidissement haut (a)et bas (b) en conditions nominales

CHAPITRE 4 : RÉALISATION ET TEST DU SMES II

12. Etudes préliminaires et réalisation

12.1 Dispositif de caractérisation

Afin de réaliser des travaux préliminaires à la réalisation du démonstrateur SMES II, un dispositif de test à température variable (entre 15 et 20 K) a été développé (Figure 4-1).

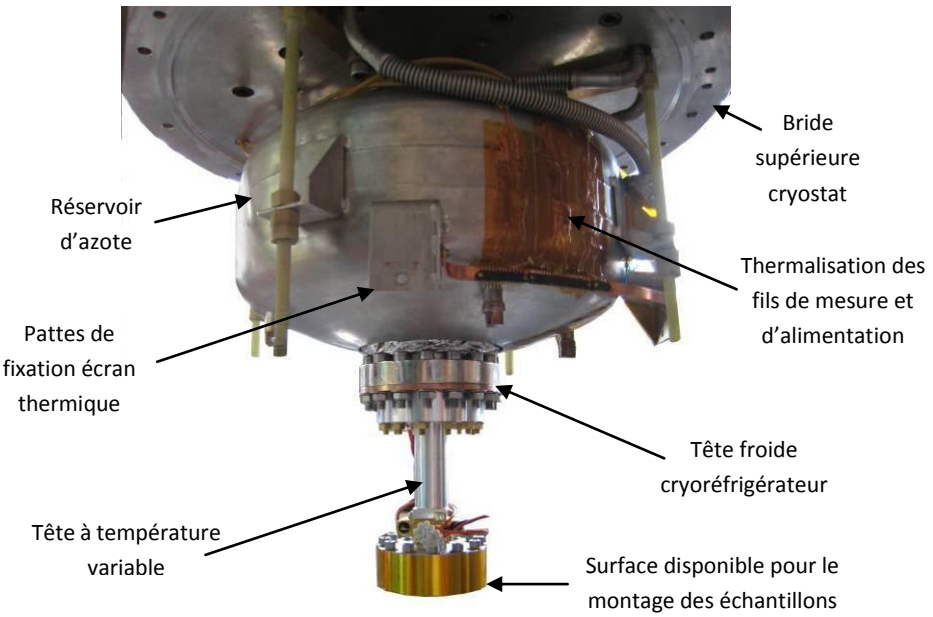

Figure 4-1 : Dispositif de caractérisation

Il a permis de tester et d'étalonner l'instrumentation de mesure de température utilisée par la suite à grande échelle dans SMES II. Il a également permis de caractériser les interfaces de thermalisation assurant l'isolation électrique, ainsi que les propriétés thermiques des matériaux et interfaces présentes dans les différents drains thermiques (interfaces cuivre-cuivre pressées, soudées, tresses de cuivre, pièces massives, etc.). Ce dispositif a également permis de tester la tenue diélectrique des interfaces isolantes, sous vide et à température cryogénique.

12.2 Réalisation du SMES II

12.2.1 Assemblage des bobines

La première étape de la réalisation du démonstrateur a été de tester la tenue diélectrique des galettes existantes du SMES I ainsi que celle des deux nouvelles galettes bobinées pour le SMES II. Cela a permis de constituer les bobines (Figure 4-2) en maximisant la tension admissible, qui atteint 4.5 kV.

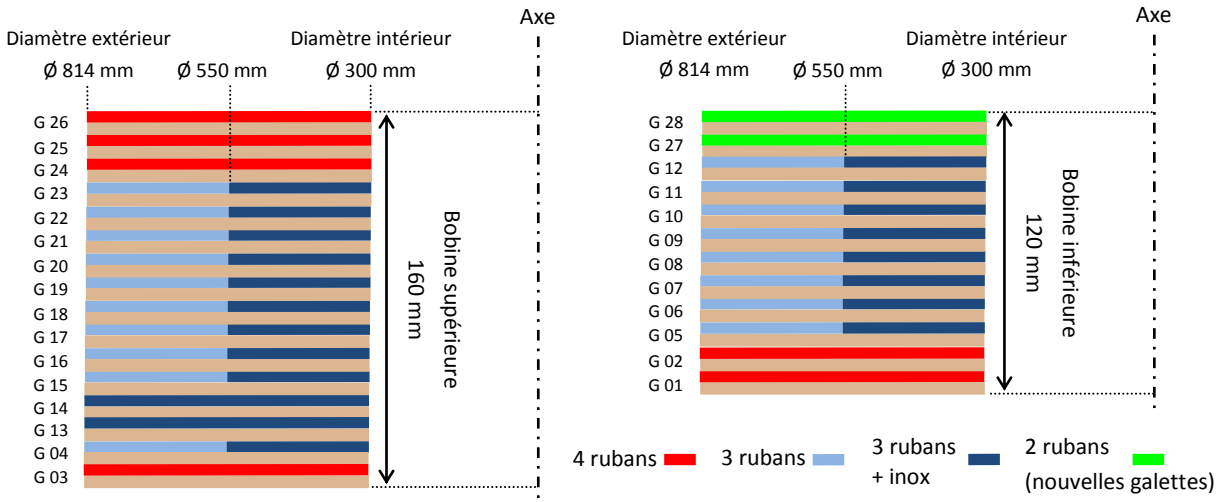

Figure 4-2 : Assemblage des galettes pour la bobine supérieure (gauche) et inférieure (droite)

Ces deux ensembles ont ensuite été montés l'un sur l'autre, l'écartement étant assuré par une entretoise en fibre de verre (Figure 4-3).

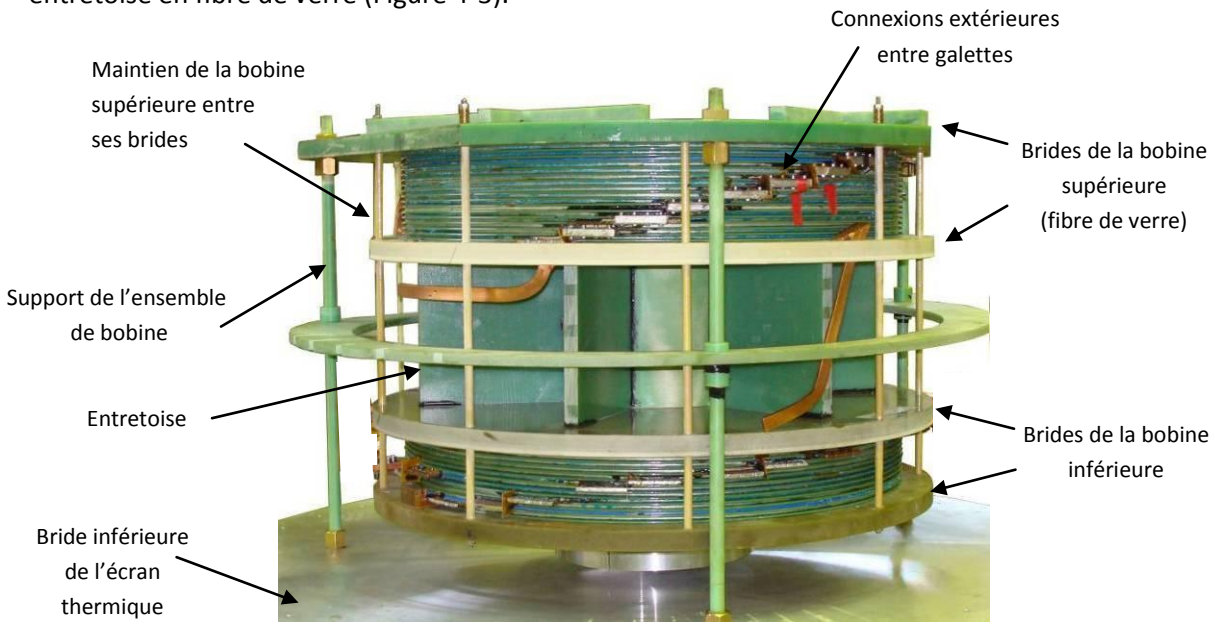

Figure 4-3 : Assemblage des bobines

Les secteurs en cuivre ont ensuite été montés, et connectés aux supports des galettes.

12.2.2 Amenées de courant résistives

La mise en œuvre des interfaces de thermalisation/isolation électrique à base de colle Eccobond® pour le démonstrateur à mis à jour un défaut de solidité, dans le cas où les surfaces de contact sont les plus grandes. Une solution de remplacement a été trouvée pour celles-ci, en remplaçant la couche d'Eccobond® par du Redux®, un film à basse température de polymérisation. Cette solution était celle qui avait été retenue pour le SMES I, mais ses caractéristiques thermiques sont inférieures. Afin de garantir la sureté d'utilisation le nombre d'amenées de courant a donc été réduit pour réduire la puissance dissipée. Le dispositif final possède donc 8 amenées de courant, la bobine inférieure étant constituée de 3 segments au lieu de 6.

Le montage des amenées de courant résistives, avec leurs interfaces de thermalisation, est présenté Figure 4-4.

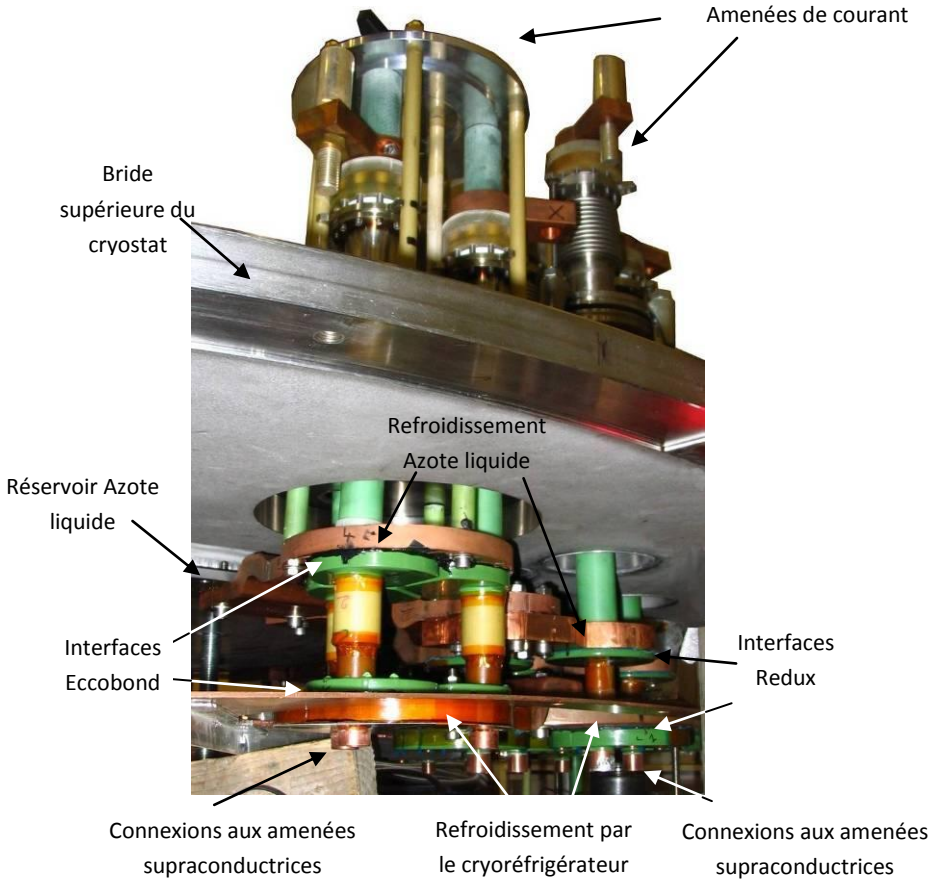

Figure 4-4 : Système d'amenée de courant résistif

12.2.3 Amenées de courant supraconductrices

Les amenées de courant de la bobine supérieure sont celles utilisées pour le SMES I, elles sont constituées de BSCCO massif, qui est un très bon isolant thermique. Pour les amenées de la bobine inférieure, qui sont plus longues, l'utilisation de telles amenées n'était pas envisageable car ce matériau est très cassant. Les amenées ont donc été réalisées en utilisant du ruban supraconducteur BSCCO à matrice en alliage Or-Argent. Ces rubans ont des propriétés mécaniques semblables aux

rubans à matrice Argent utilisés pour les bobines, mais avec une conductivité thermique inférieure. Pour garantir leur maintien, ces rubans (5 en parallèle) ont été placés dans un tube en fibre de verre rainuré, avec des pièces de cuivre soudées aux extrémités pour assurer les connexions, à la bobine d'un côté, et aux amenées résistives de l'autre (Figure 4-5).

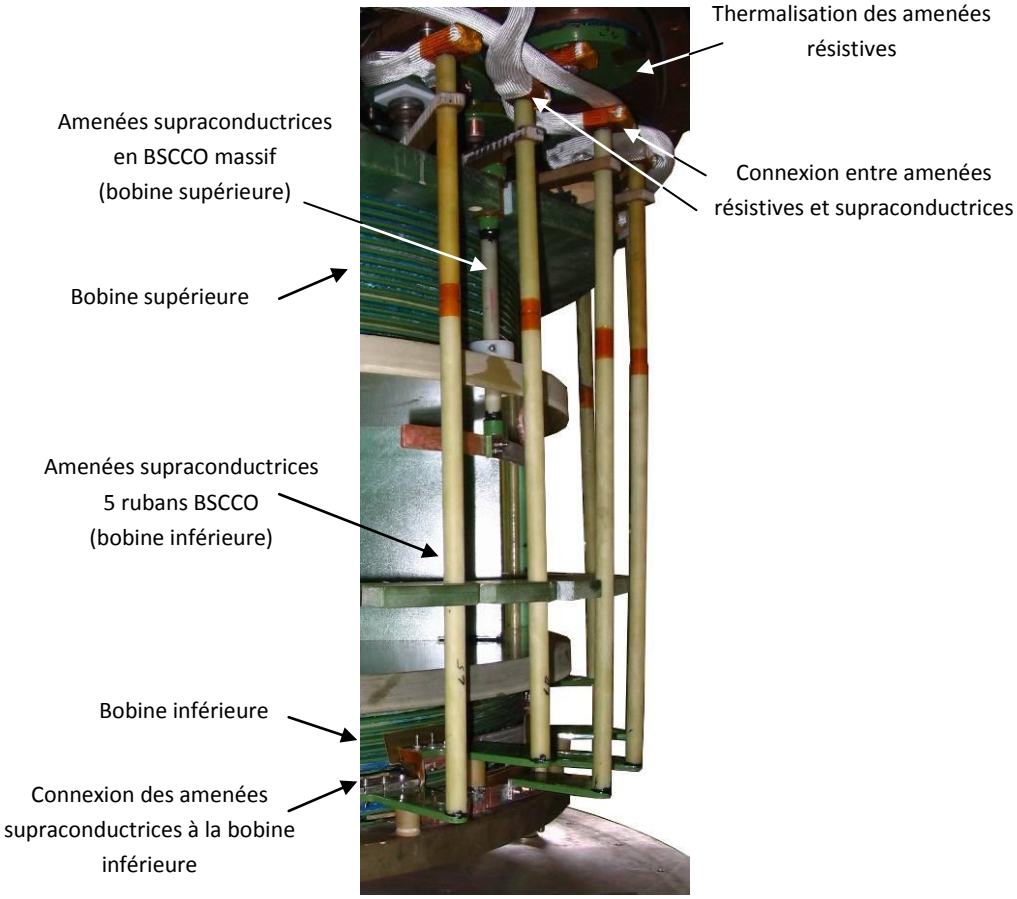

Figure 4-5 : Assemblage des amenées de courant supraconductrices dans le SMES II

13. SMES II : tests et résultats

13.1 Dispositif de protection

L'objectif de ce dispositif est de détecter l'apparition aux bornes de la bobine d'une tension de l'ordre de quelques dizaines de mV, et ce lorsque celle-ci est soit en charge soit en court-circuit (stockage). Cette tension correspond à une dissipation anormale par effet Joule, signe d'un échauffement local du conducteur. Lors de la décharge le système de détection doit par ailleurs supporter la tension totale de la bobine, qui dans notre cas peut atteindre plus de 4 kV.

Dans les systèmes utilisés classiquement, la tension de la bobine est atténuée avant le détecteur afin que l'électronique n'ait à supporter qu'une fraction de la tension de décharge. Dans ce cas il devient très difficile de détecter la tension de dissipation qui est elle aussi atténuée. C'est la solution qui avait

été retenue pour SMES I. Lors des tests, des dégâts avaient été causés au bobinage car la sensibilité n'était pas assez bonne.

Pour SMES II la sensibilité de détection a été considérablement augmentée en utilisant un nouveau concept, qui a fait l'objet d'un dépôt de brevet. L'idée est de ne pas atténuer la tension de la bobine afin de bénéficier de toute la sensibilité de mesure, mais de protéger activement le circuit électronique en le déconnectant de la bobine avant la décharge. Pour SMES II une difficulté supplémentaire est liée au couplage magnétique entre les deux bobines, qui tend à fausser la détection sur une bobine quand le courant dans l'autre bobine varie. La détection pour la bobine inférieure a donc été compensée en utilisant une image atténuée de la tension sur la bobine supérieure, obtenue à l'aide d'une petite bobine résistive couplée.

13.2 Mise en froid

La mise en froid a permis de valider la conception thermique du dispositif puisque les températures mesurées au niveau des bobinages étaient inférieures à 16 K, l'objectif visé. De même le refroidissement intermédiaire est descendu à 35 K, garantissant la sûreté d'opération des amenées de courant supraconductrices. Le refroidissement secondaire à l'azote est nécessaire puisque sans lui la température du refroidissement intermédiaire se stabilise à 52 K, mettant en danger le fonctionnement des amenées (Figure 4-6).

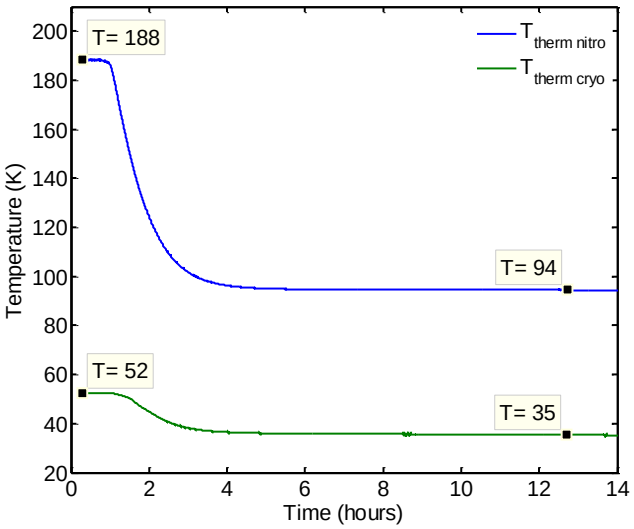

Figure 4-6 : Influence du refroidissement intermédiaire à l'azote

Le réservoir d'azote embarqué permet une autonomie de fonctionnement de 24 h, contre 26 h prévues.

13.3 Caractérisation électrique

Les premiers tests électriques ont été effectués à bas courant, pour étalonner le système de détection de transition des bobines. La caractérisation électrique des bobinages (inductances et couplages) a ensuite été menée, afin de vérifier la cohérence avec les simulations numériques. La méthode de mesure utilisée consiste à mesurer la tension et le courant aux bornes des bobines (testées séparément) afin de connaitre la puissance et, par intégration, l'énergie stockée. L'approximation de la courbe E(I) par un polynôme permet ensuite de trouver le paramètre L (Figure 4-7).

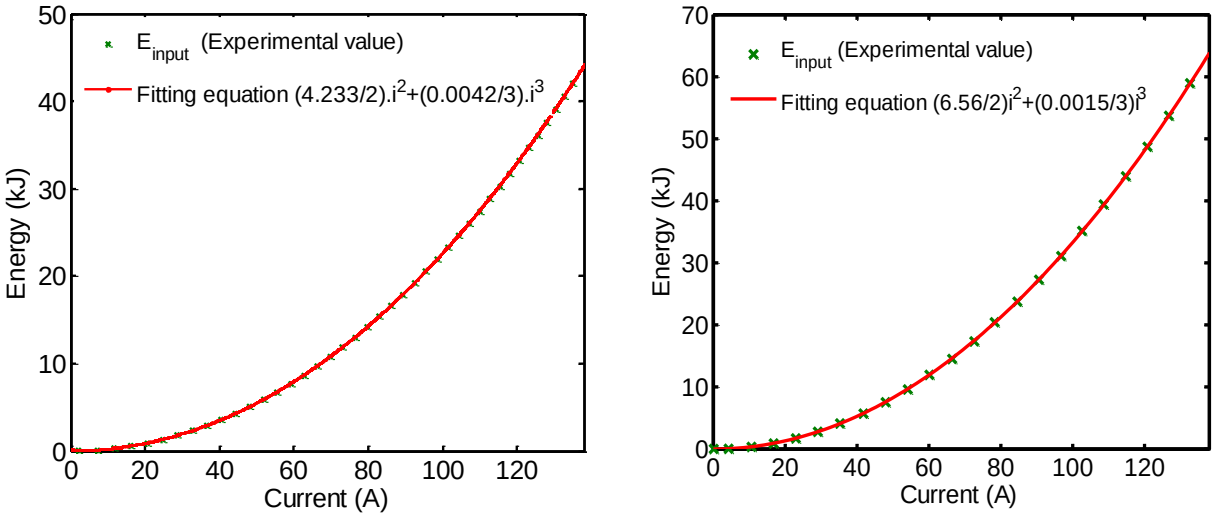

Figure 4-7 : Evolution de l'énergie stockée en fonction du courant

Les valeurs mesurées sont cohérentes avec les simulations, 4.23 H pour 4.3 attendus (bobine inférieure) et 6.56 H pour 6.6 attendus (bobine supérieure).

Les rendements de décharge ont été calculés pour différentes valeurs de résistance, à 96 %. Cela semble démontrer que les pertes sont indépendantes de la vitesse de décharge, au moins dans notre gamme de fonctionnement. Ceci indique que les pertes sont essentiellement hystérétiques.

Les courants maximums des deux bobines ont été atteints à approximativement 200 A, avec le système de détection de transition réglé sur la sensibilité la plus haute (50 mV). En utilisant un seuil plus haut, la bobine supérieure a atteint 250 A (Figure 4-8), ce qui correspond bien aux prévisions. Cette valeur a pu être atteinte plusieurs fois, ce qui prouve que les bobinages n'ont pas été endommagés par les tests, et que le système de protection possède une sensibilité suffisante.

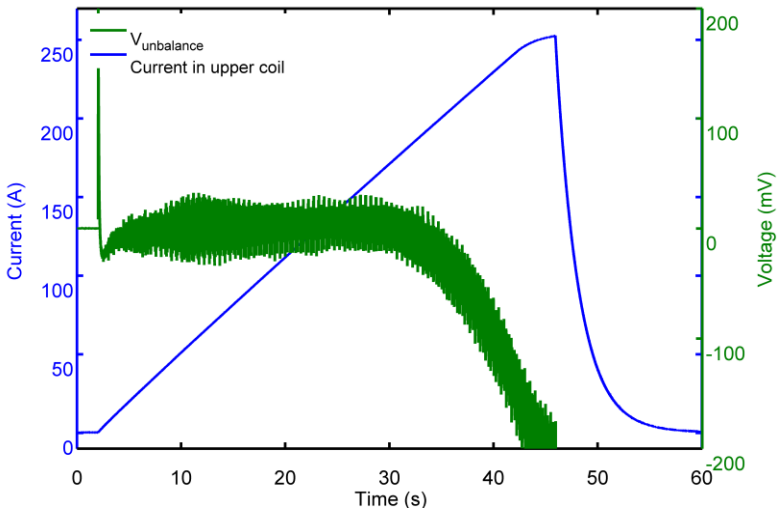

Figure 4-8 : Courant maximal sur la bobine supérieure, avec seuil de transition réglé à 200 mV

13.4 Tests de puissance

Les modes d'opération du SMES II ont finalement été testés à l'Institut Saint Louis, où sont étudiés les lanceurs électromagnétiques ainsi que les condensateurs de puissance et les systèmes de commutations semi-conducteurs utilisés pour le principe XRAM.

La recharge rapide de condensateur a été testé jusqu'à 3 kV, ce qui a permis de transférer presque 32 kJ en 400 ms, avec un rendement de 92 % (Figure 4-9). Ce rendement inclus les pertes dans la diode placée entre la bobine et le banc de condensateurs pour bloquer les oscillations.

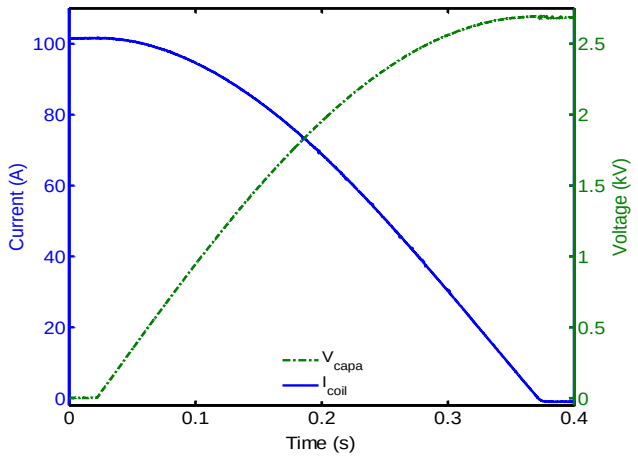

Figure 4-9 : Décharge de la bobine supérieure dans un banc de condensateurs

Le principe XRAM a lui été testé sur la bobine inférieure jusqu'à 200 A, ce qui a permis d'obtenir 600 A en sortie (Figure 4-10).

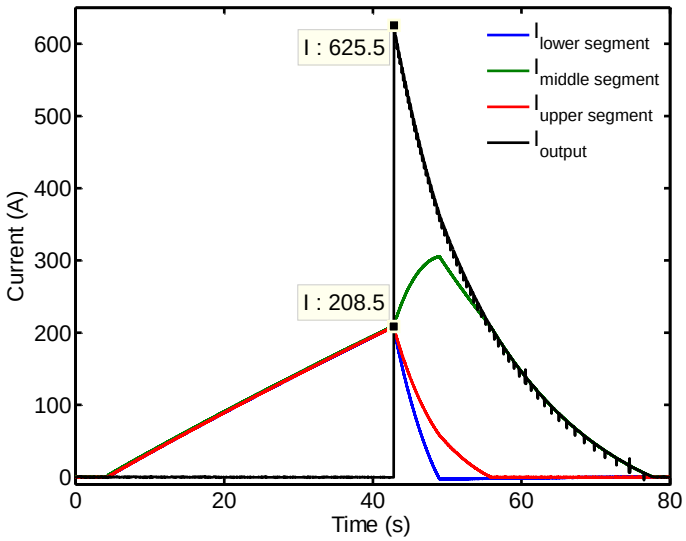

Figure 4-10 : Décharge XRAM à courant Maximum

Lors de cet essai, 60 kJ ont été dissipés dans une résistance simulant un lanceur, avec un rendement atteignant 67 % malgré la présence des commutateurs de puissance. Le courant dans l'élément milieu de la bobine inférieure a été surchargé jusqu'à 300 A lors de cet essai, sans être endommagé. Il avait préalablement été testé indépendamment des autres, jusqu'à un courant de 350 A.

La décharge séquentielle n'a par contre été testée qu'à faible puissance, avec des courants ne dépassant pas 60 A. Des essais supplémentaires seront nécessaires pour valider ce mode d'opération à la puissance nominale.

Conclusion

Ce travail de thèse a permis de démontrer théoriquement l'intérêt des SMES pour l'alimentation de lanceurs électromagnétiques en évaluant quantitativement les rendements atteignables. Ces travaux ont débouché sur le concept S^3EL de lanceur augmenté auto-alimenté, qui permet d'envisager la réalisation pratique de ce type de dispositifs, en particulier s'il est couplé avec le principe XRAM de multiplication du courant.

La conception du démonstrateur SMES II a permis d'obtenir un savoir-faire et une expérience capitale dans des domaines essentiels pour la réalisation de futurs démonstrateurs à très fort courant et grande puissance, notamment le refroidissement et l'isolation électrique des amenées de courant. Les résultats expérimentaux ont démontré, à échelle réduite, la validité des stratégies d'alimentation proposées.

Superconducting Magnetic Energy Storage using High Temperature Superconductor for Pulse Power Supply

Summary :

A SMES (Superconducting Magnetic Energy Storage) stores energy in the magnetic flux density created by a short-circuited coil. This work studies SMES using High Temperature Superconductor for pulse power applications, and more specifically for Electromagnetic Launcher powering. Comparison with conventional powering using capacitors is conducted and new adapted SMES designs are proposed for this application, leading to consequent gains in energy efficiency. In parallel, the feasibility of such system is investigated through the design and realization of a demonstrator. This demonstrator is an upgrade of an existing HTS SMES tested successfully in 2007. The tests of this new version validate technical solutions for the realization of high power HTS SMES, especially concerning the cooling system and the dielectric insulation.

This work was supported by the DGA (the French delegation for ordnance).

Superconducting Magnetic Energy Storage Haute Température Critique comme Source Impulsionnelle

Résumé :

Le principe d'un SMES (Superconducting Magnetic Energy Storage) est le stockage d'énergie dans l'induction magnétique créé par une bobine court-circuitée. Dans ce travail, les possibilités offertes par les SMES en matériau supraconducteur haute température critique sont étudiées pour l'application source impulsionnelle. L'étude est plus particulièrement orientée vers l'alimentation de lanceurs électromagnétiques, pour laquelle l'utilisation de SMES est comparée à l'alimentation conventionnelle par banc de condensateurs. Dans ce cadre, de nouveaux concepts de SMES adaptés à la charge sont proposés, permettant des gains conséquents en terme de rendement énergétique global. En parallèle, la faisabilité pratique d'une alimentation de lanceur par SMES est envisagée par la réalisation d'un démonstrateur. Celui-ci est une évolution d'un dispositif existant testé avec succès en 2007. La réalisation de ce démonstrateur a permis de valider des solutions technologiques concernant notamment le refroidissement et la tenue diélectrique d'un SMES hTc de forte puissance.

Ce travail est soutenu par la DGA (Délégation Générale pour l'Armement).